UNIVERSITÉ DE LORRAINE

ÉCOLE DOCTORALE IAEM - LORRAINE

Informatique, Automatique, Electronique-Electrotechnique, Mathématiques et Sciences de l'Architecture de l'Université de Lorraine

T H E S E

to obtain the title of

Docteur de l'Université de Lorraine

Mention Automatique, Traitement du Signal et des Images, Génie Informatique

Presented and publicly defended on September 27th, 2022 by

Victor COLAS

Modeling and estimation of human skin optical properties using spatially resolved autofluorescence and diffuse reflectance spectroscopy

Jury :

Reviewers:	Prof. Janis Spigulis	-	Latvia University
(president)	Prof. Christian Heinrich	-	Université de Strasbourg
Examiners:	Prof. Anne Humeau	-	Université d'Angers
	Prof. Dick Sterenborg	-	Amsterdam University
Guests:	Prof. Sylvain Gioux	-	Intuitive Surgical
	Prof. Wouter Saeys	-	KU Leuven
	Prof. James W.Tunnell	-	Texas University
Supervisor:	Prof. Walter Blondel	-	Université de Lorraine
Co-supervisors:	Prof. Christian Daul	-	Université de Lorraine
Advisors:	Dr. Marine Amouroux	-	Université de Lorraine

Acknowledgments/Remerciements

To begin, I would like to thank all the members of the jury for having responded favorably to our request to evaluate my thesis work, and especially the rapporteurs Prof. Spigulis and Prof. Heinrich for the examination of this manuscript. Thank you also to Prof. Sterenborg, Prof. Humeau and Prof. Gioux for accepting our invitation. Finally, a special thanks to Prof. W. Tunnell and Prof. Saeys for having constituted my thesis follow-up committee during these three years and foràààà having shared their precious advises and their expertise. I am very honored and grateful to present you the work done. Allow me now to switch to French for the continuation of the thanks.

En second lieu, je tiens à remercier mes directeurs de thèse, à commencer par Christian Daul, qui a toujours répondu rapidement et précisément à mes sollicitations. Merci pour ta disponibilité et tes nombreuses relectures durant ces trois années. Marine Amouroux, merci pour votre disponibilité, pour la confiance que vous m'avez fournie, et pour les nombreuses discussions scientifiques intéressantes que nous avons échangées. Je vous suis également très reconnaissant d'avoir patiemment partagé vos connaissances en anatomie cutanée (car je partais de très loin !), ainsi que de m'avoir donné l'opportunité d'assister aux opérations chirurgicale de Grégoire Khairallah que je remercie également. Enfin Walter Blondel, merci pour votre soutien durant ces trois années de thèse. Vous avez été disponible à chaque fois que j'en ai ressenti le besoin (disons plutôt presque à chaque fois, sans rancune !), tout en me laissant de la liberté et de l'autonomie pour mener à bien mon travail. Vous m'avez souvent permis de prendre du recul sur mes travaux quand j'avais parfois "la tête dans le guidon". J'ai beaucoup appris en travaillant à vos côtés. De manière plus générale, je vous remercie tous les trois pour votre bienveillance à mon égard, et j'espère sincèrement avoir été à la hauteur de la confiance que vous m'avez accordée.

Puis, j'aimerais remercier l'ensemble de l'équipe du labo, toujours disponible et bienveillante avec moi les rares fois où j'ai dû enfiler une blouse blanche ! Une mention particulière pour les collègues du midi avec qui les pauses repas, pleines de bonne humeur, ont toujours permis de se vider la tête avant de se remettre au travail l'après-midi. Un grand merci à Clarice, avec qui j'ai partagé de nombreuses journées enfermés en salle laser à concevoir notre manip, et dont la bonne humeur est toujours au rendez-vous, ce fût un plaisir ! Merci en particulier à Alicia et Valérie, que j'ai souvent sollicitées à la recherche d'équipements dans le labo, pour leur patience mais plus généralement pour leur bienveillance et leur dynamisme quotidien. Enfin, merci aux collègues les plus courageux avec lesquels j'ai partagé de belles soirées : mes amis russes Sergei, Maria (Bab Macha), Valentin et mexicain Fernando, ainsi que les autres Eddy (Malou), Maxime, Mickael, Justine, Yann, Cyril, Lucie, Sarah. Une mention spéciale pour les survivants de ma "promo" de doctorants, à savoir Manon et Alex (aka le boss, sauf au basket). Vous m'avez aidé à traverser les quelques moments (légèrement) plus difficiles au cours de ces trois dernières années, je vous en remercie.

Je finirai en remerciant mes proches, à savoir mes amis d'enfance qui m'ont toujours soutenu et compris durant ces (très) longues années d'études, les copains du foot de Jarville, et ceux de Supop (surtout Marin, incroyable de s'être retrouvés à San Francisco). Enfin à la famille, en commençant par mes grands-parents toujours d'une gentillesse sans pareil à mon égard. Je ne peux m'empêcher d'avoir une pensée à ceux qui ne sont plus là, à savoir mon arrière grand-mère qui nous a récemment quittés ainsi que mon grand-père. J'espère vous rendre fiers là où vous êtes.

Je dédie également ces remerciements à Asya avec qui je partage ma vie depuis huit magnifiques années, qui m'a accompagné et soutenu durant ce long marathon que sont les études supérieures. Enfin, je remercie mes parents et mon frère, sans qui je ne serai pas celui que je suis aujourd'hui. Vous êtes et serez toujours des exemples à suivre pour moi. Je ne vous remercierai jamais assez pour tout ce que vous m'avez apporté.

Contents

Acronyms

Notations

Symbol	Description		Unit
λ	-	Wavelength	$[nm]$
μ_a	-	Absorption coefficient	$[cm^{-1}]$
μ_s	-	Scattering coefficient	$[cm^{-1}]$
$\rho(\vec{u}, \vec{u}')$	-	Phase function between directions $\vec{u}$ and $\vec{u}'$	/
μ_s'	-	Reduced cattering coefficient ($\mu_s' = \mu_s(1-g)$)	$[cm^{-1}]$
μ_t	-	Exctinction coefficient ($\mu_t = \mu_s + \mu_a$)	$[cm^{-1}]$
$\mu_{a,fluo}$	-	Fluorophore absorption coefficient	$[cm^{-1}]$
ξ	-	Quantum efficiency	/
g	-	Anisotropy factor	/
D_n	-	Source-to-detector separation distance	$[\mu m]$
$AF_{Dn}(\lambda)$	-	Autofluorescence spectra at D_n distance	/
$DR_{Dn}(\lambda)$	-	Diffuse reflectance spectra at D_n distance	/
f_v	-	Volume fraction	/
$\varepsilon^m(\lambda)$	-	Mass extinction coefficient	$[cm^{-1}/(g.L^{-1})]$
$\varepsilon^M(\lambda)$	-	Molar extinction coefficient	$[cm^{-1}/(mol.L^{-1})]$
M	-	Molar mass	$[g.mol^{-1}]$
c	-	Mass concentration	$[g.L^{-1}]$
n	-	Refractive index	/
M_R	-	Total reflectance measurement	/
M_T	-	Total transmittance measurement	/
M_U	-	Unscattered transmittance measurement	/

List of Tables

List of Figures

Résumé Etendu (en français)

Contents

Introduction et définition des objectifs de thèse

Dans le contexte du **carcinome cutané**, la **biopsie optique** offre une alternative *in-vivo* non destructive à la biopsie conventionnelle pour informer le praticien dermatologue de l'état de santé du tissu en profondeur lors de la résection du cancer. Ce dernier est en effet à l'origine de **modifications morphologiques et physiologiques de la peau**, ce qui explique que les mesures optiques resultantes des interactions lumière/tissue y soient sensibles.

Les travaux présentés dans ce manuscrit sont relatifs aux données obtenues l'aide du dispositif de biopsie optique *SpectroLive* sur une centaine de patients juste avant la résection du cancer par le clinicien. Au contact de la peau, ce dispositif spectroscopique acquiert des signaux de **réflectance diffuse** (excitation large bande blanche) et d'**autofluorescence** (émission monochromatique pour exciter les fluorophores endogènes de la peau) **résolus spatialement**, *i.e.*, pour plusieurs distances de séparation entre la fibre émettrice de lumière est les fibres collectrices en périphérie. Cette résolution spatiale est particulièrement d'intérêt pour la peau, puisque les différentes distances introduites permettent de collecter des photons parcourant les différentes couches en profondeur (épiderme, derme et hypoderme) de l'organe.

L'essentiel des travaux présentés ici concerne **l'estimation des propriétés optiques de la peau** grâce à la **résolution du problème inverse** à partir de ces acquisitions cliniques. Cela consiste d'abord à établir une **simulation de transport de photons** fidèle aux caractéristiques (géométriques et spectrales) du dispositif réel avant de construire un modèle multicouche de la peau dans lequel les paramètres optiques (*e.g.* coefficients d'absorption et de diffusion, le facteur d'anisotropie) et géométriques (*e.g.* épaisseur des couches) peuvent être estimées par un processus d'optimisation visant à minimiser les différences entre les spectres générés par la simulation et les spectres "cibles" obtenus en clinique (fitting). Pour y parvenir, 3 axes de travail ont été développés durant les recherches de thèse :

1. **Développer pleinement la simulation :** Durant le processus d'optimisation qu'est le problème inverse, la comparaison entre les spectres clinique (expérimental) et numérique (simulé) est nécessaire et quantifiée par une erreur des moindres carrés. Cet axe de travail est liée aux développement de notre simulation (problème direct). Il s'agit tout d'abord de continuer l'ajustement de la simulation de transport de photons (développée par la précédante doctorante P.Rakotomanga) pour mieux correspondre au dispositif existant *SpectroLive*. Il s'agit ensuite d'également exploiter cette simulation, pour notamment enrichir l'analyse en profondeur de la

spectroscopie résolue spatialement, c'est à dire d'associer les différentes longueurs d'onde et distances de séparation source-détecteur du dispositif aux couches cutanées optiquement sondées. Un modèle de peau à 5 couches a été conçu dans lequel ont été identifiés les paramètres physiologiques à considérer variables pour représenter un large éventail de types de peau (intra- et inter-individuels), avant d'appliquer des outils numériques conçus pour caractériser la pénétration des photons dans les différents milieux cutanés résultants de ces propriétés physiologiques. Cette étude numérique approfondie permet une meilleure interprétation des spectres acquis en réflectance diffuse et en autofluorescence. Les principaux résultats associés à cet axe de travail sont (i) la distribution des profondeurs sondées, *i.e.*, la couche atteinte, par les photons détectés dans les spectres de réflectance diffuse en fonction de la longueur d'onde et de la séparation source-détecteur (voir contributions IC2, IC4), ainsi qu' (ii) une proposition de décomposition des spectres de reflectance diffuse selon la couche la plus profonde visitée (voir contribution IJ1).

2. **Adapter la résolution du problème inverses à la peau :** Cette partie se concentre sur l'estimation des propriétés optiques à partir de spectres acquis, afin de lier leur évolution spatiale autour de la lésion à leur état de santé. A partir de notre modèle de peau à 5 couches, il consiste à présenter les stratégies mises en place pour atteindre cet objectif, incluant l'établissement des paramètres variables pour s'adapter aux spectres cibles, ainsi que la conception d'algorithmes d'optimisation. En particulier, il est expliqué comment sont utilisées les informations obtenues numériquement sur la profondeur de pénétration des photons (décrite dans le paragraphe précédent) pour créer une méthode d'optimisation adaptée à la peau et ainsi remplacer la technique d'optimisation multi-paramètres conventionnelle utilisée jusqu'à présent. Les principaux résultats associés à cet axe de travail sont la présentation de ce processus séquentiel sur la résolution de problèmes inverses purement numériques (voir contribution IC5). Ce problème inverse purement numérique permet de connaître les paramètres qui ont généré le spectre cible et ainsi (i) d'assurer la convergence de la technique d'optimisation développée, ainsi que (ii) de la comparer avec des estimations issues d'autres processus d'optimisation. L'algorithme proposé augmente la vitesse et la précision des estimations des propriétés optiques.

3. **Standardisation et validation croisée :** Cette partie, plus axée sur la métrologie, peut être décomposée en deux tâches majeures. Le premier concerne le développement d'un banc optique avec des sphères d'intégration pour appliquer l'algorithme *Inverse Adding Doubling* à des échantillons de peau *ex-vivo*, qui fournit ses propriétés optiques. Les principaux résultats associés à cette tâche essentiellement instrumentale sont la comparaison des propriétés optiques estimées à partir (i) de la résolution du problème inverse de l'acquisition de *SpectroLive* et (ii) des mesures acquises à l'aide de ce montage optique, et ce pour des fantômes optiques liquides avec différents niveaux d'absorption et de diffusion (voir contribution IC7). La deuxième tâche concerne la standardisation des spectres expérimentaux de réflectance diffuse afin d'obtenir une unité d'intensité universelle commune à celle des spectres simulées, c'est-à-dire, le rapport entre la lumière détectée et la lumière émise. Le résultat principal associé à ce travail est la présentation d'un modèle photométrique expérimental et théorique qui nous affranchit de la dépendance (i) de la géométrie optique de la sonde du dispositif ainsi que (ii) de la mesure de calibration du blanc (au dessus d'un standard de reflectance à la réponse sepctrale plate) pour obtenir des spectres de réflectance diffuse dans l'unité d'intensité souhaitée (voir contributions IC6 et IJ2).

Le descriptif du manuscrit ci-dessous, expose comment sont repartis les axes de travail dans les différents chapitres qui le composent.

Developpement du manuscrit

Le Chapitre 1 pose les bases nécessaire à la compréhension des prochains chapitres de ce manuscrit. Partant des principes physiques de l'interaction lumière/matière (voir section 1.2.2) et de la description anatomique de la peau (voir section 1.3), les modalités optiques existantes pour sonder la peau *in-vivo* sont ensuite présentées (voir section 1.4), avant de se focaliser sur notre propre dispositif médical de biopsie optique, *i.e. SpectroLive* (voir section 1.4.2). L'état de l'art de la modélisation du transport de photons est enfin présenté (voir section 1.5) ainsi que la simulation de Monte Carlo modifiée pour s'adapter à notre dispositif clinique (voir section 1.5.2). Ce chapitre se conclut par la présentation du problème inverse (voir section 1.5.3).

Le Chapitre 2 concerne la mise à jour de notre simulation *i.e.* du problème direct. Il comprend tout d'abord l'amélioration du réalisme de la simulation pour mieux correspondre au dispositif médical (voir section 2.2), ainsi que la description des sorties numériques introduites pour améliorer l'analyse en profondeur de la spectroscopie résolue spatialement pour la sensibilité aux différentes couches cutanées (voir section 2.4). Un modèle de peau réaliste à 5 couches est ensuite développé dans lequel les paramètres physiologiques autorisés à varier ont été identifiés pour représenter une large gamme de type de peau (voir section 2.5), avant d'appliquer les algorithmes développés à ces différents tissus (voir section 2.6).

Le chapitre 3 se concentre sur la résolution du problème inverse. À partant de la description de l'état de l'art (voir section 2.6), la méthode actuelle utilisée jusqu'à présent pour estimer les paramètres (propriétés optiques et épaisseurs de couches) dans ce processus d'optimisation est ensuite présentée (voir section 3.2). Notre algorithme d'estimation séquentielle et adapté aux couches est ensuite présenté puis validé avec des cibles de spectres numériques (voir section 3.4). En parallèle, une normalisation des spectres expérimentaux de réflectance diffuse est présentée (voir section 3.5). En effet, celle-ci permet d'obtenir des spectres simulés et cliniques dans une même unité d'intensité, ce qui réduit l'écart entre eux et permet leur pleine comparaison lors de la résolution du problème inverse.

Le chapitre 4 traite de la conception d'un banc optique à double sphère intégrante développé en parallèle des travaux présentés jusqu'à présent pour la caractérisation *ex-vivo*, *i.e.* l'estimation de propriétés optiques, d'échantillons biologiques. En débutant avec un banc expérimental vide, les grandes étapes de la conception de ce banc optique sont présentées (voir section 4.3) ainsi que les mesures de validation associées (voir section 4.4). Nous présentons enfin les résultats d'expériences sur fantômes optiques comparant les estimations du banc avec celles obtenues à partir des techniques de résolution de problèmes inverses développées au chapitre 3 (voir section 4.5).

Conclusion et perspectives

Cette thèse intitulée "Modélisation et estimation des propriétés optiques de la peau humaine à l'aide de la spectroscopie d'autofluorescence et de réflectance diffuse résolue spatialement" a présenté les travaux réalisés pour caractériser optiquement la peau humaine dans le contexte du diagnostic du carcinome cutané. Ces **estimations des propriétés optiques** ont été rendues possibles grâce à la **résolution du problème inverse**, où les données expérimentales (acquises *in-vivo* lors d'une étude clinique) étaient des spectres d'autofluorescence et de réflectance diffuse résolus spatialement, à l'aide d'un simulation de transport de photons Monte Carlo modifiée pour correspondre aux acquisitions réelles. Notre travail s'est articulé autour de trois axes.

La première était de **garder la dimension clinique** dans notre résolution de problème inverse. Apporter une explication physiologique et morphologique aux spectres acquis était notre volonté. Cela s'est manifesté par la conception d'un modèle numérique de peau à 5 couches et dont les propriétés de diffusion et d'absorption sont directement liées aux concentrations de chromophores, ce qui permet d'ajuster les propriétés optiques pour représenter une large gamme de types de peau (intra- et inter-individu). Parmi les paramètres existants, les épaisseurs des couches épidermiques, la concentration de mélanine et le contenu sanguin dermique ont été considérés comme variables dans la résolution du problème inverse pour converger vers les spectres cibles. L'évolution locale de ces paramètres pourra alors être directement liée à l'état pathologique du tissu grâce à la base de données (en cours de développement) qui associe à chaque acquisition les résultats anamapathologiques. Des approches plus statistiques utilisant des méthodes de classification avec cette base de données seraient également intéressantes pour comparer les diagnostics issus de ces méthodes complémentaires.

La seconde était d'**améliorer les informations de profondeur** fournies par la résolution spatiale existante sur l'appareil. En effet, même si l'on savait que les courtes distances entre les fibres excitatrices et collectrices étaient associées à des trajectoires de photons moins profondes dans la peau, alors que les séparations plus grandes correspondaient à des trajectoires plus profondes, il était important de préciser ce comportement. En utilisant notre modèle de peau à 5 couches pour plusieurs configurations de peau, la simulation a été modifiée pour ajouter des sorties numériques afin de quantifier la propagation dans les couches de peau des photons détectés à différentes distances source-détecteur et à chaque longueur d'onde de l'appareil. Connaissant l'origine en profondeur de ces photons, il est alors plus facile d'interpréter les spectres résultants. Les connaissances acquises ont permis de mieux appréhender la résolution de problème inverse, en développant un algorithme d'optimisation qui estime séquentiellement le(s) paramètre(s) dans des couches cutanées isolées. L'application de cet algorithme à l'ensemble de données susmentionné de spectres cliniques est envisagée.

Enfin, la dernière consistait à apporter une **analyse métrologique aux mesures expérimentales**. Un banc optique incluant une sphère d'intégration a été conçu, permettant l'estimation des paramètres optiques d'échantillons *ex-vivo*. Bien que le travail présenté dans ce manuscrit porte davantage sur la conception de cette expérience, l'idée sous-jacente est d'utiliser prochainement ce banc comme moyen alternatif de comparer par validation-croisée les estimations de propriétés optiques *in-vivo* (à l'aide du dispositif spectroscopique clinique) avec celle obtenues grâce à ce banc optique. Une méthode de calcul (basée sur la photométrie) a également été fournie ainsi qu'une méthode expérimentale permettant d'exprimer les spectres expérimentaux de réflectance diffuse en unité absolue, *i.e.*, comme un rapport de lumière entre la quantité de lumière collectée et envoyée. Bien qu'elles méritent d'être améliorées, ces techniques permettent d'obtenir des spec-

tres dont l'intensité est directement (sans normalisation) comparable à celles des spectres issus de la simulation numérique, ce qui est évidement d'intérêt pour la résolution du problème inverse.

Publications scientifiques

Cette thèse a donné lieu à la parution de publications scientifiques, listées selon leurs natures ci-dessous.

Chapitre de livre

[BC1] Blondel, W., Amouroux M., Zaytsev S., Genina E., Colas V., Daul C., Pravdin A. and Tuchin V. (2022) "Chapter 5: Human skin autofluorescence and optical clearing", p.109-126 In "Handbook of Tissue optical clearing: New prospects in optical imaging", Valery Tuchin, Dan Zhu and Elina Genina Editors, Firt Edition, CRC Press 2022, Taylor & Francis Group LLC, pp.658 DOI: 10.1201/9781003025252 ISBN: 978-0-367-89509-9 (hbk) ISBN: 978-1-032-11869-7 (pbk) ISBN: 978-1-003-02525-2 (ebk) hal03559189

Journaux internationaux

[IJ1] Colas V., Blondel W., Khairallah G., Daul C. and Amouroux M. (2021) "Proposal for a skin layer-wise decomposition model of spatially-resolved diffuse reflectance spectra based on maximum depth photon distributions: a numerical study," *Photonics*, 8(10):444. hal-03377401 https://doi.org/10.3390/photonics8100444

[IJ2] Colas V., Amouroux M., Perrin-Mozet C., Daul C. and Blondel W. (2022) "Theoretical definition and experimental validation of an absolute correction factor to standardize the amplitudes of spatially resolved diffuse reflectance spectra simulated and acquired on an optical phantom," *Journal of Biomedical Optics*, *(Seulement soumis)*

Conférences internationales

[IC1] Blondel, W., Amouroux M., Zaytsev S., Genina E., Colas V., Daul C., Pravdin A. and Tuchin V. (2020) "Skin autofluorescence modifications during optical clearing, " SFM'20 8th International Symposium "Optics and Biophotonics" – 24th International School for Junior Scientists and Students on Optics, Laser Physics & Biophotonics, Saratov, Russia, Sept. 28- Oct. 2. hal-03018552 *(Conférence invitée)*

[IC2] Colas V., Daul C., Khairallah G., Amouroux M. and Blondel W. (2020) "Spatially resolved diffuse reflectance and autofluorescence photon depth distribution in human skin: modeling study," In SPIE/COS Photonics Asia (Digital Forum), Optics in Health Care and Biomedical Optics X; 115531B, Oct 11-16, Beijing, 11553-49, hal-03018788 *(Oral à distance)*

[IC3] Blondel W., Zaytsev, S., Colas V., Khairallah G., Rakotomanga P., Genina E., Soussen C., Daul C., Tuchin V. and Amouroux M. (2020) "Study of the impact of optical clearing on skin absorption, scattering and autofluorescence properties," In 19th International Conference on Laser Optics ICLO 2020 – 6th International Symposium on Lasers in Medicine and Biophotonics, St Petersburg, Russia, Nov. 2-6. hal-03018569 *(Conférence invitée)*

[IC4] Colas V., Daul C., Khairallah G., Amouroux M. and Blondel W. (2021) "Influence of human epidermal thickness on penetration depth of detected photons in spatially-resolved diffuse reflectance spectroscopy: a numerical study," In SPIE Proceedings, Optical Interactions with Tissue and Cells XXXII, 116400H, SPIE Photonics West conference, March 28-31, Online only, https://doi.org/10.1117/12.2578203 hal-03507088 *(Oral à distance)*

[IC5] Colas V., Daul C., Khairallah G., Amouroux M. and Blondel W. (2022) "Improved estimation of the optical properties in a skin five-layer model from spatially resolved diffuse reflectance spectra using a layer-by-layer approach and optimized combinations of wavelengths and source-detector distances," In SPIE Proceedings, Biomedical applications of light scattering XII, 11974-21, SPIE Photonics West conference, February 21-27, hal-03560298 *(Poster sur site)*

[IC6] Colas V., Daul C., Khairallah G., Amouroux M. and Blondel W. (2022) "Theoretical definition and experimental validation of an correction factor to standardize the absolute magnitude of simulated and clinical spatially-resolved diffuse reflectance spectra," In SPIE Proceedings, Biomedical applications of light scattering XII, 11974-4, SPIE Photonics West conference, February 21-27, hal-03560273 https://doi.org/10.1117/12.2606372 *(Oral sur site)*

[IC7] Colas V., Amouroux M., Daul C., Perrin-Mozet C. and Blondel W. (2022) "Comparative study of optical properties estimation on liquid optical phantoms using spatially-resolved diffuse reflectance spectroscopy and double integrating spheres methods," In SPIE Proceedings, Tissue Optics and Photonics II, 12147-7, SPIE Photonics Europe, April 3-7, Strasbourg, France. hal-03692406 https://doi.org/10.1117/12.2621496 *(Oral sur site)*

[IC8] Colas V., Amouroux M., Daul C., Perrin-Mozet C. and Blondel W. (2022) "Human skin optical properties modelling and estimation using autofluorescence and diffuse reflectance spectroscopy," In SPIE Proceedings, 9th annual Sino-French "Photonics and Optoelectronics" PHOTONET International Research Network Workshop, SPIE Photonics Europe, April 3-7, Strasbourg, France. hal-03692425 *(Conférence invitée)*

General Introduction

Contents

Context of the work

Biopsy is a medical act that consists in taking a biological sample from a tissue, or several if necessary, for the purpose of diagnosing a potential malignant state of that tissue, in particular to determine the type and stage of a **skin cancer** thanks to of anatomopathology or histopathology examinations. The analyses are carried out *a posteriori*, after removal of the tissue. Further examinations may be done according to the lesion edge estimation to ensure the non cancer recurrence. These medical examinations are very common and guarantee the diagnosis. However, they are expensive, invasive and traumatic procedures requiring removal of samples that leave scars on the patient. Methods have therefore emerged to improve both the diagnosis and the well-being of the patient by limiting invasive procedures and by lowering the cost. The **optical biopsy** is one of the alternatives. It consists in analyzing the tissue answer to light excitation, to get information about the state of a biological tissue. Its name comes from the fact that this non-invasive method aims to provide real-time and non-invasive diagnostic information to the clinician in order to (i) improve the efficiency in the biospsy sampling and (ii) help surgical guiding. The access to its information is allowed by classification methods or/and inversion of light propagation models. The final aim is the detection of pre-cancers and skin cancers for tissue resection, *i.e.*, to assist in locating and characterize the area of cancerous tissue among healthy tissue.

The skin is organized in layers: epidermis, dermis and hypodermis and has a number of chromophores such as melanin and hemoglobin. The **optical properties of the skin** (absorption, scattering or fluorescence) **reflect its structure and metabolism** from the sub-cellular to the tissue level. In the presence of a cancerous lesion, the cellular and tissue organization is modified and the biological and biochemical composition also changes. This is responsible for the modification of the optical properties of the skin. The analysis of their evolution provide appropriate information to diagnose the pathological state of the tissue. The main difficulty lies in **identifying the optical parameters** located in the various deep layers of the skin. Indeed, the opacity of the skin is a barrier to deep photon propagation.

All the experimental data used in this thesis come from acquisitions carried out using a **spatially resolved multi-modality optical spectroscopy system**, coupling measurements of **diffuse reflectance** (broadband excitation) spectra and **autofluorescence** (monochromatic excitation) spectra under multiple excitations. Spatial resolution, *i.e.*, the fact of introducing several distances between the light-emitting fiber in contact with the skin and detecting fibers connected to the spectrometer, allows to be sensitive to photons coming from different depth origins. Indeed, photons detected at a short/large source-to-detector distance result from shallow/deep trajectories into the biological tissues under evaluation. This optical biopsy device, called *Spectrolive*,

was designed by our lab and is undergoing a validation clinical trial to aid in the diagnosis of cutaneous carcinomas (the acquisitions were made at the Metz-Thionville CHR, 140 patients).

A way **to get the discriminating optical properties** from its acquisitions **is to solve the inverse problem** that consists in establishing a **photons transport simulation** that considers both the device features (geometrical and optical) and a skin multi-layer model in which optical (*e.g.* absorption and scattering coefficients, anisotropy factor) and geometrical (*e.g.* layer thicknesses) features can be estimated through an optimization process to fit clinically acquired "target" spectra. As opposed to the inverse problem, the direct problem consists in generating simulated signals from this simulation, by providing all the parameters of the skin layers under the probe. This thesis is mainly related to the inverse problem solving, *i.e.*, the estimation of skin optical properties in a skin five layer skin model thanks to a designed simulation that generate numerical acquisitions of a spatially-resolved multi-modalities spectroscopy device similarly to the clinical device. To achieve this purpose, the 3 following axes of works were developed:

1. **Direct problem improving and analyzing:** The inverse problem solving fitting procedure requires a comparison between clinical (experimental) and numerical (simulated) spectra, that is often quantified by a least square error cost function. This line of work is related to the changes introduced in our simulation. It firstly concerns the adjustment of the photon transport simulation (developed by a previous PhD student P.Rakotomanga) to better correspond to the *SpectroLive* probe. Then, it also consists in fully exploiting this simulation, for in particular enhance the numerical depth analysis of spatially resolved spectroscopy for skin layers optical probing. A 5-layer skin model was designed in which are identified the physiological variable parameters to represent a wide range of skin types (intra- and inter-individual), before applying designed numerical tools to characterize photons penetration in resulting various skin media. This numerical depth study enables the better interpretation of diffuse reflectance and autofluorescence acquired spectra. Main results associated to this axis of work are the distribution of probed depth, *i.e.*, the layer reached, by detected photons in diffuse reflectance spectra according to the wavelength and the source-to-detector separation (see contributions IC2, IC4), as well as the same spectra decomposition according to the deepest layer visited (see contribution IJ1).

2. **Adapting inverse problem solving to skin:** This part focuses on the optical properties estimation from acquired spectra, in order to link their spatial evolution around the lesion to their healthy state. Starting from our 5-layer skin model, it consists in presenting the strategies put in place to achieve this goal, including the establishing of the variable parameters to fit the target spectra, as well as the design of optimization algorithms. Especially, it is explained how is used the information numerically obtained about photons depth penetration (described in the previous paragraph) to create a skin-adapted optimization method to replace the conventional multi-parameter optimization technique used so far. Main results associated to this axis of work are the presentation of this sequential process on purely numerical inverse problem solving (see contribution IC5). This purely numerical inverse problem allows to know the parameters that generated the target spectrum and thus (i) to ensure the convergence of the optimization technique developed, as well as (ii) to compare it with estimations from other optimization processes. The proposed algorithm increases the speed and accuracy of the optical properties estimates.

3. **Standardization and cross-validation:** This part, more focused on metrology, can be bro-

ken down into two major tasks. The first one is about developing an optical bench with integrating spheres to apply Inverse Adding Method to *ex-vivo* skin samples, which provides its optical properties. Main results associated to this mostly instrumental task are the comparison of optical properties estimated from (i) solving the inverse problem from *SpectroLive* acquisition and (ii) from measurements acquired using this optical set-up, and this for liquid optical phantoms with different levels of absorption and scattering (see contribution IC7). The second task concerns the standardization of the experimental diffuse reflectance spectra in order to obtain a universal intensity unit common to the simulated ones, *i.e.*, the ratio between the detected and the emitted light. The main result associated to this work is the presentation of an experimental and theoretical photometric model that free us from the dependence of (i) the optical probe geometry of the device as well as (ii) the white calibration measurement (100% flat spectral answer) to obtain diffuse reflectance spectra in the desired intensity unit (see contributions IC6 and IJ2).

Manuscript organization

Chapter 1 lays the groundwork for understanding the PhD work appearing in the next chapters of this manuscript. Starting from the physical basis of light interaction and the anatomical description of the skin, the existing optical modalities to *in-vivo* probe the skin is then presented, before focusing on our medical device, *i.e. SpectroLive*. The photon transport modeling state of the art is finally presented as well as the Monte Carlo simulation modified to fit our clinical device from which the skin optical properties are estimated by solving the inverse problem.

Chapter 2 is related to the direct problem upgrade. It firstly includes the simulation realism improvement to better correspond to the medical device, as well as the description of numerical outputs introduced to enhance the depth analysis of the spatially-resolved spectroscopy for skin layers optical probing. A realistic 5-layer skin model is developed in which the physiological parameters allowed to vary were identified to represent a wide range of skin type, before applying the developed algorithms to these different tissues.

Chapter 3 focuses on the inverse problem solving. Starting from the state of the art description, the current method used so far to estimates parameters (optical properties and layers thicknesses) in this optimization process is then presented. Our sequential and layer adapted estimation algorithm is then exposed and validate with numerical spectra target. Also, our experimental diffuse reflectance standardization is presented. Indeed, this one allows to get simulated and clinical spectra in the same intensity unit, which reduce the gap between them and allow their full comparison during the inverse problem solving.

Chapter 4 deals with the design of a double integrating sphere optical bench developed in parallel with the work presented so far to *ex-vivo* characterize, *i.e.* estimate the optical properties, biological samples. Having started from an empty bench, the major steps in the design of this optical bench are pointed and the associated validation measurements, before presenting the

results of experiments on optical phantoms comparing the estimates of the bench with those obtained from the inverse problem solving techniques developed in Chapter 3.

Scientific contributions

Book chapter

[BC1] Blondel, W., Amouroux M., Zaytsev S., Genina E., Colas V., Daul C., Pravdin A. and Tuchin V. (2022) "Chapter 5: Human skin autofluorescence and optical clearing", p.109-126 In "Handbook of Tissue optical clearing: New prospects in optical imaging", Valery Tuchin, Dan Zhu and Elina Genina Editors, Firt Edition, CRC Press 2022, Taylor & Francis Group LLC, pp.658 DOI: 10.1201/9781003025252 ISBN: 978-0-367-89509-9 (hbk) ISBN: 978-1-032-11869-7 (pbk) ISBN: 978-1-003-02525-2 (ebk) hal03559189

International journals

[IJ1] Colas V., Blondel W., Khairallah G., Daul C. and Amouroux M. (2021) "Proposal for a skin layer-wise decomposition model of spatially-resolved diffuse reflectance spectra based on maximum depth photon distributions: a numerical study," *Photonics*, 8(10):444. hal-03377401 https://doi.org/10.3390/photonics8100444

[IJ2] Colas V., Amouroux M., Perrin-Mozet C., Daul C. and Blondel W. (2022) "Theoretical definition and experimental validation of an absolute correction factor to standardize the amplitudes of spatially resolved diffuse reflectance spectra simulated and acquired on an optical phantom," *Journal of Biomedical Optics*, *(Submitted)*

International conferences

[IC1] Blondel, W., Amouroux M., Zaytsev S., Genina E., Colas V., Daul C., Pravdin A. and Tuchin V. (2020) "Skin autofluorescence modifications during optical clearing, " SFM'20 8th International Symposium "Optics and Biophotonics" – 24th International School for Junior Scientists and Students on Optics, Laser Physics & Biophotonics, Saratov, Russia, Sept. 28- Oct. 2. hal-03018552 *(invited lecture)*

[IC2] Colas V., Daul C., Khairallah G., Amouroux M. and Blondel W. (2020) "Spatially resolved diffuse reflectance and autofluorescence photon depth distribution in human skin: modeling study," In SPIE/COS Photonics Asia (Digital Forum), Optics in Health Care and Biomedical Optics X; 115531B, Oct 11-16, Beijing, 11553-49, hal-03018788 *(remote oral)*

[IC3] Blondel W., Zaytsev, S., Colas V., Khairallah G., Rakotomanga P., Genina E., Soussen C., Daul C., Tuchin V. and Amouroux M. (2020) "Study of the impact of optical clearing on skin absorption, scattering and autofluorescence properties," In 19th International Conference on Laser Optics ICLO 2020 – 6th International Symposium on Lasers in Medicine and Biophotonics, St Petersburg, Russia, Nov. 2-6. hal-03018569 *(invited lecture)*

[IC4] Colas V., Daul C., Khairallah G., Amouroux M. and Blondel W. (2021) "Influence of human epidermal thickness on penetration depth of detected photons in spatially-resolved

diffuse reflectance spectroscopy: a numerical study," In SPIE Proceedings, Optical Interactions with Tissue and Cells XXXII, 116400H, SPIE Photonics West conference, March 28-31, Online only, https://doi.org/10.1117/12.2578203 hal-03507088 *(remote oral)*

[IC5] Colas V., Daul C., Khairallah G., Amouroux M. and Blondel W. (2022) "Improved estimation of the optical properties in a skin five-layer model from spatially resolved diffuse reflectance spectra using a layer-by-layer approach and optimized combinations of wavelengths and source-detector distances," In SPIE Proceedings, Biomedical applications of light scattering XII, 11974-21, SPIE Photonics West conference, February 21-27, hal-03560298 *(poster)*

[IC6] Colas V., Daul C., Khairallah G., Amouroux M. and Blondel W. (2022) "Theoretical definition and experimental validation of an correction factor to standardize the absolute magnitude of simulated and clinical spatially-resolved diffuse reflectance spectra," In SPIE Proceedings, Biomedical applications of light scattering XII, 11974-4, SPIE Photonics West conference, February 21-27, hal-03560273 https://doi.org/10.1117/12.2606372 *(oral)*

[IC7] Colas V., Amouroux M., Daul C., Perrin-Mozet C. and Blondel W. (2022) "Comparative study of optical properties estimation on liquid optical phantoms using spatially-resolved diffuse reflectance spectroscopy and double integrating spheres methods," In SPIE Proceedings, Tissue Optics and Photonics II, 12147-7, SPIE Photonics Europe, April 3-7, Strasbourg, France. hal-03692406 https://doi.org/10.1117/12.2621496 *(oral)*

[IC8] Colas V., Amouroux M., Daul C., Perrin-Mozet C. and Blondel W. (2022) "Human skin optical properties modelling and estimation using autofluorescence and diffuse reflectance spectroscopy," In SPIE Proceedings, 9th annual Sino-French "Photonics and Optoelectronics" PHOTONET International Research Network Workshop, SPIE Photonics Europe, April 3-7, Strasbourg, France. hal-03692425 *(invited lecture)*

Chapter 1

Theory of photon transport in skin: from light/matter interactions to modeling applied to skin cancer diagnosis

Contents

1.1 Introduction

This introductory chapter provides the necessary elements to place the thesis work and objectives in their general context. Starting from the existing light/matter interactions theory, this chapter also develops the skin physiology and pathophysiology before explaining how optical biopsies can be exploited to distinguish healthy skin from skin cancer, especially carcinoma. Then, the discussion focuses on the work of our research team, describing our multi-modality optical device and the way we exploit the generated spectroscopic signals to characterize skin and specifically estimate its optical properties through inverse problem solving using a photon transport numerical simulation. Finally, this chapter concludes with the presentation of the different thesis objectives which will be successively developed in the following chapters.

1.2 Fundamental basics

The aim here is to provide the theoretical elements necessary to understand photon transport within a medium. After some quick reminders on the notion of light, this section will present the optical parameters involved in the propagation of light in a medium.

1.2.1 The wave-corpuscle duality

In some experiments, light obeys the wave physics of electromagnetism while in others it behaves like a particle. This ambivalence is called wave-corpuscle duality.

- **The wave model :** Maxwell's theory established in the XIX^e century presents light as a beam of electromagnetic waves propagating in the vacuum at the speed of light $c = 3 \times 10^8\ m.s^{-1}$. Like any wave, light is characterized by its wavelength (the distance between two consecutive mamximas of the wave), called λ and often expressed in nm. The frequency ν, expressed in Hz, is the number of oscillations made by the wave during one second. These two quantities are then linked by the relation:

$$\nu = \frac{c}{\lambda} \tag{1.1}$$

  Light is the part of the electromagnetic spectrum for which the λ wavelength verifies $10^{-8}m < \lambda < 10^{-4}m$. This spectral region and its division into 3 parts: Ultra-Violet (UV), visible and Infrared (IR) are represented graphically in Fig. 1.1.

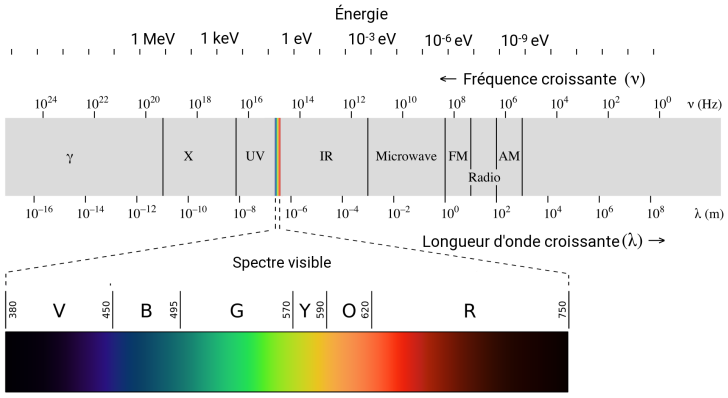

Figure 1.1: Region called "light" in the electromagnetic wave spectrum. The picture is adapted from [Moreau 2019].

- **The corpuscular model :** In the corpuscular case, the elementary particle of light is called a photon. In this model, the global behaviour of light is then described by the sum of all the individual contributions of each photon. Each photon carries an energy E_{photon} expressed in Joules (J) (sometimes in electronVolt (eV)) proportional to its optical frequency ν :

$$E_{photon}(\nu) = h \times \nu$$

With h the Planck's constant. By coupling this relation and the previous one in Eq. (1.1), we finally obtain an expression of the photon energy as a function of its wavelength:

$$E_{photon}(\lambda) = h \times \frac{c}{\lambda} \tag{1.2}$$

1.2.2 Light-biological medium interactions

Previous section allowed to introduce the elementary particle of light called the photon. Here, the existing interactions between light and matter from the corpuscular point of view will be presented.

1.2.2.1 Absorption

The propagating photon can transmit its energy to a particle (typically an atom) initially in its ground state E_0, allowing its valence electrons to enter an excited state E_1. The absorbed photon becomes devoid of energy, then disappears. The energy given up to the atom can then be used by the latter in different ways which are referred as non-radiative emission: dissipation of energy in the form of heat in the medium, agitation of the medium (called emission of a phonon, the basis of the vibrational spectroscopy [Nader 2010]) or emission of a less energetic photon. The latter is called fluorescence and will be developed in next section.

To describe the absorbent potential of a medium, it is usual to introduce the absorption coefficient μ_a which is homogeneous to the inverse of a distance (often expressed in cm^{-1}). Its physical interpretation is as follows: it is the average number of absorption events within the medium per unit of length. We often introduce the inverse quantity noted l_a, more easily interpretable since it is the average distance traveled in the medium by the photon before being absorbed (a schematic representation illustrates this parameter in Fig. 1.2). As introduced earlier, absorption is an energetic phenomenon (*cf.* Fig. 1.2). The values of this optical parameter are linked to the energy of the light quanta and thus to the wavelength λ according to Eq. (1.1). One obtains then the following relation:

$$\mu_a(\lambda) = \frac{1}{l_a(\lambda)} \tag{1.3}$$

From a macroscopic point of view, and for a purely absorbing medium, absorption is simply modelled by Beer-Lambert's law. By introducing $\Phi_{ph}(0, \lambda)$ the incident flux (in $J.s^{-1}$) and $\Phi_{ph}(z, \lambda)$ the transmitted photon flux after having traveled a depth z in the medium, we obtain the relation :

$$\Phi_{ph}(z, \lambda) = \Phi_{ph}(0, \lambda) e^{-\mu_a(\lambda) z} \tag{1.4}$$

1.2.2.2 Scattering

This effect has similarities with absorption, since it is also an energy interaction between the photon and a particle in the medium. The difference remains in the following nuance: the energy brought by the photon to the particle in question is not sufficient for it to reach an excited state. This is called the virtual energy state $E_{virtual}$, and the particle then returns to its ground state, emitting a photon with an energy similar to that of the incident photon. Because of this conservation of energy, diffusion is called elastic scattering. There are cases of inelastic scattering, where the emitted wavelength is longer than the incident one, called Raman scattering ([Nader 2010]).

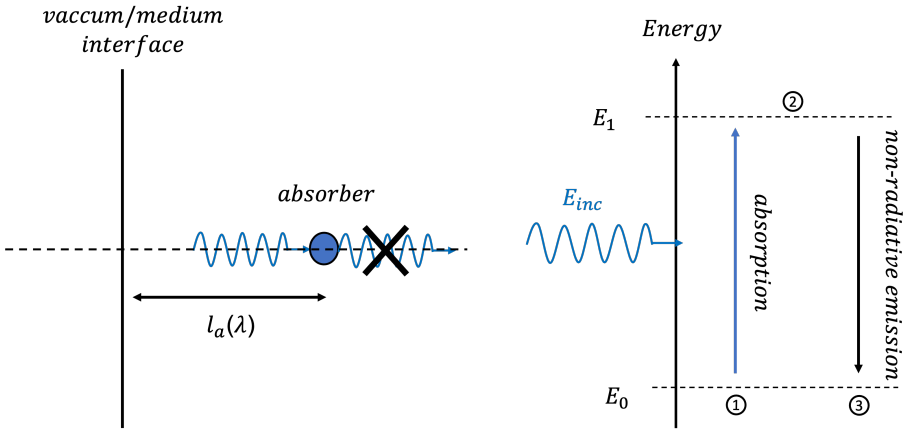

Figure 1.2: Physical meaning of parameter $l_a(\lambda)$ (left) and energy diagram associated with absorption (right).

Analogous to absorption, scattering is represented by the coefficient μ_s (illustration of this parameter meaning in Fig. 1.3), as well as by the mean characteristic distance of diffusion in the medium l_s. Both parameters are linked by:

$$\mu_s(\lambda) = \frac{1}{l_s(\lambda)} \tag{1.5}$$

From an energy standpoint, scattering is neutral (*cf.* Fig. 1.3). It manifests itself by the deviation between the incident photon and the scattered photon.

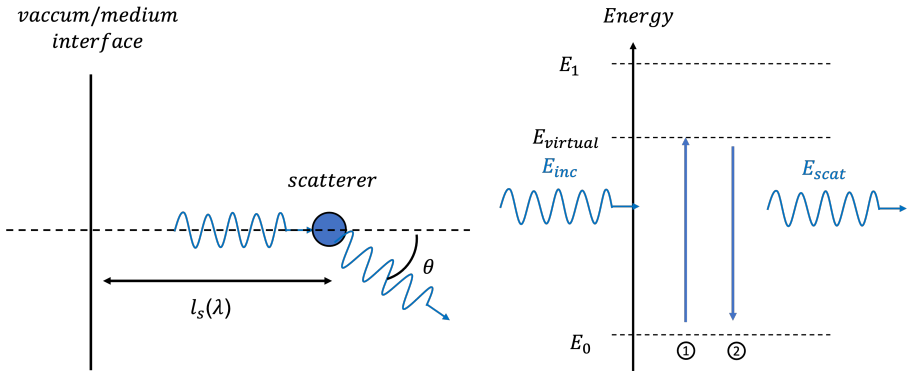

Figure 1.3: Physical meaning of the parameter $l_s(\lambda)$ (left) and energy diagram associated with scattering (right).

An information about the deviation is given by the following parameter: the phase function ρ. By introducing an incident direction $\vec{u}$ and the direction $\vec{u}'$of the scattered photon, as well as an elementary solid angle $d\Omega$, ρ is defined as the ratio of the elementary photons flux $d\Phi_{ph}(\vec{u},\vec{u}')$ coming from $\vec{u}$ direction and sent in the solid angle $d\Omega$ in the direction $\vec{u}'$ to the total flux $\Phi_{ph-tot}(\vec{u})$ scattered in all directions:

$$\rho(\vec{u},\vec{u}') = \frac{1}{d\Omega}\frac{d\Phi_{ph}(\vec{u},\vec{u}')}{\Phi_{ph-tot}(\vec{u})} \tag{1.6}$$

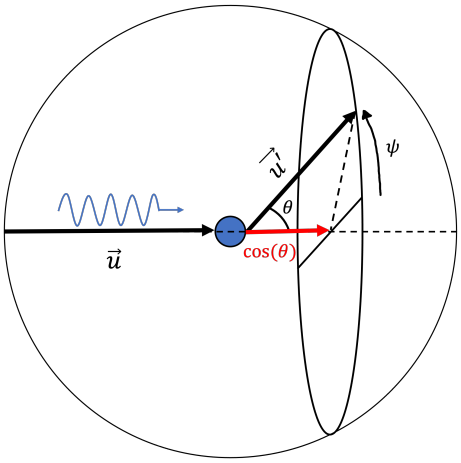

Figure 1.4: Physical meaning of the parameter $g(\lambda)$.

More simply, the phase function gives the probability per unit solid angle for a photon propagating with the direction $\vec{u}$ of being scattered in the direction $\vec{u}'$. Assuming that the scatterers are randomly distributed over the volume of the tissue, without any correlation, it is assumed that this phase function can be more simply written $\rho(\theta)$ with θ being the angle formed between the two vectors of incident and scattered directions (*cf.* Fig. 1.3).
So far, the phase function treats the angles θ on a case-by-case basis, *i.e.*, $\theta \in [0, \pi]$ assuming axial symmetry ($\rho(\theta) = \rho(-\theta)$) of the scattering. To synthesize the information contained in this phase function into a single parameter, the anisotropy coefficient $g(\lambda)$ was introduced. It is defined as the average of the $cos(\theta)$, with θ being the angle between the scattered and incident directions:

$$g = \int_0^{\pi} \rho(\theta) cos(\theta) 2\pi sin(\theta) d\theta = < cos(\theta) > \tag{1.7}$$

This expression implies rotational symmetry around the propagation axis of the incident photon, which is why the azimuth angle ψ appearing in Fig. 1.4 is not present in the expression of g in Eq. (1.7). The description of three singular values of g facilitates the physical understanding of the parameter:

- $g = 1$: The average of $cos(\theta)$ is worth 1, in other words $\theta = 0$. In this situation, the scattered photons follow the same direction as the incident photon.
- $g = 0$: The average $cos(\theta)$ is 0, which means that θ follows a uniform probability law over $[0 - \pi]$. No direction is privileged, so we call it isotropic scattering.
- $g = -1$: The average $cos(\theta)$ value is -1, in other words $\theta = \pi$. For such value of g, the scattered photons are then re-emitted to the source. This is called back-scattering.

Finally, it is interesting to note that this parameter is strongly related to the diameter a of the scattering particle. Using a, it is usual to introduce the size parameter $X(\lambda)$ defined as:

$$X(\lambda) = \frac{2\pi a}{\lambda} \tag{1.8}$$

As shown in Fig. 1.5, the orders of magnitude of the size parameter define the diffusion regime:

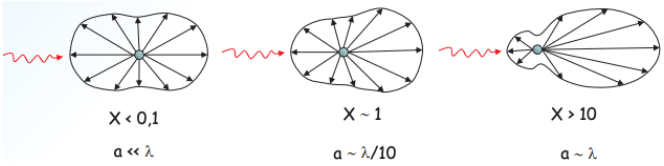

Figure 1.5: Three scattering regimes depending on the value of the size parameter $X(\lambda)$. Illustration taken from Julien Moreau course material [Moreau 2019].

- $X << 1$**:** Rayleigh's scattering, isotropic. g close to 0.
- $X \approx 1$**:** Mie's scattering, anisotropic and directive. g close to -1 or 1.
- $X >> 1$**:** Specular scattering, obeying the laws of geometric optics. $g = 1$ or $g = -1$.

To characterize the scattering with a single optical parameter (rather than with the two parameters μ_s and g), the reduced scattering coefficient is often used. This one can be linked to the scattering coefficient and the anisotropy factor according:

$$\mu_s'(\lambda) = \mu_s(\lambda)(1 - g(\lambda)) \tag{1.9}$$

1.2.2.3 Linear extinction coefficient

For a medium characterized by both scattering and absorbing properties, it is usual to introduce the linear extinction coefficient μ_t. The latter reflects the probability per length element that the photon is either scattered or absorbed. It is defined as the sum of the scattering and absorption coefficient, *i.e.*:

$$\mu_t(\lambda) = \mu_a(\lambda) + \mu_s(\lambda) \tag{1.10}$$

1.2.2.4 Fluorescence

As mentioned in section 1.2.2.1, fluorescence is a particular form of absorption. Let's first consider this phenomenon from an energy perspective (see Fig. 1.6). The energy photon E_{inc} is first absorbed, and allows the particle to reach an unstable energy level E_2. This is followed by a non-radiative energy loss up to E_1. This step has a duration of the order of nanoseconds. Finally, the particle returns to its fundamental state E_0, via a radiative de-excitation (emission of a photon). The energy of the fluorescent photon then worth $E_{fluo} = E_{inc} - \Delta E$, where $\Delta E = E_2 - E_1$.

According to Eq. (1.2), this loss of energy to the fluorescent photon is responsible for a change in wavelength: $\lambda_{fluo} > \lambda_{inc}$. This is known as redshift phenomenon. The photon is then sent in a new random direction. A fluorophore is also characterized by its quantum efficiency ξ. The fluorophore is primarily an absorber, and does not systematically emit a fluorescent photon, the quantum efficiency is defined as the ratio between the number of photons actually fluoresced and the number of photons absorbed by the fluorophore. Fig. 1.6, shows that the fluorophore is characterized by its E_1 and E_2 energy bands, since they are associated to the absorption and emission wavelengths. In reality, it is not a matter of discrete levels but rather of bands of energies. This energy range is then responsible for a certain width in the absorption and emission spectra

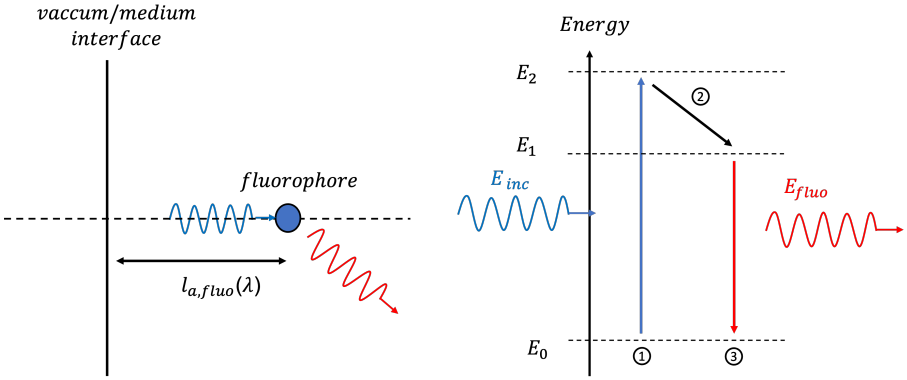

Figure 1.6: Physical meaning of parameter $l_{a,fluo}(\lambda)$ (left) and energy diagram associated with a fluorescence event (right).

of the fluorophores. An absorption coefficient is introduced, similarly to a pure absorber:

$$\mu_{a,fluo}(\lambda) = \frac{1}{l_{a,fluo}(\lambda)} \tag{1.11}$$

The emission is described by a probability density. The fluorescence emission wavelength λ_{fluo} then follows the probability law associated with this density.

1.3 Skin physiology and pathophysiology

This section presents some elements related to the anatomy of human skin. It will start with an overview of the architecture of the skin, the composition of its different layers, its optical behaviour and its evolution when a person develops a cutaneous carcinoma.

1.3.1 The skin: a multi-layered organ

The skin is a multi-layered organ (see Fig. 1.7) that covers almost the entire human body. As the true envelope of the body, it ensures several vital functions such as physical barrier and thermal isolation. The goal is not to make here an an exhaustive description of the skin, but of quickly presenting a simplified architecture of this one. More details are available in M. Amouroux's thesis [Amouroux 2008].

1.3.1.1 The epidermis

The epidermis is a continuously regenerating stratified epithelium where a gradual differentiation, called keratinization, appears from the bottom of the layer to the surface. This layer is bloodless. The sub-division of the layer, located just above the dermis, which produce the keratynocite cells (95% of the cells are keratynocites) is called the basal layer. The keratynocites gradually migrate to the surface, becoming less and less viable. Once fully differentiated, they become corneocytes. The interface between the body and the environment is then made up of these dead cells, constituting the *stratum corneum*. Its width varies with the location on the body. It can be constituted of about ten corneocytes cellular foundations (*i.e*, about 20 μm) for the skin of the neck, while its width reaches several hundreds of cellular layers (*i.e*, about 250 μm) for the sole of the foot. The total thickness of the epidermis is then in the interval $[120 - 350]$ μm.

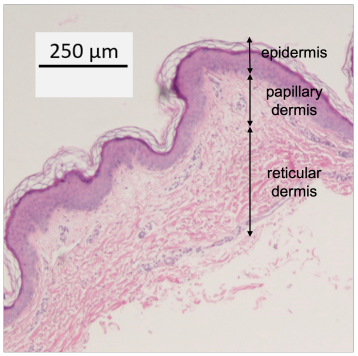

Figure 1.7: Histological section of healthy human skin performed by M. Amouroux. The hypodermis is not represented in this image.

1.3.1.2 The dermis

The dermis is irrigated by blood. It takes care of the nutrition of the epidermis by diffusion. Its protein fibers make it a real foundation for the epidermis whose age is responsible for the appearance of wrinkles and other signs of skin aging. In addition to its nutritive role, the dermis also plays an essential role in thermoregulation and healing, as well as in the elimination of toxic products (through sweat which contains urea). The collagen, elastin and fibronectin fibers, found at the epidermis/dermis junction, give the skin suppleness, elasticity and support. This upper part of the dermis, joining it with the epidermis, is called the papillary dermis. Its average thickness is about 200 μm. In contrast, the sub-division, ensuring the hypodermis anchoring is called reticular dermis, measures approximatemly 1800 μm.

1.3.1.3 The hypodermis

It is a loose connective tissue that is richly vascularized and contains more or less adipose tissue depending on the location. It acts as an interface between the dermis and the mobile structures below it, such as muscles and tendons. It also protects the body from physical shocks, temperature variations and serves as an adipose reserve. This subcutaneous tissue is formed of hypodermic fibrous cones, separated by adipocyte lobules, which constitute the adipose panicles. When adipose tissue is abundant, the hypodermis is called "subcutaneous fat". It varies in thickness depending on the location : thin on the forehead and thick in areas that have to withstand an impact such as the buttocks or heels.

1.3.2 Morphological changes during carcinoma carcinogenesis

With melanoma, carcinomas are the second type of skin cancer. In France, 80 000 skin cancers are diagnosed each year, 70% of them are carcinoma. Although less dangerous, carcinoma can still metastasize, and an untreated cancer can cause tumors to grow to aesthetically unacceptable sizes. The picture in Fig. 1.8 shows a typical carcinoma cancer, and Fig. 1.9 represents its schematic growing. It exists two types of carcinoma skin cancer:

- **BCC:** originate from cells located deep in the epidermis, more specifically in the basal layer. It is the most common form of skin cancer. BCC evolve only locally and never form metastases,

i.e., they do not spread to other organs. They are usually located on the face, neck or upper trunk.

Figure 1.8: Basal cell carcinoma on a patient (ClinicalTrials.gov Identifier: NCT02956265). The red square includes the cancer location.

- **Squamous Cell Carcinoma (SCC)** on the other hand, originate from cells on the surface of the epidermis. Their evolution is more at risk than that of the basal cell form: they have an increased capacity to form metastases. They can develop themselves on all parts of the body, but also in the oral or genital mucosa.

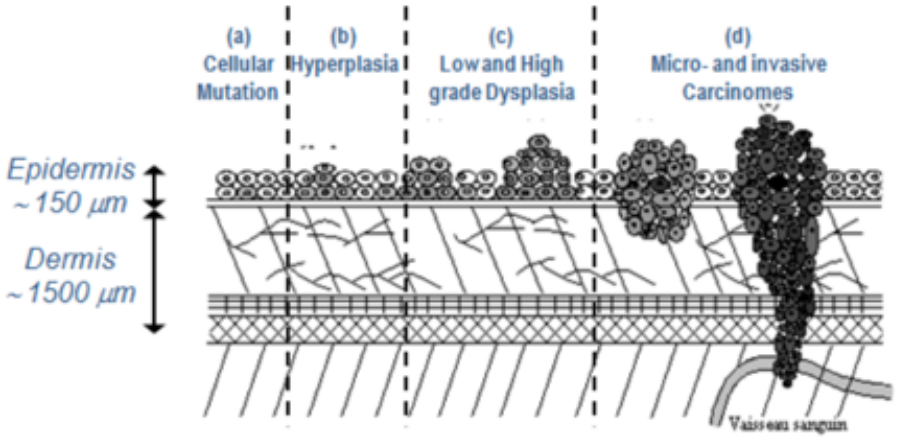

Figure 1.9: Schematic representation of basal cell carcinoma evolution. The picture is taken from the P. Rakatomanga thesis [Rakotomanga 2019].

The main pathogen is sun exposure, especially UV radiation. The risk is greatly increased with the phototype of the subject. The lighter the skin and hair, the greater the risk. Phototype classification is detailed in [Astner 2004]. Like all cancers, carcinoma is an uncontrolled repro-

duction of damaged cells. The appearance of this tumour is called dysplasia. It manifests itself, among other things, locally by the following atypia:

- An inflammatory reaction leading to an overproduction of keratynocites, mitosis is observed in all the epidermis, and not only in the basal layer. This proliferation is accompanied by a disproportionate production of keratin.
- A disorganization of the cell layers: the usual layers are no longer visible in focus, indicating cell communication problems.
- Presence of corneocytes (cells without a nucleus) in depth, and conversely, keratynocytes in the stratum corneum.
- Dermal fibroblast dysfunction called elastosis: the elastic fibres of the upper part of the dermis break and thicken.

The hystological section shown in Fig. 1.10 illustrates the morphological changes due to cancer appearance.

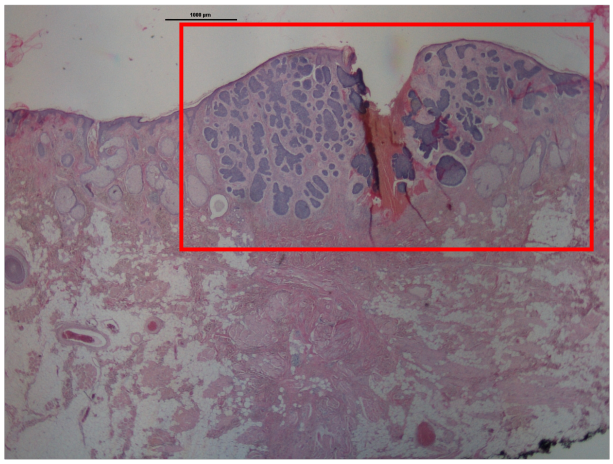

Figure 1.10: Image of a histological section of the skin with the presence of a BCC tumor (in the red square) performed M. Amouroux.

1.3.3 Optical parameters of the different layers

There is an extensive literature on the optical characterization of the skin. The aim here is to present a state of the art of these. In particular, we will focus on optical characterization by skin layer, in the near UV, visible and near IR range. It will also be a question of seeing the evolution of optical parameters following the growth of cutaneous carcinoma, responsible for the morphological modifications mentioned in section 1.3.2.

1.3.3.1 Healthy skin optical models

The optical skin characterization depends on the individual, especially on its phototype [Astner 2004]. Within the same individual, the optical coefficients and thicknesses of the different layers of the skin vary according to the location on the body, the age and the state of

health of the tissue. Large tables giving values of these coefficients for given tissues, of a given phototype, and at a given wavelength are available in extensive reviews [Tuchin 2014]. Here we will focus in particular on the state of the art providing analytical expressions of the coefficients of interest.

Absorption coefficient: The absorption in biological tissue is caused by chromophores. For human skin, the main chromophores in the visible range, responsible for the absorption spectra shape are melanin, blood, water, lipids and β-caroten. In their article [Jacques 2013], Jacques ensures that the absorption coefficient $\mu_{a,mix}(\lambda)$ of a mixed tissue can be calculated by knowing the absorption coefficients of the cromophores alone by applying the formula:

$$\mu_{a,mix}(\lambda) = \sum_i f_{v,i}\mu_{a,i}(\lambda) \tag{1.12}$$

Where $\mu_{a,i}(\lambda)$ is the absorption coefficient of the chromophore alone, and $f_{v,i}$ the volume fraction of the chromophore (dimensionless) in the mixture. After taking into account the contribution of each chromophore, there remains an absorption contribution called $\mu_{a,base}(\lambda)$, the expression of which is provided by Meglinski and Matcher in [Meglinski 2002]:

$$\mu_{a,base}(\lambda) = 7,84 \times 10^8 \times \lambda^{-3,225}\ [cm^{-1}] \tag{1.13}$$

It is usual to separate the absorption of blood into three contributions. Oxygenated hemoglobin HbO_2 can be distinguished from non-oxygenated hemoglobin Hb. The last contribution is bilirubin, which is less significant. The $f_{v,i}\mu_{a,i}(\lambda)$ term in Eq. (1.12) relating to blood is the following one:

$$f_{v,blood}\mu_{a,blood}(\lambda) = f_{v,blood}[\gamma\mu_{a,HbO_2}(\lambda) + (1-\gamma)\mu_{a,Hb}(\lambda) + \mu_{a,bilirubin}(\lambda)]\ [cm^{-1}] \tag{1.14}$$

Where γ is the ratio between oxygenated hemoglobin and non-oxygenated hemoglobin. Fig. 1.11 shows the pure blood ($f_{v,blood} = 1$) absorption spectra, for $\gamma = 0.75$ a value coherent with others studies. The absorption power of a chromophore is not always directly given by its $\mu_{a,i}(\lambda)$. Sometimes, the spectral extinction coefficient is given. It can be provided in (i) $cm^{-1}/g.L^{-1}$ and therefore called mass concentration extinction coefficient or (ii) in $cm^{-1}/mol.L^{-1}$ and therefore called molar concentration extinction coefficient. The extinction coefficient is often reffered to $\varepsilon(\lambda)$. This is the case for the extinction coefficients of bilirubin, oxy-hemoglobin and desoxy-hemoglobin, eumelanin, pheomelanin and β-caroten provided by Prahl ([Prahl 2018]). To reduce this coefficient to an absorption coefficient, the following calculation must be applied (left for the molar case, right for the mass case):

$$\mu_{a,i}(\lambda) = \frac{\varepsilon_i(\lambda)}{M_i}c_i \qquad ; \qquad \mu_{a,i}(\lambda) = \varepsilon_i(\lambda)c_i$$

Where M_i and c_i are respectively the molar weight and the mass concentration of chromophore i in the mix. Like blood, melanin absorption is decomposed in two contributions, called eumelanine and pheomelanine. One finally obtains Eq. (1.15), similar to the previous one for blood. Fig. 1.12 shows the pure melanin absorption spectra, and its decomposition in eumelanin and pheomelanin.

$$f_{v,mel}\mu_{a,mel}(\lambda) = f_{v,mel}[\mu_{a,eum}(\lambda) + \mu_{a,phe}(\lambda)] \tag{1.15}$$

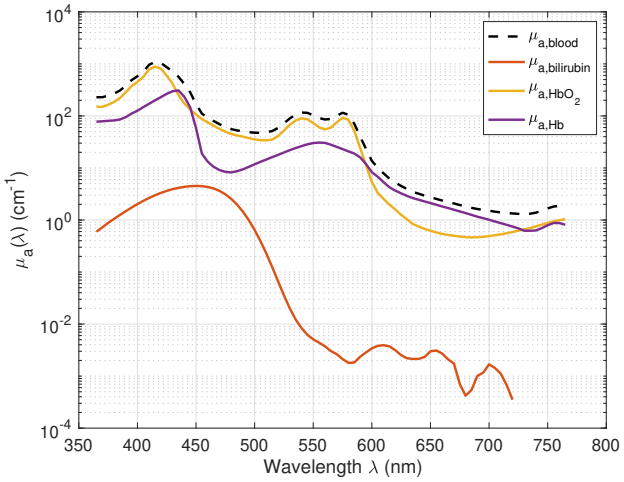

Figure 1.11: Absorption coefficient of pure blood ($f_{v,blood} = 1$), and its contributions appearing in Eq. (1.14); taken from OMLC database [Prahl 2018].

The others cromophores are not decomposed. By coupling formulas (1.12) and (1.13), we finally deduce that the absorption coefficient for a given layer can be calculated as follow:

$$\mu_{a,layer}(\lambda) = \mu_{a,base}(\lambda) + \sum_i f_{v,i}\mu_{a,i}(\lambda) \tag{1.16}$$

The contribution of each pure chromophore absorption (*i.e.*, all the $\mu_{a,i}(\lambda)$ in formula (1.16)) are summed up in Fig. 1.13.

Scattering coefficient: The literature offers more analytical expressions for $\mu_s'(\lambda)$ than $\mu_s(\lambda)$ (see Eq. (1.9)). Parametric expressions are available for wavelength ranges covering the spectrum from UV to IR:

$$\mu_s'(\lambda) = a(\frac{\lambda}{500 \times 10^{-9}})^{-b}$$

This expression, provided in [Jacques 2013], is accompanied by table, in which values are given for parameters a and b for several for several biological tissues. The unit of λ must be meters. The same article, also provides a more complex expression that takes into account the two scattering types: Mie and Rayleigh (decrease in $1/\lambda^4$) scattering:

$$\mu_s'(\lambda) = a'[f_{Ray}\frac{\lambda}{500 \times 10^{-9}})^{-4} + (1 - f_{Ray})(\frac{\lambda}{500 \times 10^{-9}})^{b_{Mie}}]$$

Values of f_{Ray}, a' and b_{Mie} parameters are also given in tables. Other studies ([Krishnaswamy 2010]) propose a model of human skin layer, in which scattering of a tissue layer can be decomposed in two contributions from blood and a scattering base bloodless value:

$$\mu_{s,layer}(\lambda) = (1 - f_{v,blood})\mu_{s,base}(\lambda) + f_{v,blood}C_{blood}(\lambda)\mu_{s,blood}(\lambda) \tag{1.17}$$

Where:

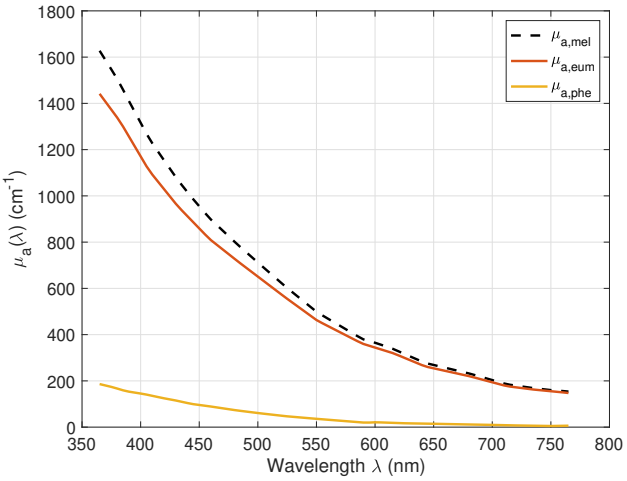

Figure 1.12: Absorption coefficient of pure melanin ($f_{v,mel} = 1$), and its contributions appearing in Eq. (1.12); taken from OMLC database [Prahl 2018].

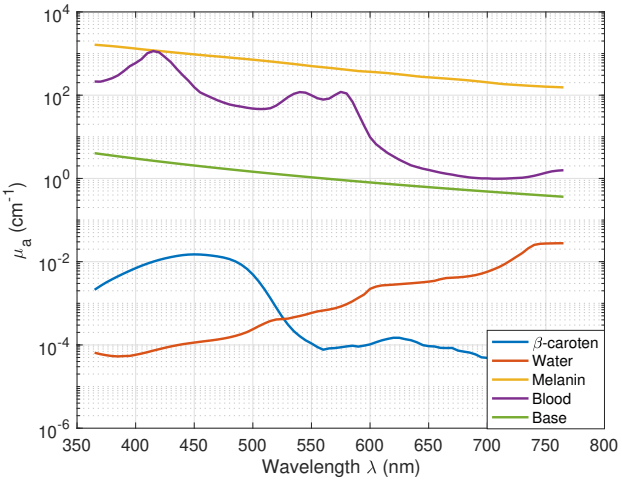

Figure 1.13: Absorption spectra of pure chromophores present in a skin layer. The absorption spectra obtained from spectrophotometer acquisitions are taken from OMLC database [Prahl 2018].

- $\mu_{s,base}(\lambda) = \mu_{s,577}(577/\lambda)$ with λ in nanometer, and $\mu_{s,577}$ is also provided in the study for each skin layer.

- $\mu_{s,blood}(\lambda)$ is the scattering coefficient of pure blood, available on OMLC site ([Prahl 2018]).

- $C_{blood}(\lambda)$ is a correction factor depending on the mean vessel diameter of the layer $d_{vessels}$, and two parameters $a = 1.007$ and $b = 1.228$ (resp. $a = 1.482$ and $b = 1.151$) for collimated (resp.

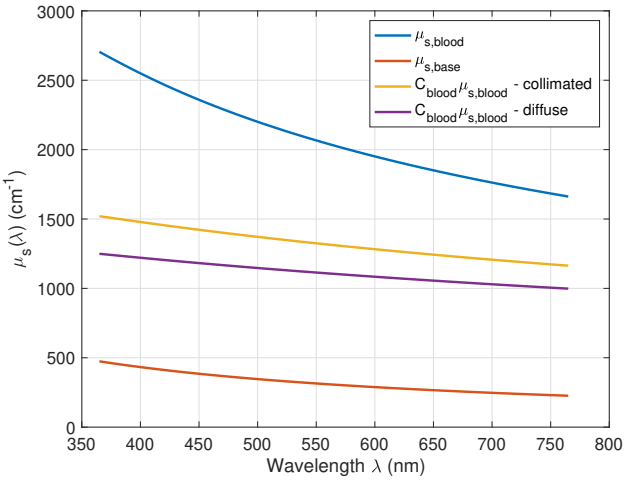

Figure 1.14: Scattering coefficients contributions appearing in Eq. (1.17).

diffuse) illumination linked by the expression: $C_{blood}(\lambda) = 1/(1 + a(0.5\mu_{s,blood}(\lambda)d_{vessels}))^b$.

Finally, $\mu_{s,base}(\lambda)$, $\mu_{s,blood}(\lambda)$ and the corrected products $C_{blood}(\lambda)\mu_{s,blood}(\lambda)$ (for collimated and diffuse illumination) are presented in Fig. 1.14. Those curves was drawn using the following parameter values: $\mu_{s,577} = 300\ cm^{-1}$ and $d_{vessels} = 6.10^{-4}\ cm$.

Anisotropy factor and phase function: The scattering is also characterized by the anisotropy factor and phase function (*cf.* section 1.2.2.2). The wavelength dependence of the anisotropy factor is often considered as negligible in the near-UV/near-IR range. However, V. Tuchin and his team ([Tuchin 2007]) offered the following analytical fitting for $g(\lambda)$ in human skin biological medium:

$$g(\lambda) = 1.1 - 0.58 \times 10^{-3}\lambda$$

As described in section 1.2.2.2, g is a summarized parameter of the phase function $\rho(\theta)$). This last one really described the scattered angle distribution. The model we used in our numerical experiment, is the Henyey-Greenstein relation (1.18), really often used in photon transport modeling:

$$\rho_{HG}(\theta) = \frac{1 - g^2}{(1 + g^2 + 2g\ cos(\theta))^{3/2}} \tag{1.18}$$

Scattering in skin tissue has the particularity to be forward, with an anisotropy factor that varies in the range of $0.7 - 0.95$ according to the layer we consider.

Endogenous fluorescence: As introduced in 1.2.2.4, fluorophores in skin are characterized by their absorption and emission. The studies conducted by Kollias [Kollias 2002] and Borisova [Ghervase 2015] explain the behavior of the main fluorophores in skin, between near-UV and near-IR wavelengths. This can be summed up by the graphs in Fig. 1.15.

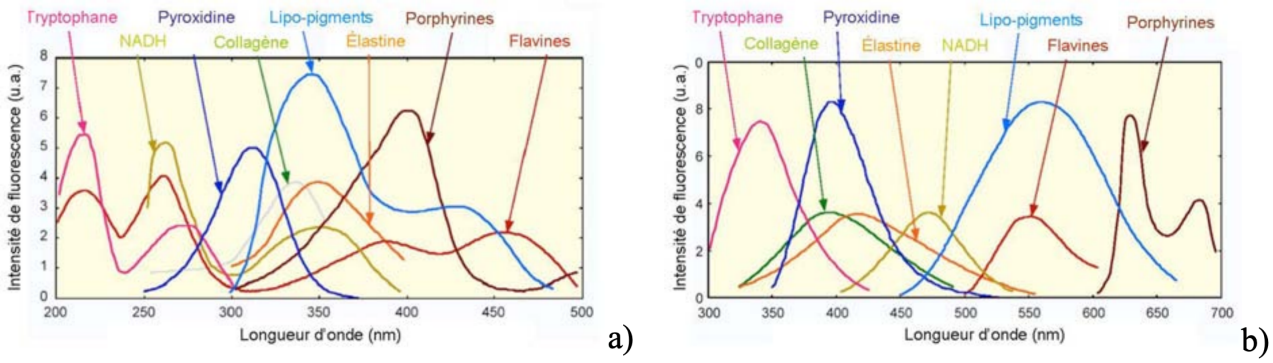

Figure 1.15: Absorption a) and emission b) of the main fluorophores in human skin. The graphs comes from the Wagnières *et al.* paper [Wagnières 1998].

Refractive index: The mismatch of the refractive index between two layers is responsible for reflection or change in the photon direction according to the Snell-Descartes laws. Here again, a wavelength dependency of the refractive index n could be considered. Like the majority of biological tissues, water is the predominant compound. It is responsible for the value of refractive index, that is really similar to the water one (*i.e.*, $n_{water} = 1.33$). However, the value differs from it when the water level does not predominate. Studies shows that the refractive index value varies with the phototype, or the pressure applied to the sample [Ding 2006a].

1.3.3.2 Evolution of optical coefficients with carcinogenesis

Section 1.3.2 gives an overview of the morphological deformations. The focus here is on the optical signature of cutaneous carcinoma. Especially, this section presents the impact of cutaneous carcinoma on two optical signal of interest (*cf.* our clinical device description in section 1.4.2.3), the AF and DR spectra.

Diffuse reflectance: The increase of keratin and the overproduction of keratynocites is responsible for an increase of the scattering and absorption coefficient. This higher light scattering in cancerous cases can be explained by the larger average effective size of the scattering centers [Garcia-Uribe 2012]. The nuclei of dysplastic epithelia have a density and size greater than those of healthy epithelia [Sokolov 2002]. Similar results are observed in the case of dysplastic naevus, the intensity of the reflectance signal is lower for a pathological skin than an healthy one [Borisova 2014]. Oxyhaemoglobin absorption is not apparent in pathological spectra [Drakaki 2009]. More locally, one effect that the reflectance spectra of pigmented lesions shows is a gradual decrease in the hemoglobin absorption peaks at 420, 540 and 575 nm in passing from normal skin to benign and dysplastic nevi. Finally, slope in a wavelength range, or ratio at a given wavelength between an healthy diffuse reflectance spectra and a pathological one can be compared and used as discrimination criteria.

Auto-fluorescence: Inter-patient repeatable tendencies are observed when some pathological changes occur, as spectral shapes and intensity trends are influenced in an analogous way for

one given kind of pathology. For example, basal cell carcinoma lesions always reveal fluorescence intensities lower than surrounding normal skin tissues, while squamous cell carcinoma usually has fluorescence brighter than surrounding skin. This observation could be used for differentiation of these two kinds of non-melanoma malignancies [Borisova 2014]. In the case of BCC, with an excitation at 337 nm, it has been shown [Drakaki 2009] that a difference in the spectral profiles between normal and cancerous tissues can be seen. The fluorescence intensity of malignant tumour is weaker than that of the normal tissue. However, the intensity of the fluorescence signal may not be a consistent parameter for a decision as several factors, such as surface morphology, can affect the signal. The distance between the tissue surface and probe can also affect the intensity. That is why the comparison of normalized spectra seems to be more reliable. Once done, cancer tissue spectra can reveal a red shift of the spectral profile. For an excitation at 405 nm, the advanced stage of BCC growth higher fluorescence signal in the area near to 635 nm, related to endogenous porphyrins accumulation near to the cancer [Borisova 2014].

1.4 Optical biopsy for carcinoma diagnosis

This section firstly introduces the main modalities of optical biopsies, by providing physical principles, advantages and drawbacks of these skin imaging and spectroscopy techniques, before focusing on our *SpectroLive* device which exploits the SR-AF and SR-DR spectroscopy modalities.

1.4.1 Quick overview of existing optical biopsy methods

1.4.1.1 Skin imaging techniques

Dermatoscopy: Dermatoscopy (or dermoscopy) is an examination performed by a dermatologist on an skin area using a dermatoscope or video dermoscope. The dermatoscope enlarges the area under observation using a magnifying lens and a light source [Nachbar 1994]. The depth visited can reach, for cutaneous tissues, the limit epidermis-dermis, invisible to the naked eye. Recent dermatoscopes use polarized light sources, allowing to get further in depth.

Reflectance confocal microscopy: The basic principle of reflectance confocal microscopy (RCM) is the use of a point source of light, which is tightly focused on a specific point in the tissue. The light is reflected back by certain tissue structures due to variations of refractive indices within the skin. Specifically, melanin, hydrated collagen, and keratin are highly reflective skin components, which appear brighter on the acquired images than the surrounding structures. Only light reflected back from the tissue focus point is allowed to enter the detector through a pinhole-sized spatial filter. By scanning in the XY plane, skin images can be acquired. Good correlations with dermoscopic and histopathologic skin cancer diagnosis were obtained from those RCM images [Ahlgrimm-Siess 2018].

Optical Coherence Tomography: It is an imaging technique sensitive to index variations, *i.e.*, optical interfaces. It therefore allows to access the structural information of the tissue, in particular between the epidermis and the dermal-epidermal junction, from different cross-sectional images of the skin. Depth maximum explored by photons is between 700 μm and 1 mm [Dubois 2018a, Dubois 2018b]. For invasive basal cell carcinoma, the surgical margin delineation is difficult to determine by OCT because of the shallow depth explored. However, the OCT can

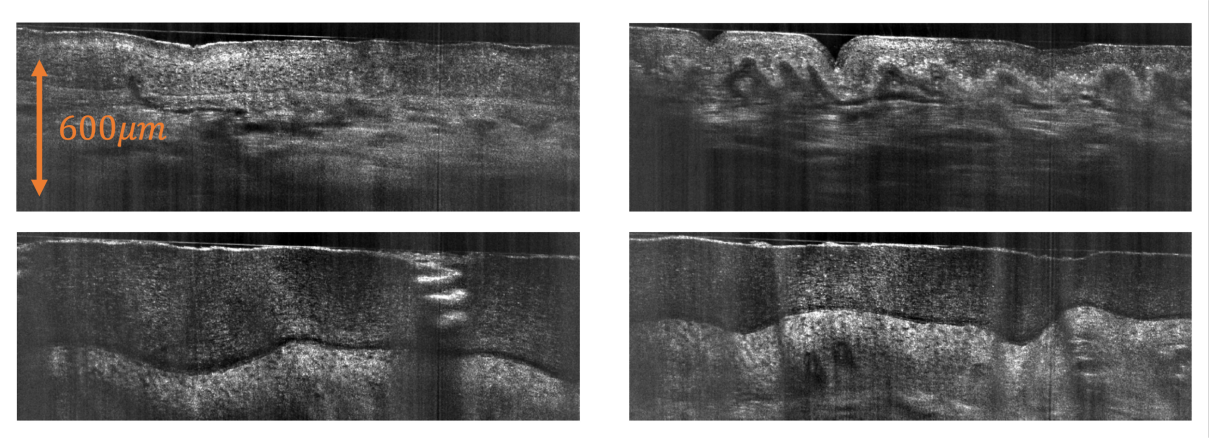

Figure 1.16: OCT images of the top and palm of the hand to illustrate the variations in skin thickness with the permission of DAMAE Medical (`www.damaemedical.fr`).

be coupled with a polarization sensitivity technique. This method allows the distinction between healthy tissue and tumour tissue and thus to delineate surgical margins for invasive basal cell carcinoma [Mogensen 2007]. Four OCT images are presented in Fig. 1.16, the two on the first line originate from the top while the second line is from palm of hand.

1.4.1.2 Skin spectroscopy techniques

Raman Spectroscopy Raman spectroscopy is a tool for studying the molecular composition tissue highlighted by vibration signatures. It is based on inelastic scattering. The depth visited by photons is weak. It is limited to the superficial layers of the epidermis. The main limitation is the weak signal, which can be masked by the presence of the autofluorescence. Despite the problems with the Raman signal, this promising technique is in development [Lui 2012]. In addition, methods of separating sources have also been applied to this type of signal from skin biopsies [Vrabie 2007]. The bands analysis appearing in Raman spectra thus allow to distinguish tumor tissue.

Diffuse Reflectance Spectroscopy It consists in illuminating, in white light, a biological tissue (here the skin) and to collect the reflected photons on the tissue surface, before sending them toward a spectrophotometer. This gives the spectrum of the light backscattered by the tissue. For this modality, it is usual to separate the light emitting source from several detectors, we are then talking about SR-DR. Depending on the axial separation between the source and the detector, the probed depth varies. Generally, in the context of the study *i.e.*, cutaneous application, this one can reach the bottom of the dermis layer.

Auto-Fluorescence/Fluorescence Spectroscopy For those two types of fluorescence, the optical protocol is almost the same. It consists in exciting a fluorophore in the skin, with a monochromatic source and to collect only the fluoresced light. This is possible by putting an optical filter allowing only photons that only verify $\lambda_{fluo} > \lambda_{inc}$ (*cf.* section 1.2.2.4) to go through. Without it, the fluorescent spectrum would be drowned in the DR signal. The nuance

between the two measures remains in the following: AF spectroscopy is obtained by exciting the endogenous fluorophores naturally present in skin whereas fluorescence spectroscopy is based on the introduction of an exogenous fluorophore. The Table 1.1 sums up the advantage and drawbacks of the two described measurements.

	Advantages	**Drawbacks**
Fluorescence	- domination of one fluorophore - signal intensity	- administration of the fluorophore - allergy risks - toxicity
Auto-Fluorescence	- no administration	- hard to extract the signal of interest - weak intensity

Table 1.1: Advantages and drawbacks of the two florescence methods.

The visited depth varies with the excitation wavelength. Endogenous fluorophores of interest (Collagen, Elastin, Nicotinamide Adenine Dinucleotide (NADH), Flavin, Porphyrin and Keratin) are often excited with near-UV wavelengths. Biological medium is optically opaque for those excitations, that is why the penetration depth only reaches at most the upper part of the dermis. AF techniques are used to detect various anomalies in the skin, particularly for tumour detection [Borisova 2014].

1.4.1.3 Optical clearing and multi-modality approaches

Optical Clearing Agent It is not a measurement method in its own right, but rather an additional increment that can be coupled with aforementioned measurements to access deeper skin layers. Indeed, the application of Optical Clearing Agents (OCA) allows the skin to become more optically transparent. Absorption and scattering coefficient of the wet tissue are then less significant [Zhu 2013b, Sdobnov 2018]. Several studies show the improvement of imaging and depth spectra. In particular, Pires et al. [Pires 2016] showed that the use of a OCA improves contrast resolution and tumour localization. Studies have investigated the impact of auto-fluorescence measurements for a wavelength of excitation given due to the use of different OCA compositions [Migacheva 2010].

Multi-modality approaches Many teams opted for a multi-modality approach, *i.e.*, the combination of several methods described before, to improve the robustness compared to a single technique. That is the case of James W. Tunnell *et al* [Lim 2014], who combined Raman spectroscopy, diffuse optical reflectance and laser induced fluorescence spectroscopy to diagnose non-invasive *in-vivo* melanoma and non-melanoma skin cancers. The same techniques have been used in [Šćepanović 2009], but in the case of atherosclerosis and breast cancer diagnosis. Some others, only combine the AF and DR spectroscopy to detect cancer. It is the case for the glioma in [Valdes 2011], while it is used for rheological properties of carotid arteries in [Péry 2009] or skin cancer in [Liu 2012]. A bi-modality only using Raman spectroscopy and AF is presented in [Bratchenko 2017] and applied to carcinoma and melanoma diagnosis.

1.4.2 *SpectroLive* description

The previous overview of the different optical biopsy techniques briefly explained the range of possibilities for the diagnosis of, among other things, skin carcinoma. Now it is time to describe

our *SpectroLive* device used in the clinic in more detail.

1.4.2.1 Clinical context ans Motivations

Our study does not exactly take place in the context of skin carcinoma diagnosis, but rather as an aid to surgical contouring. As a matter of fact, the diagnosis of carcinoma is something dermatologists have mastered. It is during the surgical removal that things can be improved. Indeed, the cancer develops beyond its visual border, and a partial removal of the lesion is often responsible for recurrences. With the retrospective of many post-operative analyses, called anatomopathology, surgeons have empirically determined safe margins around the lesion (about 4 mm for BCC and 6 mm for SCC). The ablation is then carried out systematically following this borderline, for all patients. The photography in Fig. 1.17 shows the safety border around the carcinoma (circle), and the incision limit (eye shape) that the surgeon will follow with his scalpel. The eye shape is there to promote scarring, that should be directional. This process of

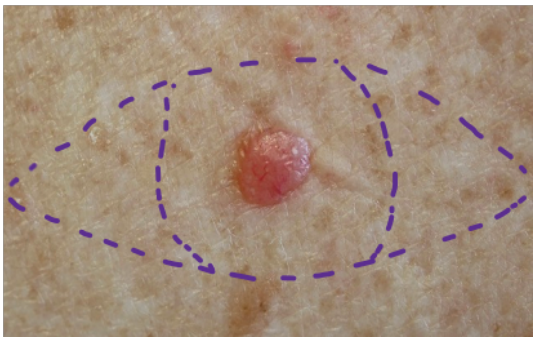

Figure 1.17: Empirical safety area around skin carcinoma.

delimitation is fast and reliable, *i.e.*, the recurrences rate is low. However, it is not unique to the individual, and the surgical margins often overestimate the actual implementation of the cancer, which is responsible for significant scarring on the patient. The underestimated case, although rarer, is problematic too since it requires a second surgery to resect the remaining cancer. The project associated with the *SpectroLive* device then intervenes with the following long term objective: to create real-time multi-modal (*cf.* section 1.4.2.3) biopsy allowing the surgeon to fix the delimitation of the carcinoma resection in an individualized and accurate way.

1.4.2.2 Probe and source description

The aim here is to technically introduce the *SpectroLive* device used in the clinic (represented in Fig. 1.19). A global opto-electronic schematic representation of the device is provided in Fig. 1.18. A more exhaustive description is given in the patent description [Amouroux 2017, Blondel 2021]. In particular, we will focus on the description of the probe, and the source of the device.

The source: It is composed of a broadband source covering a spectral range from near UV to near IR $[320 - 780]$ nm, which is used for DR measurements (*cf.* section 1.4.2.3), and 5 monochromatic LEDs (spectral width at half height 10 nm) used for AF measurements emitting at the following peak wavelengths:

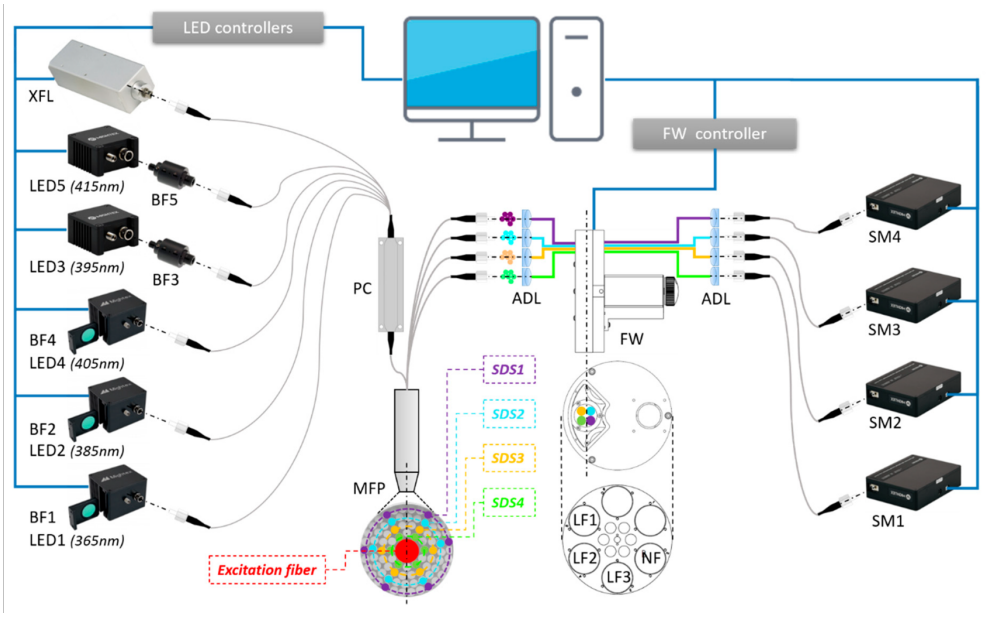

Figure 1.18: *SpectroLive* opto-electronic configuration. This image is taken from a Blondel *et al.* contribution [Blondel 2021]. L: xenon flash lamp for broadband diffuse reflectance measurements; LEDi ($i \in 1, 2, 3, 4, 5$): light-emitting diodes for narrow band together with excitation band filter (BFi) for narrow-band autofluorescence excitations ; MFP: multiple fiber probe ; PC: power combiner; ADL: achromatic doublet lens; FW: filter wheel; SDSj ($j \in 1, 2, 3, 4$): source-to-detector separations; LFk ($k \in 1, 2, 3$): emission long-pass filters; NF: neutral density filter; SMj: spectrometers.

Figure 1.19: *SpectroLive* device in the operating room (left) and clinical measurement protocol (right).

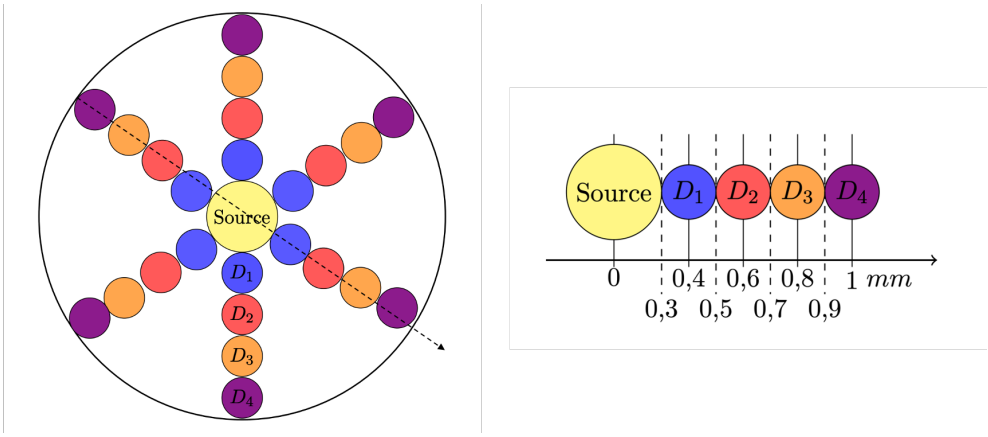

Figure 1.20: *SpectroLive* geometrical features.

$$\lambda_1^{exc} = 365\ nm \quad \lambda_2^{exc} = 385\ nm \quad \lambda_3^{exc} = 395\ nm \quad \lambda_4^{exc} = 405\ nm \quad \lambda_5^{exc} = 415\ nm \tag{1.19}$$

The probe: It consists of the excitation fiber (SF) in the center, whose emission surface is a disk of radius $r_{SF} = 300\ \mu m$. Around the source are disposed 6 collecting fibers corresponding to 4 SD distances , *i.e.*, a total of 24 collecting fibers. Their disposition around the SF is represented in Fig. 1.20. The 4 SD distances are:

$$D_1 = 400\ \mu m \qquad D_2 = 600\ \mu m \qquad D_3 = 800\ \mu m \qquad D_4 = 1000\ \mu m$$

Each collecting fiber (DF) has a sensitive area of radius $r_{DF} = 100\ \mu m$, and both SF and DF have an optical numerical aperture $NA = 0.22$. The collected light is then sent to the spectrophotometer of the device (after passing trough a cut-off filter for AF spectra, see Fig.1.18). This quick technical description of the device, and all the theoretical content developed until here will allow us to introduce the optical outputs spectra of a *SpectroLive* clinical measurement.

1.4.2.3 Optical outputs

The *SpectroLive* measurement can be qualified as "spatially resolved bi-modal spectroscopy". It seems to be important to detail each term of this qualification. To begin, it is "spectroscopy" device, since the device's final signal is a spectrum. All the wavelengths are separated in the spectrophotometer thanks to a diffraction grating. The second term, "spatially resolved", is linked to the geometrical disposition in the probe (see Fig. 1.20). Considering 4 different SD distances bring supplementary information, because each of them can be associated to a typical probed depth [Hidenobu Arimoto 2005]. Finally, "bi-modal" concerns the fact that 2 measurements are done with *SpectroLive*:

1. **Diffuse reflectance:** The probe is placed on the patient skin, and white light is emitted from the SF, during an exposure-time allowing to be in a permanent regime. The photons travel in the medium and are subject to light/matter interactions (*cf.* section 1.2.2). Only a part of

them reaches DF, and the spectrophotometer. All the light coming from a given distance D_n are gathered to obtain finally a single diffuse reflectance spectrum $DR_{Dn}(\lambda)$. The four diffuse reflectance spectra acquired on clinical patient are presented (after processing) in Fig. 1.21. Those spectra have been taken on a healthy wrist skin.

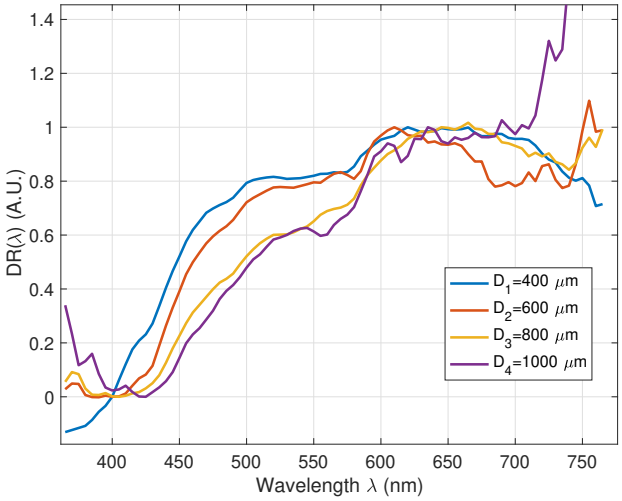

Figure 1.21: Example of *SpectroLive* SR-DR spectra for a healthy wrist skin. The color code, identical to the one in Fig. 1.20, indicates the SD distances.

2. **Auto-fluorescence:** The process is similar to the DR one, excepted that the excitation light is monochromatic, and a cut-off filter only let the fluorescent photons to reach the spectrophotometer. The five excitations are done one by one. We finally get 20 spectra $AF_{Dn}^{exc_j}(\lambda)$ with n varying from 1 to 4 (corresponding to SD distances) an j varying from 1 to 5 (corresponding to excitations available in Eq. (1.19)). Those spectra, that still correspond to an healthy wrist skin, are presented (after processing) in Fig. 1.22.

All spectra are processed in the same way. We first apply a median filter to avoid high-frequency artefacts. We then subtract the dark current. Next we apply a Savtisky-Golay filter to smooth the signal before under-sampling the signal (from ≈0.26 nm in spectrophotometer output to 1 nm). To take into account the complex spectral response of every acquisition chain item (including fiber, light source, filters and spectrometers), it was decided to apply the following operations to the spectra. For $DR_{Dn}(\lambda)$ this consists of terms to terms ratio between the measured backscattered intensity on the tissue and the intensity measured on a reflectance standard (Lambertian diffuser called spectralon with flat spectral response close to 100% reflection). More details about this calibration method will be developed later in section 3.5. The final y-axis unit (intensity) could be interpreted as the ratio of light backscattered by the tissue regarding to a perfect reflectance standard. For $AF_{Dn}^{exc_j}(\lambda)$, a spectral correction is applied for each λ. The correction coefficient is established beforehand after calibration on a standard lamp. Finally, we apply a factor to transform the photon counts output to an irradiance spectrum (in $W/m^2/nm$), by measuring the incident excitation light with a power meter.

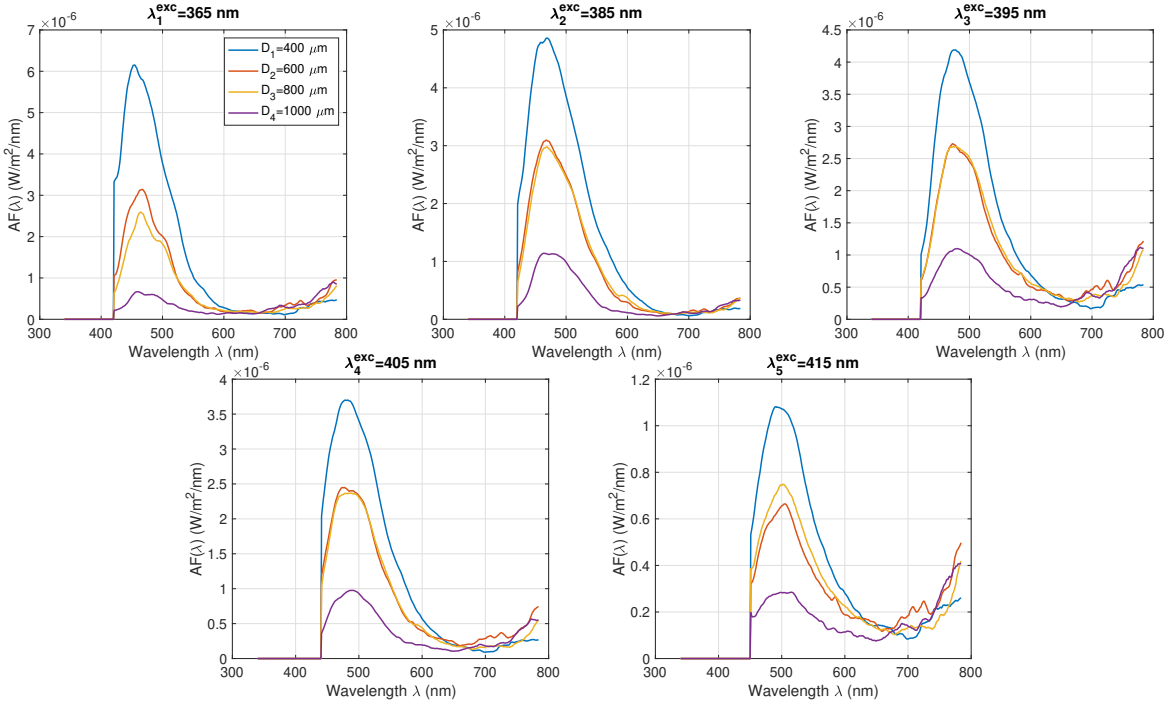

Figure 1.22: Example of *SpectroLive* SR-AF spectra for a healthy wrist skin. The color code, identical to the one in Fig. 1.20, indicates the SD distances.

1.4.2.4 Exploitation of acquired spectra

Once we obtain the spectra ready to be analysed, two alternatives are available for us. One of the possibilities for analysing the acquired spectra is to use supervised classification based on the extraction of discriminating characteristics from the spectroscopic data to improve diagnosis of pre-cancerous tissue, compensatory hyperplasia atypical and dysplasia. This method is not really linked to a biological understanding of the medium, since discriminatory criteria are often area under the curve, slope or signal amplitude. A big database of spectra are required to train the classification algorithm. Encouraging results obtained by the application of this method are described in [Abdat 2012, Amouroux 2009]. The other approach is the one developed during this PhD work. It consists in relating the obtained spectra to the optical parameters using an inversion model. The healthy state of the probed tissue is then determined by an analysis of the spatial evolution of the optical parameters around the skin carcinoma.

1.5 Photon transport modeling

This section first gives a quick overview of the sate of the art of mathematical models and the use of numerical simulation to characterize light propagation in turbid media, before presenting the

simulation we designed in details. Finally, a last subsection presents our inverse problem approach made possible by this simulation.

1.5.1 Photon propagation modeling: state of art

The aim here is to present methods of photon transport in a turbid medium, in order to see how we manage to get simulated SR-DR and SR-AF optical outputs.

1.5.1.1 Photon propagation modeling: state of art

The decision to turn to stochastic numerical solutions stems from our inability to analytically solve the radiative transfer equation that gives the luminous intensity $L(\vec{r},\vec{\theta})$ at all points $\vec{r}$ and in all directions $\vec{\theta}$ in a medium. For a permanent regime, and keeping the notation introduced in section 1.2.2, this equation has the form:

$$\nabla L(\vec{r},\vec{\theta}) = -(\mu_a+\mu_s)L(\vec{r},\vec{\theta}) + S(\vec{r},\vec{\theta}) + \int_0^{\pi}\int_0^{2\pi} L(\vec{r},\vec{\theta'})\rho(\vec{\theta},\vec{\theta'})sin(\vec{\theta'})d\vec{\theta}d\vec{\theta'} \tag{1.20}$$

This wavelength-dependent Eq., reflects the fact that the local evolution of the luminance $L(\vec{r},\vec{\theta})$ is the result of a three terms sum. The first one, $-(\mu_a+\mu_s)L$, is the light attenuation linked to the Beer-Lambert law (similar to the equation (1.4), but with a scattering contribution). The second one S, is the intrinsic gain of luminance. Typically, the fluorescent light created on this position and toward this direction will be taken into account in its term. Finally, the integral term is for the gain due to multiple scattering events, with $\rho(\vec{\theta})$ the phase function (see Eq.(1.6)). Given its inter-differential form, there is no general solution for Radiative Transfer Equation (RTE) except in simplified cases (zero or isotropic scattering, simple geometries). There are thus several types of models (deterministic and stochastic) of photon transport deriving from of the radiative transfer equation.

Deterministic resolution: As explained, no analytical solution are available for biological complex medium. The only way to get one is to make the equation simpler, by applying the diffusion approximation. This last one can only be applied by respecting some conditions:

1. The SD distances should be great enough (*i.e.*, $D_n > 5/\mu'_s$)
2. Scattering should be predominant over absorption (*i.e.*, $\mu'_s >> \mu_a$)
3. The considered source is a point beam, with normal incidence

In those condition, analytical solution of diffuse reflectance spectra for a given distance have been done by the Farrell team [Farrell 1992], for an homogeneous medium. This solution is, of course, function of the optical parameter μ_a and μ_s. Other teams upgraded the solution to a bi-layer medium, with different optical parameters in each layer [Kienle 1998]. Some other teams have validated their simplified analytical solution by comparing it to MC simulation [Liemert 2013].

Finite difference method: It's a method we can schematically sum up by the following: the 3D real space is divided in a multitude of small 3D volumes called finite elements. Those volumes are geometrically simple (tetraeds or pyramids), and allow to solve numerically the partial derivative-based analytical RTE. By solving it incrementally, between finite elements, we finally get the

macroscopic behavior of the initial volume. The method is efficient, but is only possible because of a relatively coarse mesh. Several studies validated this approaches, by comparing it to diffusion theory [Aydin 2002], or by confrontation with results from Monte Carlo simulations [Bass 2017]. This last one is about biomedical diagnosis.

Monte Carlo simulation: Before explaining our MC simulation code (see section 1.5.2.1) with more details, let's begin with a MC method presentation, and a quick state of the art of its existing variants. Monte Carlo simulation is a stochastic method, that consists in considering that global behaviour is obtained by summing the individual contributions. With its wave-corpuscle duality (*cf.* section 1.2.1), light propagation is particularly well suitable to MC simulation. In their MC review [Zhu 2013a], Caigang Zhu and Quan Liu offers a schematic presentation of MC photon transport simulation algorithm (see Fig. 1.23). To get a numerical solution of the RTE, a lot of photons packets should be thrown in the medium ($n_{photons} > 10^6$). That obviously requires an adequate computing power. It exists a lot of variances in MC. The following is a non-exhaustive

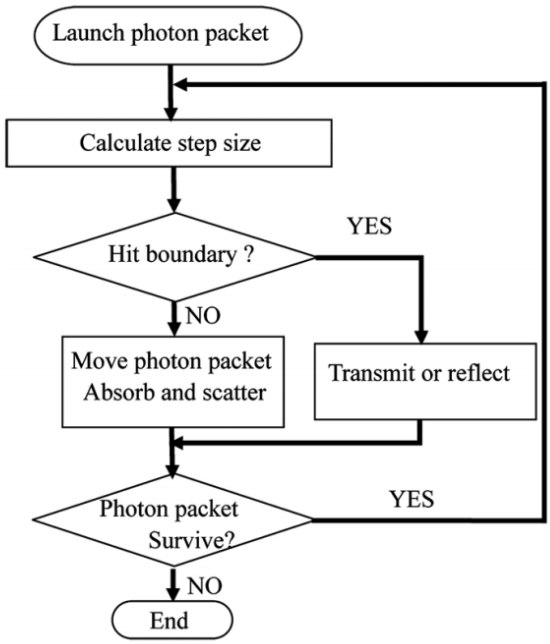

Figure 1.23: Schematic presentation of MC photon transport simulation algorithm. Issued from [Zhu 2013a]. This one describes the steps for the photon packet propagation, from its departure to its death, *i.e.* its detection (reflection or transmission) or its absorption.

list of examples of adaptations grouped by theme of the MC code found in the literature:

- **optical model improvement:** Starting from a relatively simple model, which just contains scattering and absorption, some teams have chosen to make the model more complex, by integrating fluorescence [Swartling 2003, Welch 1997] or even Raman scattering [Reble 2010, Keller 2010], for example.
- **geometrical description improvement:** Initially for a mono-layer homogeneous medium,

consideration of optical behaviour at interfaces according to Snell-Descartes laws have been done [Wang 1995]. For multi-layered tissue, they are often considered flat with a plane interface. The complexification of the skin structure does not stop here. For example, Smithies *et al.* and Lucassen *et al.* independently proposed MC models in which simple geometric shapes were incorporated into layered structures to model light transport with more accuracy. In their models, infinitely long cylinders were buried in the bottom dermal layer to mimic blood vessels [Smithies 1995, Lucassen 1996]. Most recently, Shen *et al.* as well as Fang have presented mesh-based MC methods, by which one can model much more complex structures and situations thanks to 3D non-regular voxels [Shen 2010, Fang 2010].

- **calculation acceleration:** The main disadvantage of these stochastic methods is the computation time associated with these simulations. Many teams then concentrated their efforts on reducing the computation duration. Among them, we find the scaling method that requires a single or a few baseline MC simulations, in which the histories of survival photons such as trajectories or step sizes are recorded. Then, diffuse reflectance or transmittance for a tissue model with different optical properties can be estimated by applying scaling relations on the recorded photon histories. These methods take advantage of the fact that the scattering properties determine photon paths and the absorption properties only influences the weights of survival photons. By applying this Scaling MC methods, Liu *et al.* decrease the calculation time by a factor 300 [Liu 2007]. A second technique is the perturbation MC method. It consists in knowing a spectrum for the healthy area, and to estimate, without running again the simulation, the perturbed spectrum. This method is reliable only for really small variations in the optical properties [Ostermeyer 1997]. The calculation becomes 1300 times quicker. Another method, fund by Flock *et al.* in [Flock 1988], is called hybrid Monte Carlo, and consists in incorporating fast analytical calculations such as diffuse approximation into a standard MC simulation. Finally, the last technique is the one we use in our work: Parallel computation has received increasing attention recently in the study of speeding up MC simulations due to advances in computer technology. The acceleration due to parallel computation is independent of all previous techniques and thus could be used in combination with them to gain extra benefit. Kirkby *et al.* reported in [Kirkby 1997] an approach by which one can run an MC simulation simultaneously on multiple computers, aiming to utilize the unoccupied time slots of networked computers to speed up MC simulations.

- **time and frequency introduction:** In the MC simulation of time-resolved measurements, all the steps are the same as in steady-state measurements, except that one additional parameter, *i.e.*, time, is used to keep track of the time at which each event occurs. It can be used for the simulation of pulse propagation, in which the Δt between emission and collection can carry information [Yoo 1990, Welch 1987].

1.5.2 Description of our simulation

The aim here is to develop a little, notably at the photon scale, the implementation of our MC code for photon displacement in a biological medium. This last one is an adapted version of the *CudaMCML* code developed by Alerstam and his team [Alerstam 2008]. This choice is based on several arguments, in particular the possibility of using the *Explore* calculation platform from the University of Lorraine, and its speed of execution in parallel (GPU). Indeed, the computation times involved are important. Here, we will firstly describe the initial MC code before explaining

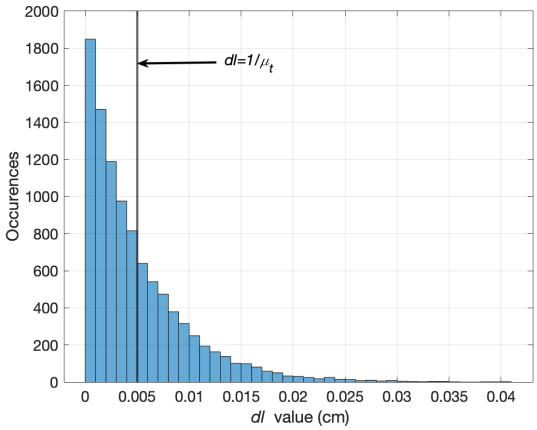

Figure 1.24: dl distribution for $\mu_t^i(\lambda) = 200\ cm^{-1}$, and 10 000 random draws. The vertical line shows the mean value of this distribution, located at $dl_{mean} = 1/\mu_t$

the additions made by P. Rakotomonga [Rakotomanga 2019] to adapt it to *SpectroLive* geometry.

1.5.2.1 Initial code description:

Medium description: Let's start with the medium description, where plane layers are defined. i^{th} layer is defined by its thickness z^i, its absorption and scattering coefficient vectors $\mu_a^i(\lambda)$ and $\mu_s^i(\lambda)$, its refractive index n^i and anisotropy factor g^i (both initially considered independent of λ).

Photon's travel description: Monochromatic photon packets, spatially indivisible but weight dividable, are sent at the top of the medium, with an initial weight $w = 1$. The photon packets travels in the 3D sampled Cartesian space being located by a position vector $\vec{p} = (p_x, p_y, p_z)$ and a normalized direction vector $\vec{d} = (d_x, d_y, d_z)$. The photon packet entrance is made with $\vec{p} = (0, 0, 0)$ and $\vec{d} = (0, 0, 1)$ (*i.e.*, a vertically descending direction). We then randomly draw a distance dl that the photon will travel in a straight line according to the random distribution:

$$dl = -\frac{log(u)}{\mu_t^i(\lambda)} \tag{1.21}$$

Where u follows a uniform law on $[0, 1]$, and $\mu_t^i(\lambda) = \mu_a^i(\lambda) + \mu_s^i(\lambda)$ is the extinction coefficient of layer i. We can notice that, in the diffusion approximation (*i.e.*, $\mu_s >> \mu_a$), the impact of μ_a in Eq. (1.21) is negligible. Fig. 1.24 shows the histogram distribution of the random variable dl for $\mu_t^i(\lambda) = 200\ cm^{-1}$, and 10 000 random draws. The average of this distribution is the inverse of μ_t, that corresponds to the physical behavior expected. The photon position is then updated according to the vector relationship:

$$\vec{p} \leftarrow \vec{p} + dl\vec{d} \tag{1.22}$$

When the new position is found, the new direction should afterwards be determined. It is possible by applying the Henyey-Greenstein formula given in Eq. (1.18). The direction being defined by

2 angles, the update of the polar angle θ, varying in $[0, \pi]$, and the azimuth one ϕ, varying in $[0, 2\pi]$, is done as follows:

$$\begin{cases} cos(\theta) & \leftarrow & \frac{1}{2g}(1 + g^2 - (\frac{1+g^2}{1-g+2gu})^2) \\ \phi & \leftarrow & 2\pi u \end{cases} \tag{1.23}$$

Where u also follows a uniform law on $[0, 1]$. This direction is then converted in a normalized direction vector to get the final vector $\vec{d}$ that will appear in the Eq. (1.22) of the next step. So far, we still have not spoken about absorption. Indeed, a pure absorption event does not exist in our simulation. The absorption of the medium is treated with the following numerical artefact: at each step, the photon weight is updated by the following formula:

$$w \leftarrow w - \frac{\mu_a}{\mu_a + \mu_s} w = w - \Delta w \tag{1.24}$$

It is noticeable that the photon packet is reduced by a part of its weight, which corresponds to the proportion of μ_a in μ_t. If the photon reaches a boundary with another layer, the choice of being reflected or transmitted is done by binary choice with a probability in accordance with the calculated Fresnel reflection factor:

$$R_{Fresnel} = \frac{1}{2}[(\frac{\sin(\theta_i - \theta_t)}{\sin(\theta_i + \theta_t)})^2 + (\frac{\sin(\theta_i - \theta_t)}{\sin(\theta_i + \theta_t)})^2] \tag{1.25}$$

With θ_i and θ_t respectively the incident and transmission angle, both linked to the refractive index of the layer i and the next layer t by the Snell-Descarte law:

$$n_i \sin(\theta_i) = n_t \sin(\theta_t) \tag{1.26}$$

The stop conditions of the photon packet flight (also called "photon death") are:

- **The photon packet escape from the boundaries of the medium:** If this boundary is the most superficial one, the photon is considered as reflected and its final weight w increment the reflection value R_d. On the opposite, the photon is considered transmitted and contribute to the transmission value T. Finally, a photon that escape on side boundary is simply lost.
- **The time-of-flight threshold is reached:** Defined by the user, it allows to be sure that the photon travel will end.
- **The minimal weight threshold is reached:** Also defined by the user, it corresponds to a photon packet that finish its travel in the medium, like physical real photon could stop its trip by being absorbed.

Simulation description and outputs: By choosing a number of photon packets to send, the photon lives are independently treated by different cores in different threads. The outputs of the initial code are the total transmittance T, the diffuse reflectance R_d, the absorbed fraction A and the specular reflectance R_s expressed in %. It is also possible to have localised information. Indeed, when a photon packet loses a fraction of its weight Δw (*cf.* Eq. (1.24)), it leaves the amputated weight in the voxel where the scattering event happens. The contribution of all photons then creates a 3D fluence matrix. By a simple angular integration, we obtain a 2D representation of this matrix, called fluence map. This map shows the absorption distribution according to the radial distance and the depth of the medium. A representation of this, for a mono-layer medium, is shown in Fig. 1.25. The log scale for the color-map is necessary to obtain an analyzable image. From this 2D map, it is also possible to proceed to a second integration, according to z or r, to finally obtain the absorption profiles shown in Fig. 1.26.

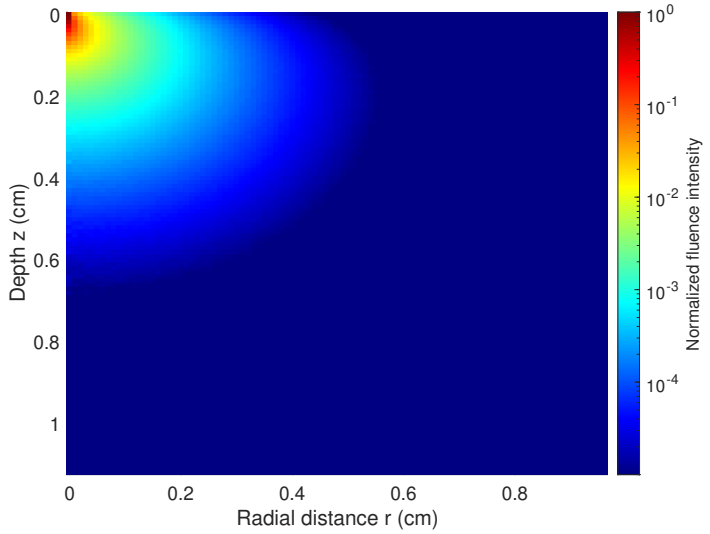

Figure 1.25: Absorption fluence map for a mono-layer medium with $\mu_a = 1.5\ cm^{-1}$, $\mu_s = 130\ cm^{-1}$ and $g = 0.85$.

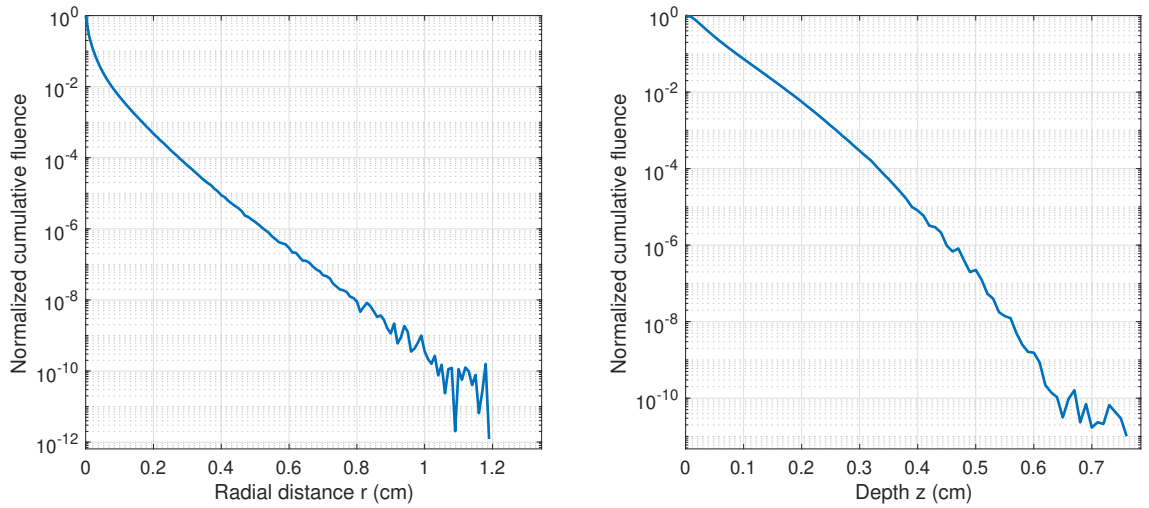

Figure 1.26: Absorption fluence profiles for a mono-layer medium. The y-axis (in log scale) is normalized, and represents the amount of absorption events.

1.5.2.2 Code adaption to fit our clinical device

The previous code has been adapted to fit our *SpectroLive* optical and geometrical configuration. The main contributions, introduced by P. Rakotomanga [Rakotomanga 2019] are presented below:

***SpectroLive* geometrical configuration** The code has been modified in order to introduce collecting fibers located on the periphery of the emitting fiber (see Fig.1.20). It consists in placing a number of collecting fibers with a given radius r_{DF} with a numerical aperture NA_{DF} at a distance D_n of the source center. When the photon exits the medium by the top layer, its radial distance from the source is calculated:

$$r_{photon} = \sqrt{p_x^2 + p_y^2}$$

The photon contribute to the $DR_{Dn}(\lambda)$ spectrum only if its radial distance from the source, and its transmission angle satisfy the 2 following conditions:

$$\begin{cases} r_{int} < r_{photon} < r_{ext} \\ \arcsin\theta_t < NA_{DF} \end{cases} \tag{1.27}$$

Where θ_t is associated to the direction of the transmitted photon. With this calculation, we have kept all the photons that exit the medium in an annular surface between $r_{int} = D_n - r_{DF}$ and $r_{ext} = D_n + r_{DF}$. It allows to collect more photons (compared to the 6 real point fibers) and thus increase the signal to noise ratio. To get back to a collection surface only limited to 6 DF (see Fig. 1.20), the tip we use is to multiply the simulated spectrum DR_{Dn} by correcting area factor C_{area}, defined by:

$$C_{area} = \frac{6A_{DF}}{A_{annular}} = \frac{6\pi r_{DF}^2}{\pi(r_{ext}^2 - r_{int}^2)}$$

With A_{DF} and $A_{annular}$ the collecting fiber and annular surfaces, respectively. Being curious about the impact of such an approximation on the acquired signals, we conducted a study available in annex A.1.1 to quantify the error introduced by this approximation. This is negligible ($< 0.5\%$ in the worst case).

The wavelength dependency: Initially, the code was done to do a monochromatic simulation. Now, it is possible to provide λ-dependent vectors containing the $\mu_a(\lambda)$ and $\mu_s(\lambda)$ components. The simulated spectrum acquisition is now simpler.

The fluorescence: Fluorescence has been added in the code. To do so, a fluorophore can be injected in a chosen layer. The last one is described by its coefficient of absorption $\mu_{a,fluo}(\lambda)$, its quantum efficiency ξ (*cf.* section 1.2.2.4), and the shape of its emission $Emi(\lambda)$. In the code, the fluorescence appears in the adding of the fluorophore contribution, that is why $\mu_{t,fluo} = \mu_t + \mu_{a,fluo}$ replaces μ_t in Eq. (1.21) and (1.24). Then, at each scattered event, by drawing a random variable, we choose if the photon become fluorescent or not according to the probabilities:

$$P_{abs} = \frac{\mu_a + \mu_{a,fluo}(1-\xi)}{\mu_{t,fluo}} \qquad P_{abs,fluo} = \frac{\mu_{a,fluo}\xi}{\mu_{t,fluo}} \tag{1.28}$$

When this random process leads to a fluorescent photon, its emission wavelength λ_{fluo} is chosen according to its emission profile $Emi(\lambda)$, by a stochastic process too. The photon keep traveling in the tissue, and can contribute to signal $AF_{Dn}^{exc_j}$ (with exc_j the initial wavelength), if it satisfy the conditions formulated in Eq. (1.27).

The new outputs: $DR_{Dn}(\lambda)$ and $AF_{Dn}^{exc_j}(\lambda)$ simulated spectra can be now be obtained, in accordance with the *SpectroLive* configuration. The exc_j are all the wavelength, but we can chose in particular a wavelength that corresponds to the excitation peak of a fluorophore. The fluoresced photons and others are numerically separated, but an *a posteriori* addition can rebuild the diffuse reflectance spectrum, with the fluorophore contribution. Examples of DR and AF simulated spectra are given in Fig. 1.27. Those were simulated for a 5 layered skin medium, including NADH excited at $\lambda_{exc} = 365\ nm$ and a maximum of emission at $\lambda_{fluo} = 470\ nm$.

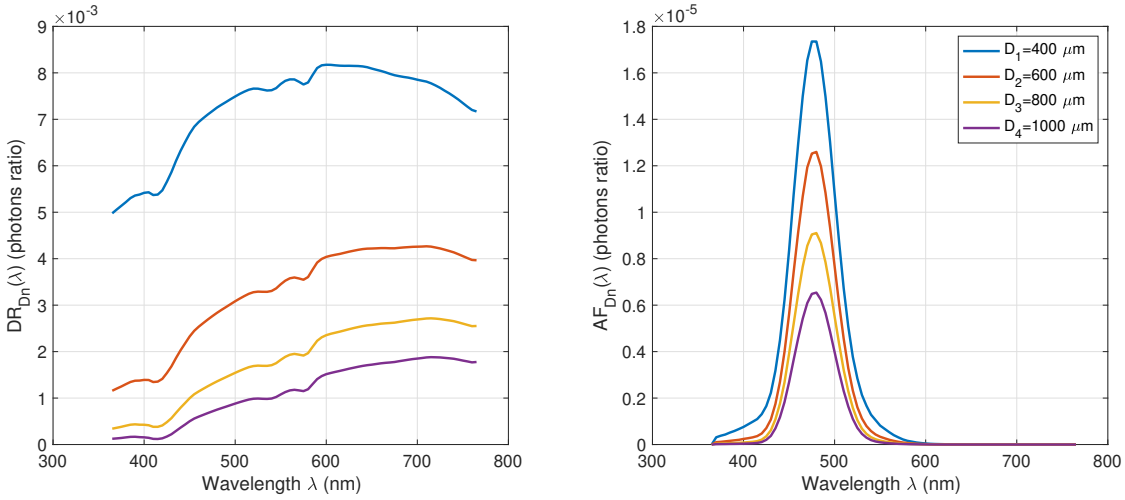

Figure 1.27: $DR(\lambda)$ (left) and $AF(\lambda)$ (right, excitation at $\lambda = 365\ nm$) obtained with the *CudaMCML* photons transport code we adapted to fit the *SpectroLive* clinical device.

1.5.3 The inverse problem resolution

Previous explanations (theory of light transport and carcinoma carcinogenesis, the *SpectroLive* device description and the Monte Carlo adapted code) have been made in order to introduce all elements required for the inverse problem we will focus on here. Firstly, let's define what we will call the "direct Method". The direct method is the fact of simulating the acquisition of $DR^{sim}(\lambda)$ and $AF^{sim}(\lambda)$ spectra having a complete knowledge of the medium characteristics. This implies the knowledge of layer optical parameters, but the thickness too, all is included in the parameter vector $\mathbf{p}$. The inverse problem, as the name suggests, is the other way around. It consists in knowing the outputs of the direct method, *i.e.*, $DR^{exp}(\lambda)$ and $AF^{exp}(\lambda)$ spectra, and to estimate the medium properties $\hat{\mathbf{p}}$ able to generate those spectra. In the absence of an analytical solution, the only way to achieve this goal is through iterative methods. This involves applying the direct method for given medium properties, comparing the simulated spectra at each iteration to the target (*e.g.* clinical spectra) thanks to a least-square cost function calculation (a similarity measure), and repeating it until that the simulated spectra of the iteration match with the target one. The schematic representation of the direct method and the inverse one are represented in Fig. 1.28. The $DR^{exp}(\lambda)$ and $AR^{exp}(\lambda)$ spectra, that is often called target spectra, can also be simulated ones. When the target spectrum is simulated, the inverse problem is purely numerical. This is especially useful for the iterative research algorithm design. Indeed, it allows to

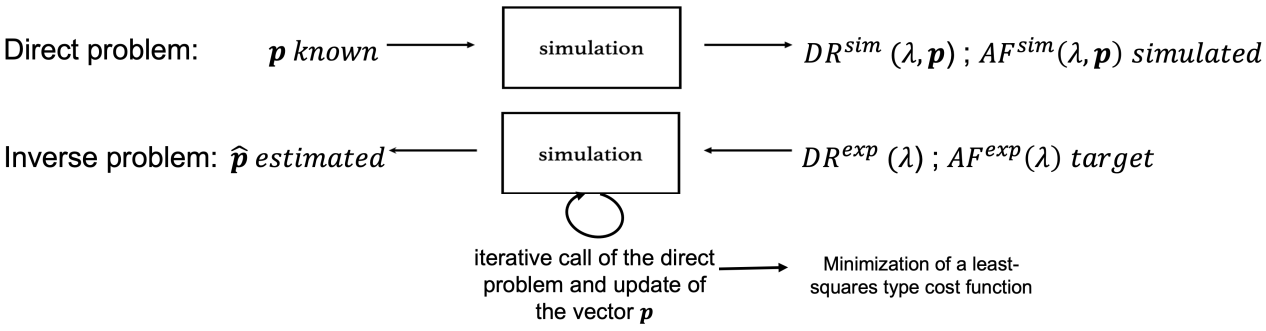

Figure 1.28: Direct and inverse problem schematic representation.

test different cost function, different optimization algorithm, and mainly to verify the convergence of the algorithm to the known ground truth. After the optimization scheme design, the target spectra will be clinical spectra from *SpectroLive* acquisition. An analysis of the local estimated $\hat{\mathbf{p}}$ components (*i.e.*, layers thickness, optical coefficients, fluorophores concentration) around the carcinoma should be discriminating enough to establish the border between the healthy and the pathological tissue (see section 1.4.2.1). The state of the art, as well as the work we made concerning this inverse problem solving is presented in Chapter 3.

1.6 Thesis framework and objectives

We would like to take a step back from our problem and present the strategies used in our approach. First, we would like to bring a clinical dimension to our estimation of optical properties. Indeed, where many research teams are content to assign a malignancy score to the spectral acquisitions of a device using machine learning or deep learning approaches (some members of our team follow this approach with *SpectroLive* data), we seek to extract one or more diagnostic parameters that can be linked to morphological and physiological healthy/pathological skin states. This relationship establishment is only possible if the skin model used in the optimization process truly reflects the multilayered nature of the organ. Thus, the construction of our 5-layer model developed in section 2.5 sets us apart from many approaches presented in the literature, which are often restricted to epidermis/dermis skin models. Our second strategy concerns the multi-modality. We believe that the combination of auto-fluorescence and diffuse reflectance, as well as spatial resolution, contributes to increasing the reliability and the robustness of the diagnosis. This is part of a more general effort to optically characterize the complete skin. Finally, we consider the importance to get an alternative validation of *in-vivo* estimates by solving the inverse problem from the clinical signals. We then turned to the gold-standard of *ex-vivo* estimation of optical properties, *i.e.*, estimates from double integrating sphere measurements. All the elements developed so far also allow us to position the objectives of the thesis work:

1. **Modeling depth study:** This aspect of the work is described in Chapter 2. It consists in improving and using the aforementioned photons transport simulation (see section 1.5.2) to know more about optical paths of photons detected by our clinical device. This includes the elaboration of an optical model able to consider intra- and inter-individual skin variations, as well as the design of numerical tools to quantify photons penetration in skin layers.

2. **Inverse problem solving:** This part of the thesis is detailed in Chapter 3. It consists in estimating optical properties from acquired signal (see Fig. 1.28). Especially, it is explained how we use the information numerically obtained about photons depth penetration in Chapter 2 to better apprehend the optimization process.

3. **Double integrating sphere optical bench design:** This instrumentation part is presented in Chapter 4. It consists in developing an optical bench including integrating spheres to *ex-vivo* estimate optical properties of biological sample such as skin. The optical properties obtained thanks to this optical bench will allow a comparison with those obtained after solving the inverse problem (see Chapter 3).

Chapter 2

Modeling depth study: using the simulation to know more about the skin layers visited by the detected photons

Contents

2.1 Introduction

This second chapter deals with works associated to the first thesis objective *i.e.*, the enhancement of the numerical depth analysis of SR spectroscopy for skin layers optical probing. We firstly present several modifications introduced in P. Rakotomanga's simulation to improve its resemblance with *SpectroLive* and to add outputs to characterize the depths probed by the detected photons. Then we develop our multi-layer skin model in which we identify the physiological parameters allowed to vary to represent a wide range of skin types (intra - and inter-individual). Finally we apply designed numerical tools to characterize photons penetration in various skin media. This study finally led to the published DR spectra decomposition model in which detected photons are separated according the skin layer(s) visited [Colas 2021a]. This numerical depth study enable the better interpretation of SR-DR and SR-AF acquired spectra.

2.2 Improvement of the simulation realism

An analysis of the existing code allowed us to become aware that three areas of improvement were possible compared to the code described in section 1.5.2: the source geometry adaptation, the correction in AF implementation and finally the introduction of the wavelength dependency of the anisotropy factor ($g(\lambda)$ rather than g) parameter.

2.2.1 The source geometry adaptation

Until here, the photons were introduced in the medium with a point source (the photon coordinates at the first step $\vec{p_0} = (px_0 = 0, py_0 = 0, pz_0 = 0)^T$) and a descendant vertical direction ($\vec{d_0} = (dx_0 = 0, dy_0 = 0, dz_0 = 1)^T$ with the z-axis defined positive toward the depth). This situation was, of course, not representative of the real geometry configuration. Indeed, the *SpectroLive* source is defined by its radius $r_{SF} = 300\ \mu m$ and its numerical aperture $NA = 0.22$. So we have chosen to respect its geometry.

Source model changes: To implement the described modification, we firstly decided to treat the photon position on the source output. We had to make a choice between the two possible solutions presented here:

1. The first one was to uniformly distribute the photons on the source output. This idea was implemented using a stochastic uniform drawing of u and v in $[0, 1]$ which is exploited to give the following polar coordinates for the photon on the source output disk:

$$\begin{cases} r_0 = r_{SF}\sqrt{u} \\ \theta_0 = 2\pi v \end{cases} \tag{2.1}$$

   It is perhaps necessary to provide some remarks about these formulas that do not seem intuitive. Indeed, the most natural idea is to consider Cartesian coordinates and to make a uniform random draw on two variables u and v in $[-r_{SF}, r_{SF}]$ to assign to the components px_0 and py_0. The distribution is then naturally homogeneous, but it describes a square and not a disk as desired. This is why it is necessary to opt for a drawing in polar coordinates. The square root $\sqrt{u}$ in the calculation of r_0 may also seem strange. Indeed, it is responsible for a distribution increasingly dense between 0 and r_{SF}. This will be perfectly compensated after

the revolution, *i.e.* the association of this r_0 with the angle θ_0. In Fig. 2.1, this compensation can schematically be observed through annular elementary surfaces of radius r and r' ($r < r'$) and thickness dr represented in gray: to have an equal density in the two different surfaces, a non-uniform draw on r_0 was necessary. The 3D Cartesian coordinates are then calculated with the following formula:

$$\begin{cases} px_0 = r_0 \cos(\theta_0) \\ py_0 = r_0 \sin(\theta_0) \\ pz_0 = 0 \end{cases} \tag{2.2}$$

A representation of this disk distribution is represented on Fig. 2.1 (left).

2. It is also possible to condense photons in the center of the SF output disk, by taking the polar coordinate of the photon according to formula:

$$\begin{cases} r_0 = r_{SF} u \\ \theta_0 = 2\pi v \end{cases} \tag{2.3}$$

The conversion in 3D Cartesian coordinates is similar to the previous one, using formula (2.2)

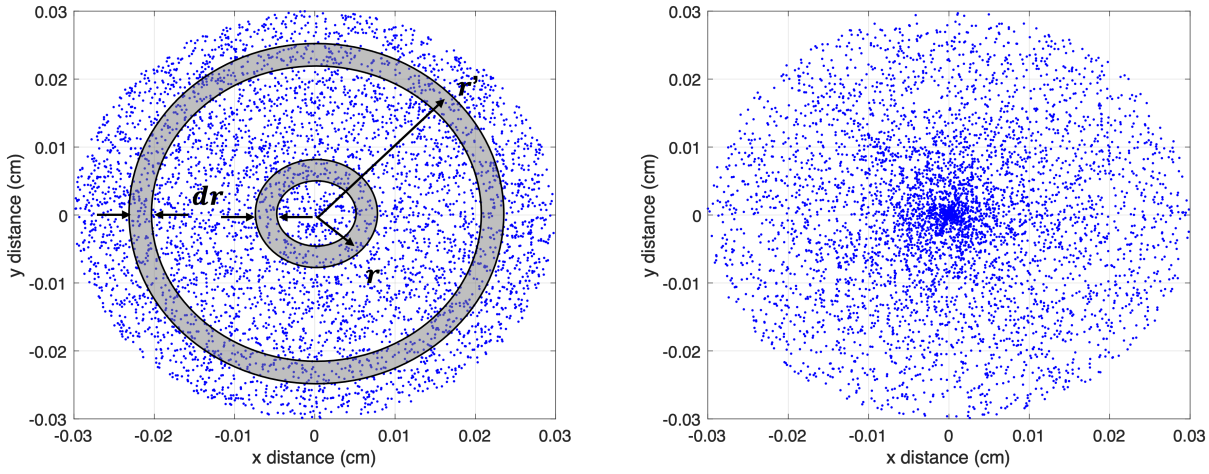

Figure 2.1: Uniform and non-uniform distribution of photon positions using (for left) Eq. (2.1) and (for right) Eq. (2.3). The annular elementary surfaces of radius r and r' and thickness dr are represented in gray.

We made the choice to keep the second solution, that takes into consideration the irradiance distribution on the fiber output, which is the stronger on the optical axis and which decreases when moving apart from this axis. We have now to take into account the angular distribution of the outgoing light. To do this, based on the scheme given the Fig. 2.2, we followed the protocol:

1. It exists an infinity of vectors that indicate a same direction. Thus, to take this fact into account, it was chosen to set its z-component to 1, *i.e.*, $dz_0 = 1$. The aim now is to uniformly distribute the incidence angle θ in the cone associated to the numerical aperture NA. In other words, we want that the vector $\vec{d_0}$ (see Fig. 2.2) points towards points uniformly distributed

in the gray disk. The first step consists in finding the radius R_{max} of this disk. The NA is by definition, associated to the maximal angle θ_{max} in vacuum with refractive index $n_0 = 1$ with the optical axis, *i.e.* $NA = n_0 \sin\theta_{max}$. We finally get that: $\theta_{max} = \arcsin NA/n_0$. From this, we deduce the radius R_{max} with the formula:

$$R_{max} = dz_0 \ \tan\theta_{max} = \tan\theta_{max}$$

2. Once this radius obtained, we can place a point on this area using uniformly distributed variable u and v, with a similar relationship than in formula (2.1), to get the radius r_0 and ϕ_0, the azimuth angle (see Fig. 2.2).

$$\begin{cases} r_0 = R_{max}\sqrt{u} \\ \phi_0 = 2\pi v \end{cases} \tag{2.4}$$

3. Once this point get, we have to transform our polar coordinates to Cartesian, in order to get the dx_0 and dy_0 components of $\vec{d_0}$, we finally have:

$$\begin{cases} dx_0 = r_0 \ \cos\phi_0 \\ dy_0 = r_0 \ \sin\phi_0 \\ dz_0 = 1 \end{cases} \tag{2.5}$$

4. The direction is now the one we want. We just have to normalize it before apply the position update according to Eq. (1.23). By introducing the the vectorial norm $||\vec{d_0}|| = \sqrt{dx_0^2 + dy_0^2 + dz_0^2}$, we finally obtain the normalized initial direction vector $\vec{d_{0,n}}$:

$$\vec{d_{0,n}} = \frac{\vec{d_0}}{||\vec{d_0}||}$$

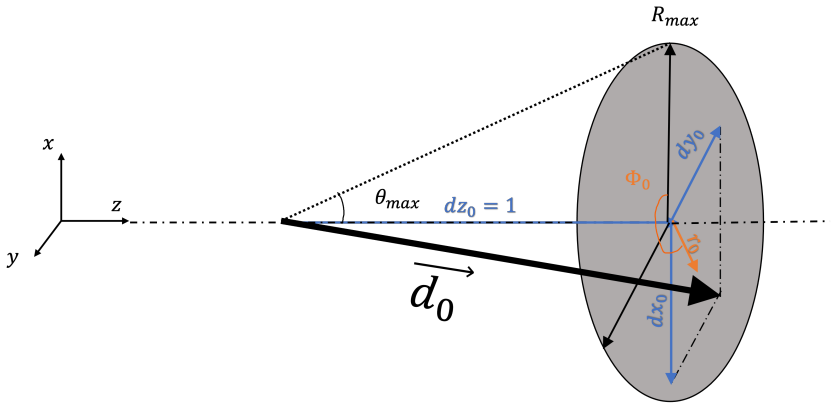

Figure 2.2: Scheme illustrating the construction of the direction vector $\vec{d_0}$ of the photon at the entrance to the medium.

Impact of the source shape consideration Now that the photon emission geometry has been introduced, it is time to analyze the impact of these changes on our outputs. After showing the differences on our qualitative outputs, we will study the impact on our outputs of interest, namely the DR and AF spectra. To visualize the modifications introduced, we firstly displayed the fluence maps for a vertical point emission as well as for a more realistic illumination (that considers the emission spreading) in Fig. 2.3. The absorption events for the realistic SF are in accordance with the expectations since they are less condensed than for the point source. This qualitative map allows us to validate the implemented code.

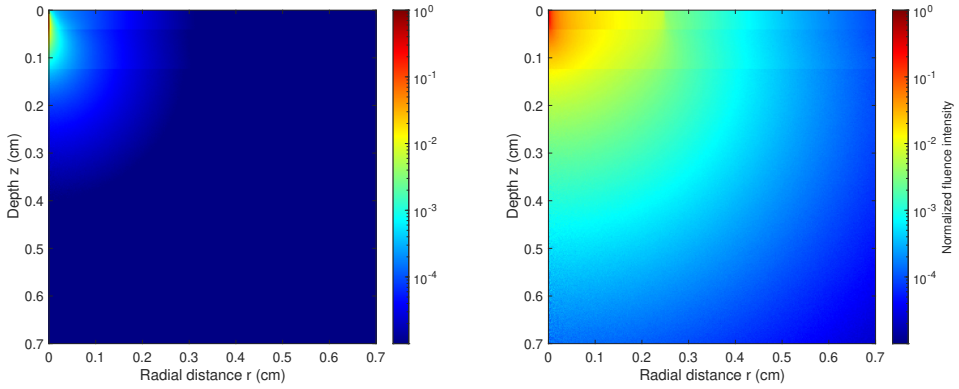

Figure 2.3: Impact of source geometry on absorption fluence map. The maps on the left and on the right were obtained for the point source, and the more realistic (non punctual) source, respectively. In both maps, the discontinuities are caused by optical parameters changes between the 4 layers of the skin model.

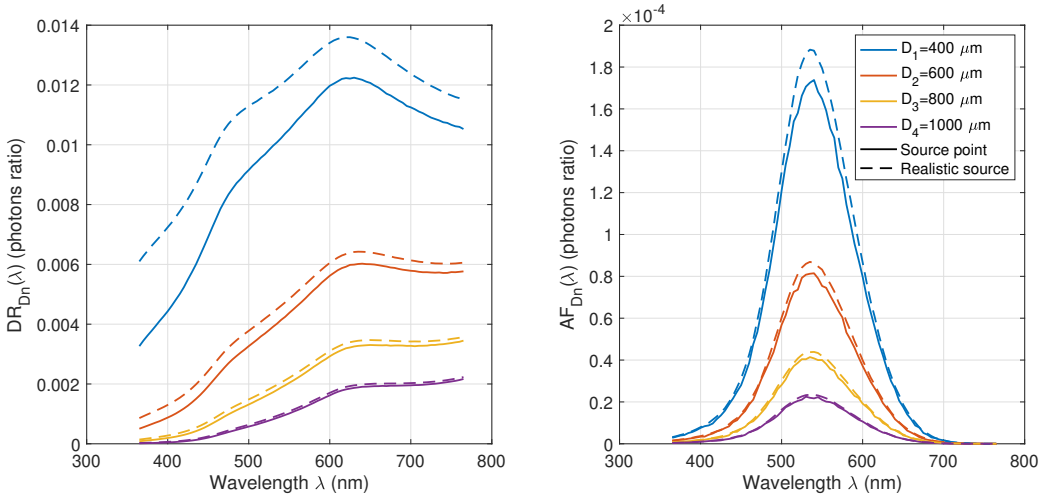

Figure 2.4: Impact of source geometry on DR (left) and AF (right) spectra. Continuous lines and dashed lines are for punctual and realistic SF, respectively.

The changes between DR and AF spectra with the new source configuration is of course function of the medium properties, but the results presented in this paragraph were get with a 4-layers medium with thickness and optical properties in accordance (in order of magnitude) with a skin model representing the stratum corneum, the epidermis, the dermis and a subcutaneous fat. A fluorophore was added in the epidermis layer, with a Gaussian absorption centered at $\lambda_{exc} = 460\ nm$ and an emission at $\lambda_{fluo} = 540\ nm$, to also analyze fluorescence signal evolution. Of course, all the simulations settings, excepted the source geometry update, were similar. Fig. 2.4 shows the different $DR_{Dn}(\lambda)$ and $AF_{Dn}^{460}(\lambda)$, for both source geometries. One can clearly notice that the signal increases with the new configuration, especially and logically for the shorter D_n. It is obviously due to the effective source-to-detector distance that decreases.

2.2.2 Adaptation of the medium properties to the fluorescent wavelength

Fluorescence behavior correction Until here, the fluorescence simulation was not completely finalized. Indeed, the fluoresced photon was traveling in the medium with the initial optical properties, that is to say the properties of the medium at the excitation wavelength. By now, the fluoresced photon at the wavelength λ_{fluo} will travel in the medium optically defined by $\mu_a(\lambda_{fluo})$ and $\mu_s(\lambda_{fluo})$.

Impact on interest output The evolution of the AF signals due to the described modification is represented in Fig. 2.5. One can observe that the signal increases (output level x2) when the propagation of the fluoresced photon is adapted to its new wavelength. Indeed, λ_{exc} belongs to the UV range whereas λ_{fluo} is in the visible spectrum, and biological medium are very opaque in the UV.

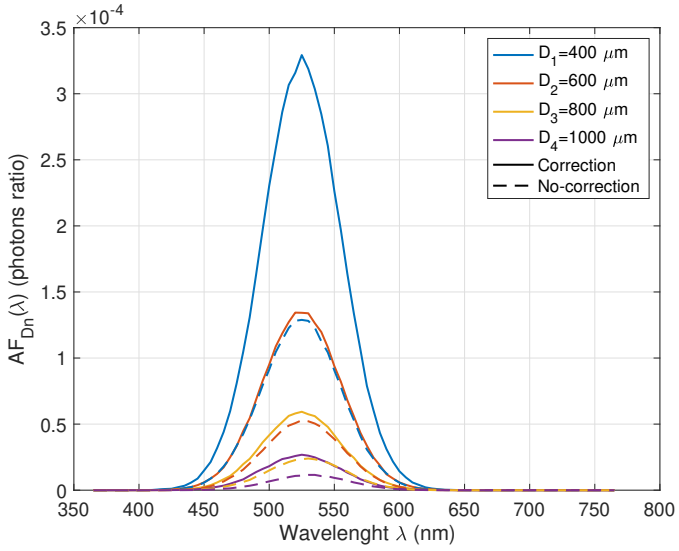

Figure 2.5: Impact of the medium optical properties update according the fluorescent wavelength on the AF spectra.

2.2.3 Wavelength dependency of the anisotropy factor

Rather than considering the anisotropy coefficient as a constant, the photon transport code has been modified to be able to take as input argument a vector g whose components are a function of λ. Fig. 2.6 shows the impact of a non constant g on DR simulated spectra in the *SpectroLive* configuration for a mono-layer medium with optical properties of methylen blue and intralipids. Colored spectra are for $g(\lambda) = c$ with $c \in [-0.8, 0.8]$ while the black dashed-line is for $g(\lambda)$ linearly varying between $g_{max} = 0.8$ (for $\lambda = 365\ nm$) and $g_{min} = -0.8$ (for $\lambda = 765\ nm$). The sole purpose of this experiment is to see the impact of a variation of g between these extreme values, *i.e.* between -1 and 1. These variations are of course too big in comparison to the variations that exist for a biological medium such as skin (where the anisotropy factor satisfies $g \in= [0.4, 1]$) Results show that, even if the range of variation of g was disproportionately large

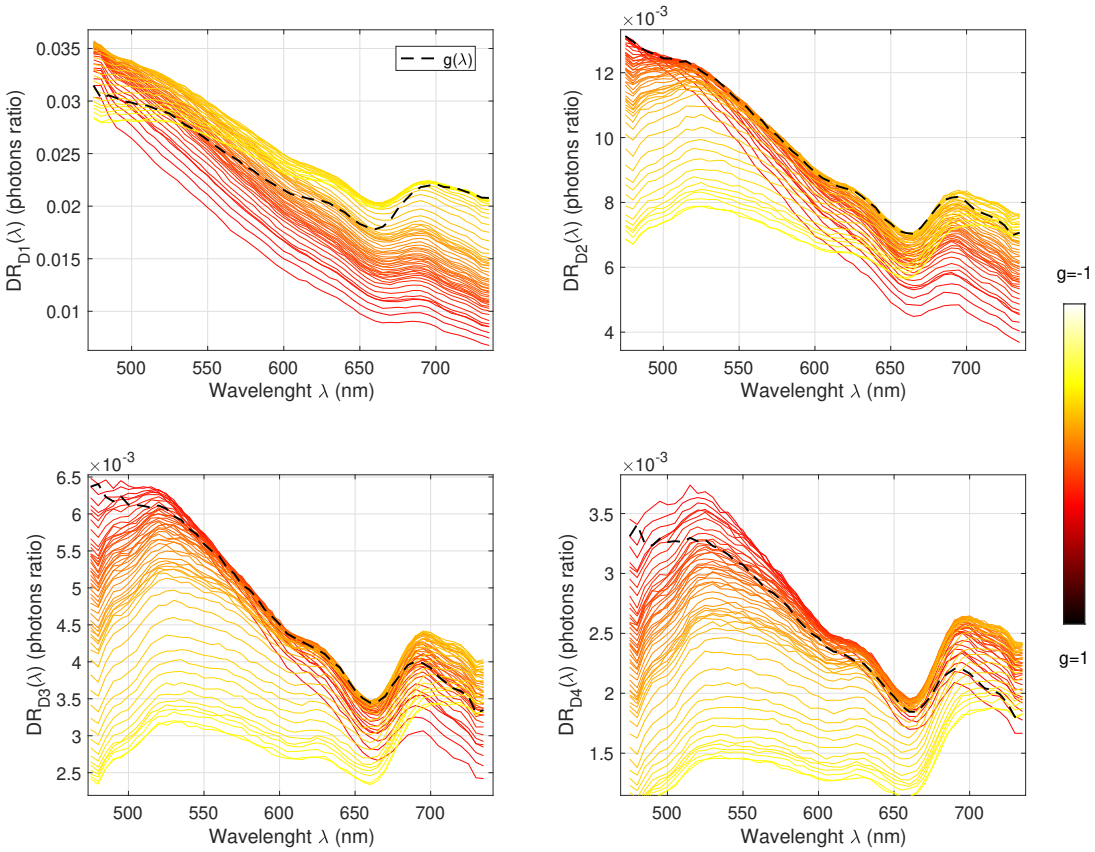

Figure 2.6: Impact of the wavelength dependency of the anisotropy factor on DR spectra. Colored spectra are for $g = constant$ while the black dashed line considers a wavelength dependency of the parameter, *i.e.*, $g = g(\lambda)$.

in this illustrative example, this significantly affects the spectral shape ans intensity level of DR spectra. From these curves, it was therefore decided to allow the user to provide a spectral vector

$g(\lambda)$ rather than a scalar in the input argument of the simulation.

2.3 Interest to know about photon penetration in skin-layers

After having described the simulation model correction we introduced to improve the simulation fidelity, this section develops the interest of knowing more about the origin in depth of the photons detected by the devices of spatially resolved spectroscopy. It also discusses the works appearing in the literature on this subject.

2.3.1 Motivations

As the metabolic modifications associated with carcinogenesis are local (see section 1.3.2), the quantitative estimation of the penetration depth of the photons detected using point spectroscopy is at stake. Indeed, obtaining a spectral signature associated with a symptom of cancer is only possible if the photons captured by the spatially-resolved device reached this local region (*i.e.*, the skin layer concerned) where carcinogenesis occurs. Among this symptom, Breslin et al. [Breslin 2003] studied the sensitivity of DR spectra to elastosis (accumulation of elastotic material in the papillary dermis located underneath epidermis). Cancer growth is also related to the enzymatic degradation of collagen fibers in the dermis leading to collagen fluorescence decrease [Ye Yuan 2008] and to the decrease of NADH fluorescence in the epidermis [Borisova 2014]. Finally, morphological changes may be significant for part of skin carcinomas such as ulceration and hyperkeratosis [Amouroux 2008], which are respectively characterized by a thinning or skin thickening (of about a factor 10) of the stratum corneum superficial layer. More generally, studying the detected photons penetration depths allow to further understand the numerically and experimental acquired spectra. Associating a spectral region and a SD distance with a probed skin layer allow to better apprehend the OP estimating when solving the inverse problem from clinical spectra (see Fig. 1.28). This idea will be developed later in section 3.4, but can be schematically roughly summed up by the Fig. 2.7 using the 5 layer skin model: the simulation allows to associate the photon at a wavelength λ and collected at the D_n SD distance to visited skin layers.

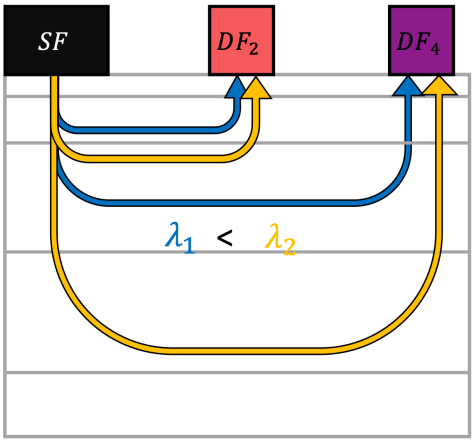

Str. Corneum
Liv. Epidermis
Pap. dermis
Ret. dermis
Sub. Fat

	λ_1		λ_2	
	D_2	D_4	D_2	D_4
Str. Corneum	✅	✅	✅	✅
Liv. Epidermis	✅	✅	✅	✅
Pap. dermis	❌	✅	✅	✅
Ret. dermis	❌	❌	❌	✅
Sub. Fat	❌	❌	❌	❌

Figure 2.7: Schematic representation of the ambition of the *in silico* depth study which aims to associate a couple (λ, D_n) with probed skin layers.

2.3.2 State of the art concerning photon depth penetration

The need to explain SR-DR and SR-AF signals acquired on the surface, resulting from light–tissue interactions in all skin layers, justifies the use of numerical simulation as a tool to interpret the acquired signals. The literature reports works by several teams using photon transport simulation in a multi-layer skin model to extract features that describe the propagation of the acquired photons [Zhang 2016, Martelli 2016]. First, in a very visual way, absorption density maps of detected photons in a three-layer skin model [Hidenobu Arimoto 2005] provide information on a photon's trajectories. In a more quantitative manner, teams have presented their results on the penetration depth of photons. In a two-layer model, histograms of probed depths have been created at 450 and 650 nm to extract the average penetration depth [Arifler 2005], while the interrogation depth (mean depth of all detected photon scattering events) [Tseng 2012], or measurement depth (median of the cumulative absorption on fluence absorption maps) [Hidenobu Arimoto 2005] can also be extracted from simulations to characterize the photon's penetration depth. Other quantities of interest are exploited to know more about the subcutaneous behavior of backscattered photons, such as the path length distribution with increasing SD distance [Nilsson 2002, Larsson 2003]. This quantity was even declined in the mean partial path length [Liebert 2004, Fredriksson 2012], which consists of dividing the total path length into layer path contributions.

2.4 Creation of new outputs to deeply characterize photon propagation

This section aims to develop all the new outputs which characterize the penetration of photons in the simulation. Subsequently (see section 2.6), these will be applied and exploited to multi-layered skin media.

2.4.1 DR trajectory and auto-fluorescence events maps

2.4.1.1 The SR-DR trajectory maps

It offers a qualitative picture of detected photon trajectories between the source and the collecting fibers, based on the following algorithm:

Result: Creation of the detected photon trajectory map *TrajectoryMap*
for *All the photons* **do**
  while *photon is alive* **do**
    store its scattering position in a list *posList*;
  end
  if *photon is detected (i.e., collected by one of the DR sensing fibers)* **then**
    store its detected weight in variable w_d;
    increment all the voxels of *TrajectoryMap* indexed by *posList* by the value w_d;
  end
end

Algorithm 1: Creation of the SR-DR trajectory map, for a given wavelength and source-detector distance.

The final trajectory map is a 2D representation of the 3D matrix described in the Algorithm 1, in which the source appears in the top left corner, the vertical axis represents the medium's depth and the horizontal axis the medium's radial distance to source. A graphical representation of the

relationship between the 3D numerical medium and the 2D output map determined by Algorithm 1 is shown in Fig. 2.8 The z-axis (color chart intensity) is to be interpreted as a volume density. Indeed, for a given pixel (i, j) corresponding to a (z_i, r_j) position in the 2D matrix medium, the intensity is the sum of the weights of all detected photons that were subjected to a scattering event on this position, divided by the voxel volume.

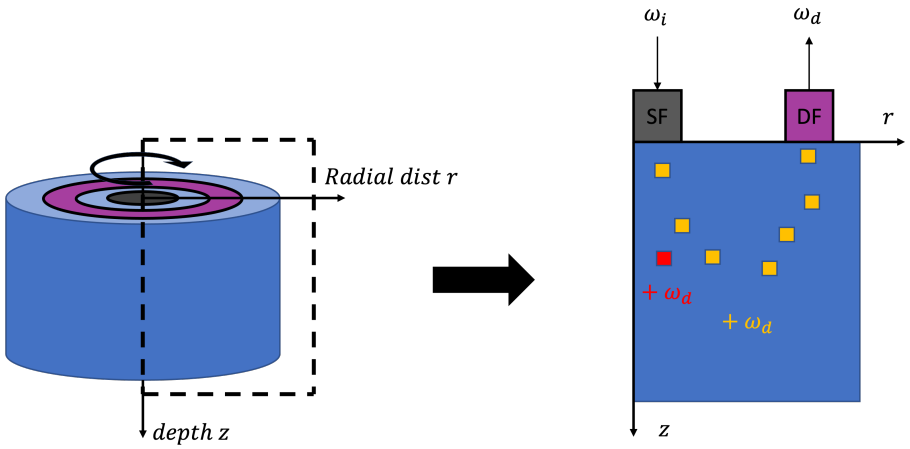

Figure 2.8: Illustration of the DR trajectory maps meaning described in Algorithm 1 (yellow trajectory) and AF events map described in Algorithm 2 (red position). w_i and w_d stand for the initial (send by the source fiber) and detected (collected by the detected fiber) photon numerical weights, respectively.

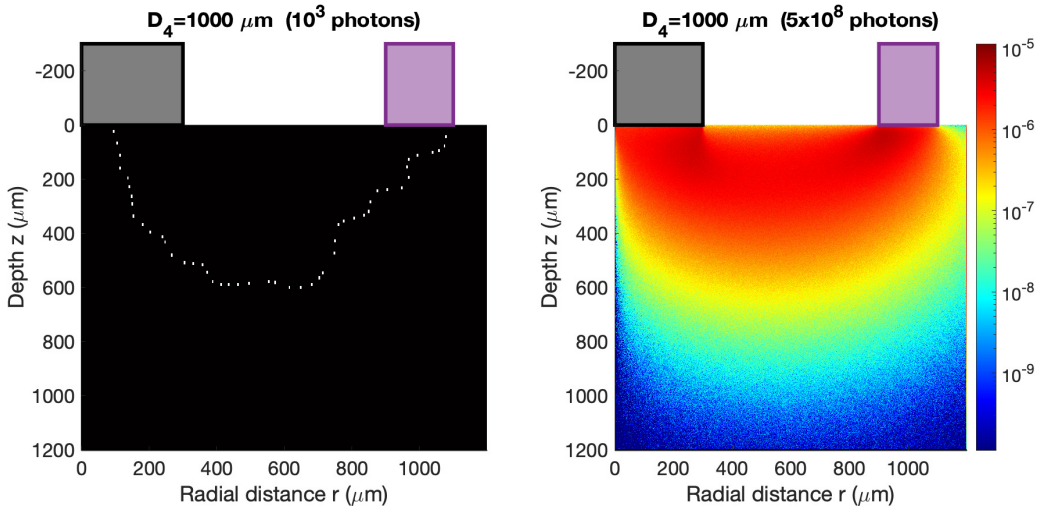

Figure 2.9: DR trajectory maps for $D_4 = 1000\ \mu m$ obtained for a mono-layer medium with $\mu_a = 1.5\ cm^{-1}$, $\mu_s = 100\ cm^{-1}$ and $g = 0.85$. For left map, the number of launched photons was reduced to isolate a single photon. The image was binarized to highlight the photon trajectory between the SF (black square) and the DF (purple square).

To validate the Algorithm 1, we managed to isolate a single photon by reducing the number of photons launched in a mono-layer medium. Fig 2.9 (left) shows the trajectory of the only one photon reaching the sensor in this simulation. Its result brings us the evidence that final trajectory map is indeed the superposition of all detected photon paths. For same medium but an increased number of photons, the trajectory map obtained is also given in log color scale (in the right part of Fig. 2.9). The contribution of all photons is responsible for a "Banana shape" pattern, often mentioned in the literature [Kazanci 2015, Stratonnikov 2001, Koenig 2015]. The geometry of the sensor imposes a high passage density just under the transmitting and receiving fibers. Between, the photons are more free and the range of possible paths increases. This freedom is at the origin of the widening in the center of the "banana". This kind of map provides a good idea of typical photons paths between the SF and the DF, and this for all the wavelength λ and every SD separation.

2.4.1.2 The SR-AF maps

It offers a qualitative picture of auto-fluorescence events positions of detected photons thanks to the following algorithm:

Result: Creation of fluorescence impact map of the detected photons *FluorecenceMap*
for *All the photons* **do**
  while *photon is alive* **do**
    if *the photon causes a fluorescence event* **then**
      store the fluorecence event position *posFluo*;
    end
  end
  if *photon is detected (i.e., collected by one of the AF sensing fibers)* **then**
    store its detected weight in variable w_d;
    increment the voxel of *FluorecenceMap* indexed by *posFluo* by the value w_d;
  end
end

Algorithm 2: Creation of the fluorescence impact map, for a given wavelength and source-detector distance.

A graphical representation of Algorithm 2 is also shown in Fig. 2.8. We created an illustrative numerical example to validate the algorithm. We first established a 2 layers-medium (with optical absorption and scattering properties of epidermis ans dermis), in which we introduced in each one a "non-physical" fluorophore (for testing). The absorption and emission profiles of these 2 fluorophores are shown in Fig. 2.10 (top-left). We choose intentionally 3 excitation wavelengths of interest: the first at 450 nm, able to only excite the fluorophore of the epidermis, the second at 500 nm, in an overlapping area of the absorption of the two fluorophores. And finally, at 550 nm, a wavelength that only excites the fluorophore in the dermis. The same Fig. 2.10 also shows the auto-fluorescence events maps (top-right $\lambda = 450$ nm, bottom-left $\lambda = 500$ nm and bottom-right $\lambda = 550$ nm) generated by Algorithm 2. This very special case allows us to validate the proper functioning of the tool created. Those data bring us numerical pieces of evidence about fluorescence localization. Especially, fluorescence maps seem to indicate that most of detected fluorescent photons come from an area vertically above the emission fiber.

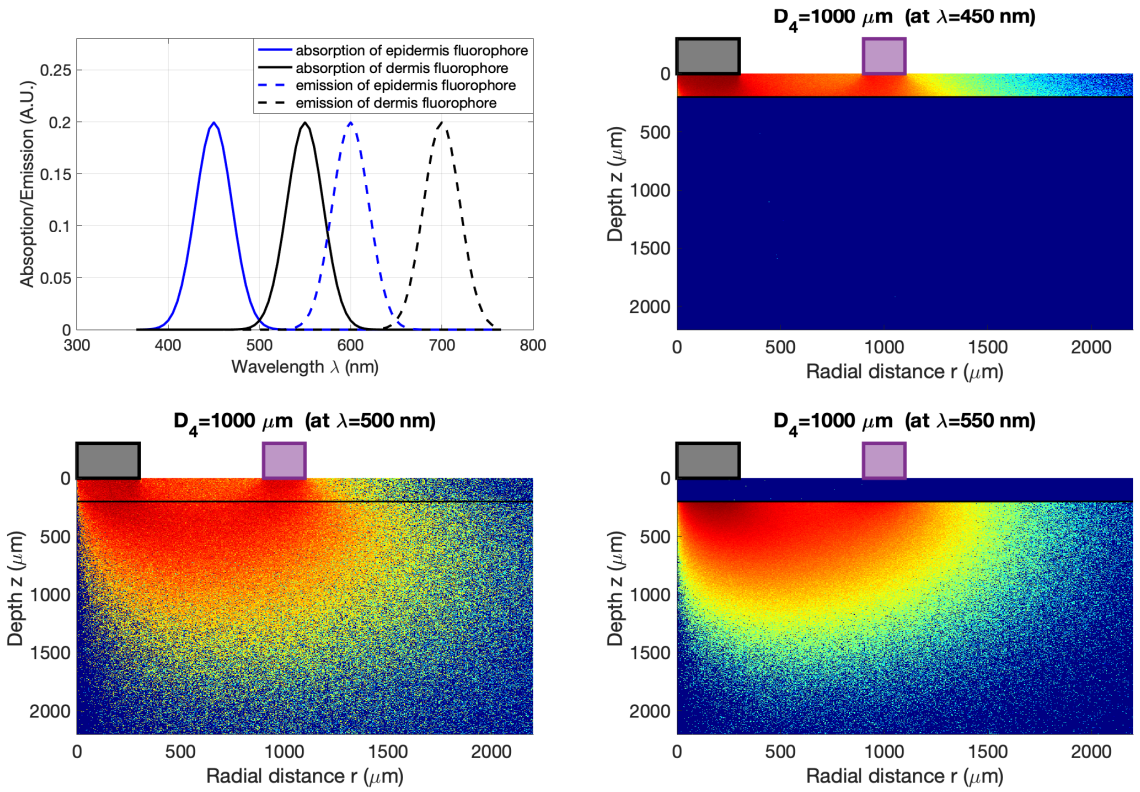

Figure 2.10: AF events maps for $D_4 = 1000\ \mu m$ obtained for a bi-layer medium with absoption $\mu_{a,fluo}(\lambda)$ and emission $Emi(\lambda)$ of both fluorophores given in top-right sub-figure. Top-right, bottom-left and bottom-right sub-figures are for excitation at $\lambda = 450\ nm$, $\lambda = 500\ nm$ and $\lambda = 550\ nm$, respectively.

Subsequently, this kind of fluorescence map resulting from a simulation in which the environment will be more realistic (multi-layer skin model) will provide interesting information about the origin of the fluorescence photons. Indeed, after having placed the endogenous fluorophores in the different layers of the model (the realistic skin medium including fluorophore is described in section 2.5.3), it will be possible to see how they are excited for each excitation of the clinical device (see Eq. (1.19)). This is done in the section 2.6.2.2.

2.4.2 Depth characterization histograms

2.4.2.1 Common algorithm

For the sake of brevity, the algorithms resulting in the creation of the DR histograms of paths lengths (total distance distance traveled by each detected photon in the medium), number of steps (number of scattering events for each detected photon in the medium) and maximum probed depths (lowest position of the trajectory in the medium for each detected photon) are all determined in a same algorithm (Algorithm 3):

Result: determination of the histograms *histoPathsLengths*, *histoStepsNumber* and *histoZmax*
for *every photon launched* **do**
  while *photon is propagating in the medium* **do**
    store the path length dl_{step} [a] for each scattering events;
    increment the real number l_{phot} for each scattering events by dl_{step};
    increment the integer number step $\#step_{phot}$ for each scattering events by 1;
    if required, update its maximal depth of scattering event $z_{max\ phot}$;
  end
  if *photon is detected (i.e., collected by one of the DF)* **then**
    store its detected weight in variable w_d;
    increment the number of *histoPathsLengths* corresponding to l_{phot} by w_d;
    increment the number of *histoZmax* corresponding to $\#step_{phot}$ by w_d;
    increment the number of *histoStepsNumber* corresponding to $z_{max\ phot}$ by w_d;
  else
    photon is lost ;
    (definitively absorbed inside medium or exits the medium outside any DF)
  end
end
normalization of the 3 histograms by dividing by $DR_{D_n}(\lambda)$;

Algorithm 3: Pathlengths, number of steps and maximum probed depths histogram of weighted detected photons.

[a] see Eq. (1.21)

A schematic representation of this Algorithm 3 (for each of the three quantities) is given in Fig. 2.11. Discussions about obtained histograms will be detailled in the following sections.

2.4.2.2 Pathlengths and scattering steps histograms

Pathlengths and scattering steps number histograms are provided in Fig. 2.12 for a mono-layer medium. As expected, the travel inside the medium is longer when the SD distance is increasing. The spreading of both distributions can also be noticed for this situation.

The 2 previous histograms were validated using the following protocol. We firstly designed a mono-layer medium for which we provide the absorption $\mu_a(\lambda)$ and scattering $\mu_s(\lambda)$ coefficients. Using the simulation, we get both histograms for each couple (λ, D_n). We then determine the maximum peak abscissa (associated with the most represented occurrence) in the steps histogram, *i.e.*, $\#steps_{max}(\lambda, D_n)$. The same procedure is repeated with the pathlengths histograms, leading to $l_{max}(\lambda, D_n)$. From it, we calculate the most likely free path between two scattering events, defined by the forward term to term division:

$$l_{t,calc}(\lambda, D_n) = \frac{l_{max}(\lambda, D_n)}{\#steps_{max}(\lambda, D_n)} \tag{2.6}$$

This wavelength depending vector should be compares with theoretical $l_t(\lambda)$, linked to the extinction coefficient μ_t introduced in Eq. (1.10) according:

$$l_t(\lambda) = \frac{1}{\mu_t(\lambda)} \tag{2.7}$$

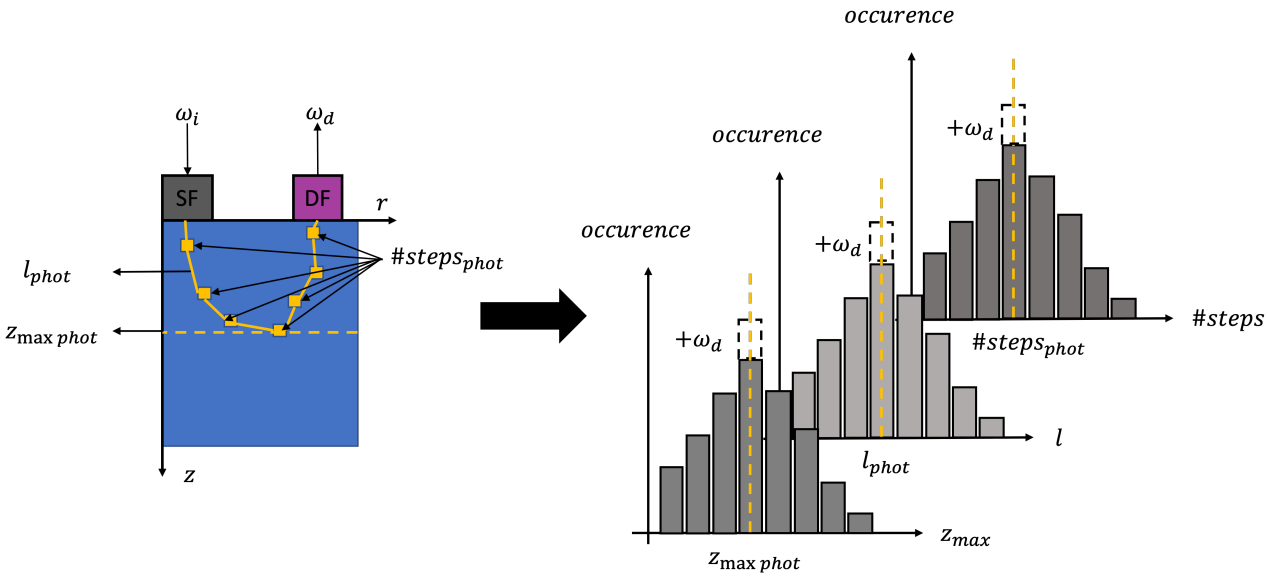

Figure 2.11: Illustration of the 3 DR histograms (*histoPathsLengths*, *histoStepsNumber* and *histoZmax*) introduced in Algorithm 3. w_i and w_d stand for the initial (send by the source fiber) and detected (collected by the detected fiber) photon numerical weights, respectively.

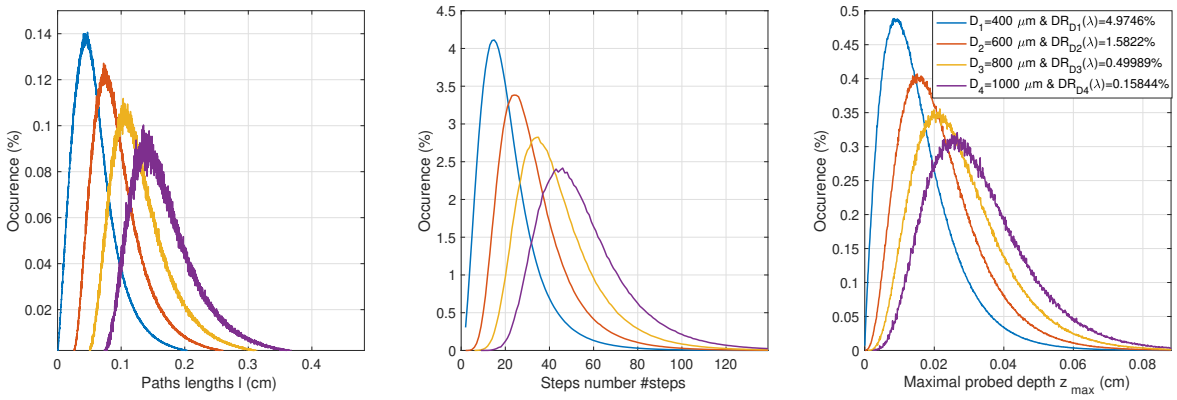

Figure 2.12: Pathlengths (left), scattering steps number (middle) and maximum probed depth (right) histograms mentioned in section 2.4.2.1 and obtained for a mono-layer medium of optical properties $\mu_a = 10\ cm^{-1}$, $\mu_s = 300\ cm^{-1}$ and $g = 0.85$ (it roughly corresponds to epidermal layer OP for $\lambda \approx 400\ nm$).

Fig. 2.13 (left), shows this comparison for a mono-layer medium. As explained in the protocol, these measurements are independent of the SD distance, which is why we have represented them for the 4 collecting fibers in the geometrical configuration of *SpectroLive*. The right sub-figure is obtained in a similar way, except that we have taken the mean of the histograms rather than the abscissa corresponding to the maximums. This explains the difference in noise between the two

sub-figures. The correspondence between the theoretical curves and those calculated extracted from the histograms allows cross-validation of the latter.

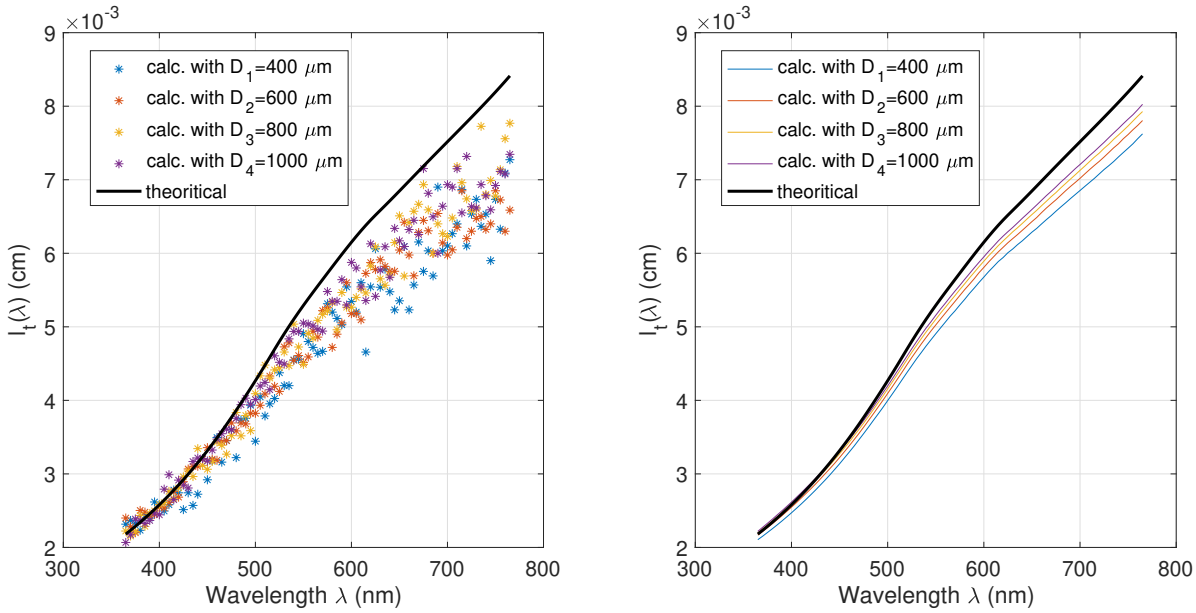

Figure 2.13: Comparison of $l_t(\lambda)$ (theoretical curve, see Eq. (2.7)) and $l_{t,calc}(\lambda, D_n)$ (calculated values, see Eq. (2.6)), with the "maximum abscissa" technique (left) and "mean" technique (right).

2.4.2.3 Maximum probed histograms

DR maximum probed depths histograms are provided in Fig. 2.12 (right). The conclusions to be drawn are quite similar to those established with steps and paths lengths histograms. This numerical output allows to know more about the volume probed by the device for each wavelength range, and each SD separation.

2.4.3 Numerical separation of fluorophore contributions in AF signals

Some modifications in the photon transport code were introduced to better understand the acquired AF signals (*i.e.*, to know which fluorophore is at the origin of the photons that contribute to the spectra. The exploitation of these modifications (developed in section 2.6.2), in terms of analysis, is here very limited, but it was for us to simply present this novelty and to expose the future interest that they raise. In order to better apprehend the AF set of spectra (*i.e.*, for all excitation λ_{exc_l} and for all SD distances D_n) acquired in clinics, we decided to use the simulation to quantify the contribution of each fluorophore in the resulting spectrum. In other words, it is necessary to determine the contribution ${}^{m}AF_{Dn}^{exc_l}(\lambda)$ of each fluorophore m among the N_{fluo} present fluorophores in the medium so that:

$$AF_{Dn}^{exc_l}(\lambda) = \sum_{m}^{N_{fluo}} {}^{m}AF_{Dn}^{exc_l}(\lambda) \tag{2.8}$$

In terms of code, it is simply a matter of memorizing the absorbing fluorophore at the time of the fluorescence event, then in case of detection, to store separately the contribution to the fluorescence signal of each fluorophore.

2.5 Design of a skin medium optical model made of 5 layers

The simulations carried out until now in this thesis were done with simple mono-layer or bi-layer media which do not reflect the reality of the human skin. To get closer to human skin multilayered complexity, and fully exploit the depths characterization outputs, we present here a 5-layer skin model which will be used for photon depth penetration study (see section 2.6) and for solving the inverse problem (see Fig. 1.28). Based on explanations provided in section 1.3, this section details more this skin model.

2.5.1 Layer thicknesses and modeled skin types

The numerical model mimicking the skin was designed following a five planar multi-layered medium, representing (from superficial to deepest layers) the stratum corneum (1-SC), the living epidermis (2-LE), the papillary dermis (3-PD), the reticular dermis (4-RD) and the subcutaneous fat (5-SF). The total thickness was fixed to $z^{tot} = 6120\ \mu m$, while the total radius of the simulation medium was set to $r^{tot} = 3000\ \mu m$. The results presented hereafter are valid under the assumption that the optical properties of each of the skin layers are homogeneous in the cylinder thus described (*cf.* Fig. 2.14). Considering the order of magnitude of skin optical properties and the position of the the farthest collecting fiber ($D_4 = 1000\ \mu m$), edge effects (*i.e.*, photons that would be collected by DF after reflection on the side or bottom border of the medium) were negligible. This was verified numerically with absorption maps of detected photons: none of them reached the bottom (in the worst case-*i.e.*, a wavelength in near IR, great SD distance and fair phototype-only 1% of detected photons were scattered in the SF), while less than 0.1% were collected after having reached the side border.

Consequently, five combinations of SC and LE thicknesses were defined, among which three featured a thin, medium and thick healthy epidermis and two represented some specific values encountered in carcinoma. SC and LE thicknesses may significantly vary according to age, gender, and body location [Maiti 2020, Chopra 2015, Robertson 2010] and also for different skin physiological states. For instance, the stratum corneum can either completely disappear or thicken 10-fold [Amouroux 2008] in the case of ulceration or hyperkeratosis, respectively. Indeed, other epidermal layers are also affected by cell proliferation due to skin carcinoma. However, for the sake of comparison with healthy conditions, only SC thickness was varied to model these two subtypes of skin carcinomas; *i.e.*, in the case of ulceration, the absence of SC was modeled through the removal this superficial layer. As shown in Fig. 2.14, the thickness values of middle layers PD and RD were fixed (200 and 1800 μm, respectively), while those of the top layers (SC and LE) were varied to simulate different tissue conditions. The thickness of the underlying SF layer was consequently adjusted to keep the total thickness z^{tot} of our simulation model constant. We considered the range of values of SC and LE thicknesses as well as their approximate ratio ($\sim 1/4$) reported for sun-exposed skin sites only (head including face, scalp, ear, cheek and shoulders, back, arms, back of hand and legs), which are $10-30\ \mu m$ and $60-120\ \mu m$ for SC and LE layers, respectively. The numerical values associated with the elaboration of these three healthy and two other pathological epithelium (carcinoma) simulation media configurations are summarized

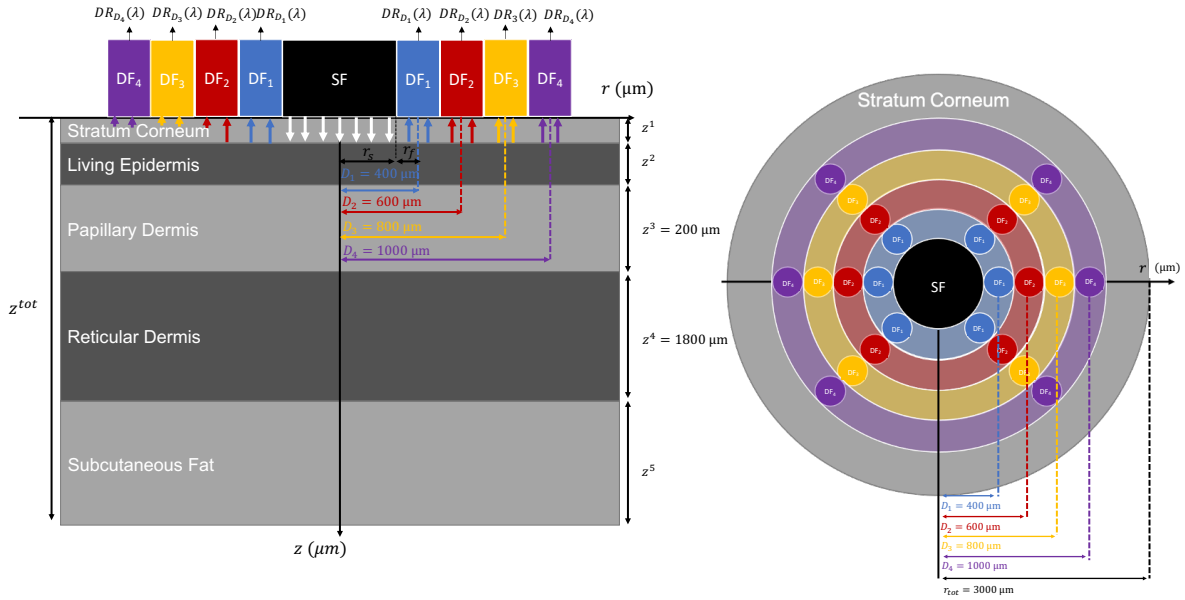

Figure 2.14: Schematic representation of the SR-DRS fiber probe geometry and of the five-layer skin implemented for simulations: vertical section view (left) and top view (right). SF, DF and $DR_{D_n}(\lambda)$ stand for Source Fiber, Detection Fiber and Diffuse Reflectance spectrum at the distance D_n ($n \in [\![1\ ;\ 4]\!]$), respectively.

in Table 2.1.

Skin Categories		SC thickness z^1 (μm)	LE thickness z^2 (μm)
Healthy	Smallest thicknesses	10	60
	Mean thicknesses	20	90
	Highest thicknesses	30	120
Carcinoma	Ulcerated	0	90
	Hyperkeratosed	300	90

Table 2.1: Values of the SC (stratum corneum) and LE (living epidermis) layer thicknesses implemented in our skin model to simulate 5 different healthy skin and carcinoma conditions.

2.5.2 Skin optical properties

The optical properties defined for each skin layer in terms of absorption and scattering are synthesized in the following paragraphs. Complementary details can also be found in [Colas 2020].

Absorption properties: Absorption coefficients $\mu_a^k(\lambda)$ were defined for each layer $k \in \{1, ..., 5\}$ of the numerical skin model taking into account the contribution of the five main endogenous absorbers i of human skin, which are blood (decomposed in oxygenated hemoglobin HbO_2, deoxygenated hemoglobin Hb, and bilirubin contributions), water, melanin (decomposed in eumelanin and pheomelanin), lipids and β-caroten, respectively, as well as their volume fraction $f_{v,i}^k$, in the mixture. A residual absorption baseline was also added according to [Meglinski 2002] (*cf.* $\mu_{a,base}$

in Eq. (2.9)). Thus, the total absorption coefficient of a skin layer was defined as the sum of the latter baseline and the contributions $\mu_{a,i}^k$ of each of the five chromophores, weighted by their respective volume fraction, in accordance with [Jacques 2013]:

$$\begin{aligned}\mu_a^k(\lambda) = \mu_{a,base}(\lambda) \\ &+ f_{v,blood}^k[\gamma\mu_{a,HbO_2}^k(\lambda) + (1-\gamma)\mu_{a,Hb}^k(\lambda) + \mu_{a,bilirubin}^k(\lambda)] \\ &+ f_{v,water}^k\mu_{a,water}^k(\lambda) \\ &+ f_{v,mel}^k[\mu_{a,eum}^k(\lambda) + \mu_{a,phe}^k(\lambda)] \\ &+ f_{v,lipids}^k\mu_{a,lipids}^k(\lambda) \\ &+ f_{v,\beta-caroten}^k\mu_{a,\beta-caroten}^k(\lambda)\end{aligned} \tag{2.9}$$

where $\mu_{a,i}^k$ are all expressed in cm^{-1}, $\mu_{a,base}(\lambda) = 7.84 \times 10^8 \times \lambda^{-3225}$ (λ in nm), and γ is the ratio between HbO_2 and Hb, set to $\gamma = 0.9$ in our simulations. Lipids and water absorption spectra, as well as extinction coefficients of the other compounds were directly implemented in our model from [Prahl 2018]. It is noticeable that, for β-caroten and blood (namely both hemoglobins and bilirubin), molar extinction coefficients $\varepsilon_i^{mol}(\lambda)$ (in $\mathrm{cm}^{-1}/\mathrm{mol{\cdot}L}^{-1}$) were given, while for melanin, the mass extinction coefficients $\varepsilon_i^{mass}(\lambda)$ (in $\mathrm{cm}^{-1}/\mathrm{g{\cdot}L}^{-1}$) of eu- and pheo-melanin were provided. These are linked to absorption coefficients according to the following formulas:

$$\mu_{a,i}^k(\lambda) = \frac{\varepsilon_i^{mol}(\lambda)}{M_i}c_i^k \qquad \mu_{a,i}^k(\lambda) = \varepsilon_i^{mass}(\lambda)c_i^k \tag{2.10}$$

where c_i^k is the mass concentration (in g/L) of chromophore i in the mixing model and M_i the respective molar weight with the following values implemented in our simulations:

$$M_{\beta-Caroten} = 587\ \mathrm{g\cdot mol}^{-1} \quad M_{bilirubin} = 585\ \mathrm{g\cdot mol}^{-1} \quad M_{HbO_2,Hb} = 66,500\ \mathrm{g\cdot mol}^{-1}$$

In order to take into account skin pigmentation-related absorption variations, four different melanosome volume fraction values in the LE layer were used to simulate very light skin (phototype I) to dark skin (phototype IV) types. Considering our targeted clinical application of interest, it was chosen to firstly consider a melanosome volume fraction $f_{v,mel}^2 = 0.01$, corresponding to phototype I, which is much more prone to the development of skin carcinomas. In section 2.6.4.3, darker skins are considered. The correspondence between phototypes and volume fractions of melanosome, adapted from [Karsten 2012], is summarized in Table 2.2.

Skin type	Very fair	Fair	Moderately fair	Dark skin
Phototype	I	II	III	IV
Melanosome volume fraction $f_{v,mel}^2$	0.01	0.04	0.08	0.11

Table 2.2: Values of the volume fraction of melanosome in the living epidermis used for simulating skin phototypes I to IV.

In our skin model, this parameter only influences the LE absorption coefficient, but its impact is significant. The absorption spectra resulting from the different calculations are finally shown in Fig. 2.15. The top right subplot focuses on the absorption coefficient of LE.

Similarly, the impact of the amount of blood in the dermal layers, modified by the volume fraction of blood $f_{v,blood}^3$ and $f_{v,blood}^4$, was considered as an additional parameter of interest [Nishidate 2007]. Simulations were then conducted for three pairs of blood volume fractions to

represent three media; respectively, weakly, moderately and strongly vascularized. The numerical values of these configurations are shown in Table 2.3. Here again, the couple of mean values—*i.e.*, $f^3_{v,blood} = 0.024$ and $f^4_{v,blood} = 0.02$—was used for all simulations, except in section 2.6.4.4, which focuses on this blood amount effect.

Blood Content	Weak	Mean	Strong
PD blood volume fraction $f^3_{v,blood}$	0.0144	0.024	0.0336
RD blood volume fraction $f^4_{v,blood}$	0.012	0.02	0.028

Table 2.3: Values of the volume fraction of blood in the papillary dermis (PD) and reticular dermis (RD) used for simulating a dermis with more or less blood content.

This variation influences mainly the absorption coefficient of the two dermal layers (*cf.* Eq. (2.9)) but slightly influences the scattering coefficient (*cf.* Eq. (2.11)). The optical parameters of these three couples are then isolated in the middle-right (μ^3_a and μ^4_a) and bottom-right (μ^3_s and μ^4_s) subplot of Fig.2.15.

The values of the volume fraction and mass concentration of each chromophore applied in every layer of our numerical model are summarized in Table 2.4. They were chosen following (i) a literature review [Krishnaswamy 2010, Prahl 2018, Meglinski 2002, Altshuler 2005] and (ii) comparisons between simulated spectra and experimental data acquired in clinics [Khairallah 2018] using our SR-DRS device [Blondel 2021].

Scattering properties: The values of skin scattering coefficients $\mu^k_s(\lambda)$ in the different layers of our model, were obtained with Eq. (2.11) given from [Altshuler 2005] featuring two contributions: a blood scattering component and a bloodless "base" scattering component, such that

$$\mu^k_s(\lambda) = (1 - f^k_{v,blood})\mu^k_{s,577}\frac{577}{\lambda} + f^k_{v,blood}\frac{\mu_{s,blood}(\lambda)}{(1 + a(0.5\mu_{s,blood}(\lambda)d^k_{vessels})^b} \tag{2.11}$$

In this first term, $\mu^k_{s,577}$ stands for the scattering coefficient value at 577 nm of the k^{th} layer, and λ in the denominator is in nm. For the second term, $\mu_{s,blood}(\lambda)$ is the scattering coefficient of pure blood in cm^{-1} [Prahl 2018]. Moreover, we set $a = 1.007$ and $b = 1.228$ [Altshuler 2005], while $d^k_{vessels}$ is the mean vessel diameter of the layer, expressed in cm. The numerical values of the parameters implemented in our simulation are summarized in Table 2.4, and the corresponding scattering spectra $\mu^k_s(\lambda)$ used in our model are presented for each layer in Fig. 2.15.

Other optical parameters: Both anisotropy factor g and refractive index n were considered as wavelength-independent in our spectral range of study. For example, concerning near UV wavelengths, this assumption results in a maximum relative error of respectively 3% and 1.5% for the LE and two dermis layers [Ding 2006b]. The values of the former were set to $g^1 = 0.92$, $g^2 = 0.75$, $g^3 = 0.72$, $g^4 = 0.72$ and $g^5 = 0.9$ for each of the five layers [Tsui 2018], while the second values were set to $n^1 = 1.55$, $n^2 = 1.44$, $n^3 = 1.39$, $n^4 = 1.38$ and $n^5 = 1.34$ in each of the five layers, respectively [Krishnaswamy 2010].

2.5.3 Skin intrinsic fluorescence

Simple gaussian model: Based on data available in the literature [Borisova 2014, Ghervase 2015, Kollias 2002, Wu 2006] and the analysis of our own experimental data, five main

Name (unit)	Symbol	SC	LE	PD	RD	SF
Absorption parameters						
Volume fraction (dimensionless)	$f^k_{v,water}$	0.35	0.6	0.5	0.7	0.05
	$f^k_{v,lipids}$	0.2	0.15	0.173	0.173	0.753
	$f^k_{v,\beta-caroten}$	0.45	0.24	0.303	0.125	0.141
	$f^k_{v,mel}$	0	See tab. 2.2	0	0	0
	$f^k_{v,blood}$	0	0	See Table 2.3	See Table 2.3	0.005
Concentration (g/L)	$c^k_{\beta-caroten}$	2.1×10^{-4}	2.1×10^{-4}	7.0×10^{-5}	7.0×10^{-5}	0
	c^k_{eum}	0	80	0	0	0
	c^k_{phe}	0	12	0	0	0
	$c^k_{bilirubin}$	0	0	0.05	0.05	0.05
	$c^k_{HbO_2/Hb}$	0	0	150	150	150
Scattering parameters						
Volume fraction	$f^k_{v,blood}$	0	0	See Table 2.3	See Table 2.3	0.05
Vessels diam. (cm)	$d^k_{vessels}$	/	/	6.0×10^{-4}	1.5×10^{-3}	7.5×10^{-3}
Scat. coeff. (cm^{-1})	$\mu^k_{s,577}$	400	300	120	120	130
Other optical properties and medium geometry						
Layer thick. (μm)	z^k	See tab. 2.1	See tab. 2.1	200	1800	See tab. 2.1
Anisotropy factor	g^k	0.92	0.75	0.72	0.72	0.9
Refractive index	n^k	1.55	1.44	1.39	1.38	1.34

Table 2.4: Values of the geometrical and optical parameters of our five layer skin model. SC, LE and SF thickness ranges, $f^k_{v,mel}$ melanosome fraction range in LE and $f^k_{v,blood}$ blood fraction in dermis layers refer to Tables 2.1–2.3, respectively.

fluorophores of human skin were implemented in our model *i.e.*, keratin, NADH, flavin, elastin and collagen. In the first instance, simple analytical models of absorption and emission spectra were used. For the absorption coefficients, the shape of the spectrum was a normalized Gaussian curve (*i.e.*, featuring a maximum unitary value (arbitrary unit) centered on the peak absorption wavelength $\lambda_{p,abs}$ and a standard deviation σ_λ. The latter was then multiplied by a scale factor $c_{p,abs}$ to make the maximum absorption correspond to the desired value in units cm^{-1}. The emission spectra were also modeled using Gaussian curves. Quantum efficiency values were set to $\xi = 0.9$. By condensing the orders of magnitudes of the absorption of fluorophores in comparison with the main chromophores, the latter value has a negligible impact on the DR spectra obtained. However, the quantum efficiency has been deliberately chosen high, in order to obtain a satisfactory signal to noise ratio in AF spectra. Table 2.5 and Fig. 2.16 summarize the information relating to the fluorescence properties of the 5-layer numerical model.

Fluorophore	**Layer**	$\lambda_{p,abs}$ (nm)	$\sigma_{\lambda,abs}$ (nm)	$c_{p,abs}$	$\lambda_{p,emi}$ (nm)	$\sigma_{\lambda,emi}$ (nm)	ξ
Keratin	LE	355	60	6.0E-3	525	25	0.9
NADH	LE	342	25	1.0E-3	460	50	0.9
Flavins	LE	465 (380)	30 (30)	1.0E-3	510	25	0.9
Elastin	PD	350	33	1.0E-3	395	40	0.9
Collagen	RD	370	10	8.0E-2	475	22	0.9

Table 2.5: Numerical values of the parameters for the five fluorophores implemented in our multilayer skin tissue model. LE: Living Epidermis, PD: Papillary Dermis, RD: Reticular Dermis.

Spectrophotometer characterization: Because of the incomplete characterization of endogenous fluorophores in the literature concerning their absorption and emission spectra (in our

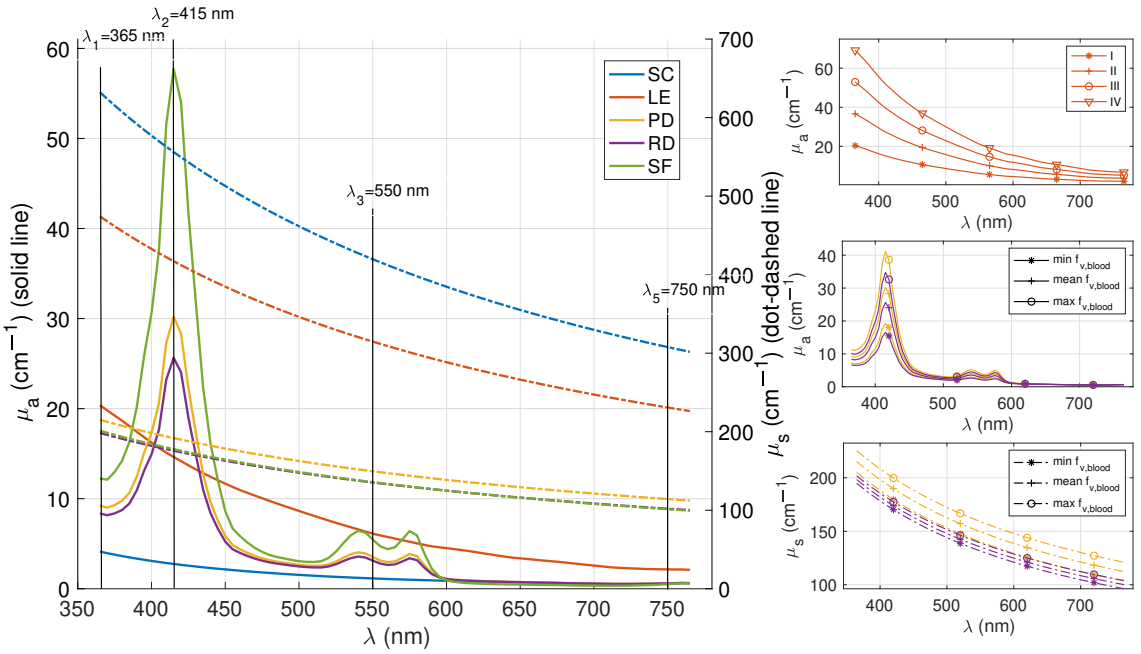

Figure 2.15: Absorption (μ_a solid line) and scattering (μ_s dashed-dot line) coefficients of each layer (SC, LE, PD, RD and SF in blue, red orange, violet and green, respectively) of the designed numerical medium set for skin phototype I and mean dermal blood volume fraction. Black vertical lines are visual cues to point some wavelength of interest in section 2.6.3. The spectral curves of the LE absorption coefficient μ_a^2 as a function of skin phototypes I, II, III and IV appear in the top-right subplot, while middle-right and bottom-right subplots focus on the dermal blood volume fraction impact over the PD and RD absorption coefficient μ_a^3 and μ_a^4, as well as their scattering coefficient μ_s^3 and μ_s^4. LE: living epidermis; SC: stratum corneum; PD: papillary dermis; RD: reticular dermis; SF: subcutaneous fat.

wavelength range of interest), we decided to proceed ourselves to an optical characterization of these last ones thanks to a spectrophotometer put at disposal by the ENSIC[1]. The protocol followed and established by the chemists present was as follows:

1. Preparation of pure fluorophores solution in 10 *mm* optical path *Cuve Quartz Suprasil* from *Hellma* (designed for fluorescence characterization). Details on solution preparation are provided in Table 2.6.

2. Acquisition of absorption spectrum using *Shimadzu UV-3600* spectrophotometer. Definition of the excitation wavelength specific to the fluorophore λ_{peak} (indicated in Table 2.6), located in the peak of the absorption spectrum spectrally closest to the excitation wavelengths of *SpectroLive* device (see Table 1.4.2).

3. Acquisition of emission spectrum for monochromatic excitation at λ_{peak}. Due to saturation of photo-sensors, the initial solution of concentration C_0 was sometimes diluted in their solvent. This dilution factor for the emission spectrum c_{emi} also appears in the Table 2.6.

[1] École nationale supérieure des industries chimiques.

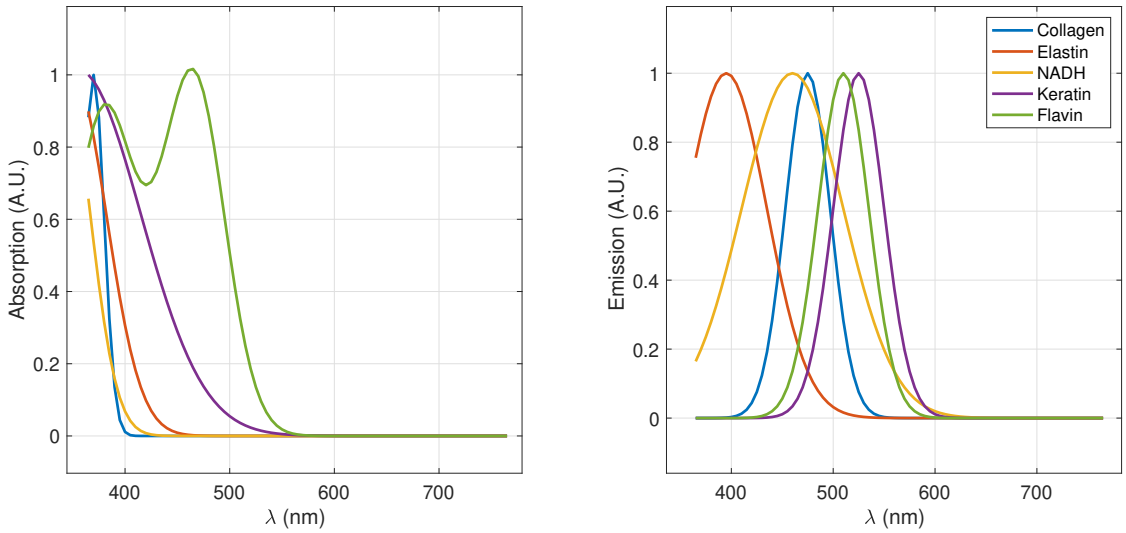

Figure 2.16: Normalized curves of fluorescence absorption (left) and emission (right) spectra for the five fluorophores implemented in our multi-layer skin tissue model (simple Gaussian model).

Fluorophore	**Ref.**	**Solvent**	C_0 $(g.L^{-1})$	λ_{peak} **(nm)**	c_{emi}
Keratin	K0253 *Merck*	Water	5.65	300	1:10
NADH	07735001 *Merck*	Bicarbonate buffer	10	340	1:100
Flavins	F6625 *Merck*	Water	5	376	1:100
Elastin	E6902 *Merck*	Water	1	350	1:10
Collagen	234138 *Merck*	Acetic acid	5	268	1:1

Table 2.6: Information on the dilution of pure fluorophores for fluorescence characterization measurements with spectrophotometer.

Fig. 2.17 shows the normalized absorption and emission spectra of fluorophores introduced in the different layers of our model. The $x-axis$ is quite different and exceeds visible spectrum border. Indeed, absorption peaks of endogenous fluorophores are located in the UV range. The quantum efficiency of those fluorophore were also estimated:

$$\xi_{ker} = 0.011 \quad \xi_{NADH} = 0.026 \quad \xi_{fla} = 0.021 \quad \xi_{ela} = 0.022 \quad \xi_{coll} = 0.011 \tag{2.12}$$

Fluorophores being characterized in solution and not in biological tissue (*i.e.*, their natural environment), the values of absorption, emission and quantum yields are not to be considered as absolute truths but bring nevertheless an *a priori* on the values introduced in our skin model. One can also notice than keratin absorption is almost null for the *SpectroLive* excitation wavelengths.

2.6 Photons propagation in our skin model

Having now successively presented the in-depth characterization tools (see section 2.4)and our realistic skin model in which we have identified the variable parameters that can cover the range of skin possibilities (inter- and intra-individual variations, see section 2.5), this section consists in applying those tools to the medium to know more about photons travels inside skin.

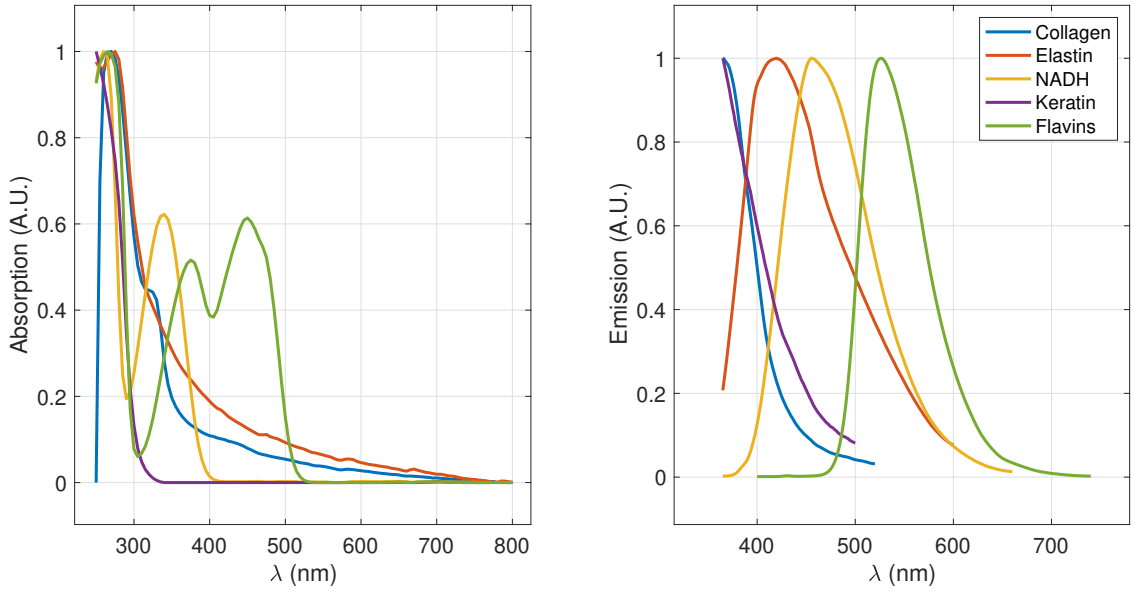

Figure 2.17: Normalized curves of fluorescence absorption (left) and emission (right) spectra for the five fluorophores implemented in our multi-layer skin tissue model (Spectrophotometer results).

2.6.1 SR-DR and AF-DR simulated spectra

Before focusing on the depth information of the captured photons, we present here the simulated output spectra *i.e.*, the DR and AF spectra generated for a configuration of the 5-layer medium described previously (section 2.5) and for the fluorophore model established as a result of spectrophotometer measurements (*cf.* "Spectrophotometer characterization" paragraph in section 2.5.3).

2.6.1.1 SR-DR simulated spectra and DR skin model validation

Fig 2.18 (left) shows the DR spectra simulated for a model configuration corresponding to healthy skin of intermediate thickness (*cf.* Table 2.1), intermediate blood content (*cf.* Table 2.3) and phototype I (*cf.* Table 2.2) at each SD distance. DR intensities tend to increase toward the red spectral range due to the lower opacity of the near-infrared (near IR) wavelengths. Local minimums at 415, 540 and 575 *nm* correspond to hemoglobin absorption.

Fig. 2.18 (right) shows the superposition of the normalized simulated spectra and the clinical spectra for each SD distance. Each of the subplots is composed of the the average clinical spectrum of three acquisitions $\overline{DR}^{clin}$ (dashed line) of this same quantity, to which we added the standard deviation (dash-doted line) and finally the simulated spectrum (continuous line), for which model parameters (epidermal thickness, phototype, dermal blood content) were determined by inverse problem solving to fit clinical data. Those experimental DR spectra were acquired on the anterior skin surface of a patient's wrist. This skin site was clinically considered as healthy by the plastic surgeon in charge of the patient's inclusion in the *SpectroLive* clinical trial (ClinicalTrials.gov Identifier: NCT02956265) approved by the Institutional Board for Ethics and Patients Safety (CPP Est III authorization: 16.06.03) and by the French National Agency for Medicines

and Health Products Safety (ANSM authorization: DMDPT-RIAL/MM/2016-A00608-43). Comparing spectra from a MC simulation with clinical spectra is not an easy task [Sun 2021]; thus, both sets of spectra were normalized (*i.e.*, we set the minimum value to 0 and the maximum value to 1 in the 400–650 nm exploitable spectral band). The approximate fitting between acquired and simulated spectra partly validate the developed skin model and more generally the fidelity of the simulation.

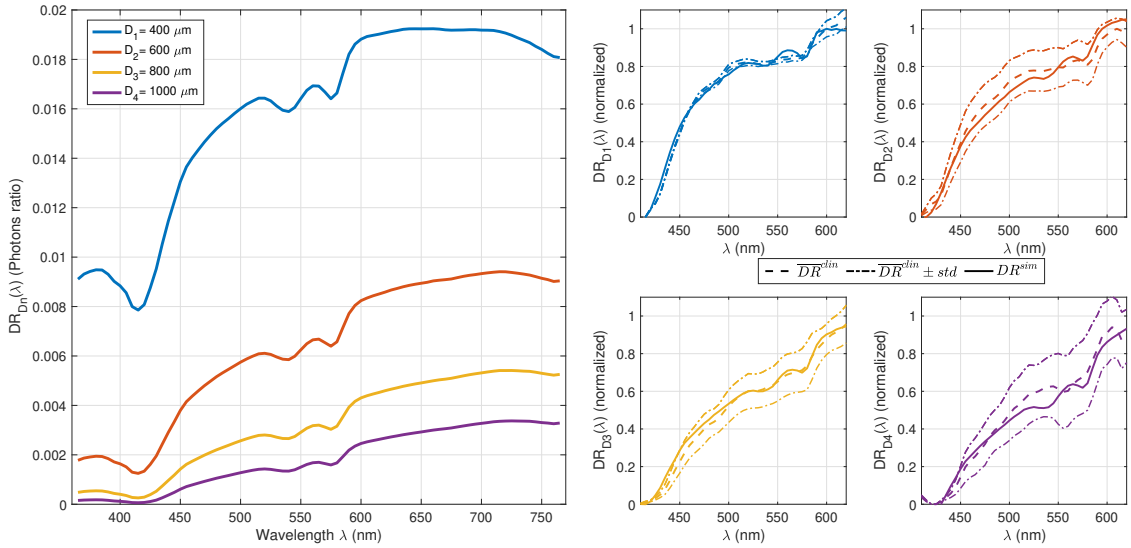

Figure 2.18: DR spectra simulated for the four SD distances (left). The considered medium is the healthy skin model with intermediate thicknesses, mean dermal blood content and phototype I. The four other figures (right) show the superposition of the normalized $\overline{DR}^{clin}$ (dashed line) clinical spectra from *SpectroLive* acquisition on a patient's wrist, within a confidence interval calculated as $\overline{DR}^{clin} \pm std$ (dash-dotted line), as well as the estimated DR^{sim} (continuous line) from our simulation.

2.6.1.2 SR-AF simulated spectra

Realistic management of fluorescence is more complicated than that of DR, mainly for two reasons. The first one is that concentrations of endogenous fluorophores is not provided in the literature, so that it is difficult to know an order of magnitude of each fluorophore volume fraction, even if we can assume that fluorophore absorption coefficients are small compared to those of the chromorophores. The second is that, because of the weak values of fluorophores absorption coefficients regarding the chromophores ones and the small quantum efficiency (see Eq. (2.12)), the probability that absorption event provides a fluorescent photon is weak (see Eq. (1.28)). That is why getting AF spectra with satisfying signal to noise ratio requires a huge number of launched photons ($> 10^8$). This is associated to a long computation time (≈ 200 s to generate $AF(\lambda)$), that make it difficult to deal with inverse problem solving which require successive calls of the simulation (see Fig. 1.28).

The reasons explained above have led us to develop less AF than DR model, and more specifically not to have done inverse problem solving from clinical data (see Fig. 1.22). So we just introduced NADH and flavins in the LE, as well as elastin in PD and collagen in RD described

by absorption and emission shape given by the spectrophotometer characterization (arbitrary imposing $\max(\mu_{a,fluo}(\lambda)) = 1\ cm^{-1}$, see Fig. 2.17) in the medium described before that generate $DR(\lambda)$ spectra provided in Fig. 2.18 (left). The resulting AF spectra are given in Fig. 2.19.

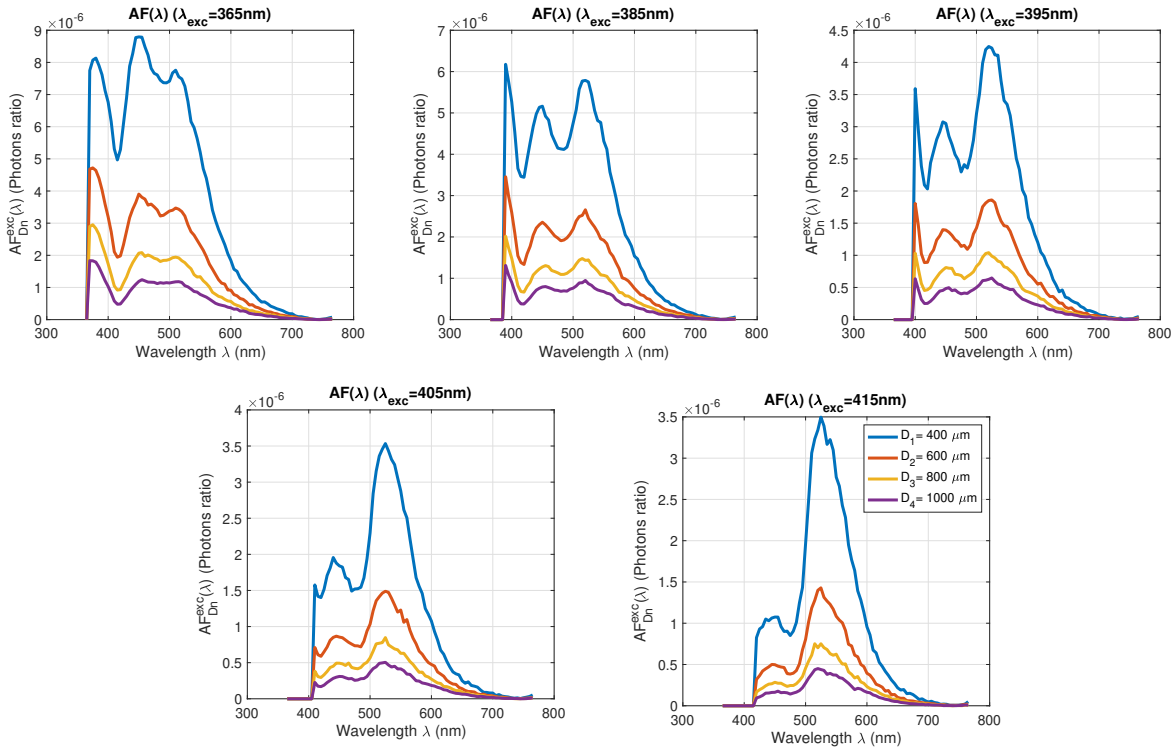

Figure 2.19: AF spectra simulated for the four SD distances. The considered medium is the healthy skin model with intermediate thicknesses, mean dermal blood content and phototype I in which we introduce the endogenous fluorophores described in the section 2.6.1.2.

2.6.2 Depth characterization of skin AF

The aim is here to know more about acquisition of the AF spectra available in Fig. 2.19 by applying the algorithms described in section 2.4.

2.6.2.1 Decomposition of SR-AF skin spectra in fluorophores contribution

The method described in section 2.4.3 was applied on our realistic skin medium including intrinsic fluorophores introduced earlier. This allows to generate the spectra given in Fig. 2.20.

For the reasons exposed earlier, no results can seriously be discussed since fluorophores have been arbitrary introduced in skin layers (in terms of concentrations). Indeed, it was above all a question of presenting the novelty introduced in the simulation and of discussing the interest that this could raise. However, some interesting interpretations can be made from these different curves. For example, we can see that the relative contribution from fluorophores in superficial layers (respectively deep layers) decrease (increase) when D_n distance increases.

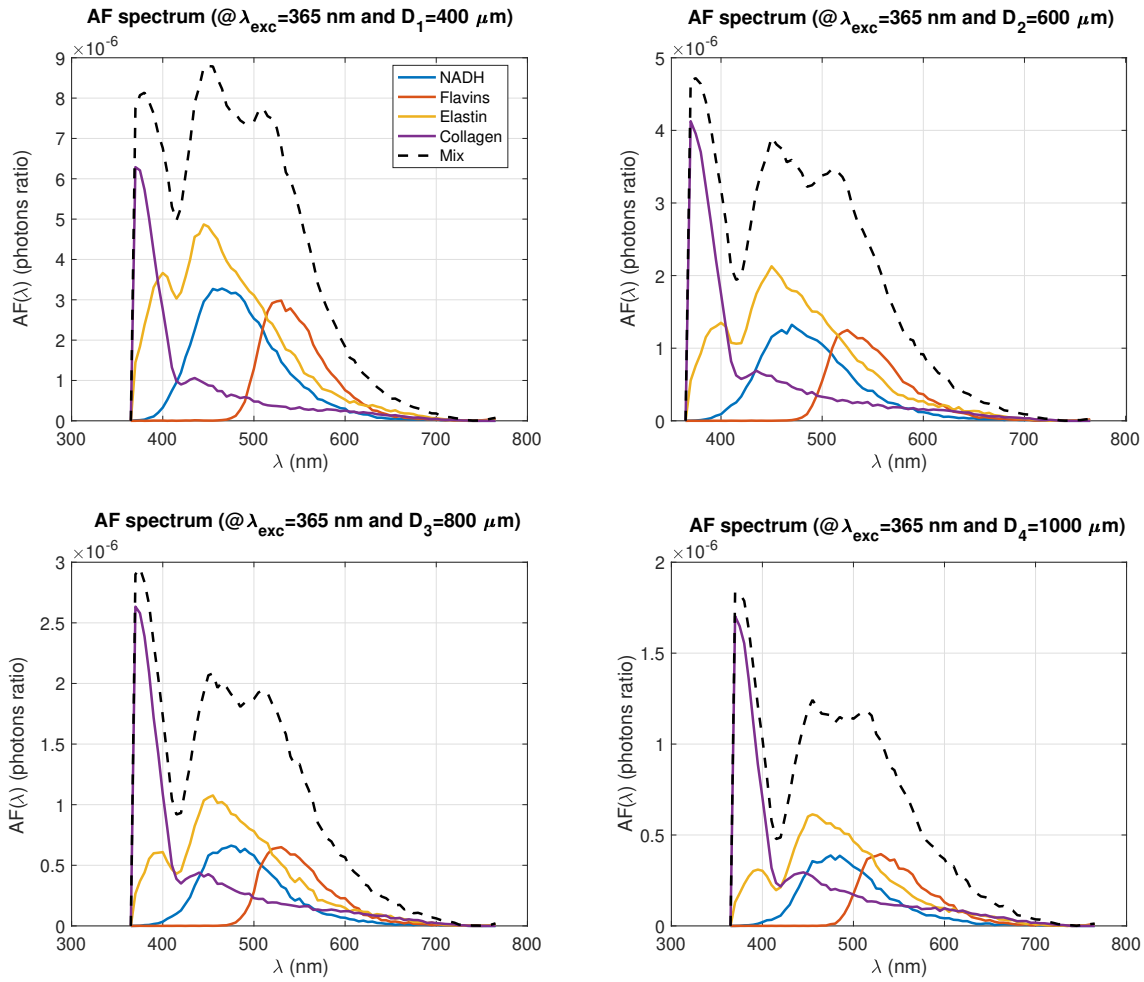

Figure 2.20: Decomposition of auto-fluorescence spectra in fluorophores contributions for the 4 SD distances and an excitation wavelength of 365 nm. SD distances are indicated in the different titles of the sub-figures.

Thanks to this code improvement, it is also interesting to see the deformation of the emission signal introduced by the propagation of photons between the fluorescence event and the eventual detection. The left part of Fig. 2.21 shows the contributions (normalized to 1) of elastin in the AF spectrum for excitation at 365 nm for the 4 SD distances, while the same contribution to flavins also appears on right. The dashed line shows the emission spectrum of the fluorophores. The differences between emission shapes and fluorophore contributions in the signal are only due to the light/matter interactions. For elastin (located in papillary dermis including blood), we notice notably the absorption of hemoglobin at 405 nm which strongly attenuates the AF signal for this wavelength. On the opposite, the spectral distortion introduced by the propagation of the medium is more homogeneous for the fluorescent photons coming from the flavins, the impact of the SD distance seems also more negligible.

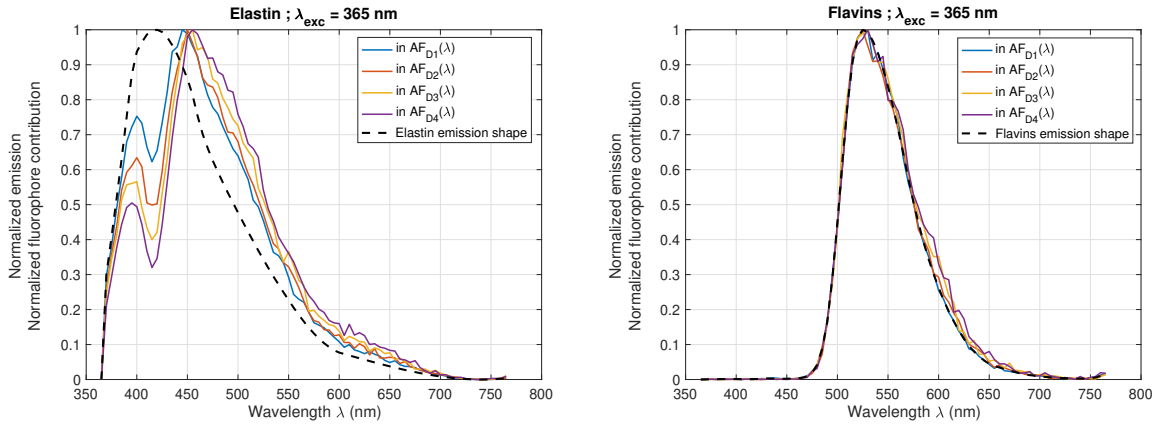

Figure 2.21: Deformation of fluorescence signal by the medium for the 4 SD distances and an excitation wavelength of 365 nm. Elastin contribution (left) and Flavins contribution (right).

2.6.2.2 Localization of fluorescent events in skin layers

This section refers to the simulation output described in section 2.4.1.2. It offers a qualitative picture of the positions of the fluorescence events for detected photons. This map is available for all the excitation wavelengths and for all the SD distances. Fig. 2.22 illustrates those maps for 2 excitation wavelengths: 365 nm (left) and 405 nm (right). They were obtained for the 5-layer medium described previously (which generate the $AF(\lambda)$ spectra provided in Fig. 2.19). We notice that the absorption of hemoglobin at 405 nm limits the propagation in depth of the excitation photons, which is manifested by a more superficial signal of fluorescence events.

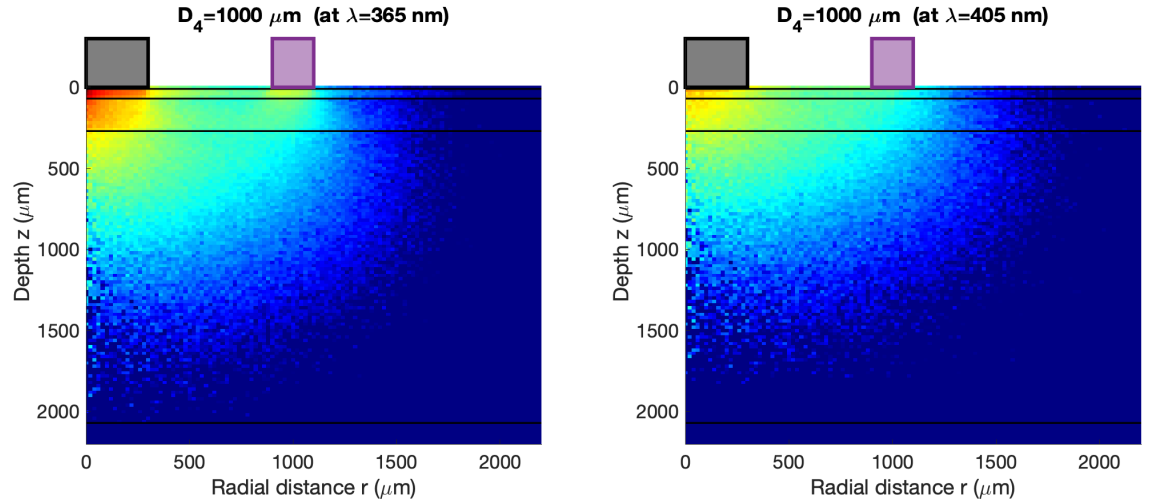

Figure 2.22: Fluorescence maps at $\lambda_{exc} = 365\ nm$ (left) and $\lambda_{exc} = 405\ nm$ (right) for $D_4 = 1000\ \mu m$. The color scale is in logarithm units.

2.6.3 Depth characterization of skin DR

The aim is here to know more about acquisition of the DR spectra available in Fig. 2.18 (left) by applying the algorithms described in section 2.4.

2.6.3.1 Localization of scattering events in skin layers

This section refers to the simulation outputs described in section 2.4.1.1. It offers a qualitative picture of the positions of the scattering events for detected photons.

Wavelength dependency on trajectory maps: The optical device offers the possibility to play on 2 parameters, namely the value of the SD distance and the wavelength, to access different deep layers of the skin. Thus, Fig. 2.23 shows the probed volume for $\lambda_2 = 415\ nm$ (left) and $\lambda_3 = 550\ nm$ (right) for the same SD distance $D_4 = 1000\ \mu m$. By looking at the optical properties for these wavelengths (see black vertical lines in Fig. 2.15), we can conclude that the detected photons come from deeper trajectories because of the greater optical transparency of the medium for the second wavelength, *i.e.*, $\mu_a(\lambda_2) + \mu_s(\lambda_2) > \mu_a(\lambda_3) + \mu_s(\lambda_3)$.

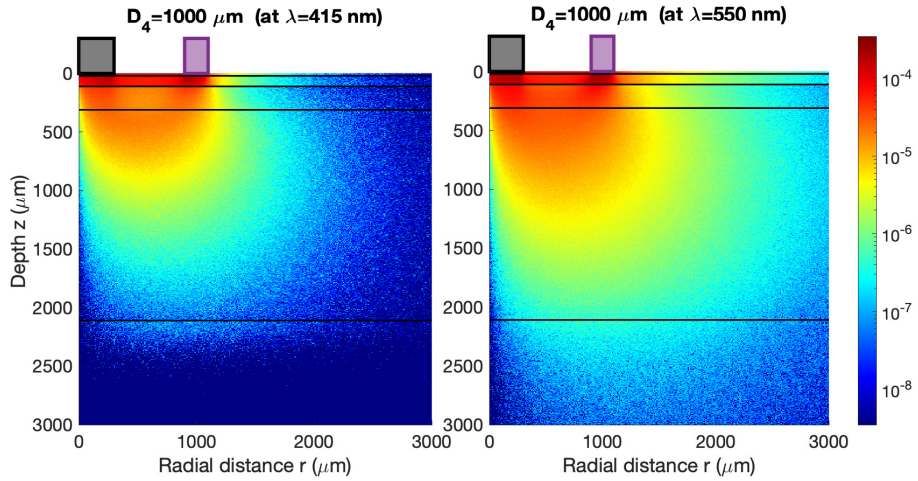

Figure 2.23: Trajectory maps at $\lambda_2 = 415\ nm$ and $\lambda_3 = 550\ nm$ for the 4^{th} SD ($D_4 = 1000\ \mu m$) distance simulated for the 5-layer skin model. A zoom on a 3000 μm × 3000 μm top-left square area was performed for a better visualization of the photons trajectories. Black and purple squares respectively represent the SF and DF.

SD distance dependency on trajectory maps: It is also possible to adjust the SD distance to access different skin tissue depths. Fig. 2.24 shows the evolution of the trajectory maps for $\lambda_1 = 365\ nm$ and the 4 SD distances. We can observe the typical path between emitting and collecting fibers called "Banana shape" [Kazanci 2015, Stratonnikov 2001, Koenig 2015], and the expected behavior when D_n increases: DR spectra are composed of photons that have plunged deeper into the medium.

2.6.3.2 Depths distribution of scattering events in skin layers

This section refers to the simulation outputs described in section 2.4.2.3. It consists in storing the lowest point of the optical path z_{max} between the SF and DF for each detected photon before grouping and then counting those that have reached the same depth (in an interval of $dz = 5\mu m$). We thus obtain an histogram in which the abscissa is the maximal probed depth z_{max} and the ordinate is the occurrence in photons count. To better represent the depth distribution and being able to compare those histograms for different wavelengths and SD distances, it was chosen to

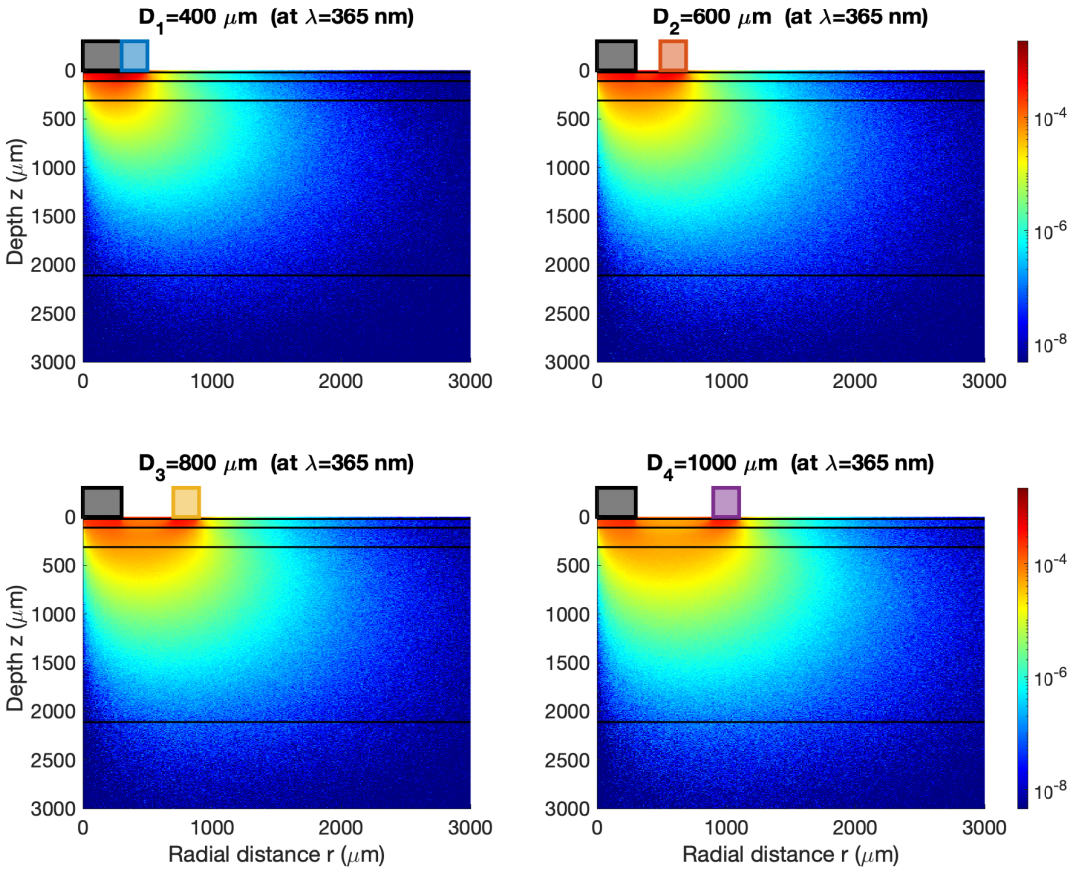

Figure 2.24: Trajectory maps at $\lambda_1 = 365\ nm$ for the 4 SD distances simulated for the 5-layer skin model. A zoom on a 3000 $\mu m \times 3000\ \mu m$ top-left square area was performed for a better visualization of the photons trajectories. Black square represents the SF and DF.

normalize this output by dividing the occurrence value by the total number of collected photons for the couple (λ, D_n). The y-axis finally becomes a relative photons count occurrence that appears in percentage. The layout has been slightly modified from those initially described in Fig. 2.12, but its meaning is still the same.

Wavelength dependency on maximum probed depth histograms: The aim is to study more quantitatively the impact of each parameter of the pair (λ, D_n) through the histograms of maximum depth probed. Fig. 2.25 illustrates the λ dependency, by providing the histograms for the four wavelengths pinned with black vertical lines in Fig. 2.15 for D_4 SD distance. We can notice the global increase toward deeper probed depths when λ scans the visible range from near UV to near-IR wavelengths, excepted for $\lambda_2 = 415\ nm$ corresponding to hemoglobin absorption peak. The presence of abrupt transitions is also noticeable in the histograms corresponding to refractive index mismatch (*i.e.*, reflection) between consecutive layers, represented by a black vertical line. Finally, a box-plot approach was chosen to extract a characteristic probed depth associated to the couple (λ, D_n). Thus, the 3 vertical colored lines for each of the histograms represent from left to right: the 1^{st} quartile (dotted) Z_{q1}, the median (solid line) Z_{med} and the

3^{rd} quartile (dotted) Z_{q3}. The colored area under the histogram, between the two quartiles, then represents 50 % of the total area. In other words, half of the photons contributing to the $DR_{D_n}(\lambda)$ value have reached at most a depth between Z_{q1} and Z_{q3}.

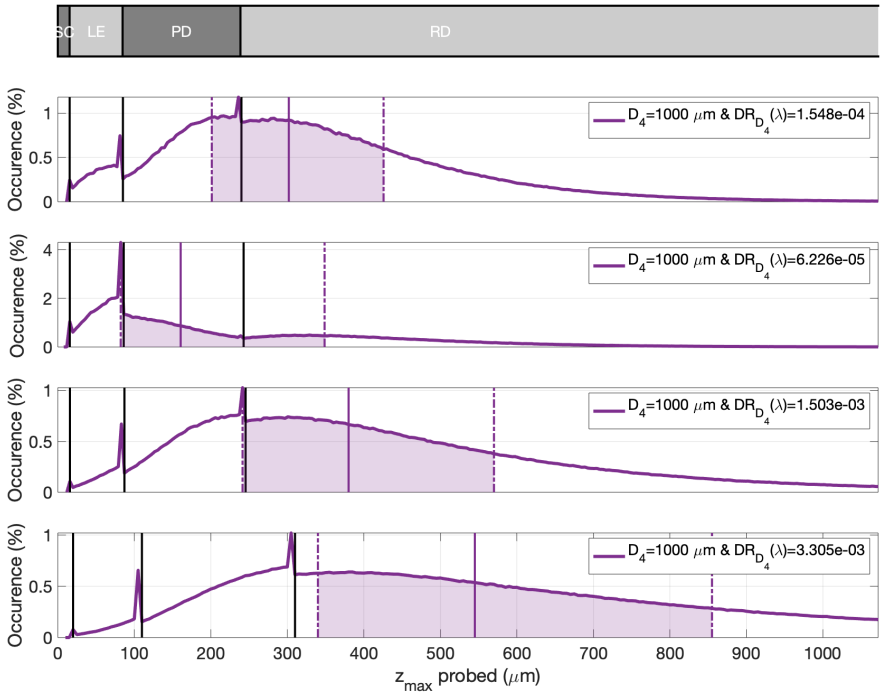

Figure 2.25: Maximum probed depth histograms at (from top to bottom) $\lambda_1 = 365\ nm$, $\lambda_2 = 415\ nm$, $\lambda_3 = 550\ nm$ and $\lambda_4 = 750\ nm$ for the 4^{th} SD ($D_4 = 1000\ \mu m$) distance simulated for the 5-layer skin model. SF does not appear because the amount of photons that reach this layer is negligible.

SD distance dependency on maximum probed depth histograms: For the impact of SD distance, Fig. 2.26 displays the histograms at $\lambda_1 = 365\ nm$ for the 4 available detector positions. The graphic conventions are the same as in Fig. 2.23. We can notice that photons go deeper, as well as the widening of the probed volume (visible here in the form of the inter-quartiles enlargement) for longer SD distances than shorter ones.

Extraction of a typical probed depth and spectral behavior: The histograms presented in Fig. 2.26 are available at all wavelengths and for each of the 4 SD distances, from which a median and quartiles of the maximal penetration depth can be calculated. The choice to synthesize our depth histograms using a box-plot approach rather than the mean penetration depth [Arifler 2005] of these histograms is justified by its simplicity of interpretation from the point of view of the resulting DR signal. Indeed, by considering the signal captured for the pair (λ, D_n), we can decompose it into 4 equal contributions of different depths, for which the quartiles and medians

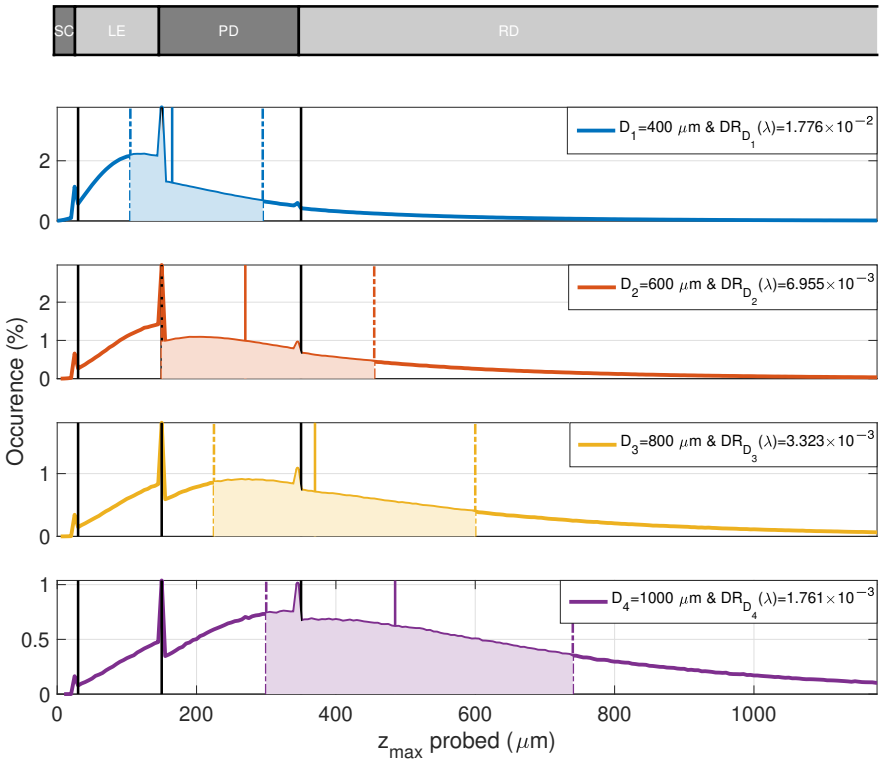

Figure 2.26: Normalized probed depth histograms of weighted detected DR photons at $\lambda = 565\ nm$ (central wavelength of the spectrum $[365 - 765]\ nm$) for the 4 SD distances. Vertical black lines represent the borders between layers. Colored vertical lines represent from left to right: the first quartile (dot-dashed), the median (solid) and the third quartile (dot-dashed).

represent the boundaries. Moreover, the interquartile range highlights the depth interval of the photons around the median, thus illustrating the enlargement of the probed volume in the 3 dimensional medium.

Other alternatives were developed to extract a penetration depth for collected photons in SR-DR spectroscopy. In their study [Tseng 2012], Tseng *et al.* introduce a quantity called "interrogation depth" and quantified it by the z-average of all detected photon scattering events, in a two-layer skin model. The photons penetration was not the main study, but the paper revealed that their SD distances in a range $[1440 - 2880]\ \mu m$ allow to probe between $[293 - 949]\ \mu m$ within the $[550 - 860]\ nm$ wavelength region. Other teams have adopted an original and experimentally transposable technique to extract a sampling depth Z_S in a mono-layer medium defined by its thickness Z_0, and its optical coefficients μ_a and $\mu'_s = \mu_s(1 - g)$. This one consists in varying Z_0 from 0 to a sufficiently large thickness so that it no longer has any impact on the DR signal. For very thin thicknesses, photons escape by the bottom of the layer, which is responsible for a very weak signal. Thickening the medium allows more photons to reach the DF, until it becomes wide enough to converge to a maximum (semi-infinite medium). Z_S is then defined as the thickness

at which the DR signal reaches 50 % of its final maximum value [Hennessy 2014, Greening 2018]. Unfortunately, this method can not be led for multi-layered tissue. Finally, the depth measurement can be defined as the median of the cumulative absorption of fluence absorption maps. This was applied in the Arimoto *et al.* study [Hidenobu Arimoto 2005], for a three-layer skin medium considering the water absorption and scattering in the near IR spectral range.

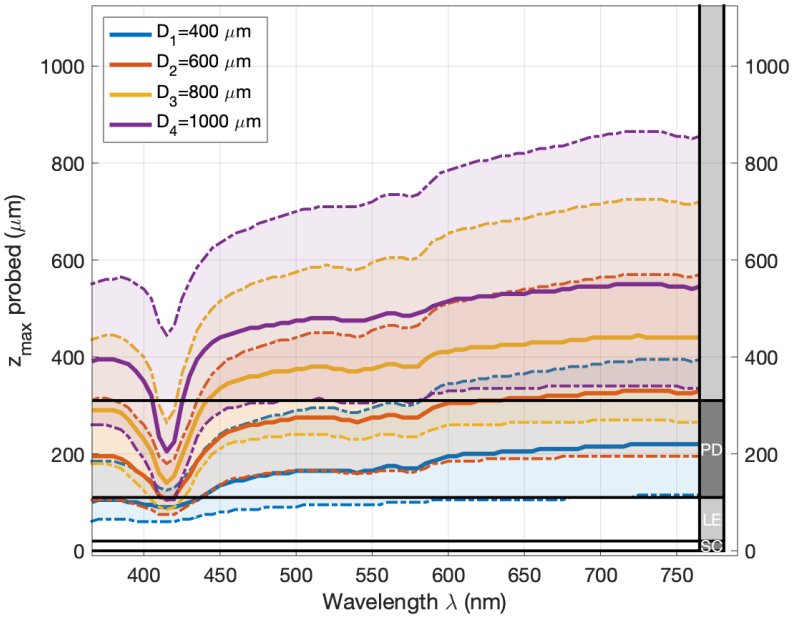

Figure 2.27: Maximal probed depth values of detected photons for the previously described SD distances. Solid and dot-dashed lines represent median and quartiles values respectively. The right column and the black horizontal lines illustrate the position of the interface between the layers (SC: stratum corneum ; LE: living epidermis ; PD: papillary dermis ; RD: reticular dermis ; SF: subcutaneous fat (not represented here)).

The results obtained from our box-plot approach from maximum depth histograms are presented in Fig. 2.27, with the same graphic conventions as in Fig. 2.26. The quasi-linearity of the probed depth can be seen as a function of the two varying parameters, *i.e.*, the SD distance and the wavelength, except at the first hemoglobin absorption peak (415 nm). More importantly, it can be noticed that by choosing a couple (λ, D_n), it is possible to probe depths in a range of values covering the interval $[50 - 900]$ μm. Moreover, one can read there, that the photons having contributed to the spectrum $DR_{D_4}(\lambda)$ and verifying $\lambda > 450$ nm have mostly visited the RD layer. On the other hand, it is visible that the photons of $DR_{D_1}(\lambda)$ satisfying $\lambda < 450$ nm remained globally confined in SC, LE and PD layers. One can also observe that the inter-quartiles range widens when λ increases for all distances D_n. Indeed, the probed volume is very localized for the near UV wavelengths and spreads when it approaches the near IR.

2.6.4 Analysis of the probed depth according to the medium configuration

2.6.4.1 Epidermis thickness modifications in healthy skin model

Some studies have focused on the impact of the thickening of the most superficial skin layer on DR spectra acquisition in a skin multi-layered medium [Yudovsky 2010]. Among them, six levels of epidermis thickness in the range $[0-500]$ μm have been tested in the three-layer model (epidermis and two dermal layers) [Fredriksson 2012], leading to the conclusion that its impact on the simulated spectra is very significant. In [Sharma 2014], the authors quantified the accuracy of estimating the optical properties of the upper and lower layers in a bi-layer medium when the thickness of the most superficial layer varies. Thus, they showed that the accuracy of estimation of the upper (respectively lower) layer increases (decreases) when the thickness of the surface layer increases over the range $[0-1000]$ μm. However, those studies do not show an evolution of the probed depth with the thickening of the superficial layer(s). We presented this added value in [Colas 2021b]. Three combinations of SC and LE thicknesses were defined featured thin, medium and thick healthy epidermis. The numerical values associated with the elaboration of these 3 healthy simulation media configurations were summarized in Table 2.1.

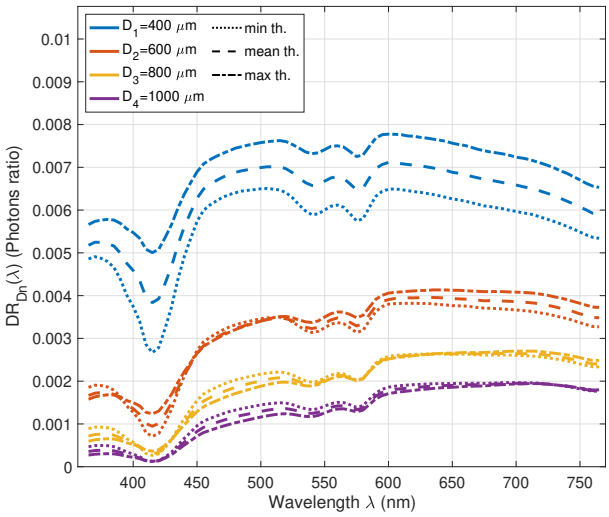

Figure 2.28: DR spectra for the 3 thin (dotted line), mean (dashed) and thick media (dashed-dot). The distance SD D_n is indicated by the color code, while the line style refers to the medium.

By observing the DR spectra available on Fig. 2.28, it is noteworthy to point that (i) at D_1, the amplitude of the DR spectrum for the maximal thickness of the epidermis is greater than the one for the minimal, whatever the wavelengths, while (ii) along with longer SD distances, the amplitude of the DR spectra for the maximal thickness of the epidermis tends to be lower than the one of the minimal. It is possible to explain this behavior by analyzing the origin of the detected photons (*i.e.*, the skin layers they visited) for each of the thin, median and thick media.

The maximal probed depth values of detected photons for the small, mean and high thicknesses media (see Table 2.1) is available on Fig. 2.29. If we observe the probed depth at D_1 for the thickest epidermis model, we notice that most of the photons having contributed to $DR_{D_1}(\lambda)$ remained confined in SC and LE layers. For the thinnest epidermis model, the photons have largely visited the PD layer, and even the RD one especially for the near IR wavelengths. The evolution of the

spectra of $DR_{D_1}(\lambda)$ for the different thicknesses may be explained by the high scattering capacity of the SC and LE layers at the origin of a short path length return of many photons to the surface (and thus captured at D_1). If we now consider D_4, the figure of the probed depths shows us that, in general, the increase of the SD distance forces the photons to dive into the depths of the medium: the superficial back-scattering effect is no longer observed. The refinement of the SC and LE layers allows the photons to penetrate deeper into the RD one. The resulting optical path is then more consequent, which could explain a decrease of $DR_{D_4}(\lambda)$ with the thickening of the skin. The photon propagation of the distances D_2 and D_3 would then correspond to a transitional state between these two modes.

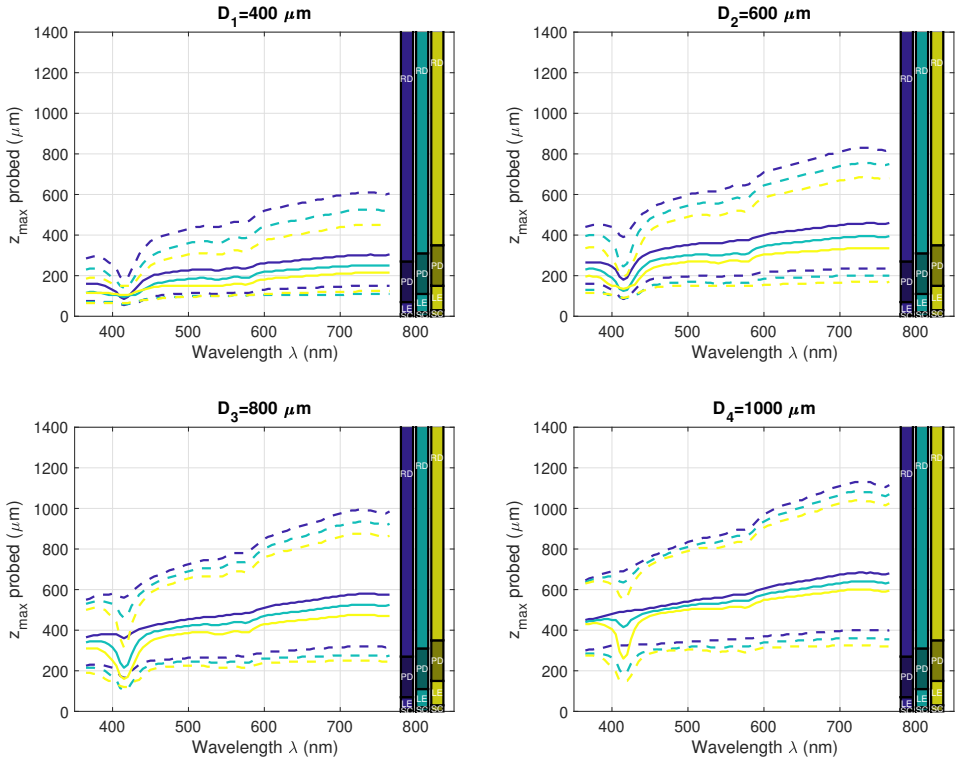

Figure 2.29: Maximal probed depth values of detected photons in the skin model with minimum (blue), intermediate (green) and maximum (yellow) thicknesses of SC and LE layers, as a function of wavelength and SD distances. Solid and dot-dashed lines represent median and quartiles values respectively. The right column illustrate the position of the interface between the layers, in every medium configuration (*cf.* Table 2.1).

As indicated in section 2.5.1, both dermal layers (PD and RD) were considered of fixed thickness. This choice results from a preliminary study in which the impact of the dermal thickness was considered secondary in comparison with the other parameters that decide to vary. As we have treated the impact of the epidermal thickness, we obtained results for three pairs $(z^3 = 150\ ;\ z^4 = 1600)$, $(z^3 = 200\ ;\ z^4 = 1800)$, $(z^3 = 250\ ;\ z^4 = 2000)$ μm of PD and RD thicknesses, respectively, representing minimum, mean and maximum dermal thicknesses. The DR and maximal probed depth appear in Fig. 2.30. It can be noticed that the impact of this parameter on

the signal (left) and on the detected photon penetration (right) is very small (variations smaller than 2% in DR for D_1 and for $\lambda > 600$ nm).

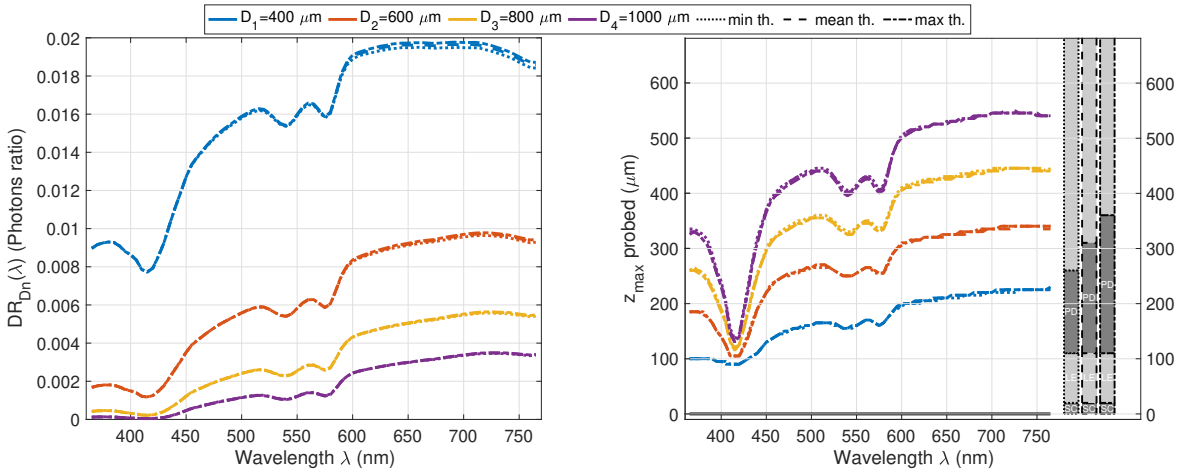

Figure 2.30: DR spectra (left) and maximum probed depth (right) for the thin (dotted line), mean (dashed) and thick dermal thickness media (dashed-dot). SD distance D_n is indicated by the color code. The three right columns represent the position of the border between the layers of each skin model (thin, mean, thick).

2.6.4.2 Epidermis modifications in healthy and pathological skin

Morphological changes may be significant for part of skin carcinomas such as ulceration and hyperkeratosis respectively characterized by a skin thinning or thickening (of about a factor 10) of the stratum corneum superficial layer. These 2 cases of carcinomas, encountered in clinics, were studied using the aforementioned numerical tools. By way of comparison, output data related to a healthy skin of mean thicknesses also appears in the presented figures. Table 2.1 synthesize the thicknesses introduced in the simulation for the 3 considered media.

DR spectra appearing on Fig. 2.31 for healthy and ulcerated skin models are very similar, *i.e.*, identical for D_2, D_3 and D_4. Slight distinct amplitudes are observed at D_1 but with globally identical spectral shape. Indeed, the disappearance of the SC layer, which differs from both, can be seen as an overall decrease in the thickness of the epidermis $z^{Epi} = z^1 + z^2$. The back-scattering effect for D_1 is then more important when z^{Epi} is greater (healthy medium) than when it decreases (ulcerated medium). The associated signal gain then fades when the SD distance increases.

Unlike healthy as well as ulcerated skin models, the results obtained for the hyperkeratosis show (see Fig. 2.32) that the majority (more than 50%) of photons detected, whatever the SD distance, remained confined in SC (for D_1 and D_2) and LE (for D_3 and D_4). This information is confirmed by the shape of the DR spectra, since the dermal hemoglobin signature (pits at 415, 540 and 575 nm) appears only slightly. One can again notice the superficial back-scattering effect, responsible for much larger amplitudes for every D_n, excepted D_1 for the near IR wavelengths. Such results emphasize the importance of taking into account the skin layers thickness of each pathological case to properly diagnose it.

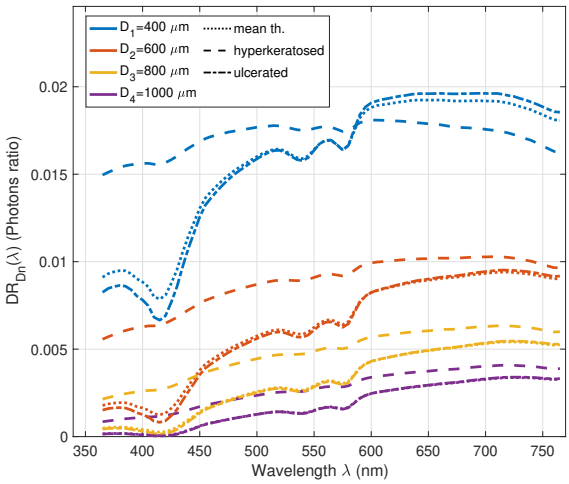

Figure 2.31: DR spectra for the 3 mean healthy (dotted line), hyperkeratosed (dashed) and ulcerated (dashed-dot). The distance SD D_n is indicated by the color code, while the line style refers to the medium.

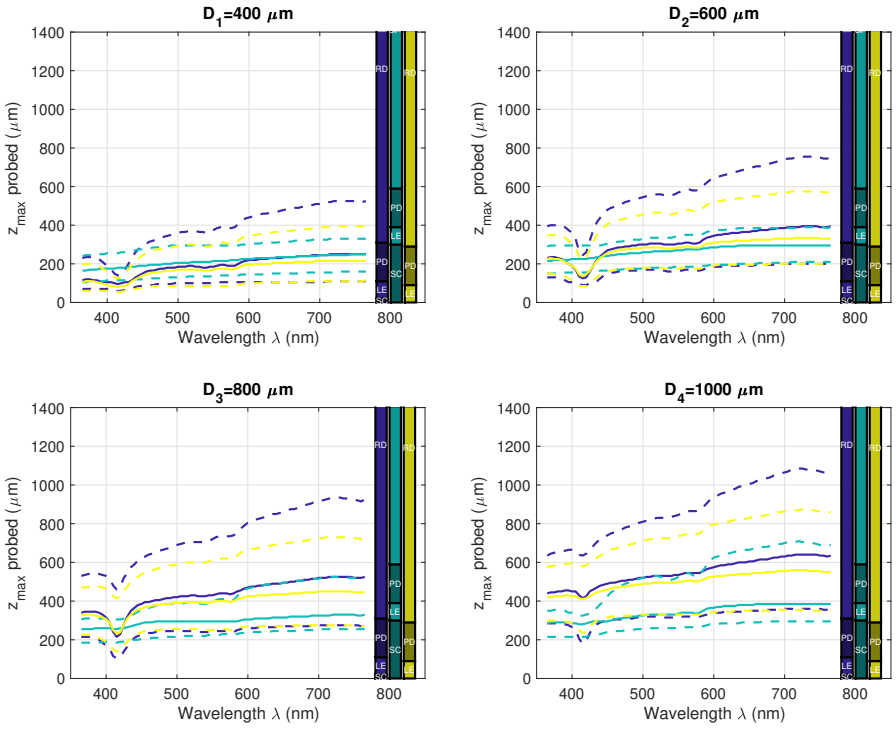

Figure 2.32: Maximal probed depth values of detected photons in the skin model with healthy mean thickness (blue), hyperkeratosed (green) and ulcerted (yellow) as a function of wavelength and SD distances. Solid and dot-dashed lines represent median and quartiles values respectively. The right column illustrate the position of the interface between the layers, in every medium configuration (*cf.* Table 2.1).

2.6.4.3 Phototype modifications in healthy skin model

Fig. 2.33 shows the DR spectra for the healthy skin medium of intermediate thickness (*cf.* Table 2.1) and for the four skin phototypes considered (*cf.* corresponding values of volume fraction of melanosome $f^2_{v,mel}$ in Table 2.2 and LE absorption coefficient μ^2_a in Fig. 2.15 top right insert).

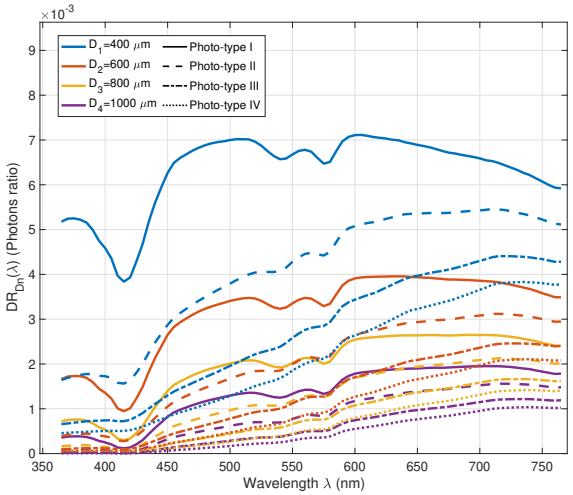

Figure 2.33: DR spectra for the 4 phototypes I (line), II (dashed), III (dashed-dot) and IV (dotted). SD distance D_n is indicated by the color code.

The decrease of the signal in the near UV and the beginning of the visible light, when the skin darkens was expected and is the most obvious characteristic. Not only diffusing, the LE becomes more absorbing with increasing pigmentation. The optical barrier of the epidermis (including SC+LE), becomes more and more difficult to penetrate for photons verifying $\lambda < 450\ nm$. For D_1 (shortest paths), the maximum depth (*cf.* Fig. 2.34) probed by the detected photons decreases when $f^2_{v,mel}$ increases. The information carried by $DR_{D_1}(\lambda < 450)$ appears then very superficial with z_{max} confined in LE layer. The very weak signature of the hemoglobin peak in the spectra for the dark phototypes confirms the previous assertion, since photons having reached the vascularized layers are rare. Still for this same distance and for the rest of the spectrum ($\lambda > 500\ nm$), it is interesting to note that the probed depth, in the PD, is virtually unchanged with the phototype. The path (*i.e.*, the trajectory) traveled by these photons seems then globally identical, and only the absorption during the forward passage, then the way back in the LE, justifies the signal drop in the DR spectrum. This specific behavior observed at short distance (D_1), might be of particular interest. Indeed, it allows to improve the robustness and precision of the estimation of the absorption coefficient $\mu^2_a(\lambda)$ (and thus by extension a value for the volume fraction of melanosome) of the LE layer specifically when solving complex inverse problem of multiple optical properties in multilayer skin models.

For the other longer SD distances, one can notice that all the detected photons reach at least the RD layer for D_2, D_3, D_4 and $\lambda > 500\ nm$. One can also observe that the sensitivity of z_{max} with respect to the hemoglobin absorption peak (at 415 nm), especially for D_2 and D_3. The increasing probed depth with phototype, for all longer SD distances D_n (n>1) can be explained by considering two complementary behaviors during the photon penetrating trajectory from SC to RD layers. The first is to dive as little as possible into the medium, and thus reduce the optical

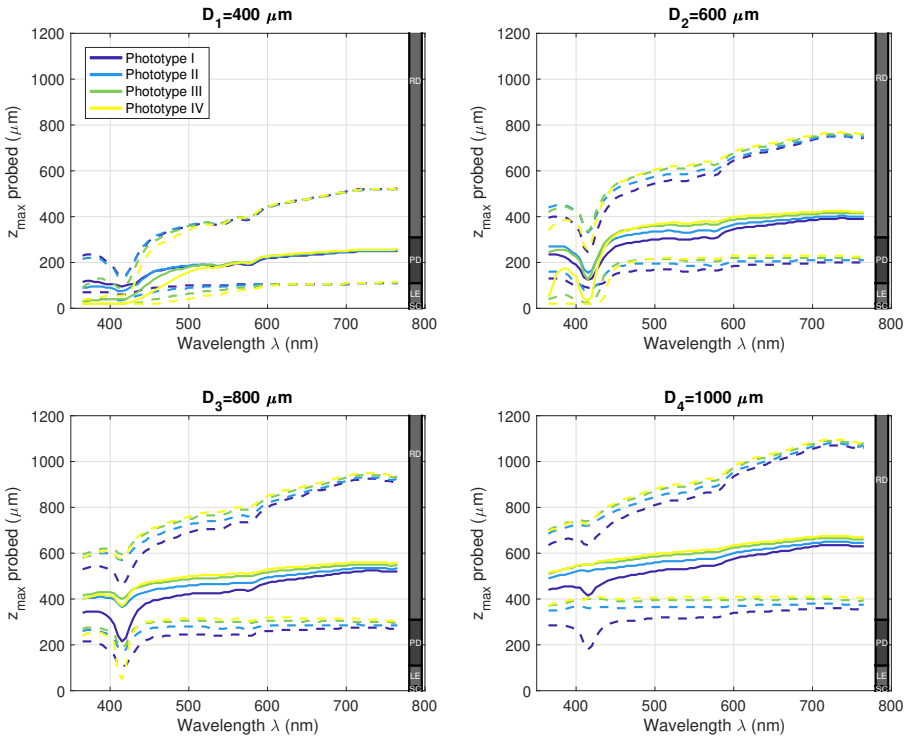

Figure 2.34: Maximal probed depth values of detected photons in the skin model with phototype I (purple), II (blue), III (green) and IV (yellow) as a function of wavelength and SD distances. Solid and dot-dashed lines represent median and quartiles values respectively. The right column illustrate the common position of the interface between the layers.

path traveled. The second is to quickly reach the PD in order to escape the LE with its high absorbing capacity. For fair phototypes, where the LE absorption is moderate, the first behavior seems to have more impact, that is detected photons resulted from shallower paths. On the other hand, for dark phototypes, more probably detected photons are those having crossed the LE layer with shortest path lengths, *i.e.*, as vertically or straight as possible. These photons then need more time to make their way back towards the detection fiber: the probed depth is then more important.

2.6.4.4 Blood content variation in healthy skin model

Fig. 2.35 shows the DR spectra obtained for the healthy skin medium of intermediate thickness (*cf.* Table 2.1) for the fair phototype I (*cf.* Table 2.2) and for the three media representing dermal layers with more or less blood content (*cf.* Table 2.3), for which absorption and scattering coefficients of the two concerned layers (PD and RD), respectively, appear on the middle-right and bottom-right subplots of Fig. 2.15. The most remarkable and expected observation is the relative signal decrease in the three hemoglobin absorption peaks (415, 540 and 575 nm). This can be linked to the probed depth plot where provided in Fig. 2.36, for distances D_2 to D_4, the spectral region where hemoglobin is absorbed (*i.e.*, 365–630 nm) is affected by a decrease in the detected photon penetration with increasing blood concentration.

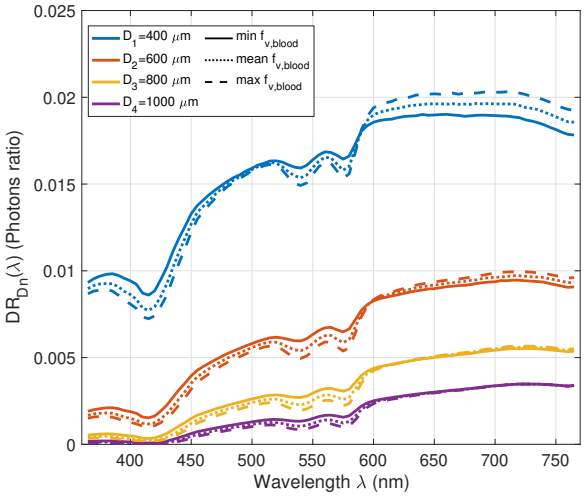

Figure 2.35: DR spectra for the 3 blood concentration levels. The distance SD D_n is indicated by the color code, while the line style refers to the medium.

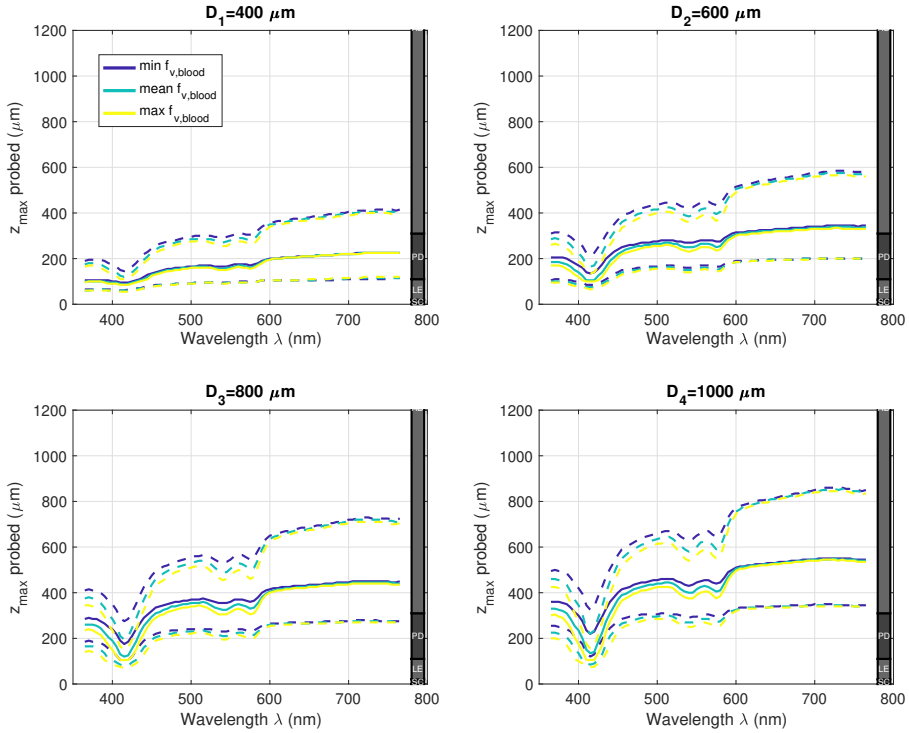

Figure 2.36: Maximal probed depth values of detected photons in the skin model with min (blue), mean (green) and max (yellow) blood concentration levels as a function of wavelength and SD distances. Solid and dot-dashed lines represent median and quartiles values respectively. The right column illustrate the common position of the interface between the layers.

Concerning D_1, the interpretation is even simpler, because of the quasi-non-influence of the quantity of blood on the path of the detected photons. In $DR_{D_1}(\lambda)$, we notice that for the first part of the spectrum (365–600 nm), the blood concentration is responsible for an attenuation of the signal, while it is associated with a gain of intensity for the rest of the spectrum (600–765 nm). The analysis of the optical properties on these spectral bands leads us to the interpretation that the first phenomenon is caused by the absorption of hemoglobin in the dermal layers. For the second phenomenon, the absorption of blood becomes negligible, and only the scattering coefficients remain significantly different (about 15% between the two extremes maximum and minimum $f_{v,blood}$). This means then that the scattering power caused by the increase of the blood concentration of the dermal layers (particular PD for this shorter distance D_1) is at the origin of many short optical paths between SF and DF and therefore responsible for this non-obvious signal increase.

2.6.5 Proposal of a model for DR signal decomposition by skin Layer

In order to more quantitatively determine the content of the global DR signal in terms of layer contributions, we propose to exploit the results of the analysis of the aforementioned developed maximum probed depth histograms and spectra to decompose the total signal $DR_{D_n}(\lambda)$, as a sum of the DR contributions related to each of the five skin layers considered, such that for each SD distance D_n,

$$DR_{D_n}(\lambda) = DR^{SC}_{D_n}(\lambda) + DR^{LE}_{D_n}(\lambda) + DR^{PD}_{D_n}(\lambda) + DR^{RD}_{D_n}(\lambda) + DR^{SF}_{D_n}(\lambda) \tag{2.13}$$

where $DR^{layer}_{D_n}(\lambda)$ is composed of photons that reached at deepest the *layer* appearing in exponent verifying $d^{layer}_{min} < z_{max} < d^{layer}_{max}$ with d^{layer}_{min} and d^{layer}_{max}, respectively, the minimum and maximum depth coordinates of the *layer*. In practice, this decomposition was obtained by integrating the histograms of probed depths (*cf.* section 2.6.3.2 and Fig.2.12) between the upper and lower border of each skin layer. Fig. 2.37 illustrates this decomposition for the four SD distances and the healthy skin model with intermediate thicknesses, mean dermal blood content for SC and LE layers and phototype I. This "deepest layer probed" separation criterion has already been proposed in the literature. In [Fredriksson 2012], Fredriksson and his team studied the path length distributions for detected photons in a three-layered skin model, although they did not propose any decomposition approach. However, a different "layer"-based approach of DR signal decomposition has been proposed in a few studies. In [Arifler 2005], the contribution of the detected photon associated with the k-layer was defined as the quotient of the number of scattering events undergone in this layer on the total number of scattering events between SF and DF. In [Liebert 2004], the authors proposed to explain the skin layer sensitivity by the mean partial path length, which consists of assigning to the layer k the relative weight l_k/l_{tot} in the DR signal, with l_k the path length in the layer k and l_{tot} the total path length between SF and DF.

The approach proposed in the present contribution differs from the latter by the following points. First, our proposed decomposition provides a straightforward and simple interpretation regarding the layer reached by the detected photons making the global DR signal, compared to less non-trivial interpretations linking the mean path length or the ratio of scattering events to the layer's weight in the DR signal. Second, as a consequence, the proposed decomposition should help in designing a method to estimate sequential optical properties by studying the layers from the shallowest to the deepest and by providing new *a priori* knowledge on the selection of the sensitive distances and wavelength range. This approach will bring a physical and anatomical

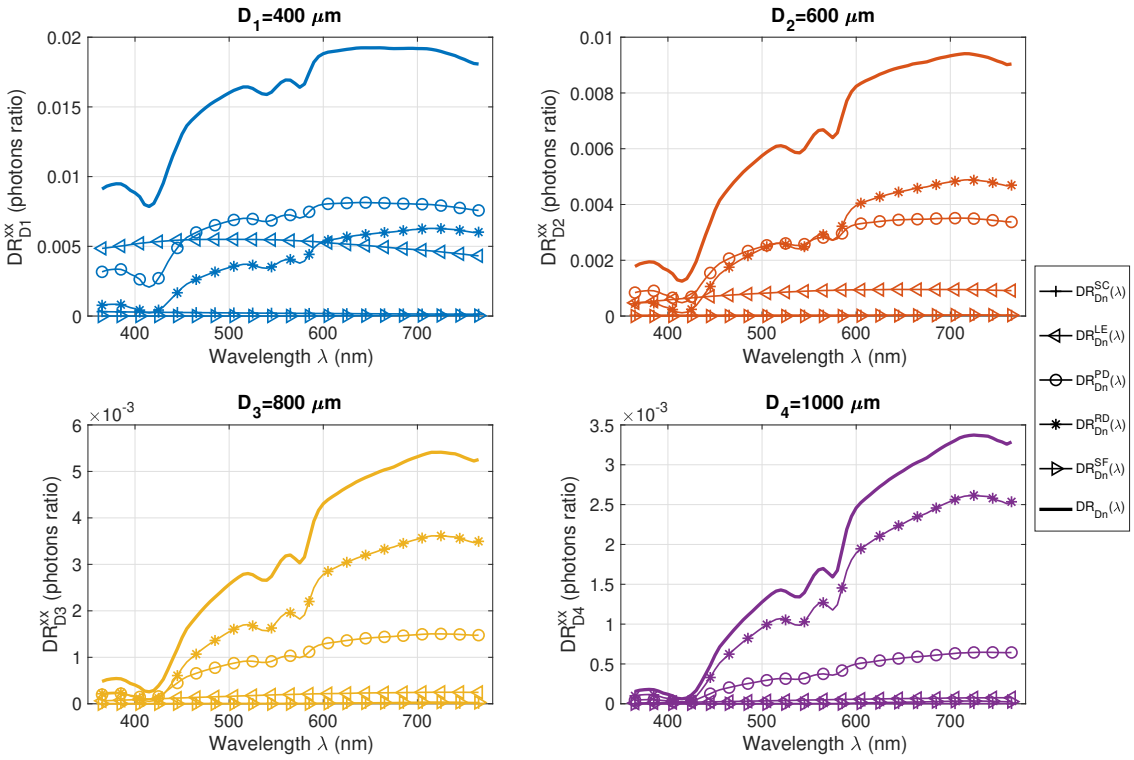

Figure 2.37: DR signal decomposition according to Eq. (2.13) for the distances D_1–D_4 in the healthy skin model with intermediate thicknesses of SC and LE layers, mean dermal blood content and phototype I. The correspondence between symbols and layers considered is indicated in the legend on the right.

sense to the estimation and should be less time consuming due to the successive isolation of the parameters.

The analysis to be drawn from Figure 2.37 is in accordance with that performed qualitatively in the section 2.6.3 but it also allows us to better explain the DR signal in layer decomposition. To further compare the proportion of a signal from a layer, for a fixed couple (λ, D_n), we defined the weight fraction of the layer contribution in percentage, as follows:

$$w_{D_n}^{layer}(\lambda) = 100 \times \frac{DR_{D_n}^{layer}(\lambda)}{DR_{D_n}(\lambda)} \quad (\%) \tag{2.14}$$

Finally, Fig. 2.38 shows the associated evolution of $w_{D_n}^{layer}(\lambda)$ defined in Equation (2.14) as a function of the wavelength and the SD distance. This decomposition turns out to be very useful to extract the spectral band and SD distance of a DR signal that is susceptible to carry information associated with local depth information. For instance, the spectral "signature" of elastosis (accumulation of disordered elastic tissue in the PD due to carcinogenesis) should be looked for in the UV range ($365 < \lambda < 400$ nm) at the D_2 distance, where more than 40% of the DR signal is constituted of photons that have visited the concerned layer.

It is worth noting that all the geometrical and optical parameters considered in the model described above were chosen within standard ranges of values, accounting for anatomical and

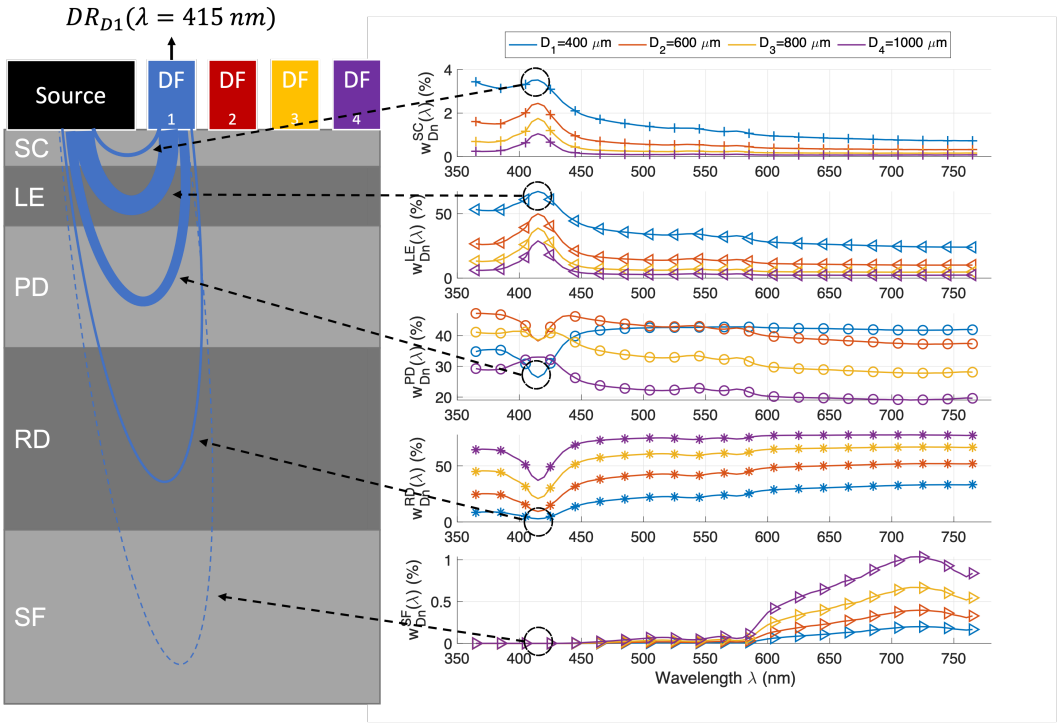

Figure 2.38: Weight of each layer (from SC at the top to SF at the bottom) in the DR signal according to Eq. (2.14) for distances D_1–D_4 in the healthy skin model with intermediate thicknesses of SC and LE layers, mean dermal blood content and phototype I. The correspondence between symbols and layers is still the same as indicated in Figure 2.37. The physical meaning of the weights is represented on left sub-figure for the couple ($\lambda = 415\ nm, D_1 = 400\ \mu m$).

physiological variability. The aim of the present work was not to perform a complete variation study taking into account those variability intervals but rather to investigate the variation with respect to epidermal thickness (see section 2.6.4.1), pathological state (see section 2.6.4.2), phototype (see section 2.6.4.3) and dermal blood content (see section 2.6.4.4) by considering a unique set of basic, but representative values for all other parameters of the model. However, appendix B.2 provides the DR spectra and the associated weights per layer for 36 DR spectra correponding to 3 levels of epidermal thickness, 3 level of dermal blood content and 4 phototypes. A possible extended study could be conducted with other parameters, such as the individually variable scattering coefficient [Jonasson 2018], the blood oxygen saturation [Yudovsky 2010] or the average blood vessel diameter [SL. 2010], even if those parameter have a more limited impact on the layers' optical coefficients and thus on the penetration of photons in depth. It would also be interesting to consider 3D tumor models, since the assumption of semi-infinite layers imposed by *CudaMCML* is a limitation. A study shows that the validity of this assumption depends on the type of tumor simulated (squamous cell carcinoma in epithelium or a basal cell carcinoma in upper dermis), the angular incidence of the exciting fiber, the height of the tumor and its width relative to the SD distance at which the signal is acquired [Zhu 2011].

2.7 Conclusion and prospects

All the results established so far allow us to extend our discussion towards the targeted clinical application of SR-DRS devices. Firstly, the in-depth elements characterizing the path of the detected photons within the various skin layers allow us to assert that the geometrical layout of the probe and its spectral configuration provide access to the different layers of the skin with a sensitivity depending on the chosen couple (λ, D_n) and on the physiological and morphological skin configuration. In particular, the results showed that the photons contributing to the DR spectra were likely to carry the discriminating local information that distinguishes healthy and pathological tissues. It should be noted, however, that the results presented here are valid for the case of fiber-based contact-type DRS configurations, and under the assumption that the optical properties of each of the skin layers do not significantly vary laterally within the 2 mm diameter circular region covered by the multi-fiber optics probe tip. Moreover, for the estimation of diagnostically relevant optical parameters from in vivo SR-DRS measurements through an inverse problem solving method [Palmer 2006, Cen 2010], such results should be useful to understand this iterative process better by defining a cost function adapted to the layer structure of the skin. This idea will be developed in section 3.4.

Chapter 3

Skin optical properties estimation through inverse problem solving

Contents

3.1 Introduction

This chapter focuses on the inverse problem solving. Starting from the state of the art description, we then present the method used so far (*i.e.*, before this thesis) to estimates parameters (optical properties and layer thicknesses) in the optimization process. The new sequential and layer adapted estimation algorithm is then exposed and validated with numerical spectra targets. We also present here our experimental diffuse reflectance standardization. Indeed, this one allows to get simulated and clinical spectra in the same intensity unit, which reduce the gap between them and allow their full comparison during the inverse problem solving.

3.2 State of the art of inverse problem solving and method used up to now

The aim here is to quickly introduce the methods than can be used to solve the inverse problem. More details were provided in the P. Rakotomanga thesis [Rakotomanga 2019], for whom the optimization process was the main topic of her PhD work. This section briefly sums up her work, in order to provide the bases on which my work is founded.

3.2.1 Estimates of optical properties in the literature

This section gives a short overview of the literature relating to the use of a simulation to solve the inverse problem and to estimate the properties of the skin (see Fig. 1.28). Firstly, Palmer and Ramanujam [Palmer 2006] estimated absorption and scattering coefficients from an inverse problem solving in several mono-layer skin mimicked by liquid phantoms having their optical parameters in the the ranges $\mu_a \in [0-20]\ cm^{-1}$ and $\mu_s \in [7-33]\ cm^{-1}$. In their paper, Frederiksson *et al.* [Fredriksson 2012] estimated (using a Levenberg-Marquardt optimization algorithm) 9 parameters including geometrical properties, light scattering properties, tissue chromophores such as melanin and hemoglobin, oxygen saturation and average vessel diameter. Their direct method used the MC multi-path-length multilayered Beer-Lambert algorithm to generate DR spectra. For Sharma *et al.* [Sharma 2014] 4 parameters *i.e.*, top layer thickness, absorption coefficient of the top and bottom layer, as well as common scattering coefficient are estimated in a bi-layer model. To improve optimization speed, a look up table (LUT) was previously build by the authors. It consists in firstly comparing the target spectra with a large number of spectra generated by the simulation for several medium configurations stored in this LUT. This preliminary step ensures starting the optimization process with a spectrum relatively close to the target spectrum, and thus reduces the convergence time. The rest of optimization (kind of adjustment) is done using an interior-point optimization routine.

3.2.2 The starting method: a bimodal least squares cost function coupled with a multivariate optimization algorithm

P. Rakotomanga thesis work led to the choice of using a Particles Swarm Optimization (PSO) [Kholodtsova 2016] algorithm for the inverse problem solving. Technically, this is done using a *Matlab®* routine with the *particleswarm* function. One will very briefly describe the principle of this algorithm. To begin, we provide information about the cost function we want to minimize during the optimization process.

The cost function: The cost function to be minimized should reflect the resemblance between the simulated diffuse reflectance $DR^{sim}(\lambda)$ and auto-fluorescence $AF^{sim}(\lambda)$ spectra, with the target ones, namely $DR^{exp}(\lambda)$ and $AF^{exp}(\lambda)$. The cost function was a least square function including contributions of both spectrum modalities. For a given numerical medium fully described by the unknown vector $\mathbf{p}$, the cost function is given by the formula:

$$cost_{total}(\mathbf{p}) = cost_{AF}(\mathbf{p}) + cost_{DR}(\mathbf{p}) \tag{3.1}$$

Where:

$$cost_{DR}(\mathbf{p}) = \sum_{i=1}^{N_\lambda} \sum_{n=1}^{4} [\frac{DR_{D_n}^{sim}(\lambda_i;\mathbf{p}) - DR_{D_n}^{exp}(\lambda_i)}{DR_{D_n}^{exp}(\lambda_i)}]^2 \tag{3.2}$$

In Eq. 3.2 N_λ is the number of points that form a DR spectrum. For the auto-fluorescence spectra at five exitation wavelengths exc_j and four source positions D_n, the cost contribution is given by:

$$cost_{AF}(\mathbf{p}) = \sum_{i=1}^{N_\lambda} \sum_{n=1}^{4} \sum_{j=1}^{5} [\frac{^{exc_j}AF_{D_n}^{sim}(\lambda_i;\mathbf{p}) - {}^{exc_j}AF_{D_n}^{exp}(\lambda_i)}{^{exc_j}AF_{D_n}^{exp}(\lambda_i)}]^2 \tag{3.3}$$

The choice of considering relative least square errors rather than absolute errors is justified by the fact that the intensities order of magnitude differs for signals. Indeed, the short SD distance are associated to strong level of signal while the longer measurement distances correspond to weaker one. The DR intensities are also generally larger than AF ones. Dividing by the experimental spectra allows to give similar weight to the terms appearing in Eq. (3.2) and Eq. (3.3).

The particles behaviour: The parameters we want to determine with the inverse problem are stored in vector $\mathbf{p}$, of dimension $1 \times N$, with N the number of unknown parameters. For each, we delimit the range of possible values by indicating an upper and lower bound. A particle is defined by its position, *i.e.*, a vector $\mathbf{p}_{par}$ of dimension $1 \times N$ where the p_i are the value of parameters. The main simulation parameters are the iterations number N_{iter}, and the particles number (set by default to $N_{part} = 10 \times N$ for *Matlab*). A simplified algorithm is presented here:

Result: Determination of $\hat{\mathbf{p}}$ that minimize $cost_{tot}$
the N_{part} particles are randomly distributed in the space range of possible;
(*i.e.*, each particle is associated with a point of the N-dimensional space)
for *iteration = 1 : N_{iter}* **do**
  for *particle = 1 : N_{par}* **do**
    calculation of simulated spectra $DR^{sim}(\lambda;\mathbf{p}_{par})$ and $AF^{sim}(\lambda;\mathbf{p}_{par})$;
    calculation of cost $cost_{tot}(\mathbf{p}_{par})$;
  end
  storage of the particle position associated to the lowest cost;
  particles position update[a];
end
storage of the particle position associated to the lowest cost, all iterations combined in $\hat{\mathbf{p}}$;
return $\hat{\mathbf{p}}$;

Algorithm 4: Particle Swarm Optimization principle.

[a] see explanations below

The algorithm efficiency remains in the particles position update. More details can be found on the *Matlab* documentation. One will simply says that, at the particle level, this new one is calculated taking into account 3 criteria:

1. Maintaining the direction of the previous iteration (memory of the previous iteration).
2. Move toward the nearest local minimum (gradient descent, local minimum research).
3. Move toward the particle (among the N_{part}) that indicates the best score, *i.e.* the global minimum at this iteration (inter-particles communication).

As indicated in Algorithm 4, the inverse problem requires $N_{iter} \times N_{par}$ calls to the direct method. This quantity is function of the number of parameters to estimate, that is why a complex problem including numerous unknown parameters could be time consuming. As an illustrative example, an

inverse problem solving with a numerical target spectra (and therefore whose associated ground truth parameter values) with 2 unknown parameters is exposed in appendix C.

3.3 PSO-based inverse problem solving in our 5-layers skin medium

After having briefly described the PSO algorithm, as well as the associated cost functions, one now studies the algorithm's behavior for target spectra of skin, whether the latter are numerical (obtained from the simulation) or clinical (from *SpectroLive* device) data. Many parameters are variable, but it was decided to restrict in this section the number of unknowns to 3, namely the volume fraction of melanosome in the living epidermis ($f^2_{v,mel}$ in the range of $[0.002 - 0.05]$), the volume fraction of blood in the papillary dermis ($f^3_{v,blood}$ in a range of $[0.01 - 0.05]$) and reticular dermis ($f^4_{v,blood}$ in a range of $[0.001 - 0.005]$).

3.3.1 Inverse problem solving using purely numerical data

First, we work here with an inverse problem using target DR spectra issuing from simulation with our 5-layer model. This allows us to make sure that there is a $\mathbf{p} = (f^2_{v,mel}\ f^3_{v,blood}\ f^4_{v,blood})$ vector able to generate the spectra that the optimization tries to fit (which is obviously not the case with clinical spectra). On the other hand, we need to know this vector $\mathbf{p}$ in order to compare it to the one determined by the estimation (access to the ground truth).

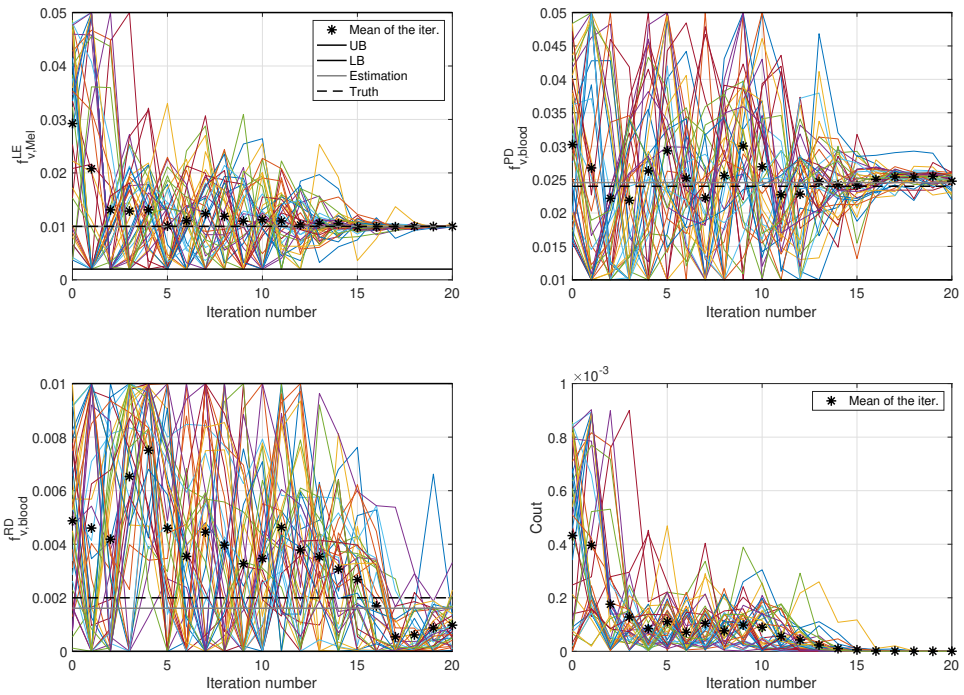

Figure 3.1: Dynamic of convergence of the parameters in PSO (3 first figures) and associated cost function evolution (last right-bottom figure).

In our experiment, $\mathbf{p}_{target}$ was arbitrary set to $\mathbf{p}_{target} = (0.01\ 0.024\ 0.002)$. The number of particles was $N_{par} = 30$ ($10\times$ unknowns), while the iteration number was set to $N_{iter} = 20$, leading to a total of 600 calls from the direct model. 10^7 photons were sent for every spectra acquisition ($\approx$ 10 hours to get the results using the *NVIDIA Tesla P100* GPU). Fig. 3.1 shows the dynamic of the convergence of the particles toward the estimations. One can observe in this figure the successive particle positions (color continuous lines) and their average position ($*$) varying between the upper and lower bounds of the parameters intervals (black continuous lines) for the volume fraction of melanosome in the living epidermis $f^2_{v,mel}$, the volume fraction of blood in the papillary dermis $f^3_{v,blood}$ and reticular dermis $f^4_{v,blood}$. Black dashed-line represent the truth value of the parameter, while the gray continuous one represent the final estimation resulting from the optimization. The fourth figure (bottom-right) also shows the dynamic of convergence with the evolution of cost function (see Eq. (3.2)). The estimation converges toward $\hat{\mathbf{p}} = (0.01\ 0.0244\ 0.0016)$. A slight bias appears for the estimation of the last two parameters (*i.e.*, $f^3_{v,blood}$ and $f^4_{v,blood}$). This is explained by their weaker impact on DR spectra in comparison with the melanin $f^2_{v,mel}$ parameter. The DR spectra generated by this estimated vector $\hat{\mathbf{p}}$ appears in dashed-line on Fig. 3.2 while the ground truth generated by $\mathbf{p}_{target}$ appears in continuous line. Both sets of spectra are almost identical, and only the noise caused by the relative low number of photons sent (10^7) is responsible for the visible difference.

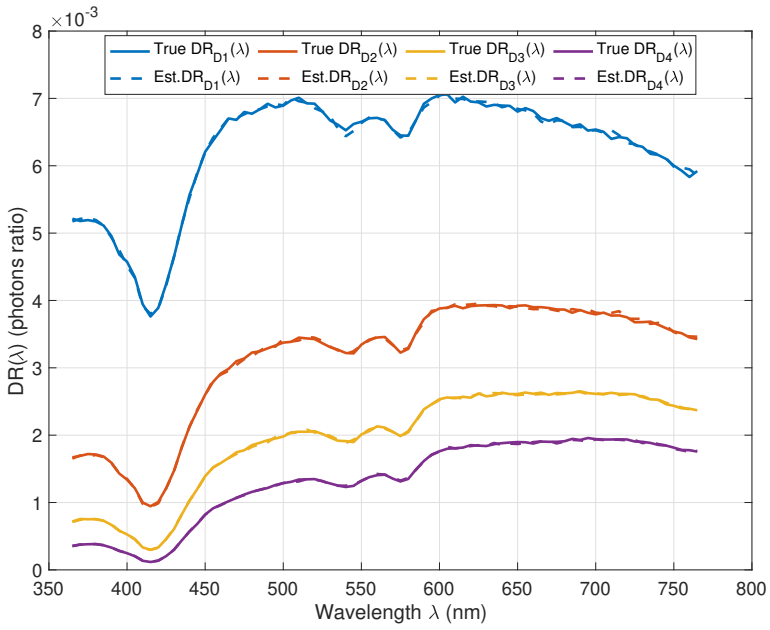

Figure 3.2: Comparison between target DR spectra generated by $\mathbf{p}_{target}$ vector (line) and estimated ones generated by $\hat{\mathbf{p}}$ (dashed-line).

3.3.2 Inverse problem solving from clinical target spectra

After getting familiar with the PSO convergence algorithm on purely numerical inverse problems, it is now appropriate to try to test our optimization on a set of clinical DR spectra. The clinical spectra results from an acquisition on healthy phototype I wrist. This body site was chosen because it corresponds to a mean thickness location, *i.e.*, a stratum corneum and an epidermis

approximate thicknesses of respectively $z^1 = 20\ \mu m$ and $z^2 = 90\ \mu m$ (*cf.* section 2.5 and Table 2.1). This was important because in the inverse problem presented here, the thickness of these layers was not a parameter to be estimated, *i.e.*, at fixed values.

The PSO optimization was conducted for 30 iterations, still with 30 particles and 10^7 photons sent for each spectra. This corresponds to 900 calls to the simulations. Fig. 3.3 shows the dynamic of the convergence of the particle toward the estimations (gray line). One can observe in this figure that the successive particle positions (colored continuous lines) and their average position ($*$) are varying between the upper and lower bounds of the parameter interval (black continuous lines). The ground truth value for the 3 parameters is not known with clinical spectra. The fourth figure (bottom-right) shows again the dynamic of convergence with the evolution of cost function (least square function between normalized spectra, as appearing in Fig. 3.4). The estimation converges toward $\hat{\mathbf{p}} = (0.0102\ 0.023\ 0.002)$.

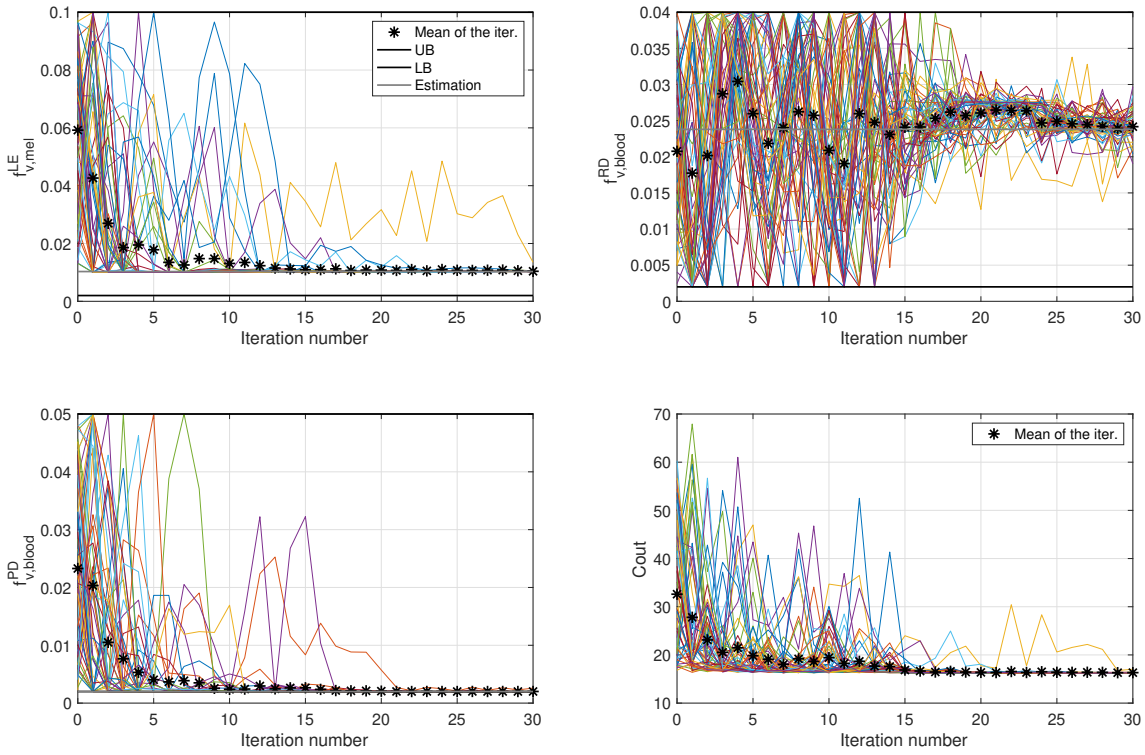

Figure 3.3: Dynamic of convergence of the parameters in PSO (3 first figures) and associated cost function evolution (last right-bottom figure).

Here, there is no way to access the ground truth to confront the estimations made by solving the inverse problem with the physiological values at the origin of the acquired clinical spectra. The only solution to assess the optimization quality is to observe the simulated spectra for the estimated $\hat{\mathbf{p}}$ vector. Those are shown in Fig. 3.4 for each distance D_n. We notice measurement and signal processing artifacts at the borders of the clinical spectra (near UV and near IR), which force us to restrict the spectral range on which a term-to-term difference of the spectra between the simulation spectra and the clinical spectra makes sense. For this term-to-term difference, it

was also mandatory to normalize both spectra by matching maximums (respectively minimums) to the value 1 (to the value 0) in the restricted valid spectrum *i.e.*, $[450 - 600]$ nm to bring both simulation and clinical data on a common scale. The fitting is quite satisfying, which validates our skin optical model.

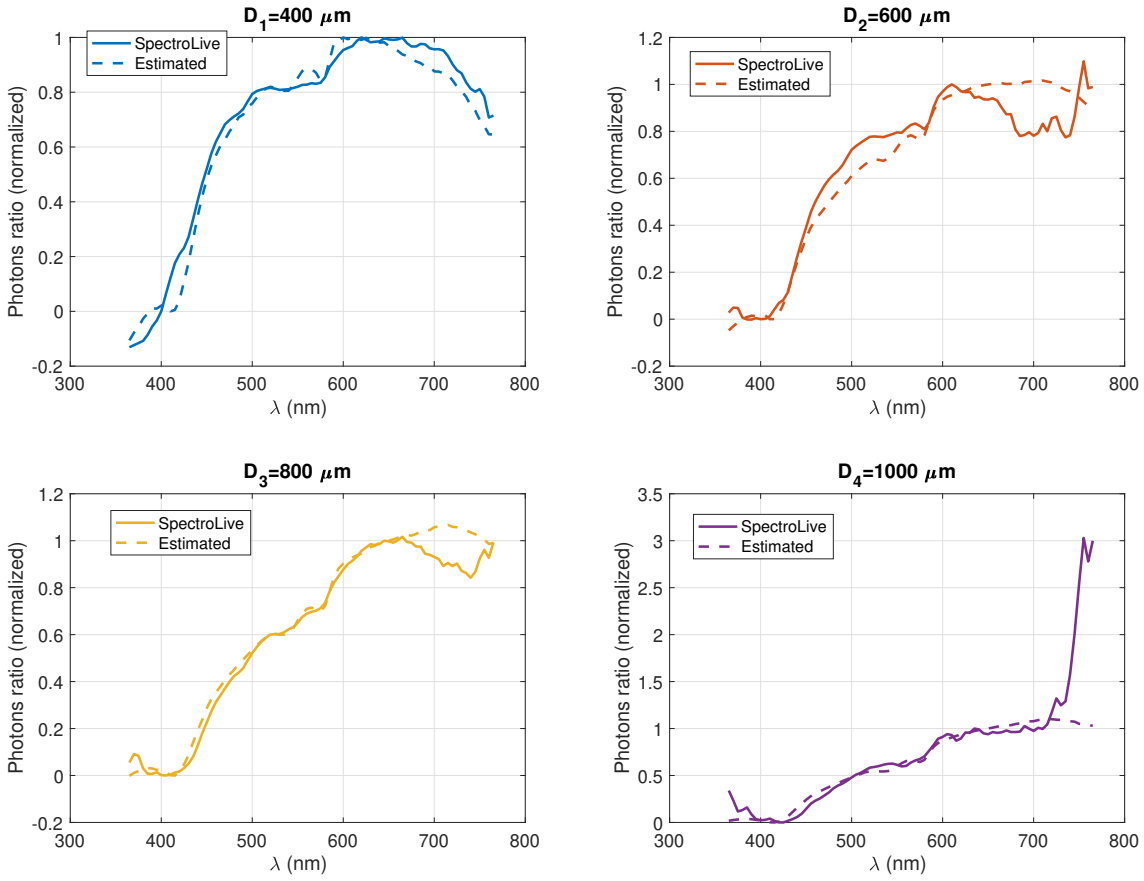

Figure 3.4: Comparison between normalized target DR spectra acquired in clinic by *SpectroLive* (line) and normalized estimated ones generated by $\hat{\mathbf{p}}$ (dashed-line).

3.4 An optimization approach adapted to the skin's layered structure

We present here some elements of our new approach using the previously described depth study (see Chapter 2, especially section 2.6) to solve the inverse problem. The idea is to create a sequential layer-wise estimation process using a custom cost function adapted to the layered structure of skin.

3.4.1 Motivations

Several arguments are at the origin of this decision to stop using the PSO-based optimization (see section 3.2.2) and to establish a method of research of the optical properties of the various layers of skin adapted to its structure. Firstly, we are looking for a method that relates to a morphological and physiological dimension to the inverse problem solving. Then, although PSO is very efficient for multi-variate optimization problems, this efficiency has a drawback: a long calculation time. This is explained by the number of particles (10×unknowns), *i.e.*, the number of calls to the simulation for each iteration, which is consequent. Especially, the fact of estimating all the parameters together constrains us to generate spectra with a lot of photons ($\approx 10^7$) to be able to perceive in DR spectra also the slight modifications caused by variation of the less impacting parameters (such as dermal blood content), while only 10^6 photons are enough for the main parameters (such as melanin epidermal content and its thickness). The complexity and the computation time, hence the difficulty, to solve this estimation problem drastically increase as soon as the skin multi-layer model involves more than three layers and considers several physiological parameters varying in every layer. To address this problem, an alternative optimization process was developed, based on sequential estimation (isolation of parameters in each layer), and a custom cost-function adapted to the layered structure of the skin, *i.e.*, which considers the sensitivity of a wavelength and the source-detector distance to each layer. The present section describes in details this sequential layer-wise estimation process, and compares its performance to former method used, *i.e.*, a least squares cost function coupled with a multivariate optimization algorithm (see section 3.2.2). A set of reference simulated SR-DR spectra was considered as targeted ground truth to characterize the convergence efficiency of the proposed method. The estimation process was developed in [Colas 2022b].

3.4.2 Simulated target spectra description

Among the parameters of the model, four of them were selected to form the parameter vector $\mathbf{p}$ to be optimized. The chosen parameters were considered as being major (and of prime interest) due to their strong impact on DR spectral shape. These parameters are the SC thickness ($p_1 = z_{SC}$), the LE thickness ($p_2 = z_{LE}$), the volume fraction of melanin in LE ($p_3 = f_{v,mel}$) and finally the blood volume fraction in PD and RD dermal layer, *i.e.*, ($p_4 = f_{v,blood}$). Ground-truth values of the target parameters $\mathbf{p}_{true}$ were arbitrary chosen among the variation ranges corresponding to a skin site of mean thickness ($p_1 \in [5-30]$ and $p_2 \in [70-110]$ μm), phototype I ($p_3 \in [0.5-2]$ %) and physiological blood dermal level ($p_4 \in [1-4]$ %), such that:

$$\mathbf{p}_{true} = [p_{1,true}\ p_{2,true}\ p_{3,true}\ p_{4,true}] = [15\ \mu m \quad 100\ \mu m \quad 1.8\ \% \quad 1.6\ \%] \tag{3.4}$$

3.4.3 Sequential method description

The optimization process requires to first establish the layer sensitivity ranking in the resulting DR spectra. In our case, LE including $p_2 = z_{LE}$ and $p_3 = f_{v,mel}$ is the most prominent one before dermal layers with $p_4 = f_{v,blood}$ and finally the SC including $p_1 = z_{SC}$. The following algorithm summarizes the main steps of the sequential estimation process:

Result: $\hat{\mathbf{p}}$ parameters estimation
for *Every layer including parameter(s) (ranked by sensitivity)* **do**
  if *It is the first layer which is considered* **then**
    Rough estimates of the parameter with cost function adapted to the layer [a];
    (considering the initial values of the parameters as the middle of the physiological range)
  else
    Consider a cost function adapted to this new layer;
    Estimate the parameter(s) value of this new layer while refining the other ones previously estimated;
    (considering the initial values of the old parameter as their estimated values)
  end
end

Algorithm 5: Sequential estimation process of the parameters included in $\hat{\mathbf{p}}$.

[a] See explanations in section 3.4.4

In our case, it means that three steps are required to get the final estimates $\hat{\mathbf{p}} = [\hat{p_1}\ \hat{p_2}\ \hat{p_3}\ \hat{p_4}]$.

3.4.4 Custom-made cost function description

We propose a custom-made cost function based on an *a priori* knowledge provided by the clinician who gave us information about the skin epidermal thickness and the phototype of the probed skin site *i.e.*, in our special case a mean thickness site of phototype I. In parallel, the sensitivity of a pair (λ, D_n) for a layer has been summed up in the spectral weight vector $w_{D_n}^{layer}(\lambda)$ for typical values corresponding to this skin configuration [Colas 2021a]. The five weights (corresponding to the five layers of the skin model) appear in Fig. 2.38, for this skin type, but more generally for all phototypes combined with all epidermal thicknesses in the appendix B.2.

As a reminder, it is to be noticed that for a couple (λ, D_n), the percentage on the y-axis in $w_{D_n}^{layer}(\lambda)$ is the fraction of a $DR_{Dn}(\lambda)$ signal made of photons that reach at maximum the considered *layer*. For example, $w_{D_4}^{RD}(\lambda = 365\ nm) = 59\%$ (see Fig. 2.38) means that 59% of the photons contributing to $DR_{D4}(\lambda = 365\ nm)$ had their lowest points of their trajectories between SF and DF in the reticular dermis layer. The cost function adapted to the layer of interest is then a cost function of relative least squares (similarly to Eq. (3.2)), but simply corrected by this weight vector *i.e.*,:

$$cost_{layer}(\mathbf{p}) = \sum_{i=1}^{N_\lambda} \sum_{n=1}^{4} w_{D_n}^{layer}(\lambda)\left[\frac{DR_{D_n}(\lambda_i;\mathbf{p}) - DR_{D_n}(\lambda_i;\mathbf{p}_{true})}{DR_{D_n}(\lambda_i;\mathbf{p}_{true})}\right]^2 \tag{3.5}$$

Thus, this cost function gives relatively more importance to the wavelengths and SD distances for which numerous photons have traveled in the considered layer. As a further example to understand the changes caused by this factor, when estimating the thickness of the SC (parameter p_1), $cost_{SC}(\mathbf{p})$ will strongly penalize spectral differences in near UV and short SD distances (spectral parts where the "signature" of the SC is important), whereas differences in near IR and long SD distances will be only weakly considered.

3.4.5 Procedure to valid the new approach

To validate the previously described method, 3 series of inverse problem solving were conducted, with the target spectra and parameter earlier described (see section 3.4.2). Each solution of $\mathbf{p}$ was based on a 10 times random repetition of the same estimation. The first series of inverse solving consisted in applying the custom sequential method (*cf.* Algorithm 5) with layer-wise adapted cost function (*cf.* Eq. (3.5)), tagged as "layer-cost&sequential" and associated to color ■ in next plots. The second was similar to the first one, excepted that the cost function was unweighted, *i.e.*, simply a relative least square cost function:

$$cost_{normal}(\mathbf{p}) = \sum_{i=1}^{N_\lambda} \sum_{n=1}^{4} [\frac{DR_{D_n}(\lambda_i;\mathbf{p}) - DR_{D_n}(\lambda_i;\mathbf{p}_{true})}{DR_{D_n}(\lambda_i;\mathbf{p}_{true})}]^2 \tag{3.6}$$

This second series is tagged as "normal-cost&sequential" and associated to color ■ in the next plots. Finally, the last configuration used the PSO-based method to simultaneously estimate the 4 parameters, tagged as "normal-cost&PSO" and associated to color ■ in the next plots. These 3 series of estimates were all carried out on *Matlab®* using *fmincon* (using interior points optimization function, for series one and two) and *partcileswarm* (for the third) functions, with same initial bounds (see section 3.4.2), same number of photons launched (10×10^6) and finally the same maximum number of calls to the cost function (< 280, that guarantee a similar calculation time whatever the method). To quantify the convergence of each method, the relative error $err(p_i)$ (expressed in %) for each parameter p_i at the end of estimates was introduced and calculated as follows:

$$err(p_i) = |\frac{p_i - p_{i,true}}{p_{i,true}}| \times 100 \quad (\%) \tag{3.7}$$

3.4.6 Comparison of estimate performance

Before focusing on the parameters estimation, let's first consider the spectral shape convergence. Fig. 3.5 shows the comparison between target and estimated spectra for each of the 3 methods previously described. The estimated spectra being very similar to the target ones, it was decided to show the target spectra (left) and the relative errors (error bar representation of the 10 simulations) with respect to these targets for the three estimation methods previously described (right). In view of the reliable relative errors, it can be concluded that the convergence process is correct whatever the method, with (however) more consequent deviation for the "normal-cost&PSO" method which locally reaches (in the near UV) errors of around 10%. When looking at the presented curves, a possible improvement caused by the weighted cost function in comparison to the unweighted one (*i.e.*, between "layer-cost&sequential" and "normal-cost&sequential" methods) can not be significantly observed.

A boxplot representation of the 4 parameters estimates appears in Fig. 3.6, together with statistics related to the realization of 10 inverse problem solving series for every method. These errors were calculated according to the formula (3.7). Firstly, we can draw the conclusion that PSO-based is not convincing with a maximum of 280 function calls. The appearance of the spectra (see Fig. 3.5) was nevertheless satisfactory. This implies that non-unicity of the solution, *i.e.*, different vectors of parameter values can provide very similar DR spectra (related to cross-talk between parameters), is a difficulty existing in our skin model that should be avoided. Fortunately, the 2 other sequential methods proposed (weighted or not), appear to overcome this difficulty and allows for converging towards the target parameter ground truth values. Also, it can be

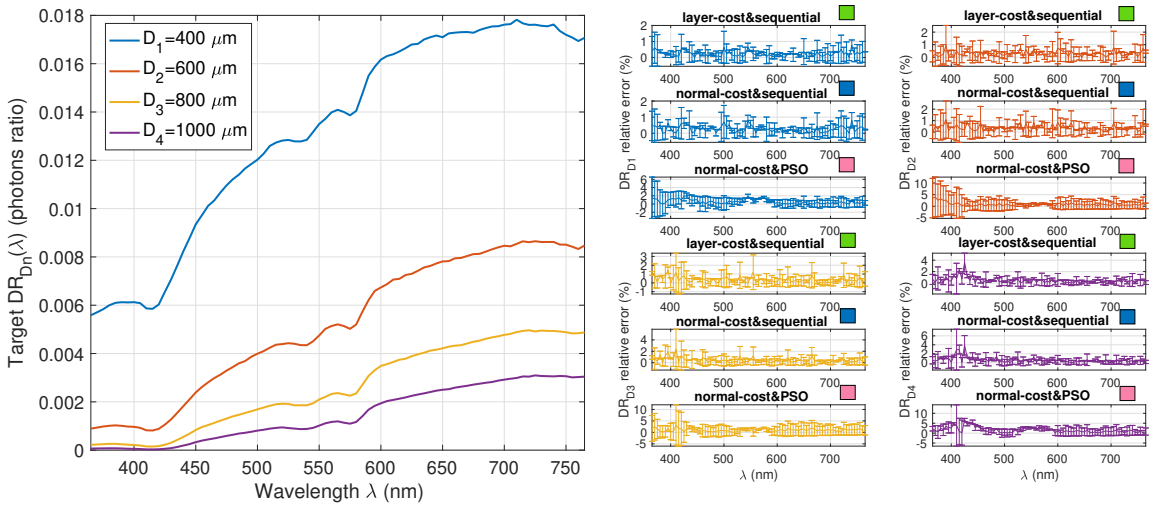

Figure 3.5: Simulated target spectra (left) and relative error (error bar representation for the 10 repeated estimates) for each of the three estimation methods compared (right). The color code refers to the 3 different techniques described in section 3.4.5.

noticed that the dispersion of the estimates is unsurprisingly proportional to the sensitivity of the parameters. Finally, the improved accuracy of our estimates is validated with the custom layer-wise adapted cost function proposed, including less bias and less dispersion compared to the unweighted traditional least square function.

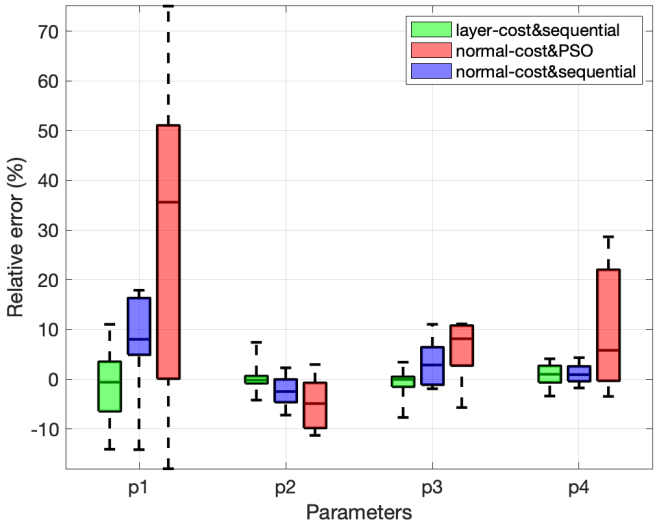

Figure 3.6: Relative error in parameter estimates for the three methods compared, *i.e.*, the sequential layer-wise adapted weighted cost function (green), the sequential least squares cost function (blue) and the non-sequential PSO cost function (red).

3.5 Standardization of experimental DR spectra

This section describes the work undertaken to standardize the DR spectra from a *SpectroLive* acquisition, and indicates how this standardization is useful in solving the inverse problem.

3.5.1 Motivations of the willing to standardize DR spectra

This fitting procedure during the inverse problem solving implies a comparison between clinical (experimental) and numerical (simulated) spectra, that is often quantified by a least squares error cost function. This comparison is not trivial because obtaining DR spectra intensities in absolute values, defined as the fraction of collected over emitted light and expressed in photons ratio, still presents difficulties for experimental signals. Indeed, the raw spectra in photon counts provided by the spectrometer, is dependent on the broadband white light source spectral characteristics, on the spectral responses of the probed medium and on the components of the optoelectronic acquisition chain such as fibers, grating, and photo-detector. To compensate for the light source spectral shape and for the acquisition chain spectral response, which can also vary over time, it is an established practice to carry out a calibration measurement using a spectrally flat reflectance standard, made of *spectralon*® [Thueler 2003, Yu 2011]. For the same illumination condition, by dividing raw spectra acquired on skin by raw spectra acquired on *spectralon*®, the resulting spectral shape depends only on the probed medium spectral response. However, the unit of this spectrum is difficult to interpret and not only depends on the optical probe geometrical features (SD fiber distances, fibers core diameter and numerical apertures), but also on the calibration measurement set up: distance between the optical fiber probe tip and the *spectralon*® surface.

This lack of standardization in experimental DR spectra limits any comparison with simulated ones and it only become possible after normalizing both spectra to bring them back to a common scale (imposing that both maxima correspond to 1, this has been done in every case presented so far in this manuscript). More generally, any comparison of experimental data requires normalization, especially when confronting data to those provided by other research teams raising the issue of inter-devices comparison. Therefore, the definition of a corrective factor allowing to standardize any experimental SR-DR spectrum spectrum to absolute magnitude is at stake.

To the best of our knowledge, contributions that explain how to perform an absolute comparison of simulated and experimental spectra are rare and only deal with experimental values of the calibration factor without dealing with calculation methods. Thueler *et al.* [Thueler 2003] developed a two-step calibration procedure using a (i) spectrally flat reflectance standard and (ii) a solid turbid siloxane phantom of known optical properties to get absolute reflectance spectra of stomach tissues. The optical properties were estimated at 675 nm by combining frequency-domain and spatially resolved measurements. Those estimates were used as parameters in Monte Carlo simulations which allow to get the absolute diffuse reflectance, and thus the calibration factor to finally obtain spectra in the same unit as the simulated ones. We can also mention the Sun *et al.* paper [Sun 2021], in which the mismatches between measurements and simulations were explored by studying the influences from light source and the incident and detection angle on the diffuse reflectance profiles. The current section will present a similar approach exploiting Double Integrating Sphere (DIS) measurements coupled to the Inverse Adding Doubling [Prahl 2011] (IAD) (this protocol description is fully explained in Chapter 4) method to characterize phantom optical properties used for the generation of the Monte Carlo simulated spectra. This experimental factor thus obtained will be compared with theoretical and simulated calculations of the same factor.

3.5.2 New normalization procedure and definition of the standardization factor

3.5.2.1 Description of the normalization procedure

For the reasons mentioned above, it is common practice to firstly calibrate the device using a reflectance standard. The process to obtain a $DR_{Dn}(\lambda)$ spectra is made of the three following steps:

1. **Acquisition on a reflectance standard:** The *SpectroLive* probe is vertically placed in a light-isolated box at a distance z ($z = 10000\ \mu m$ in our case) from a *spectralon®* reflectance standard (*SRS-99, Labsphere*). The latter reflects a fraction R of incident light ($R = 99\%$ for all wavelengths in our case) in the entire half-space on the source side (Lambertian-like behavior). A part of the photons is then captured by the detection fibers located at all D_n distances and sent to a spectrometer which provides a raw spectrum $S_{Dn}^{stand}(\lambda, z, R)$ whose unit is photon counts.

2. **Acquisition on skin:** The *SpectroLive* probe is then apply on a skin surface with gentle contact, and same amount of light is sent again. This second measurement also provides a raw spectrum $S_{Dn}^{skin}(\lambda)$, also expressed in photon counts.

3. **DR spectra calculation:** From the two previous measurements, the diffuse reflectance spectrum is obtained by:
$$DR_{D_n}(\lambda, z, R) = R\frac{S_{Dn}^{skin}(\lambda) - S_{Dn}^{dark}}{S_{Dn}^{stand}(\lambda, z, R) - S_{Dn}^{dark}} \tag{3.8}$$
Where S_{Dn}^{dark} is the dark photon counts spectrum which is obviously the same for both acquisitions on *spectralon®* and skin.

One can notice in Eq. 3.8, that the intensity (*i.e.*, the y-axis) unit of a clinical spectrum is then the photon ratio between the light collected by a fiber located at a D_n distance on skin and the light collected for the same D_n SD distance when illuminating a Lambertian standard of reflectivity R at a z vertical distance. This non-elementary unit is difficult to physically interpret.

3.5.2.2 Definition of the standardization factor

This problem may be solved by determining a way to transform these experimental spectra into spectra expressed in the unit of the definition, *i.e.*, the ratio between the light received by the DF and sent by the SF. In other words, the idea to define the standardization factor $c_{D_n}(z, R)$ so that:
$$DR_{D_n}(\lambda)[photons\ ratio] = c_{D_n}(z, R) \times DR_{D_n}(\lambda, z, R)[actual\ unit] \tag{3.9}$$

The previously introduced factor $c_{D_n}(z, R)$ corresponds in reality to the ratio between incident collected and emitted light during calibration measurement *i.e.*, the normal illumination of a Lambertian standard of reflectance R at a distance z. The next sections present the two approaches proposed to theoretically calculate this value: the first one according radiometric calculations and the second one using Monte Carlo simulation based (Ray-tracing) calculations.

3.5.2.3 Geometry of the calibration measurement

The aim here is to describe the path of the photons during the calibration measurement. The successive steps can be visualized on the schematic representation given in Fig. 3.7. Incident flux F_{inc} is emitted by SF, and propagates in a light cone according to the NA_{SF} divergence. It illuminates an $A_{SRS-99}(z)$ area on the standard. This area increases when z increases. $A_{SRS-99}(z)$ is then considered as a secondary Lambertian light source emitting the reflected flux $F_{ref} = RF_{inc}$ in all the half-space. Only a part of F_{ref} is sent toward detection fibers at D_n by satisfying the angular detection conditions of NA_{SF}. This flux is called $F_{det}(z, R)$ and the light ratio, *i.e.*, $c_{D_n}(z, R)$ is then defined as:

$$c_{D_n}(z, R) = F_{det}(z, R)/F_{inc} \tag{3.10}$$

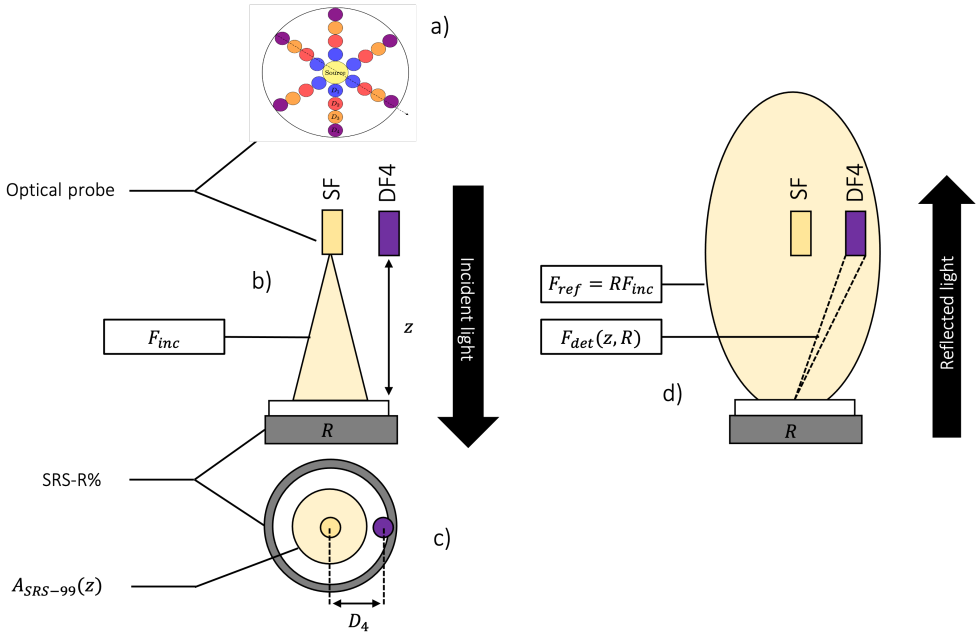

Figure 3.7: Schematic (not scaled) representation of the calibration geometry. a) Geometry of the probe, b) side view of the incident light spreading on the reflectance standard, c) top view and d) side view of the reflected light distribution.

3.5.3 Two different methods to determine the standardization factor

3.5.3.1 Photometric calculation of the correction factor

In this section, the theoretical calculation of the $c_{D_n}(z, R)$ factor is presented based on radiometry, developed hereafter in 3 steps. For this purpose, a schematic representation geometry of the reflected light configuration is provided in Fig. 3.9.

1. F_{inc} is spread according to the angular distribution at the SF output on a disk area $A_{SRS-99}(z)$ of radius $r(z) = r_{SF} + z \cdot \tan(\arcsin(NA_{SF}))$ on the reflectance standard (an image of the real flux distribution exited from the SF and reaching the reflectance standard surface is shown in the left part of Fig. 3.8). This flux quantified by surface unit *i.e.*, the irradiance, is defined for a elementary region centered on point $P(r, \theta, 0)_{\mathcal{R}}$ in the cylindrical coordinates system

associated to the mark $\mathcal{R}(O, \vec{u_x}, \vec{u_y}, \vec{u_z})$ with origin O in the center of the illuminated source on reflectance standard and noted $I(P, z)$. The later is the ratio between elementary flux and the disk area element $dA = rdrd\theta$ on the surface $A_{SRS-99}(z)$. In other words, irradiance in each point P on the reflectance standard is defined as:

$$I(P, z) = \frac{dF_{inc}(P, z)}{dA} \tag{3.11}$$

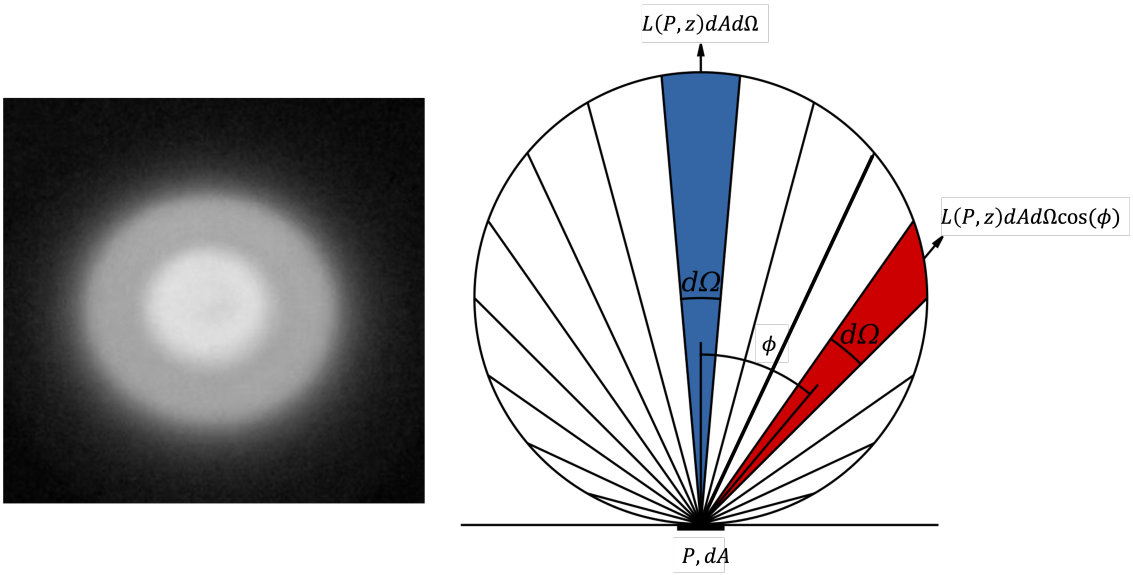

Figure 3.8: Distribution of the flux on the reflectance standard at the fiber output (left) and schematic representation of the angular emission of the photon flux for a Lambertian source (right).

2. Luminance $L(P, \vec{u}, z)$ defines the quantity of the light emitted from a point P in the direction $\vec{u}$. In the case of a Lambertian light source like the one re-emitted by the *SRS-99 spectralon*® surface (schematic representation in the right part of Fig. 3.8), the luminance is (i) equal in all the directions, *i.e.*, $L(P, \vec{u}, z) = L(P, z)$ and (ii) distributed in the entire half-space. Combining both conditions, the luminance is related to aforementioned irradiance and standard reflectance R by the formula:

$$L(P, z) = \frac{R}{\pi} I(P, z) \tag{3.12}$$

3. Then, an infinitesimal integral calculation is performed to determine the fraction of the flux re-emitted by the standard which can be captured by the detection fiber. Analogously to the elementary surface dA, we introduce the surface element $dA' = r'dr'd\theta'$ located on the collecting surface S_{DF} of the DF, *i.e.*, inside a disk centered at $O'(0, D_n, z)_{\mathcal{R}}$ (in Cartesian coordinates) around point $P'(r', \theta', 0)_{\mathcal{R}'}$ defined by its cylindrical coordinates in the secondary system $\mathcal{R}'(O', \vec{u_x}, \vec{u_y}, \vec{u_z})$). From the radiometry laws, the infinitesimal flux dF_{det} coming from the surface dA captured by the surface dA' is given by the formula:

$$dF_{det} = L(P, z) dA d\Omega \cos(\phi) \tag{3.13}$$

Where ϕ is the angle between the normal to the surface and the direction $\vec{u}_{PP'}$ provided by the line connecting the source point P and the detection point P', and $d\Omega$ is the solid angle

defined as the ratio between the projected surface of dA' on $\vec{u}_{PP'}$ direction and the square of distance d between P and P' *i.e.*, $d\Omega = dA' \cos(\phi)/d^2$. Considering all the surface elements of the source and the detection surfaces, the detected flux F_{det} is obtained after a double integration on $A_{SRS-99}(z)$ and S_{DF} surfaces:

$$F_{det}(z, R) = \iint dF_{det} \tag{3.14}$$

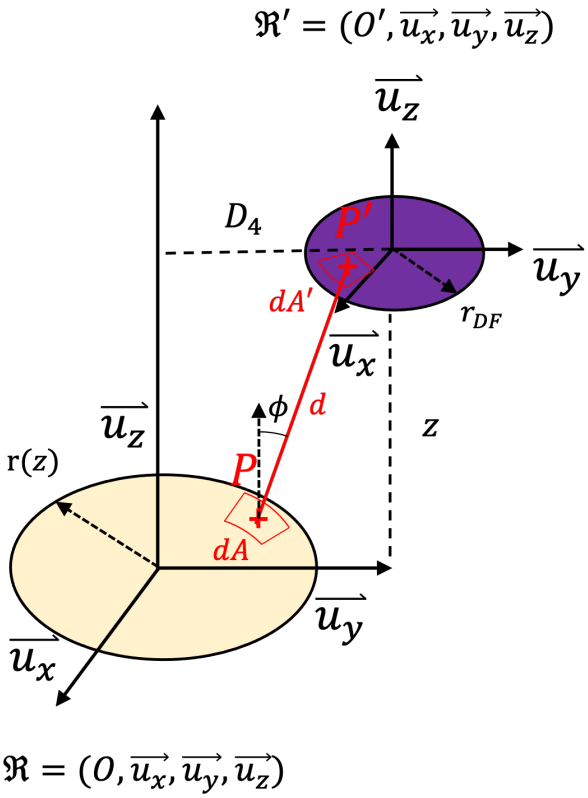

Figure 3.9: Geometrical representation of the reflected light configuration with the parameters involved in radiometric calculation of $c_{D_n}(z, R)$.

In practice, the numerical calculation of the double integrals in Eq. (3.8) was performed using *Matlab* with a discretization of the surfaces $A_{SRS-99}(z)$ and S_{DF} into 900 elements corresponding to 30 angular and 30 radial divisions. The angular detection condition (ϕ should verify $\phi < \arcsin(NA_{DF})$) is considered in the numerical sum, to allow or not the elementary flux (*cf.* Eq. (3.13)) to enter the fiber, and the transmission is weighted according to the Fresnel transmission coefficient in intensity R_F, such as:

$$R_F = \frac{n_{DF}\cos(\phi')}{n_{air}\cos(\phi)} t^2 \quad \text{where} \quad t = \frac{2n_{air}\cos(\phi)}{n_{air}\cos(\phi) + n_{DF}\cos(\phi')} \tag{3.15}$$

With ϕ' linked to ϕ according to the refraction Snell–Descartes law ($n_{air}\sin(\phi) = n_{DF}\sin(\phi')$).

3.5.3.2 Numerical simulation-based calculation of the correction factor

In order to cross-validate the radiometric calculations undertaken so far with numerical simulations of photon propagation, a Monte Carlo (MC)-based algorithm of Ray-Tracing (described in

Algorithm 6) was designed to compute $c_{D_n}(z, R)$:

Result: calculation of $c_{D_n}(z, R)$
Define number *photonNb* of photons launched;
Initialize number *detPhotonNb*=0 of detected photons;
for *every photon launched* **do**
  Random drawing of point P on $A_{SRS-99}(z)$ surface (According to flux distribution [a]);
  Random drawing to decide if the photon is re-emitted (According to R value);
  if *photon is re-emitted* **then**
    Random drawing to defines its $\vec{u}$ direction [b];
    Propagation from point P toward $\vec{u}$ until a height z;
    if *photon inside* [c] *annular surface of median radius* D_n *and thickness* $2r_{DF}$ **then**
      Increment *detPhotonNb* by R_F [d];
    else
      Photon is not counted;
    end
  else
    Photon is not counted;
  end
end
Define the area correction factor f (Ratio between S_{DF} and annular surface);
Calculate $c_{D_n}(z, R) = f \times detPhotonNb/photonNb$;

Algorithm 6: MC simulation to determine the fraction of light reaching DF.

[a] see left sub-figure in Fig. 3.10 that represent the real flux distribution appearing in left sub-figure in Fig. 3.8.
[b] see explanation below and middle and right sub-figure in Fig. 3.10.
[c] angular detection condition related to NA_{DF} are also considered.
[d] see Fresnel factor definition in Eq. (3.15).

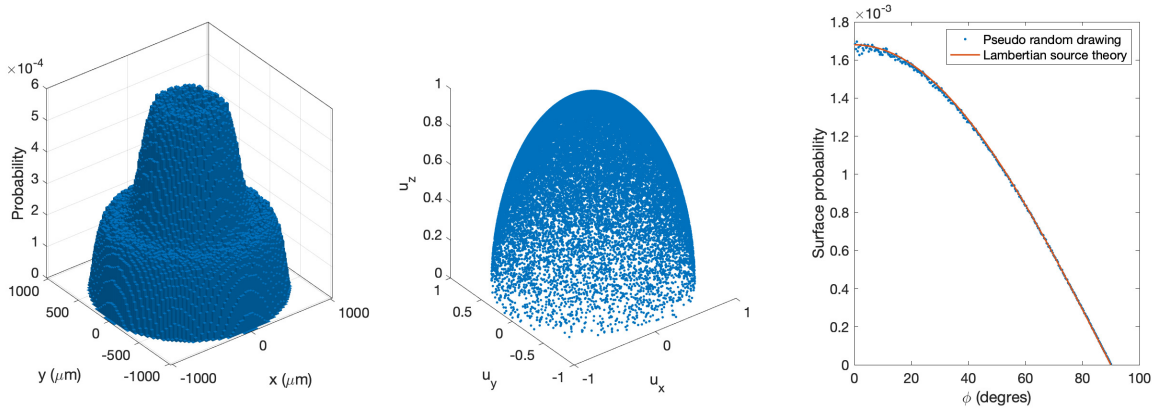

Figure 3.10: Light flux distribution on the reflectance standard used for Monte Carlo calculation (left), representation of the random drawing of the unit directing vector $\vec{u}$ appearing in algorithm 6 and Eq. (3.16) (middle), and verification of the Lambertian cosine behavior in ϕ distribution (right).

Some details are provided here to explain the light re-emission direction $\vec{u}$ random drawing to simulate a Lambertian bidirectional reflectance distribution [Prokhorov 2003]. The random

draw which allows to reproduce such a reflection is made thanks to two pseudo random angles θ (azimuthal angle) and ϕ (polar angle) obtained from two $[0-1]$ uniform variables u_θ and u_ϕ such as:

$$\begin{cases} \phi = \arcsin(\sqrt{u_\phi}) \\ \theta = 2\pi u_\theta \end{cases} . \tag{3.16}$$

3.5.3.3 Comparison of the theoretical photometric results with the Monte Carlo simulation ones.

In this section, $c_{D_n}(z, R = 0.99)$ values obtained using radiometry calculation (see section 3.5.3.1) and MC ray-tracing approaches (see section 3.5.3.2) are compared. Fig. 3.11 sums up those results (continuous line for radiometry and dashed-line for MC) for the 4 SD distances of our *SpectroLive* device and for z values (calibration vertical distance) in the range of $[0 - 2.10^4]$ μm. One can observe a typical curve shape for all the D_n: the z distance is firstly too short to allow the optical flux to reach the DF, before reaching an optimal position. This position shifts toward greater z when D_n increases. Both sets of curves are globally in high agreement, which allows us to validate both calculation techniques. However, slight differences can be seen, especially for the short SD distances. This is explained by the geometrical approximation of considering annular detected surfaces rather than real point DF (this approximation was already quantified in appendix A.1). Subsequently, we will consider as reference value the curves of $c_{Dn}(z, R)$ obtained by photometry calculation.

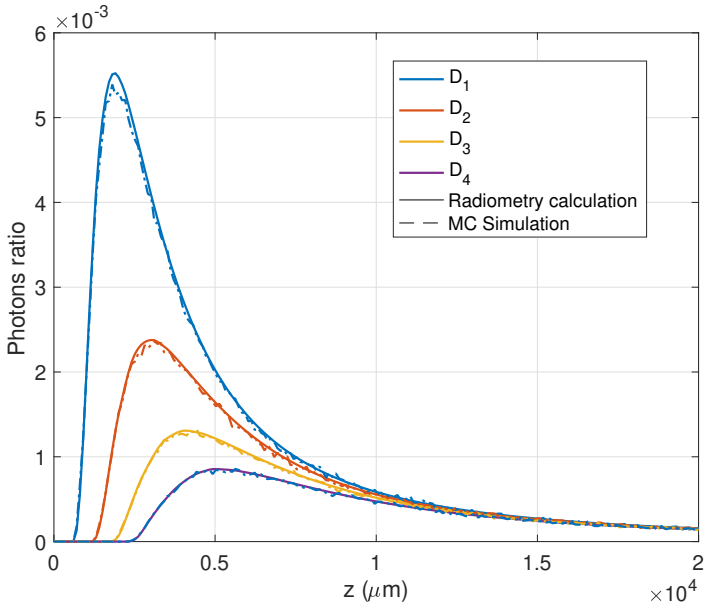

Figure 3.11: Photometric (continuous line, see section 3.5.3.1) and Monte Carlo (dashed-line, see section 3.5.3.2) calculations of the $c_{D_n}(z, R)$ factor.

3.5.4 Experimental validation

3.5.4.1 General presentation of the experimental procedure

This section describes the experimental approach developed to calculate the correction factor from SR-DR measurements on optical phantoms. A block diagram representation of this experimental factor calculation method is provided in Fig. 3.12. As noticeable in Eq. (3.9) the correction factor is defined as the ratio between the spectrum of DR (expressed in photon ratio) and those calculated with the current method described in section 3.5.2 for the same probed medium. In order to obtain SR-DR spectra in photons ratio unit, we naturally used our photon transport simulation modified to match spectrally and geometrically our real device *SpectroLive* (see section 1.5.2). From the MC simulations, the output unit of simulated spectra $DR_{Dn}^{sim}(\lambda)$ is intrinsically the photon ratio between detected and emitted light (or photons weights). The geometrical and optical parameters of the medium required for this simulation are its thickness, the absorption $\mu_a(\lambda)$ and scattering $\mu_s(\lambda)$ coefficients, as well as the anisotropy factor $g(\lambda)$. The experiment then consists in making a mono-layer liquid optical phantom, and to divide its volume into two parts: the majority intended for a measurement of SR-DR with the *SpectroLive* device, and the rest of the volume dedicated to Inverse Adding Doubling (IAD) [Prahl 2011] optical properties characterization from Double Integrating Sphere (DIS) measurements. The raw signal $S_{Dn}^{skin}(\lambda)$ acquired on the optical phantom, associated to $S_{Dn}^{stand}(\lambda, z, R)$ (*cf.* Eq. (3.8)) for several probe to *spectralon*® distances z allow for calculating $DR_{D_n}(\lambda, z, R)$ ($R = 0.99$ in our experiment). In parallel, the IAD algorithm provides us with an estimation of the OP of the liquid phantom which is used to design the simulation corresponding to $S_{Dn}^{skin}(\lambda)$ acquisition, *i.e.*, the *SpectroLive* probe immersed in semi-infinite optical phantom. The simulation finally provides the $DR_{Dn}^{sim}(\lambda)$ spectra, allowing to obtain the following experimental factor:

$$c_{D_n}^{exp}(z, R) = \frac{DR_{Dn}^{sim}(\lambda)}{DR_{D_n}(\lambda, z, R)} \tag{3.17}$$

3.5.4.2 Optical phantom description

A 500 mL liquid optical phantom made of Methylen Blue (MB, M9140, *SigmaAldrich*, Missouri, USA) at a concentration of 8 μM (M for molair *i.e.* , $mol.L^{-1}$) and 4% (vol/vol) *Intralipid*®20% (68890-65-3, *SigmaAldrich*, Missouri, USA) was poured into (i) a custom-made glass (*Borofloat33*, *Schott*, Germany) cell of 4 mL volume and 1 mm thickness, and (ii) a square black silicone mold 50 mm side. The manufacturing procedure for this phantom is that detailed in Aernouts *et al.* [Aernouts 2013], which also provides the optical properties of interest determined by DIS-IAD. This allows us to compare our estimates with a reference in the literature. The liquid sample in its two previously described forms appears in Fig. 3.13. The refractive index of this sample, mostly containing distilled water, was set at $n = 1.33$.

3.5.4.3 Double integrating sphere measurements and inverse adding-doubling-based estimation of phantom optical properties

Total reflectance and transmittance spectra were acquired in the range $[500 - 750]$ nm in our DIS set-up. Because of technical issues concerning unscattered transmittance measurements, the value of the anisotropy factor g was not estimated, but set according to the analytical formula from Michels *et al.* [Michels 2008], available in Aernouts *et al.* [Aernouts 2013]. The 6 measurement

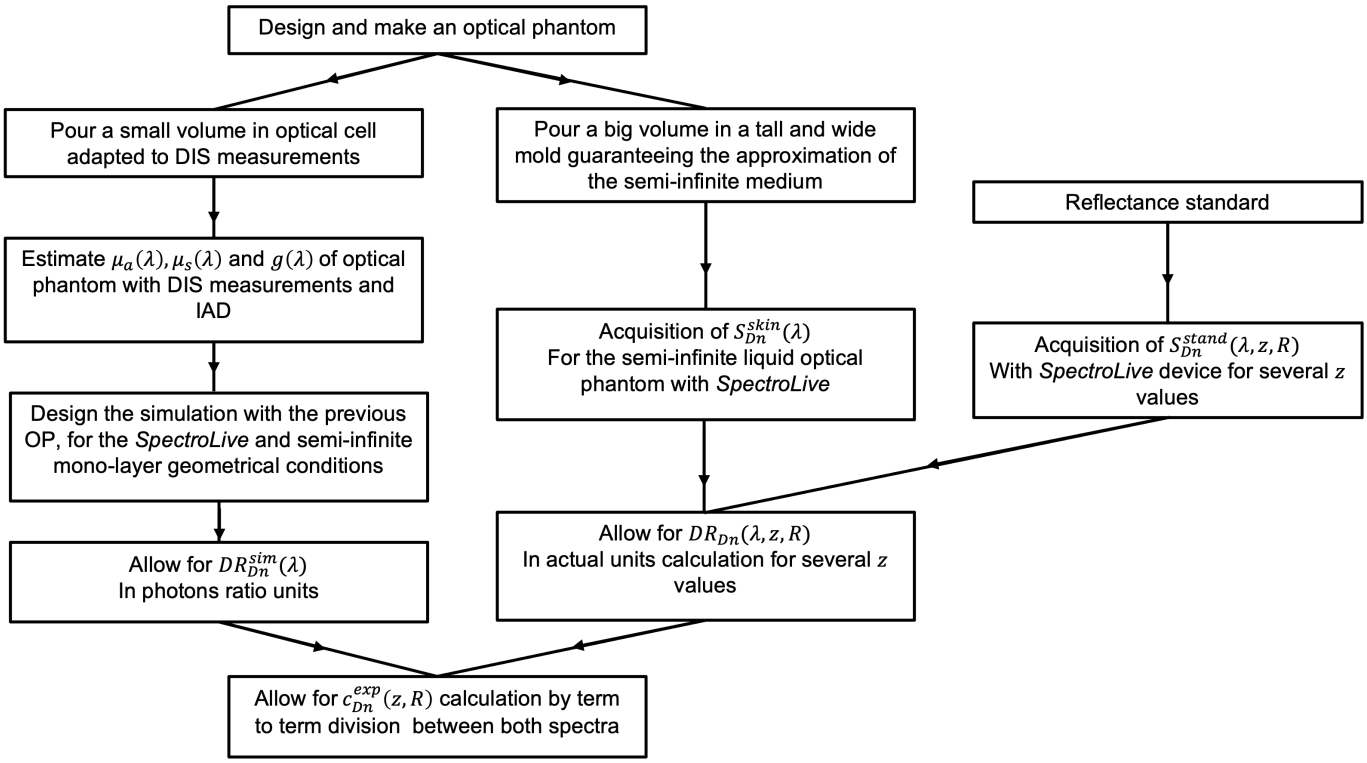

Figure 3.12: Block diagram representation of the experimental methodology leading to experimental correction factor $c_{D_n}^{exp}(z, R)$ calculation.

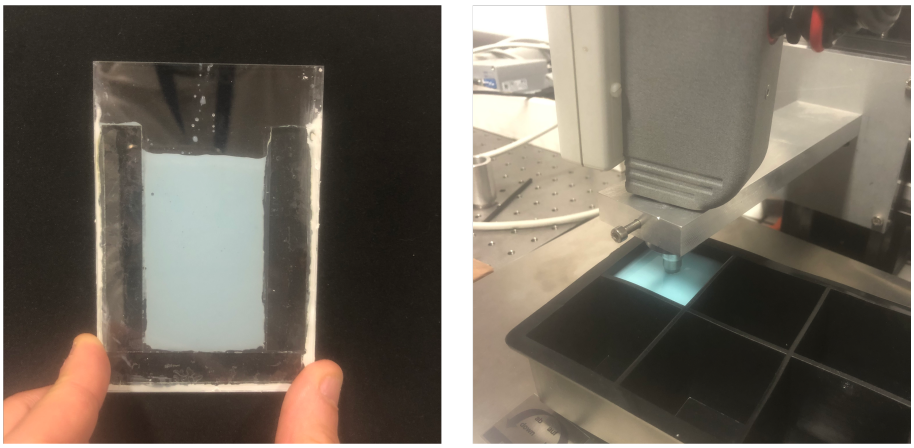

Figure 3.13: Liquid optical phantom poured in a glass cell for DIS measurements (left) and in a square black silicone mold for the acquisition with *SpectroLive* device (right).

results are given in Fig. 3.14. In the $\mu_a(\lambda)$ spectrum, sharp absorption peaks can be seen in the $[600 - 700]$ nm range from MB, while the order of magnitude and the spectral decay of $\mu_s(\lambda)$ agrees with those from literature [Aernouts 2013]. As indicated earlier, there is no repeatability uncertainty on $g(\lambda)$ because it does not result from measurements.

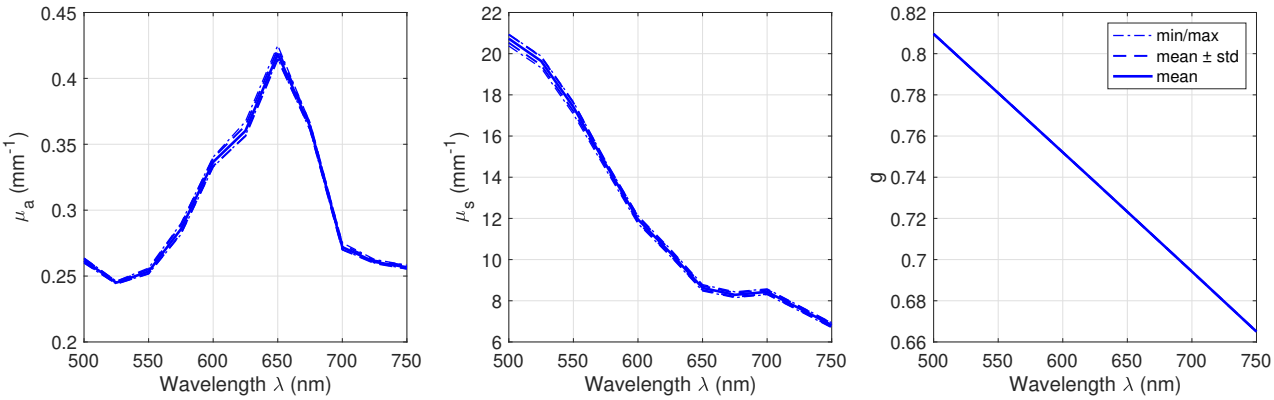

Figure 3.14: Estimation of phantom OP from IAD calculation. Average ± standard deviation representations from 6 measurements is on the left and center graphs for μ_a and μ_s, respectively. There is no uncertainty on g (right) because it does not result from measurements, but from an analytical expression taken from the literature [Aernouts 2013, Michels 2008].

3.5.4.4 Impact of the calibration measurement on DR spectra

In accordance with Eq. (3.8), $S_{Dn}^{skin}(\lambda)$ spectra were acquired for the optical phantom. Ten acquisitions were carried out and averaged by repetitively immersing the *SpectroLive* device optical probe into the liquid phantom (see right picture in Fig. 3.13). Concerning the signals acquired on the reflectance standard $S_{Dn}^{stand}(\lambda, z, R)$, 76 raw spectra were collected for z distances lying in a range of $[0 - 15000]$ μm, with a 200 μm Δz step. The *SpectroLive* probe was fixed on a vertical micro-metric translation stage above the $SRS - 99$ reflectance standard. Those acquisitions allow then to finally get the $DR_{D_n}(\lambda, z, R)$ spectra.

After following the experimental protocol earlier described, the DR spectra obtained from the SRS-99 standard and expressed in the actual unit by applying the formula appearing in Eq. (3.8) were represented as a function of SD distances and for different distances z between the reflectance standard surface and the probe tip (see Fig. 3.15). Spectra acquired closer to *spectralon*® contact ($z < 3800$ μm) are not represented, because of infinite values caused by the very weak, *i.e.*, almost null $S_{Dn}^{stand}(\lambda, z, R)$ signals (the height of DF associated with long SD distances is not sufficient to meet the conditions of light entry into fibers). From the $DR_{Dn}(\lambda)$ curves in Fig. 3.15, one can notice that the z calibration optimal distance, *i.e.*, the one that satisfies the highest DR amplitude and the best signal to noise ratio considering the four SD distances, is in the range $[6000 - 10000]$ μm.

3.5.4.5 Comparison between simulated and normalized acquired spectra

Numerical simulations were run considering the geometrical features of the SR-DRS probe of the *SpectroLive* device (see Fig. 1.20) and using a mono-layer semi-infinite model of the optical phantom with $\mu_a(\lambda)$ and $\mu_s(\lambda)$ values estimated from the DIS-IAD procedure (see section 3.5.4.3). In order to compare the spectral shape of the $DR_{Dn}(\lambda)$ signals obtained from simulations and through acquisition, a normalization step was performed consisting in imposing maximum (respectively minimum) value to 1 (respectively to 0) in the $[500 - 700]$ nm range. Resulting curves for the four SD distances, are given in Fig. 3.16. Each plot also provides the means ± standard

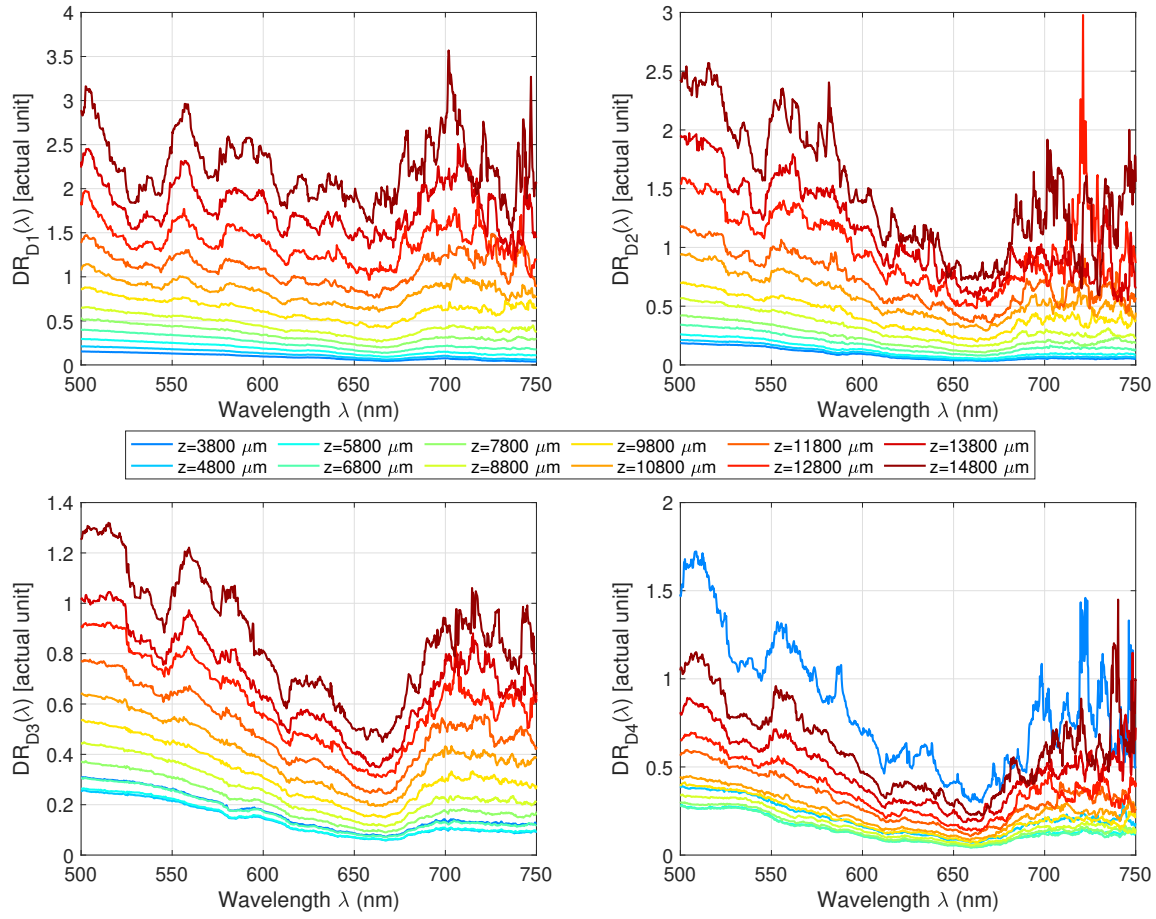

Figure 3.15: Diffuse reflectance spectra $DR_{D_n}(\lambda, z, R = 0.99)$ obtained for 4 SD distances $D_{1,2,3,4} = 400, 600, 800, 1000\ \mu m$ and for 12 standard-to-probe calibration distances $z = 3800, ..., 14800\ \mu m$ expressed in their actual experimental unit.

deviation representation of normalized *SpectroLive* signals $DR_{D_n}(\lambda, z, R)$ for the 21 "valid" z calibration heights between 6000 and 10000 μm (*cf.* explanations in section 3.5.4.4). Although some differences are noticeable, in particular the red-shift of the absorption peak (660 nm) of the MB for the real signals, the correspondence of spectral shapes is satisfying. Non-normalized simulated spectra $DR^{sim}_{Dn}(\lambda)$ expressed in photons ratio also appear in top-right insert.

3.5.4.6 Experimental calculation of the standardization factor

Following the protocol described in Fig. 3.12, the final step to perform is to determine the term-to-term quotient of the experimental spectra $DR_{D_n}(\lambda, z, R)$ (the non-normalized ones shown in Fig. 3.15) to the simulated ones $DR^{sim}_{Dn}(\lambda)$ (also non-normalized, appearing in Fig. 3.16 top-right insert) using Eq. (3.17). Spectra from the device were re-sampled in 48 points between 500 and 735 nm to match both simulation and experiment DR vector sizes and to allow for the division. In the approach taken so far, the assumption of the independence of the wavelength

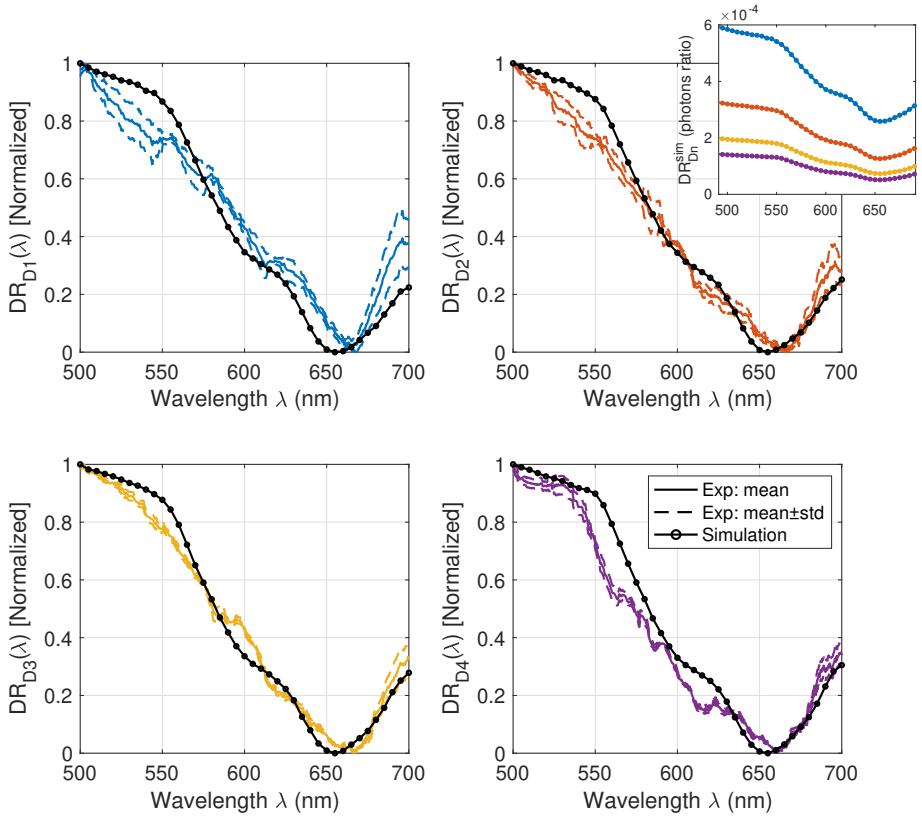

Figure 3.16: Normalized experimental (mean ± std representation) and simulated (black) DR spectra obtained at the 4 SD distances D_n. Non-normalized simulated spectra $DR^{sim}_{Dn}(\lambda)$ expressed in photons ratio appear in top-right insert.

was made during the theoretical calculations of the standardization factor, that is why λ does not appear in $c_{D_n}(z, R)$. However, the aforementioned term-to-term quotient provides vectors of 48 components (function of z) leading to slight differences from a wavelength to another due to the non-perfect superposition of the simulated and clinical spectra (see Fig. 3.16). On the one hand to overcome this dependence on λ, but also to take into account the existing variations between the wavelengths, we decided to sum up the $c^{exp}_{D_n}(z, R = 0.99)$ by a deviation calculation with these 48-components vectors. The results appear in Fig. 3.17 for the 4 SD distances, with the theoretical photometric calculation (*cf.* section 3.5.3.1) in continuous line.

The correspondence between the shape and the order of magnitude of the correction for the theoretical and experimental curves is encouraging. However, visible differences can be noticed, particularly in terms of amplitudes for D_3, as well as a z-shift for the farthest D_4 SD distance. Among the possible explanation is the wavelength independence assumption. Indeed, in theoretical calculations, none of the parameters $NA_{DF/SF}$ (numerical aperture of DF and SF), n_{DF} (DF refractive index) and R (reflectance of the standard) considered any chromatic behavior. The second important source of discrepancy concerns the geometric approximations of the theoretical calculation. This one was considered as "perfect", *i.e* that the center-to-center SD distance was the D_n distances, and that the optical axes of DF and SF were parallel. In reality, the DF of the SR-DRS probe are arranged in concentric circles around the SF and held together with an epoxy

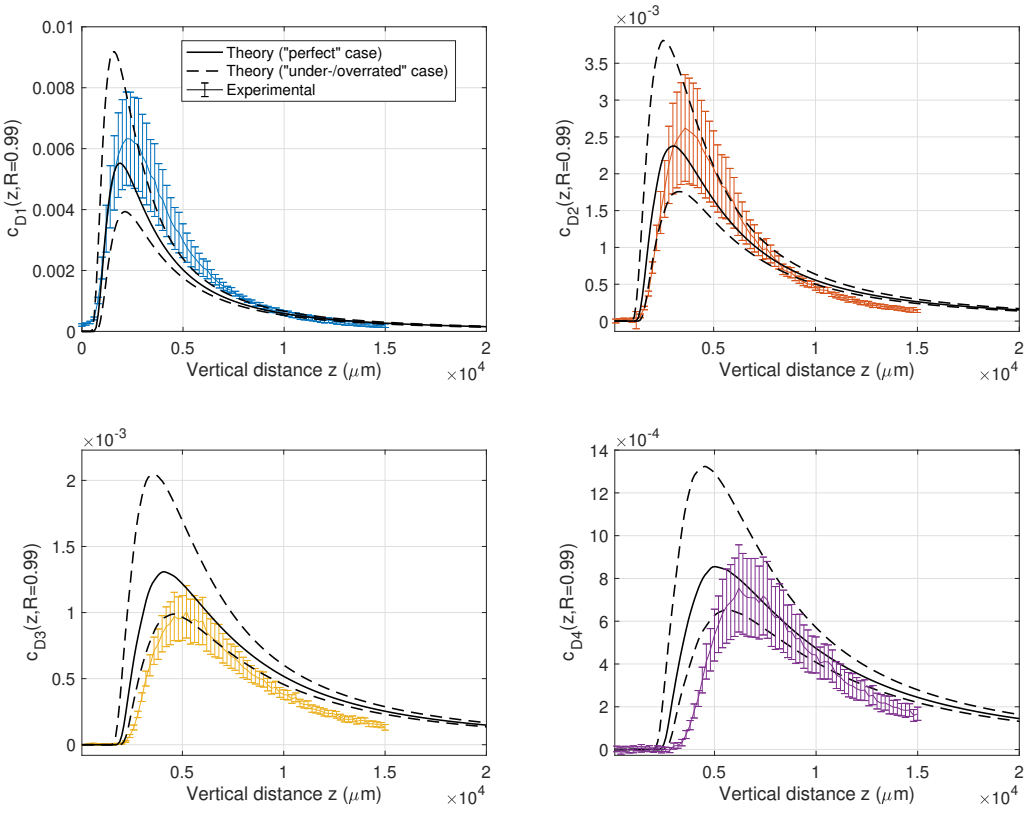

Figure 3.17: Comparison between experimental and theoretical values of $c_{D_n}(z, R = 0.99)$ for the 4 SD distances. The experimental representation synthesizes (by averaging and calculating the standard deviation) the 48 wavelengths for which the quotient was calculated. Continuous line is for the "perfect" case, whereas dashed-lines are for "underestimated" and "overestimated" cases (*cf.* Eq. (3.18)) which gives the spread of this factor by considering the possible geometric errors of the real optical probe.

resin subsequently sanded to eliminate the interface between the end of the fibers and the probed medium.

To verify this second assumption, two supplementary radiometry calculations were conducted to quantify how those geometrical uncertainties can have an impact on $c_{D_n}(z, R)$. The first one correspond to an "underestimated" collection of light, *i.e.*, with (i) the SF and DF optical axes slightly convergent (which can at first glance be regarded as an increase of NA_{DF}) and (ii) an effective SD distance slightly smaller than the "perfect" case. Similarly, the case "overestimated" was studied using slightly divergent optical aperture and larger SD distances. The geometrical features we change in the radiometry calculation (see section 3.5.3.1) to get those opposite situations are in both cases:

$$\begin{cases} NA_{DF}^{over} = 0.24\ (+9\%) & NA_{DF}^{under} = 0.20\ (-9\%) \\ D_n^{over} = D_n - \sigma_{Dn} & D_n^{under} = D_n + \sigma_{Dn} \end{cases} \tag{3.18}$$

For the "overestimated" and "underestimated" cases, respectively, and with $\sigma_{Dn} = 30\ \mu m$ the

uncertainty on the position of the detection fibers. It is noticeable in Fig. 3.17 that those two possible geometrical errors have a strong impact on the shape (start of growth, upward slope, peak position and downward slope) and the amplitude of $c_{D_n}(z, R)$, which could indeed partially justify the differences between theory and experimentation.

3.5.5 Conclusion about the standardization factor

The ambition of this section was to define a correction factor able to link the unit of experimentally acquired DR spectra to spectra expressed in photons ratio, *i.e.*, the fraction of detected over emitted light. This factor will not only allow us to compare the spectral shapes of the DR signal (between simulated and experimental spectra, or experimental ones from several devices), but also their amplitude. Obtaining this theoretical factor leads us to quantify the fraction of light collected by a DF during a calibration measurement, *i.e.*, the illumination of *spectralon*® standard (flat spectral behavior) at a given z vertical distance. An experimental protocol involving (i) a liquid optical phantom whose optical properties have been characterized, (ii) a simulation of DR spectra acquisition faithful to the real device, and (iii) finally real acquisitions in this same optical phantom was designed and followed to get an experimental value of such a factor. Despite some small differences explained in part by geometric approximations in the theoretical calculation, the similarity of the experimental and theoretical curves make it possible to validate the calculation model of the factor.

3.6 Conclusion and prospects

After becoming familiar with the inverse problem solving methods used so far to estimate optical properties, *i.e.*, PSO, we wanted to integrate a clinical dimension in our work and also reduce the computation time associated with this optimization process. For that, we decided to integrate the knowledge acquired thanks to our simulation in terms of impact of skin model parameters, as well as depth propagation of photons detected at different wavelengths and different SD distances. This led to an optimization method adapted to the layered structure of the skin where (i) the parameters are isolated in each of the layers successively, and (ii) the least square type cost functions are weighted by a sensitivity factor which penalizes more strongly the couples (λ, D_n) for which many photons have traveled in this isolated layer. The interest of this original approach has been demonstrated in a purely numerical inverse problem for a set of target parameters. Extending these results to other target parameters that synthesize the intra- and inter-individual skin variation should be done to confirm those results before applying in to clinical DR spectra targets. Finally, in order to fully exploit the comparison between simulated and experimentally acquired spectra, and overcome the necessary normalization which have been mandatory up to now, we offered a standardization method for DR spectra. Indeed, theoretical and experimental standardization factor calculation were provided to get signal expressed in photons ratio between collected and sent light, like the numerically acquired ones. It will then be necessary to check the importance of this standardization in improving the inverse problem. This is partly verified in an inverse problem solving from liquid optical phantom in section 4.5.

Chapter 4

A double integrating sphere optical bench to *ex-vivo* cross validate the optical properties estimates

Contents

4.1 Introduction

This chapter deals with the design of a double integrating sphere optical bench developed in parallel with the work presented so far enabling a standardized characterization of the optical properties (absorption and scattering) of biological samples *ex-vivo*. Having started from a scratch bench, we firstly describe here the major stages in the design of this optical bench and the associated validation measurements. Next, we present the results of experiments on optical phantoms to compare the values of OP estimates obtained from the latter reference bench with those estimated from the spectroscopic-based inverse problem solving techniques developed in previous Chapter 3.

4.2 Theory of integrating sphere and inverse adding doubling

This section firstly describes the optical features of integrating spheres, before presenting the IAD method to obtain the OP of *ex-vivo* samples from an optical bench composed precisely of these integrating spheres.

4.2.1 Integrating sphere description

4.2.1.1 Context of use

An integrating sphere is an optical component consisting of a cavity whose interior is coated with a high diffuse reflectance material and has relatively small size of input and output ports. The coating has to be Lambertian, meaning that the incident light is reflected in an isotropic way. For applications in the visible range, the most commonly used coating is white barium sulphate ($BaSO_4$). In the infrared range, the usual coating is gold. The shape of the cavity is usually a sphere. Light beams from any point on the inner surface of the sphere are distributed, due to multiple diffuse reflections, equally to all other points on the sphere regardless of the original direction of light. An integrating sphere can be seen as a light diffuser that conserves power but destroys spatial information. Integrating spheres are typically used as a light source and as an optical power measurement system. They are found in a wide range of optical, photometric, and radiometric measurements, such as quantifying the total light power emitted by a lamp in all directions, measuring the reflection and transmission factors of surfaces, creating a Lambertian light source, measuring accurately the ambient light or finally characterizing a laser beam.

4.2.1.2 Brief technical overview

In our case, the integrating sphere offers a controlled environment adapted to photon flux quantification. Its effectiveness comes from the fact that it is a cavity with a reflectivity ρ very close to 1, which is defined as:

$$\rho = \frac{F_{diff}}{F_{inc}}$$

Where F_{diff} is the photon flux ($J.s^{-1}$) diffused after reflection on the wall while F_{inc} is the incident. Thus, the quasi-totality of photons that enter the sphere have an optical path leading to the photodiode sensor located on the sphere wall (after multiple reflections). The irradiance (*i.e.*, flux divided by area) of the detector is calculated as follows. By not taking into account the direct flux from the source to the sphere (which is the case for the detector since it is masked from the direct flux of the source by a cover and only receives indirect flux) and by neglecting leaks (holes in the sphere), the flux received at any point by the surface of the sphere is the total flux emitted by the light diffused a very large number of times over the sphere. This indirect flux F_{ind} is therefore linked to the flux of the source F_{laser} by the expression:

$$F_{ind} = F_{laser}(\rho + \rho^2 + \rho^3 + ...) = F_{laser}\frac{\rho}{1-\rho} \tag{4.1}$$

This indirect flux hits all the sphere wall surface. To get an information related to the fraction of flux that reach the photodiode, we calculated the irradiance I_{ind} ($W.m^{-2}$) associated to this flux, defined as follow:

$$I_{ind} = \frac{F_{ind}}{S_{sphere}} = \frac{F_{ind}}{4\pi R^2} \tag{4.2}$$

With R the radius of the sphere. This irradiance is independent from the surface location inside the sphere, including the sensitive area of the photo-detector. By coupling (4.2) and (4.1), we finally get:

$$I_d = \frac{\rho}{1-\rho}\frac{1}{4\pi R^2}F_{laser} \tag{4.3}$$

This expression brings the evidence that knowing some parameters about (i) the sphere characteristics and (ii) the photo-sensor features, allows the user to empirically determine the photon flux of the source. By placing the sample in reflection or in transmission configuration on the sample port (see Fig. 4.1) and considering light incidence (collimated or diffuse source), the calculations become quickly less obvious. This work has been done by W.Pickering *et. al.*, and detection power expressions are provided in [Pickering 1992] for a variety of configurations. To quote an example, in the cases of reflectance and transmittance measurements for a collimated excitation (*cf.* the corresponding geometries on Fig. 4.1), the power on the detector $P_{d,T}$ (for transmittance configuration) and $P_{d,R}$ (for reflectance configuration) are linked to the laser power P_{laser} by the formula:

$$P_{d,R} = \frac{\delta}{S_{sphere}}\frac{\rho R_c + R_{cd}}{1-(\rho\alpha + R_d(s/S_{sphere}) + r(\delta/S_{sphere}))}P_{laser} \tag{4.4}$$

$$P_{d,T} = \frac{\delta}{S_{sphere}}\frac{\rho T_c + T_{cd}}{1-(\rho\alpha + R_d(s/A) + r(\delta/S_{sphere}))}P_{laser} \tag{4.5}$$

Where δ is the sensitive detector area. R_c, T_c [1] respectively are the collimated (specular) reflection and transmission factors of the sample with collimated incident light. R_{cd}, T_{cd} are the diffuse reflection and transmission factor of the sample with collimated incident light. α is the area of the sphere wall relative to the total sphere area, taking into account holes for sample and photodiode. R_d is the diffuse reflection factor of the sample with diffuse incident light. r is the reflection factor of the photodiode and finally s is the area of the sample. Putting a shutter between the sample and the detector allows to avoid the collection of the specular light. The terms R_c, T_c present in the numerator of formulae (4.4) and (4.5) then disappear. This addition to the optical assembly enables the detector and source powers to be linked directly. The transmission and reflection factors of the sample can thus be deduced. To sum up, an integrating sphere offers a controlled optical environment in which analytical solutions, based on radiometry calculations, can be proposed.

4.2.2 Inverse Adding Doubling presentation (IAD)

4.2.2.1 IAD presentation

The inverse adding doubling method is an inverse problem solving method based on the Adding-Doubling forward problem. This numerical method, that allows to solve the radiative transport equation in a slab geometry, is more widely explained in [Prahl 1995] and [van de Hulst 1980]. The Doubling method assumes the knowledge of the reflection and transmission properties for a single thin homogeneous layer, and its following dimensionless optical parameters:

$$a = \frac{\mu_s}{\mu_s + \mu_a} \qquad b = \delta(\mu_s + \mu_a) \tag{4.6}$$

[1] We should have written $R_c(\lambda)$ and $T_c(\lambda)$, but to lighten the handwriting, the λ dependency is deliberately omitted. It is the same for the wavelength-dependent parameters that follow.

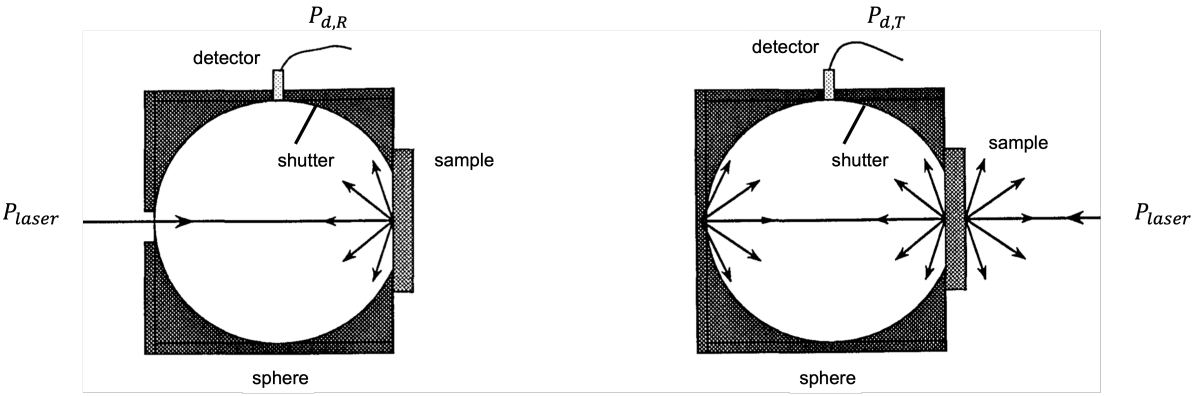

Figure 4.1: Reflection (left) and transmission (right) geometries for sample measurement. Schemes are adapted from Pickering *et al.* paper [Pickering 1992].

a is called albedo whereas b is the optical thickness. To know the transmission and reflection of a slab twice as thick, the method consists in juxtaposing two identical slabs and summing the contribution of each. To get the same information, but for a given thickness, the algorithm repeats the approach until the slab reaches the desired thickness. The Adding method is an extension of the previous one, allowing multi-layered and dissimilar slab, which takes into account the optical management of the interfaces. The IAD technique consists in determining the albedo and the optical thickness of a sample (from which are deduced μ_s and μ_a) from optical measurements (more details are given in 4.2.2.3), like reflectance and transmittance. In [Prahl 1993], Prahl *et.al.* summed up the IAD algorithm including the 4 following steps:

1. Guess a set of optical properties
2. Calculate the reflection and transmission by using the Adding-Doubling method
3. Compare the calculated values with the measured reflection and transmissions.
4. Repeat until a match is made

More information about theory and algorithm use are available in the Prahl documentation [Prahl 2011].

4.2.2.2 *Ex-vivo* tissues characterization by applying IAD

The association of a single or two integrating spheres and the IAD methods is often offered in the literature. Investigation on optical mono-layer [Vincely 2018] and multi-layered [Saager 2010] phantoms have been performed. Optical phantoms bring the advantage of ensuring flatness and homogeneity of the optical properties. Moreover, protocols for the fabrication of optical phantoms, consisting of pure absorbers (like India ink) and pure scatterers (like intralipids), are available in the literature [Spinelli 2014] and provide quite accurate relations linking their concentrations to targeted μ_a and μ_s values.
Among IAD experiments closer to our clinical final application, Dhiraj K. Sardar and Michael L. Mayo studied melanin optical properties, by analyzing samples coming from melanosomes isolated

from the bovine retinal pigment epithelium [Sardar 2001]. Optical characterization based on IAD for stomach mucosa[Bashkatov 2007], or pig subcutaneous adipose tissue were also made using two integrating spheres [Zamora-Rojas 2013].
Finally, some teams studied concrete clinical problems. Firstly, the storage impact on optical characterization was made in [Genina 2009]. Indeed, IAD is an *ex-vivo* method, requiring the sample conservation between the removal time on the patient and the measurement time on the optical bench. The study showed that from one preservation method to another, the reduced scattering coefficient μ_s' can vary by a factor close to 2. Secondly, a recurrent problem for *in vivo* optical biopsy measurements was analyzed with IAD: the impact of the pressure of the probe applied to the patient's skin on the optical characterization [Chan 1996]. It was shown that compared with the no-load controls, there was an increase in absorption (of $\approx$ 100% for 2 $kgf.cm^{-2}$) and scattering (of $\approx$ 150% 2 $kgf.cm^{-2}$) coefficients among most of the compressed specimens.

4.2.2.3 Optical Measurements For IAD

To apply the IAD algorithm, 4 measurements are needed, using one or two integrating spheres, in order to get the wavelength dependent optical parameters $\mu_a(\lambda)$, $\mu_s(\lambda)$ and $g(\lambda)$:[2]

Thickness: The sample thickness δ is determined experimentally using a caliper.

Reflectance: The reflectance $M_R(\lambda)$ is defined as the fraction of light re-emitted in the source-side half-space for normal and collimated illumination. It is composed of the so-called specular surface reflectance, which is eliminated in the sphere thanks to an optical trap, and the diffuse reflectance. The latter is composed of the photons having penetrated the sample medium, and which, by a succession of scattering events, have been re-emitted in the half-space on the source side. The schematic representation in Fig. 4.2 show the typical paths of photons contributing to this quantity. The sphere is used as a cavity, allowing all those backscattered photons to finally reach the detector.

Transmittance: The transmittance $M_T(\lambda)$ is defined as the fraction of light re-emitted in the half-space on the opposite side of the source for normal collimated illumination. It is composed of the photons passing through the sample after a succession of scattering events. Once again, the sphere acts as a cavity. A representation of those photons is also presented in Fig. 4.2.

Collimated transmittance: The collimated transmittance (or unscattered transmittance) $M_U(\lambda)$ is a part, often a tiny part, of $M_T(\lambda)$. It concerns the photons that have passed through the sample while keeping the incident direction imposed by the collimated laser illumination. A schematic representation of those photons are presented in Fig. 4.2. This measurement does not require an integrating sphere, but only a diaphragm (or aperture) optically aligned with the laser and the photo-detector to ensure the only collection of ballistic photons.

[2] In 1.2.2.2, g was considered independent from λ, because its variation was considered negligible in the visible range for biological medium. The IAD process treats the data for each wavelength, that is why the wavelength dependency appears here.

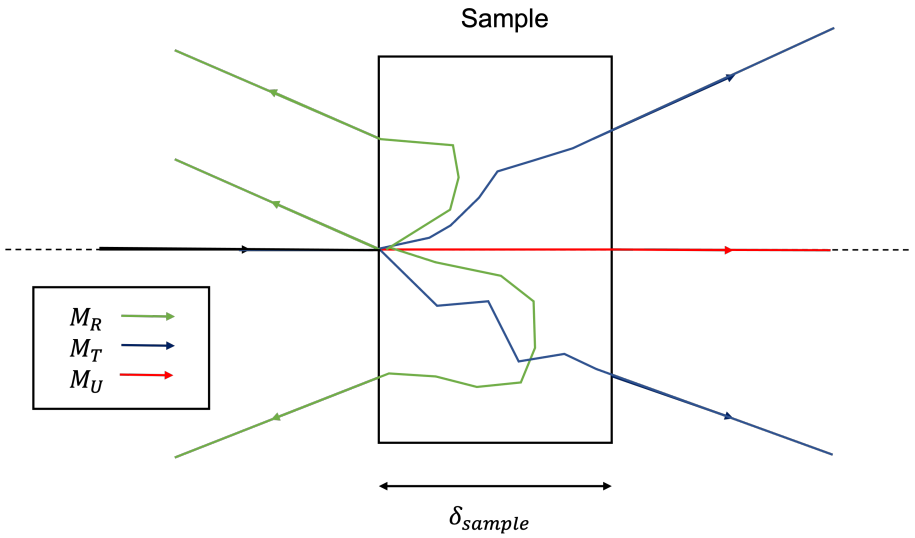

Figure 4.2: Schematic representation of the reflectance, transmittance and unscattered transmittance.

4.3 Double Integrating Sphere (DIS) optical bench description and experimental procedure

Starting from a complete description of the optical set-up, this section also describes the experimental protocol including the optical measurements and the IAD configuration to get the OP of biological samples.

4.3.1 Optical bench description

The light source used is a super-continuum laser (*SuperK Fianium FIU15* manufactured by *NKTPhotonics*) tunable in power and wavelength (spectral range $375 - 825$ nm using a monochromator featuring a minimum spectral width of 10 nm at half height). The integrating spheres are a *LabSphere* product, referenced as *RT-060-SF*. Its diameter is 6 inches, and its internal coating is *Spectraflect*, of reflectivity close to 0.96 in our spectral range. Finally, the detectors are *Hamamatsu's H7827* photo-multipliers. They are connected to an acquisition card (*National Instrument*) connected to computer on which a *Labview* program has been developed by Clarice Perrin-Mozet and myself to automate laser control sequences and PM signals acquisition (more details on this interface are offered in appendix D). An overview of the optical set-up is shown in Fig. 4.3.

4.3.2 Experimental protocol

4.3.2.1 Reflectance and transmitance measurements

Those measurements are related to top picture given in Fig. 4.3. The idea of obtaining transmittance and reflectance powers by applying formulas (4.5) and (4.4) is a bit idealistic. Indeed, in addition to requiring very precise knowledge of the geometric parameters of the integrating sphere, the knowledge of the power of the incident laser light at each wavelength is also needed.

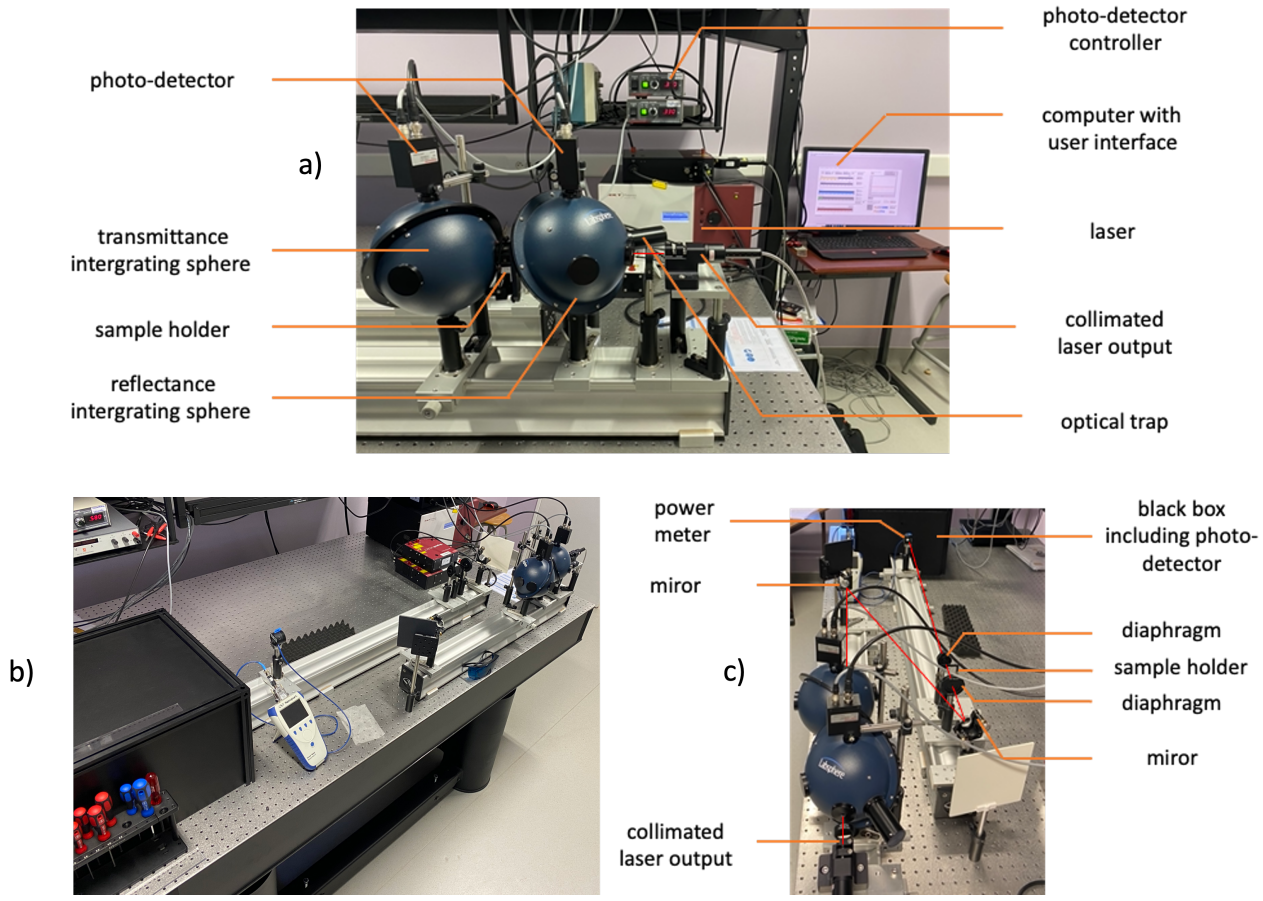

Figure 4.3: Overall view of the optical bench (b)), and zoom on reflectance and transmittance measurements part using DIS (a)) as well as on the collimated transmittance arm (c)).

P_{laser} is moreover dependent on several parameters such as temperature variation or even wear. To avoid this acquisition chain study, which is a source of error, we followed the protocol developed in [Prahl 2018] related different acquisition geometries illustrated in Fig. 4.4 including the associated following steps:

1. We separate both spheres, open the exit port so that the laser beam passes through the reflectance sphere and measure the output voltage. By keeping the Fig. 4.4 writing conventions, we obtain the tension $R_2(0,0,0,0;\lambda)$ (see Fig. 4.4 d)) at every wavelength of the spectrum of interest.

2. We reattach the two spheres (see Fig. 4.4 e)), still leaving the gap between them, before turning off the laser, then measuring the dark voltage in the transmittance sphere $T_2(0,0,0,0;\lambda)$.

3. Keeping the same geometry, we simply turn on the laser, to measure the transmittance of vacuum (air to be more rigorous) $T_2(0,0,1,1;\lambda)$ (see Fig. 4.4 c)), corresponding to the spectrally flat 100% transmittance.

4. We separate the two spheres again and place the reflectance standard (of reflectance r_{std}) at the exit of the first sphere to measure $R_2(r_{std},r_{std},0,0;\lambda)$ (see Fig. 4.4 b)), corresponding to

the spectrally flat $r_{std}\%$ transmittance.

5. Finally, we connect our two spheres by placing the sample to be characterized between them (see Fig. 4.4 a)). We then measure both voltages of the reflected light $R_2(r_s^{direct}, r_s, t_s^{direct}, t_s; \lambda)$ and transmitted light $T_2(r_s^{direct}, r_s, t_s^{direct}, t_s; \lambda)$.

The reflectance and transmittance of the sample can be calculated once the acquisitions are completed according formulas:

$$M_R(\lambda) = r_{std} \frac{R_2(r_s^{direct}, r_s, t_s^{direct}, t_s; \lambda) - R_2(0,0,0,0;\lambda)}{R_2(r_{std}, r_{std}, 0, 0; \lambda) - R_2(0,0,0,0;\lambda)} \tag{4.7}$$

$$M_T(\lambda) = \frac{T_2(r_s^{direct}, r_s, t_s^{direct}, t_s; \lambda) - T_2(0,0,0,0;\lambda)}{T_2(0,0,1,1;\lambda) - T_2(0,0,0,0;\lambda)} \tag{4.8}$$

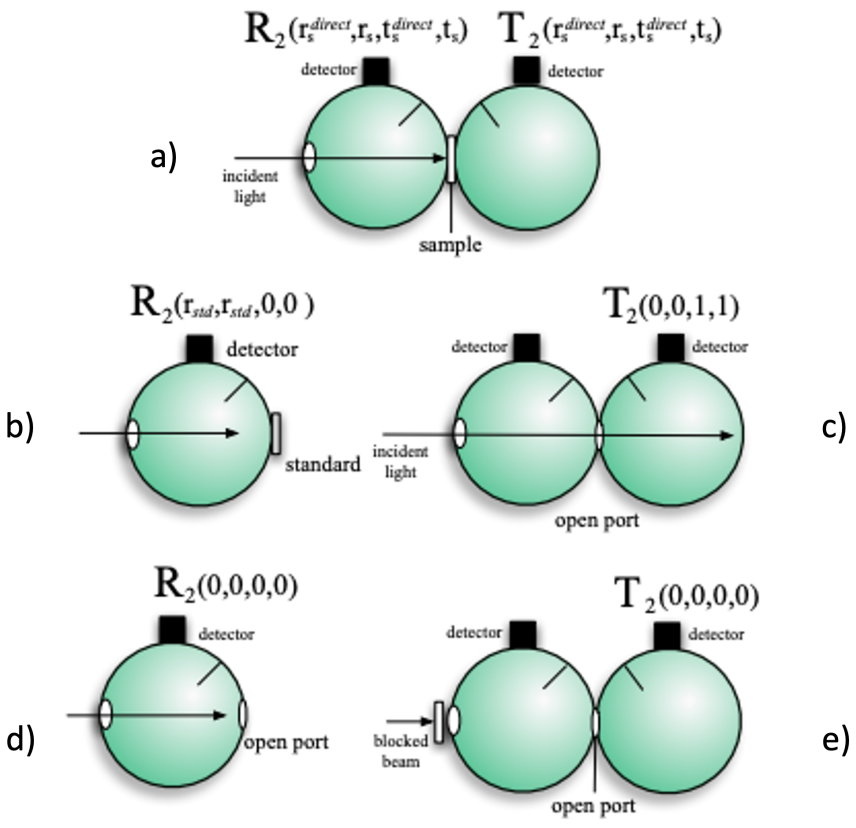

Figure 4.4: Schematic representation of the 6 measurements configuration to perform to calculate the reflectance M_R and transmittance M_T of the sample. This picture was taken from [Prahl 2011].

4.3.2.2 Unscattered transmittance measurement

This measurement is related to picture given in Fig.4.3 c) configuration and results from a 3 steps procedure, where notations are introduced in the Fig. 4.5:

1. We firstly let the sample holder empty, before turning on the laser, then measuring the voltage $U_{100}(\lambda)$ in the light isolating black box under direct illumination corresponding to the 100% value of collimated transmittance.

2. After having placed the sample so that it is illuminated with normal incidence, we simply turn off the laser, to measure the dark $U_0(\lambda)$, corresponding to dark voltage acquisition.

3. Finally, the laser is switched on to acquire the signal $U_s(\lambda)$ associated to unscattered transmittance trough the sample.

At the end of these acquisitions, we can calculate the ballistic contribution in transmittance for every wavelength of interest $M_U(\lambda)$ according formula:

$$M_U(\lambda) = \frac{U_s(\lambda) - U_0(\lambda)}{U_{100}(\lambda) - U_0(\lambda)} \tag{4.9}$$

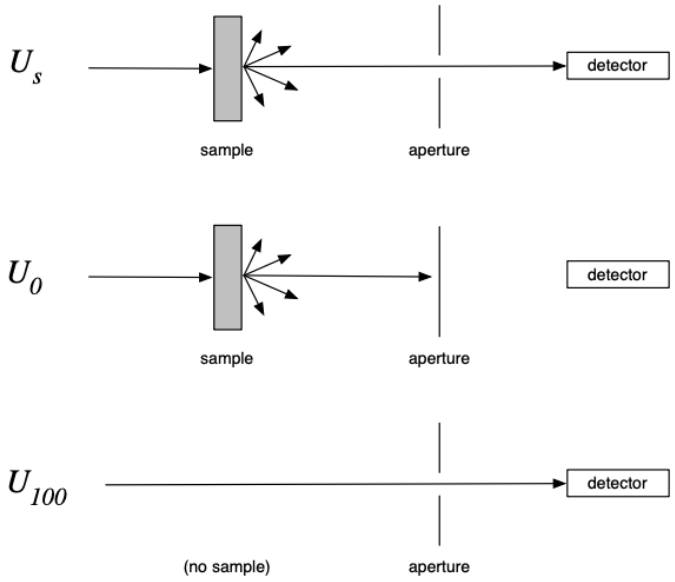

Figure 4.5: Schematic representation of the 3 measurements that have to be done to calculate the unscattered transmittance M_U of the sample. This picture was taken from ref [Prahl 2011].

For unscattered transmittance calculation as well as total reflectance and total transmittance, the measurement is valid only if the photo-detector provides output intensity proportional to optical flux (see Eq. (4.8), (4.7) and (4.9)). The linearity of this response has been tested and results are provided in the appendix D.

4.3.2.3 Sample positioning

For biological sample: The sample must be sandwiched between two glass slides before being positioned between the two spheres (see Fig. 4.3). The refraction and reflection effects at the air/glass and glass/ sample interfaces are taken into account in the algorithm by providing the glass index (for each λ) to apply Snell-Descartes laws. The material we used is a 1 mm thick

optical glass *Borofloat 33* manufactured by the German company *Schott*. The pressure imposed by the glass (compressed by the spring of the integrating sphere sample holder) raise questions about thickness measurements and also optical properties modifications caused by this pressure [Shangguan 1998]. Unfortunately, we do not perform measurements on clinical biological samples because of time constrains and had to restrict ourselves to measurements on optical phantoms, for which the holder we have developed is described in the following paragraph.

For optical phantoms: To quantify the error caused by the inaccuracy of sample thickness measurement, it was decided to carry out a study to investigate how it affects the optical properties estimation. For that, a 3 mm thick mono-layer optical phantom of agarose gel, intralipids and India ink was made and positioned on the DIS optical bench. M_T and M_R were acquired as described earlier. Then, with those vectors, several IAD calculation were done by varying the considered sample thickness so that $\delta \in [2.1 - 3.9]$ mm. By considering the optical properties calculated for the measured thickness as the truth (*i.e.*, $\mu_{a,truth}$ and $\mu'_{s,truth}$ for $\delta_{truth} = 3$ mm), the absolute error $|\mu_x - \mu_{x,truth}|$ was calculated for every other thickness. Those errors are plotted in Fig. 4.6, in which abscissa is the thickness deviation $\Delta z = \delta - \delta_{truth}$. The vertical dashed lines on the x-axis represent the imprecision on the measurement of the sample thickness estimated at 100 μm, while the horizontal lines show the consequences on the measurement of the optical coefficient. In each case, the associated error is about 5 %.

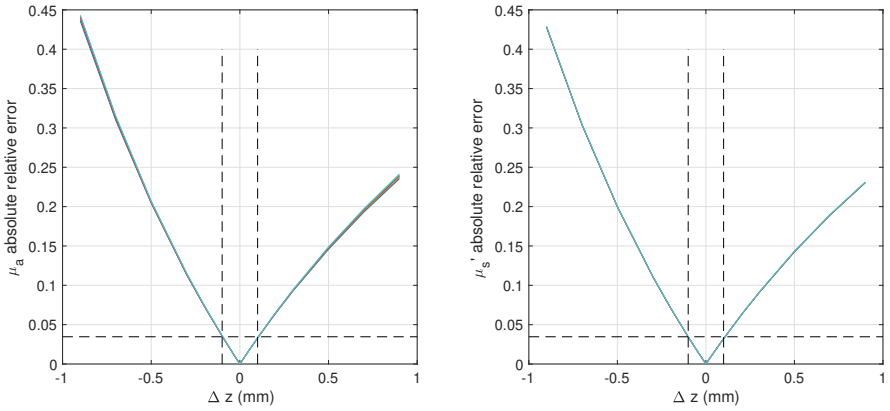

Figure 4.6: Absolute relative error on μ_a and μ'_s estimations with sample thickness measurement inaccuracy.

This error of 5% is of course a function of the optical properties of the medium considered, but this value allows to quantify the importance of this measurement. Also, it was noticed that the sample compression by the spring was particularly strong for agarose-made sample. This is responsible for narrowing of the sample, and probably for a modification of the optical properties of the medium due to the pressure constraints. To get rid of it, molds were made with glass slides (see Fig. 4.7). A "U"-shape holder made of microscope slides is sandwiched between 2 larger glass slides (still in *Borofloat 33*). The hot agarose gel is poured in and solidifies as it cools. The sample thickness is then imposed by the holder thickness (*i.e.*, the slide thickness), and the spring force is applied on the glass "U" rather than on the sample, ensuring known thickness. By gluing the glass sides with the "U" and adding a silicone seal, this cell also becomes compatible with liquid samples (without any agarose). Finally, it should be known that the thickness of the sample is

critical to ensure an optical thickness (see Eq. (4.6)) allowing to obtain non-zero measurements of M_T and M_U. That is why we made optical cells with 1 mm and 1/2 mm thicknesses.

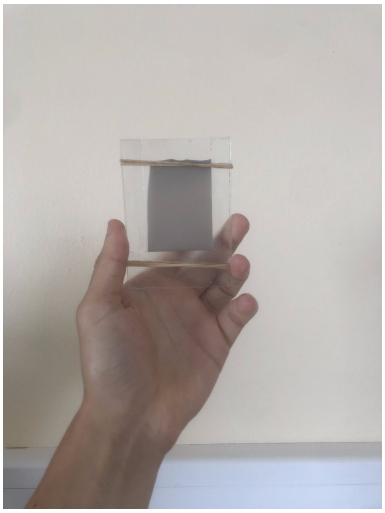

Figure 4.7: Optical phantom made of agarose gel poured in our "U"-shape glass mold.

4.3.3 Getting OP with the IAD

From the $M_R(\lambda)$, $M_T(\lambda)$ and $M_U(\lambda)$ vectors and the sample thickness δ, the getting of optical properties is possible by applying the IAD algorithm. The table 4.1, adapted from the program documentation [Prahl 2011] associates the estimable OP with the measurements needed to provide.

Optical properties	Measurements to provide	Assumptions
μ_a	M_R	infinite thickness ; $\mu_s = 1\ cm^{-1}$; g fixed
μ_a ; μ_s'	M_R ; M_T ; δ	g fixed (default $g = 0$)
μ_a ; μ_s ; g	M_R ; M_T ; M_U ; δ	no assumption

Table 4.1: Measurements to provide to the IAD program in order to estimate the corresponding optical properties of sample.

To facilitate the application of the program, a *Python*-based graphic user interface (presented in appendix D) was developed and a dedicated *Matlab* function created to obtain the OP of interest from the measurement files resulting from DIS bench acquisitions. In addition to the data related to the sample, the program also receives as input arguments the optical and geometric parameters of the spheres to correct for the losses of light and to obtain vectors of reflectance, transmittance and collimated transmittance closer to their theoretical definition (see Fig. 4.2).

4.4 Preliminary measurements on the DIS set-up

First validation tests and metrological characterizations were made from liquid samples. They are presented here.

4.4.1 Experimental repeatability study

The aim here is to study, for a given sample (optical phantom), the errors associated with the experimental repeatability, especially in terms of consequences on OP estimation. The protocol and results associated with this study are discussed below.

4.4.1.1 Sample description

For its scattering properties, its low price and its easy access, milk is an interesting ingredient to design optical phantoms. It can be considered at first sight as a pure scatterer due to its weak absorption properties. That is why we mix it with India ink (whose absorption properties are quite documented in the literature [Spinelli 2014]) before pouring the resulting liquid in the 1 mm thick glass-made mold (see Fig. 4.7). The fat milk (UHT) concentration of the designed sample was 20% (v/v) while the India ink one was 100 μM. India ink was homogenized using 2 MHz-ultrasounds for 5 minutes.

4.4.1.2 Results of optical bench measurements

Six measurements on optical bench were acquired with the previously described optical phantom according to the protocol described in section 4.3. The total transmittance M_T, reflectance M_R and unscattered transmittance M_U of the six associated series are provided in Fig. 4.8. We can notice the decrease of the reflected signal in favor of the transmitted one when λ increases. Concerning repeatability, we can see that the total reflectance and total transmittance measurement are satisfying with a relative error less than 10%. However, the zoom on collimated transmittance (top-left insert) illustrates that despite a small absolute error, the relative variations are significant, reaching 100% in the worst case. These variations reflect the difficulty of making a reliable measurement of M_U.

4.4.1.3 Results of IAD and discussion

What about the impact of these uncertainties on the OP estimates from the IAD application? Fig. 4.9 shows a box-plot representation of these results. As expected, both coefficients decrease with λ but we can notice that the $\mu_a(\lambda)$ curve is "chaotic" which probably reflects a problem with the measurements or/and calculations. Relative deviations are about 6% on the absorption coefficient, 10% on the scattering coefficient and finally 20% for the anisotropy factor.

The main measurement errors were associated to collimated transmittance (see Fig. 4.8). It was then decided to investigate the fate of the estimates when limiting the inputs of IAD to the 2 measurements of total transmittance and total reflectance. As described in Table 4.1, it implies that the user has to provide the anisotropy factor value, which was set in our phantom case to $g = 0.55$ for all the wavelengths. Results are given in Fig. 4.10, from which we can conclude that the accuracy on $\mu_a(\lambda)$ is not affected, while the one on $\mu_s(\lambda)$ increases with a relative error about 5%.

Following these results, the measurement protocol and especially the part concerning the measurement of collimated transmittance was updated to obtain more reproducible results. Among the improvements, we decided to isolate from the surrounding light the PM collecting the ballistic transmittance (see Fig. 4.3), to ensure a thirty minutes duration for the laser stabilization and finally the use of detergent to clean the glass container (see Fig. 4.7) and avoid stains.

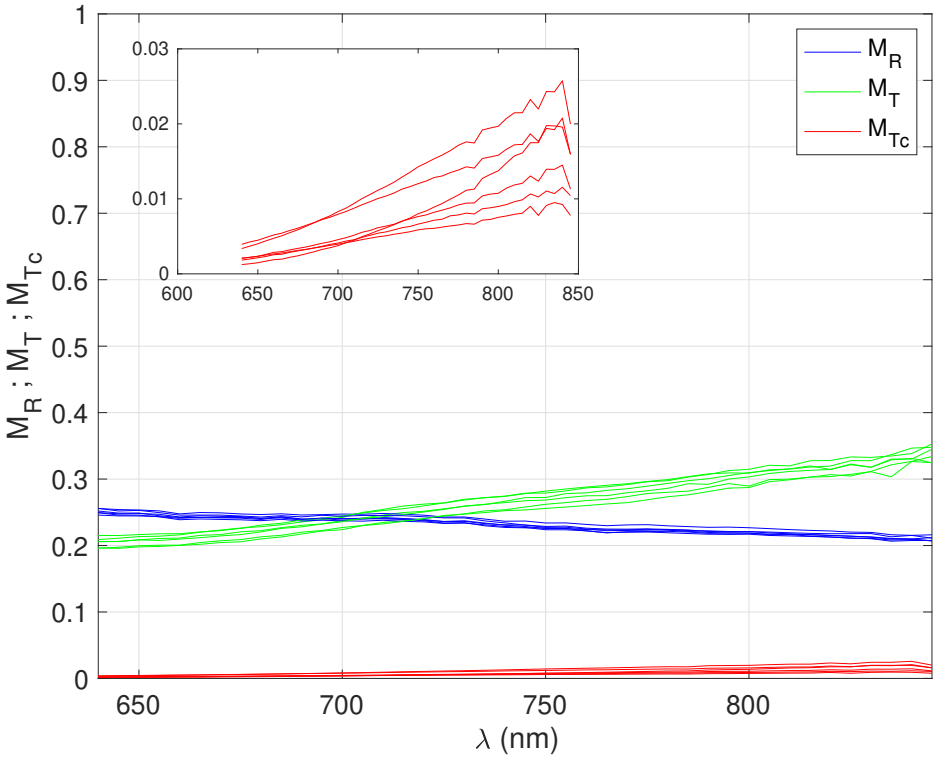

Figure 4.8: The total transmittance M_T, reflectance M_R and unscattered transmittance M_U of the six series measured on the DIS set-up. Top-left insert focuses on unscattered measurement.

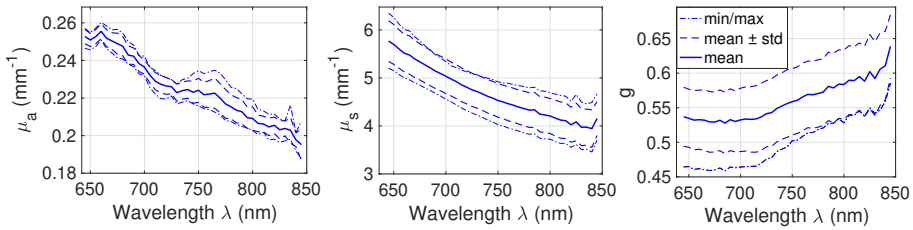

Figure 4.9: Optical properties obtained with IAD from the 3 DIS signals provided in Fig. 4.8.

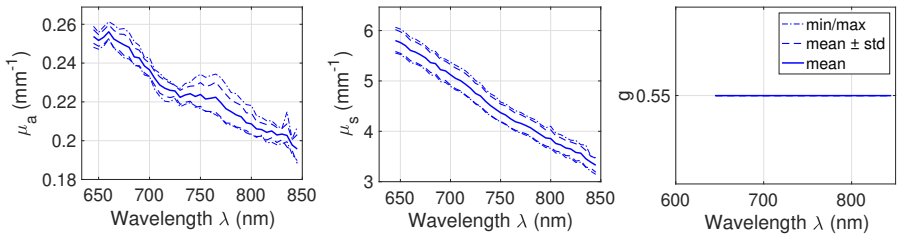

Figure 4.10: Optical properties obtained with IAD from the 2 total transmittance and reflectance DIS signal provided in Fig. 4.8. g was set to 0.55 when calling IAD.

4.4.2 Dilution ranges with milk

As quickly introduced earlier, the milk can be considered at first sight as a pure scatterer due to its weak absorption properties. The theory of scattering informs us that μ_s must be proportional to the concentration of the scattering particles, and thus to the concentration of milk in a sample. It is this proportionality that we wanted to verify through the characterization of milk-based dilution range.

4.4.2.1 Samples description

Two types of milk were characterized: cow fat milk (whole milk) and soy milk. The unscattered transmittance is the limiting measurement, since the optical thickness b (see Eq. (4.6)) has to be weak enough to allow some ballistic photons to get through the sample (enough for the sensitivity of the photo-detectors). Indeed, for fat milk sample with high volume concentration and 1 mm thick glass container, this optical thickness was too large so that we decided to reduce the geometrical sample thickness δ by making a thinner 0.4 mm glass cell. Table 4.2 sums up the concentrations and optical cell thicknesses used for each of the optical phantom of the dilution range.

Milk type	Concentration (% v/v)	Sample thickness δ (mm)
Fat	10	1
	20	1
	30	1
	100	0.4
Soy	60	1
	80	1
	100	1

Table 4.2: Summary of the different samples thicknesses and milk concentrations.

4.4.2.2 Results of optical bench measurements

Soy milk This paragraph presents the DIS optical measurements of the 3 soy milk samples for which concentrations and thicknesses are provided in Table 4.2. The Fig. 4.11 provides the M_R, M_T and M_U acquired for each of the 3 phantoms. As expected, we can notice the reduction of reflected signal for the benefit of the transmitted signal when the concentration of scattering particles increases.

Fat milk Similarly to soy milk-based sample, the Fig. 4.12 provides the M_R, M_T and M_U acquired for each the 4 fat milk-based phantoms for which concentrations and thicknesses are provided in Table 4.2. It is important to remember that the pure milk sample (*i.e.*, 100% concentration) had a thickness of 0.4 mm unlike the three others whose thickness was 1 mm. The analysis of these curves is similar to the one exposed in the previous paragraph on soy milk.

4.4.2.3 Results of IAD and discussion

Soy milk Estimates of optical properties associated to DIS signal presented in Fig. 4.11 are given in Fig. 4.13. As expected, we can notice the proportionality of μ_s to the soy milk concentration.

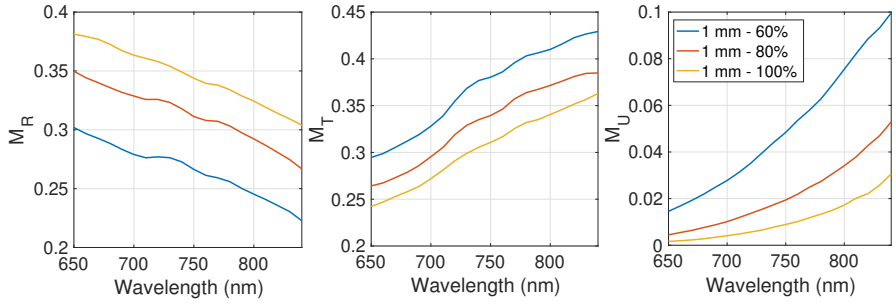

Figure 4.11: DIS measurements of the 3 soy milk-based phantoms described in Table 4.2

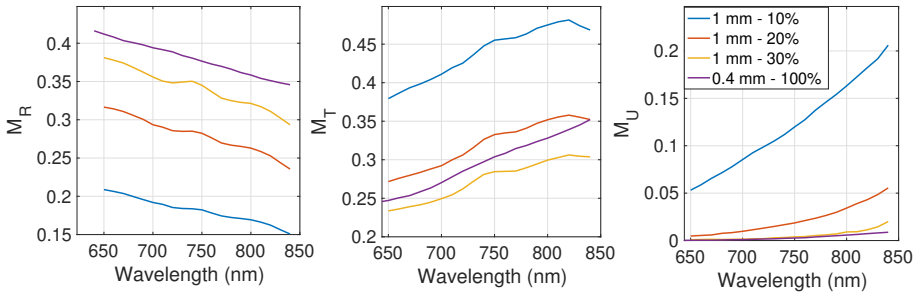

Figure 4.12: DIS measurements of the 3 fat milk-based phantoms described in Table 4.2

Concerning μ_a, we notice a (i) non-uniform spectral decrease and (ii) especially an unexpected decreases when the concentration increases (taking as reference the pure milk, $\approx +8\%$ for the 80% concentration and +14% for the 60% one). Considering the negligible absorption of the diluent (distilled water) in the visible spectrum, these discrepancies probably result from calculation artifact during the call to the IAD algorithm. Finally, we can mention that the estimates of anisotropy factor are similar whatever the concentration of soy milk. This is normal since g is determined by the shape and size of the scatterers and not the concentration.

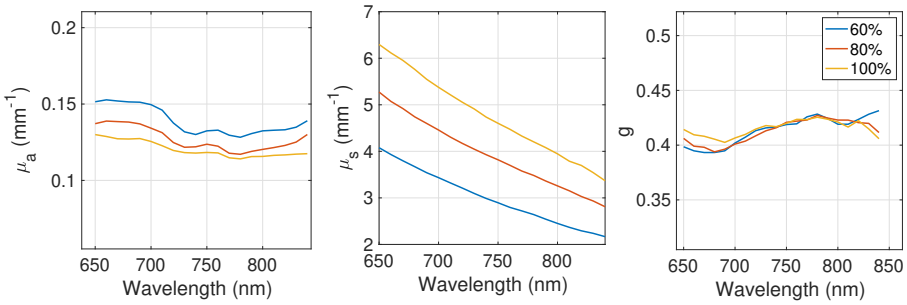

Figure 4.13: Optical properties obtained with IAD from the DIS signal provided in Fig. 4.11.

Fat milk Similarly to soy milk-based sample, estimates of optical properties associated to DIS signal presented in Fig. 4.12 are given in Fig. 4.14. The comments to be made are again quite similar to those made to describe the curves obtained from soy milk. However, it is important to note that IAD has correctly taken into account the thickness of the sample which is different for

the pure milk sample. Indeed, despite the fact that DIS measurements are very different because they depend on the thickness of the sample, the associated IAD estimates are consistent (*i.e.*, μ_s proportional to concentrations and g globally identical whatever the concentrations).

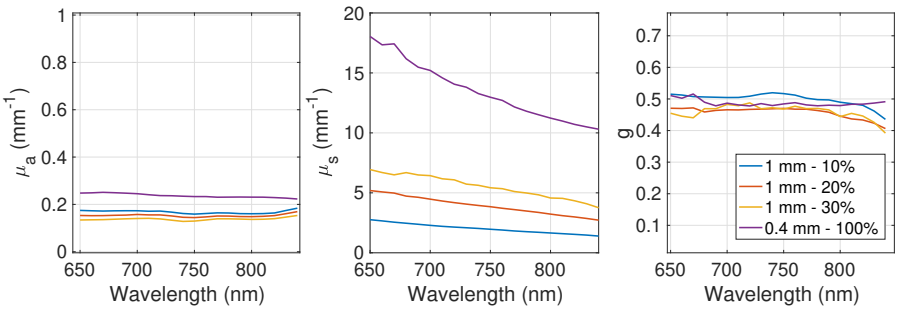

Figure 4.14: Optical properties obtained with IAD from the DIS signal provided in Fig. 4.12.

4.4.3 Dilution ranges with synthetic melanin phantom

We characterize here with our optical bench the OP of synthetic melanin-based optical phantoms. For this pure absorber, we also proceed through a dilution range. This one could be useful later for the realization of optical phantoms. Indeed, it will be possible to adjust the concentration of this one to target a phototype to represent.

4.4.3.1 Samples description

Ten samples were made using synthetic melanin (*M8631*) manufactured by *Sigma-Aldrich*. Half of them contained 1% (v/v) IL. The aim of this IL adding was to (i) verify that melanin could be considered as a pure absorber (*i.e.*, that its scattering power is negligible) and (ii) observe how the estimation of the absorption properties of melanin evolves in the presence of a scatterer. For both groups, 5 liquid samples with melanin concentrations of 2, 4, 6, 8 and 10 mM were poured in our glass optical cell.

4.4.3.2 Results of optical bench measurements

Fig. 4.15 show M_R, M_T and M_U signals of the ten samples. We can clearly notice the very weak part of reflected signal without IL as expected, since only scatterers can back-reflect the incident light (melanin is a pure absorber). Accordingly the M_R signal should then be zero, which is not the case. It turns out that the origin of this light is actually the light not absorbed by the sample during the first pass through the sample, which reflects on the wall of the transmittance sphere before part of this light passes again (return path) through the sample and ends up in the first sphere. Fortunately, this known measurement artifact [Pickering 1993] is considered in the IAD algorithm which estimates and subtracts this light quantity. This is the reason why the M_R signal for samples without IL was considered insufficient, which led the program to only take into consideration the M_T signal an so only estimating the absorption coefficient (see Table 4.1). Otherwise, we observe the light attenuation corresponding to melanin absorption in the 3 signals.

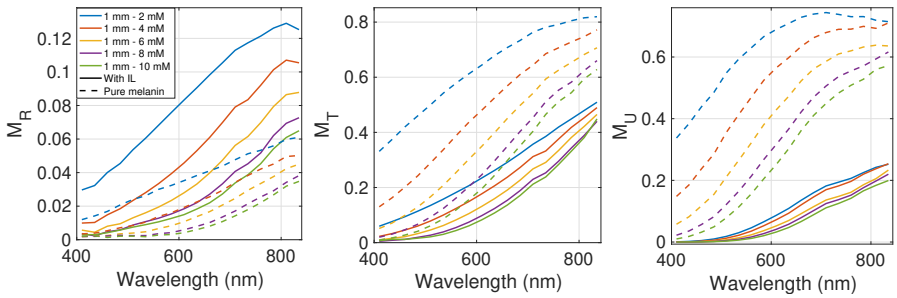

Figure 4.15: DIS measurement of the synthetic melanin-based optical phantoms. Color code indicates the melanin concentration while the line style refers to the presence (continuous line) or absence (dashed line) of intralipids in the sample.

4.4.3.3 Results of IAD and discussion

Fig. 4.16 shows the optical properties estimations provided by IAD from DIS measurements presented earlier. As indicated, only μ_a was properly estimated for pure melanin (without intralipids). Except for the highest molar concentration in the near UV range, the values of the absorption coefficient proportionally increases with melanin concentration. For samples combining melanin and IL, we can observe an non negligible offset on the estimated values of $\mu_a(\lambda)$ which brings into question the purely scattering behavior of IL. About μ_s, except in the near UV where the weak level of optical signal is responsible for noisy estimations, the melanin concentration does not affect the scattering coefficient estimates and its spectral decay. Finally, the anisotropy factor estimation is not very satisfying. We observe indeed (i) a drop at 710 nm which is not of physical origin and (ii) an offset associated to melanin concentration increase which should not appear since the scatterers are for all the intralipids particles. These errors were partly related to the non-linear operation range of the photo-detector (PM of the collimated transmittance measurement) associated to the very low gain initially set (see appendix D). This was then considered and corrected on the optical bench but due to lack of time, we were unfortunately unable to reproduce these measurements.

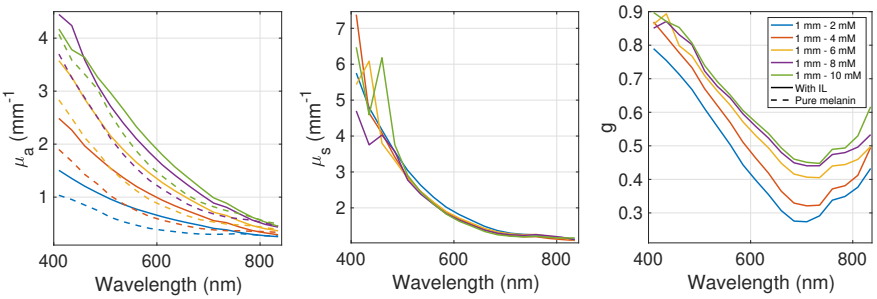

Figure 4.16: IAD optical properties estimates of the synthetic melanin-based optical phantoms. Color code indicates the melanin concentration while the line style refers to the presence (continuous line) or absence (dashed line) of intralipids in the sample. Scattering properties (μ_s and g) were not estimable for pure melanin samples (*i.e* without intralipids).

4.5 Towards cross-validation between *SpectroLive* and the DIS optical bench estimates

Before moving on to real biological samples, we decided to conduct here a preliminary experimental study using nine liquid optical phantoms made of different concentrations of intralipids (Ai, Bi, Ci $i \in \{1,2,3\}$) and methylen blue ($j1, j2, j3$ $j \in \{A,B,C\}$) to tune scattering and absorption coefficients, respectively. This experiment was presented in [Colas 2022a]. For each of the nine samples, the molar concentration of the absorber as well as the volume fraction of the scatterer were estimated using the two aforementioned approaches (inverse problem solving from SR-DR spectra and IAD from DIS measurements). The work presented here describes the two methods, and compares the results obtained from DIS-IAD and SR-DR spectroscopy in terms of concentrations estimates accuracy for every phantom and with reference to expected theoretical values.

4.5.1 Description of the experimental protocol

4.5.1.1 Optical phantoms and optical properties model

Analogously to the experiments described in Aernouts *et al.* paper [Aernouts 2013], nine liquid optical phantoms were designed to correspond to 3 absorption levels (using MB M9140, *Sigma-Aldrich*) and 3 scattering levels (using IL-20% I141, *Sigma-Aldrich*). Table 4.3 provides the MB molar concentration c_{MB} (μM) and the volume fraction of IL-20% f_v^{IL} (%) in each of the nine 100 mL (the complement is distilled water) liquid optical phantoms. The optical models linking the absorption and scattering coefficients (in cm^{-1}) to both variables are the following:

$$\mu_a^{theo}(\lambda) = c_{MB} \times 2.303\ \varepsilon(\lambda) \qquad \mu_s^{theo}(\lambda) = f_v^{IL}/100 \times 1.5 \times 10^7 \lambda^{-1.6} \tag{4.10}$$

With c_{MB} in $mol.L^{-1}$, the molar extinction coefficient $\varepsilon(\lambda)$ (in $mol^{-1}.L.cm^{-1}$) from OMLC database [Prahl 2018] and λ in nm. For each phantom, the volume prepared was divided into two parts. A first part (3 mL) intended to be poured into a 1 mm thin glass cell to get measurements on the DIS optical bench, while the second (97 mL) was poured into a bigger mold that satisfiesoptical semi-infinite conditions for the SR-DR acquisition. Both natures of samples are represented on Fig. 4.17.

		IL-20% volume fraction f_v^{IL} (%)		
		1	2	3
MB molar concentration c_{MB} (μM)	8	A1	B1	C1
	20	A2	B2	C2
	32	A3	B3	C3

Table 4.3: c_{MB} and f_v^{IL} values for each of our optical phantoms.

4.5.1.2 DIS measurements and IAD estimation

DIS measurements: At the time these experiments were done, we were having difficulty to obtain a reliable measurement of the collimated transmittance on the DIS set-up. Thus, only $M_R(\lambda)$ and $M_T(\lambda)$ were acquired for these experiments. That is why the anisotropy factor g was

not estimated (see table 4.1) and its values were set according to the analytical formula from Michels *et al.* [Michels 2008], available in Aernouts *et al.* [Aernouts 2013].

IAD and concentration estimates: From $\mu_a^{IAD}(\lambda)$ and $\mu_s^{IAD}(\lambda)$ obtained for each phantom, we estimated $\hat{\mathbf{p}}_{IAD} = [c_{MB}, f_v^{IL}]$ by varying both concentrations in theoretical model (see Eq.(4.10)) to fit the experimental data. Those fitting are available in the results and discussion section 4.5.3.

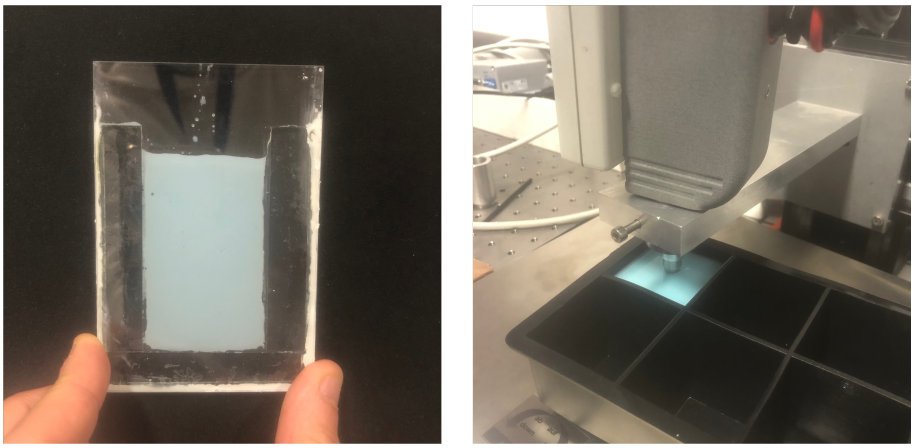

Figure 4.17: Liquid optical phantom poured in glass cell for DIS measurements (left) and in square black silicone mold for SR-DR spectroscopy acquisition (right).

4.5.2 SR-DR measurements and inverse problem solving

SR-DR measurements and standardization: Ten DR spectra were acquired and averaged with the optical probe tip immersed into each of the liquid phantom (see Fig.4.17). The white calibration measurement [Colas 2022c] was made illuminating a $SRS-40$ % standard (reflectance $R = 40\%$) at $z = 8000$ μm vertical distance. The DR spectral shapes between phantoms are very similar. For instance normalized DR spectra A2, B2 and C2 are very similar, as we can see in Fig. 4.18. The normalization was done by multiplying all the $DR_{Dn}(\lambda)$ by c_{norm} which imposes the maximum of the DR spectra at the distance D_1 to have unit value.

These results highlight that normalized spectra are very similar, and therefore that exploiting the spectra before normalization is necessary. That is why it is very important to deal with non-normalized spectra, *i.e.*, expressed in absolute magnitude in photons ratio (detected/emitted light) as described in section 3.5. To get the experimental spectra in such unit, we multiplied the acquired spectra by a corrective factor $c_{Dn}(\lambda, z, R)$. This was obtained applying the following formula:

$$c_{Dn}(\lambda, z, R) = \frac{DR_{Dn}^{sim}(\lambda)}{DR_{Dn}^{calib}(\lambda, z, R)} \tag{4.11}$$

Where $DR_{Dn}^{calib}(\lambda, z, R)$ is the DR spectra acquired (for a spectrally flat white measurement at a z vertical distance and reflectance standard of reflectance R) in an calibration optical phantom for which OP are known. Same OP were then used to run a simulation corresponding to *SpectroLive* acquisition with same calibration medium. The output of the simulation is $DR_{Dn}^{sim}(\lambda)$ which is independent from flat white measurement geometry, and expressed in the wanted y-axis unit *i.e.*,

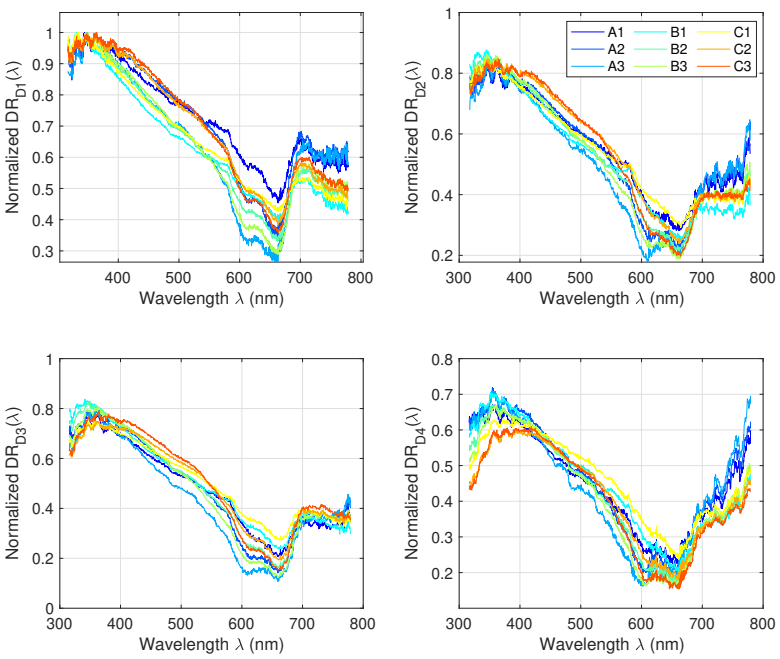

Figure 4.18: Normalized $DR_{Dn}(\lambda)$ spectra of the 9 optical phantom corresponding to increasing concentration of IL (Ai, Bi, Ci) and of MB $(j1, j2, j3)$.

photons ratio. In other words, $c_{Dn}(\lambda, z, R)$ is the factor allowing to (i) get experimental signal in photons ratio and (ii) reduce the spectral and geometrical differences between simulation and real clinical probe signals. A very similar experimental method of spectra standardization was used in Thueler *et al* work [Thueler 2003]. This experimental factor had been presented in the Eq. (3.17); here it also depends on λ in order to take chromatic dispersion into account.

Getting the simulated spectra: The simulation presented in section 1.5.2 requires the OP as input parameters, of each of the layers of the medium (mono-layer phantom in our case), namely the absorption and scattering coefficients. These OP, were update in according to previously described optical model available in Eq.(4.10) to generate the simulated spectra $DR_{Dn}^{sim}(\lambda; \mathbf{p})$ associated to $\mathbf{p} = [c_{MB}, f_v^{IL}]$.

Inverse problem solving: Experimental spectra were sampled to correspond to simulated ones. Both were expressed in absolute magnitude, *i.e.*, photons ratio (light collected/light emitted). The following cost function to be minimized during the optimization procedure of the inverse problem solving associated to variables $\mathbf{p} = [c_{MB}, f_v^{IL}]$ was proposed:

$$cost(\mathbf{p}) = \sum_{n=1}^{N_D} \frac{1}{D_n^3} \sum_{i=1}^{N_\lambda} [\frac{DR_{Dn}^{sim}(\lambda_i; \mathbf{p}) - DR_{Dn}^{exp}(\lambda_i)}{\overline{DR_{Dn}^{exp}}}]^2 \tag{4.12}$$

Where N_λ is the common number of wavelengths in experimental and simulated spectra, and N_D the number of SD distances (*i.e.*, 4 for our device). It was proposed to divide by $\overline{DR_{Dn}^{exp}}$, the mean of DR signal acquired at the D_n distance on each phantom, in order to get a modified relative

error. Hence, differences in spectra for D_4 (weak intensity) and D_1 (strong intensity) will have the same relative weight in the total cost while preventing from dividing by zero as it can happen with a classic relative error. The least squares are finally weighted by a weight $(1/D^3)$ inversely proportional to the distance cubed to favor short distances for which the experimental signals are less noisy. A *Matlab* optimization script using hybrid process (5 iterations of *particleswarm* to get a starting point closer to the solution followed by 10 steps of *fmincon* function) was created using bounds allowing $c_{MB} \in [2-50]$ μM and $f_v^{IL} \in [0.5-5]\%$. The computation time for each of the phantom was about seven minutes for 2×10^6 numerical photons sent. The optimized estimates are denoted $\hat{\mathbf{p}}_{DR}$. Results for this inverse problem solving, *i.e.*, comparison between $DR_{Dn}^{exp}(\lambda)$ and $DR_{Dn}^{sim}(\lambda; \hat{\mathbf{p}}_{DR})$ as well as the $\hat{\mathbf{p}}_{DR}$ parameters estimates are available for each phantom in the next results and discussion section 4.5.3.

4.5.3 Comparison of both estimates

4.5.3.1 Estimates using DIS optical bench and IAD

Fig. 4.19 sums up the experiments associated to DIS and IAD parameters estimates. Top subplots shows the DIS reflectance (M_R) and transmittance (M_T) of our phantoms. One can notice the expected behavior: optical phantom with same level of IL-20% are grouped together and differs more or less only in the MB peak according the absorber concentration. IAD results associated with those measurements, *i.e.*, $\mu_a^{IAD}(\lambda)$ and $\mu_s^{IAD}(\lambda)$ appears on bottom subplots. Results are globally satisfying, since we can observe three levels of absorption with MB double peaks and three levels of scattering with the expected wavelength decay. However, the signal to noise ratio on the edge of the spectra (the laser power is lower for these wavelengths) but above all the crosstalk [Selifonov 2020] (the absorption pattern appears in μ_s) between μ_a and μ_s in the MB absorption region limit the fitting accuracy. Finally, for the sake of clarity, only the fitting (according Eq.(4.10)) of the B2 optical phantom is represented in black dashed-line, but it was done for each of our 9 phantoms.

4.5.3.2 Estimates using DR clinical device and inverse problem solving

Fig. 4.20 sums up the experiments associated to inverse problem estimates from experimental DR spectra, in which simulated $DR_{Dn}^{sim}(\lambda; \hat{\mathbf{p}}_{DR})$ (continuous line) and experimental $DR_{Dn}^{exp}(\lambda)$ (dashed line) spectra are plotted. Columns are for each of our 4 SD distances, while lines correspond to the 3 IL-20% volume fractions (Ai, Bi, Ci) which has an impact on the global level of intensity. We first can notice the good likeness of estimated (simulated) spectra with the experimental ones. In particular, we can observe a decrease of the signal as a function of the wavelength caused by the decrease of μ_s more or less attenuated by the absorption of the MB around 660 nm. We also noticed the noise increase with weak value of f_v^{IL}: the scattering particles become too rare to obtain a well backscattered signal. The most noticeable difference appears at D_4 where our simulation overestimates the signal reaching the detector. This is not very surprising because of the cost function designed is weighted to strongly penalize short SD distances rather than larger one (see Eq.(4.12)).

4.5.3.3 Comparison of both approaches with parameters estimates

Fig. 4.21 summarizes the parameters estimates using the two previous procedures. Circle makers (○), labeled as "Theory" corresponds to concentrations introduced in the samples during phantoms

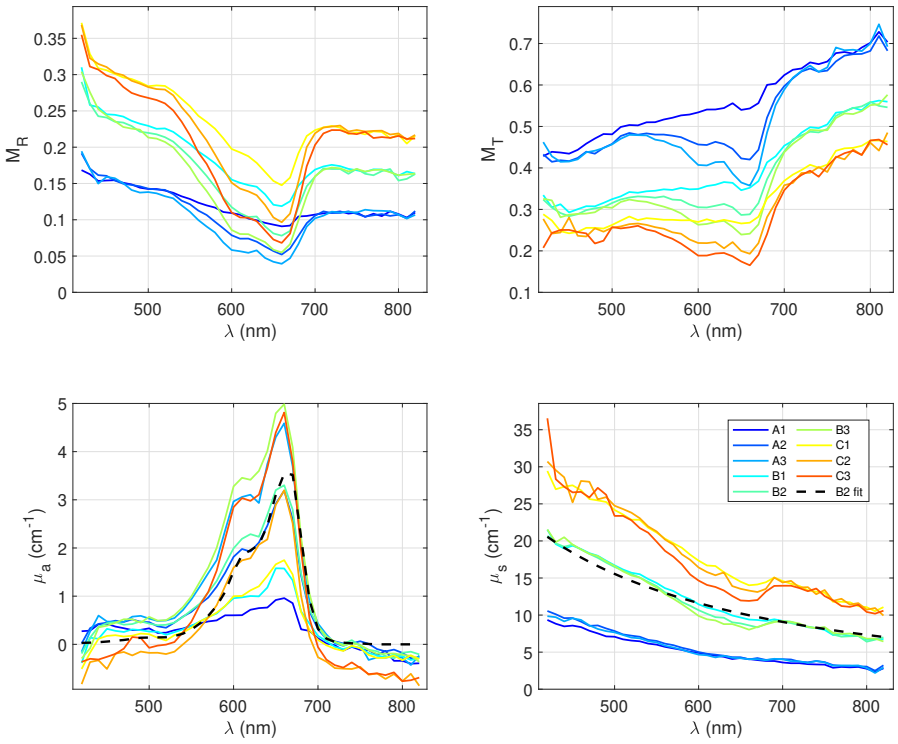

Figure 4.19: Reflectance (M_R) and transmittance (M_T) from DIS measurements for each of our 9 optical phantoms (top) and associated absorption (μ_a) and scattering (μ_s) coefficients (bottom). Black dashed line represent the fitting of Eq.(4.10) for B2 phantom.

design *i.e.*, including some pipetting uncertainties. The cross markers (+) and stars ones (∗) are respectively for DIS-IAD and SR-DR-based inverse problem solving estimations. We can notice than both approaches provide coherent estimates, with absolute errors less than 4 μM for c_{MB} and 0.2 percentage point for f_v^{IL}. For each of the methods, the estimates are sometimes over- or under-estimated. However, it can be observed that the estimates resulting from the inverse problem are globally more accurate. This implies that in the current state, considering the estimates from the DIS optical bench as an access to the ground truth is not possible and that increasing its accuracy is mandatory. We are currently working on improving the quality of DIS signal acquisition and IAD settings to obtain more accurate estimates and particularly limit the μ_a and μ_s crosstalk (see section 4.5.3.1).

4.5.4 Discussion about the two estimation methods

For the future purpose to compare skin optical properties estimations using inverse problem solving from clinical SR-DR spectra, an optical bench using DIS set-up and IAD algorithm was designed. Before moving on to real biological samples, we presented here preliminary results using liquid optical phantoms with 3 levels of scattering (tunable thanks to intralipids) and 3 levels of absorption (tunable thanks to methylen blue). For each of them, estimates of methylen blue and intralipids concentrations which respectively rules absorption and scattering coefficients were

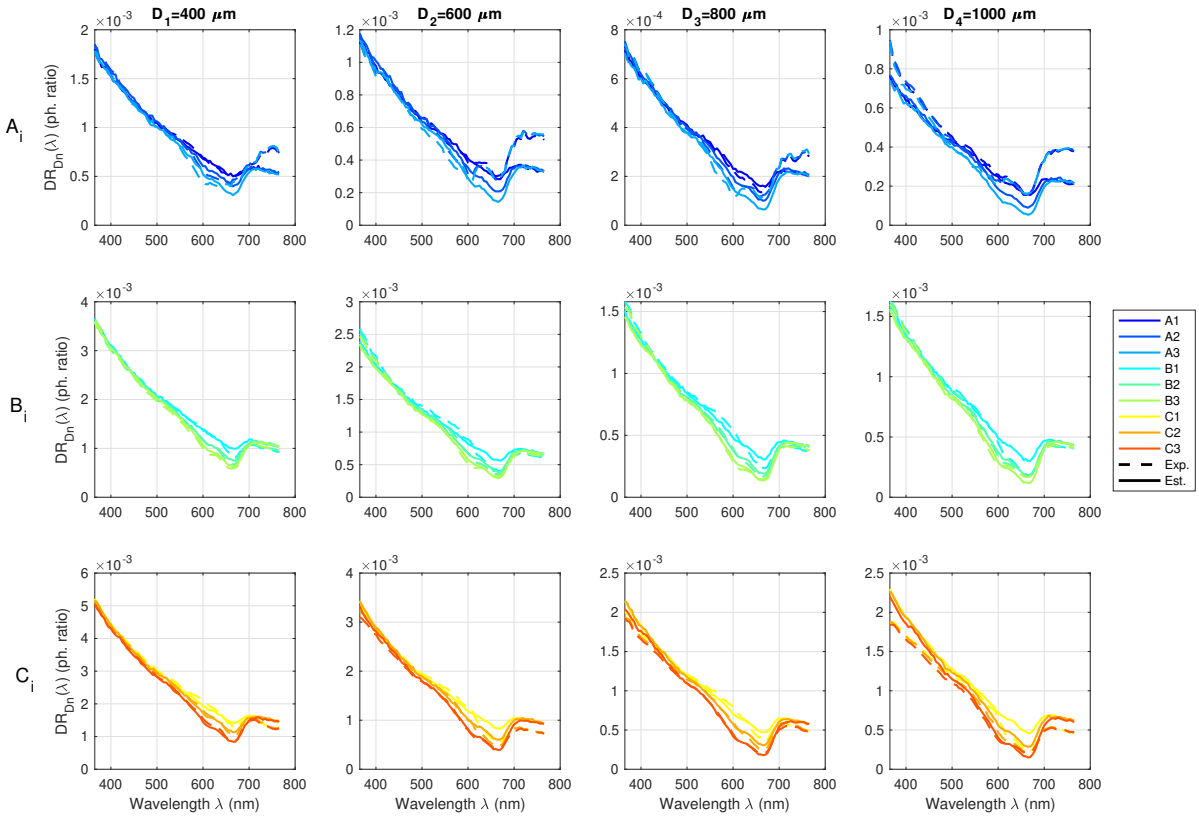

Figure 4.20: Comparison of estimated $DR_{Dn}^{sim}(\lambda; \hat{\mathbf{p}}_{DR})$ (continuous line) and experimental $DR_{Dn}^{exp}(\lambda)$ (dashed line) DR spectra. Columns are for each of our 4 SD distances, while lines correspond to IL-20% volume fractions (Ai, Bi, Ci) which is responsible for the global level of intensity.

provided using both methods. Although the accuracy of estimation using integrating spheres has so far been insufficient to consider it as a ground truth, the work has made it possible to prove the feasibility of this comparative approach. But it also allows to validate the estimation protocol from experimental DR spectra (*i.e.*, inverse problem), with an absolute error less than 4 μM for MB concentration and 0.2 percentage point for intralipids volume fraction.

4.6 Conclusion and prospects

In parallel to the works articulated around the *SpectroLive* device, an optical bench allowing the *ex-vivo* optical characterization of biological samples was realized. The measurements of reflectance, transmittance and collimated transmittance (acquired thanks to the integrating spheres) coupled to the IAD algorithm allows indeed to obtain the coefficients of absorption μ_a, scattering μ_s as well as the anisotropy factor g of this sample. Later intended to characterize biological samples such as *ex-vivo* skin, this chapter focused mainly on all the preliminary work done to design this experiment including the realization of the optical assembly, the design of an user interface allowing

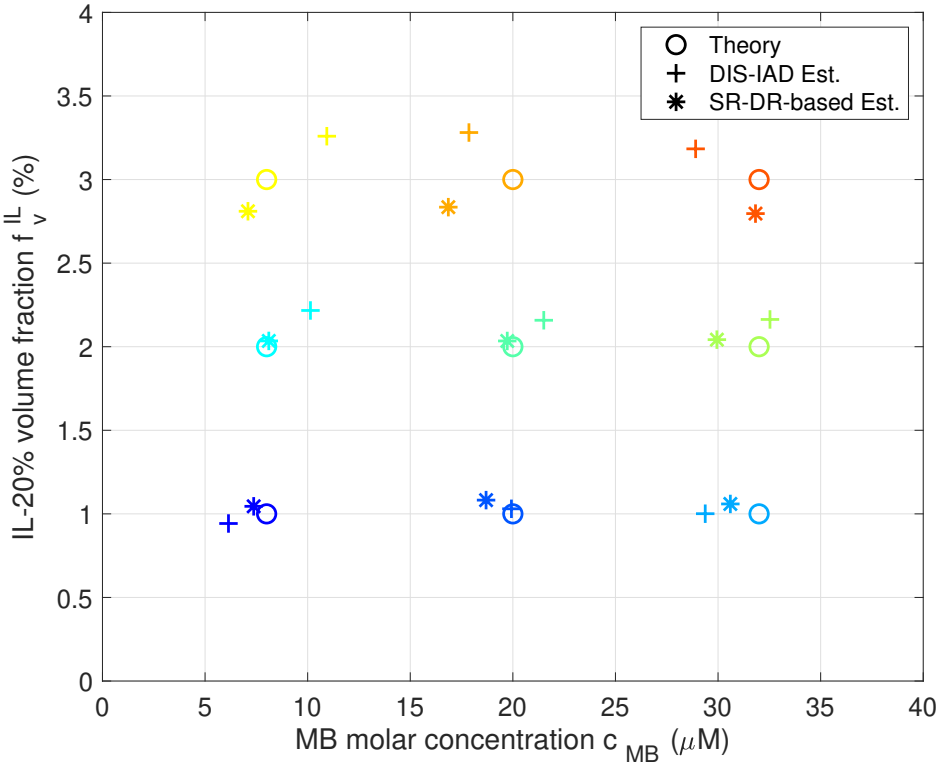

Figure 4.21: Comparison of parameters estimates obtained with IAD (+) and inverse problem solving (∗). Theoretical values (∘) corresponds to concentrations introduced in the samples during phantoms design.

the automation of the various acquisitions and data processing leading to the OP estimates. Some preliminary characterization measurements of milks and synthetic melanin were then provided before finally presenting an experiment fully related to the previous chapters, *i.e.*, the comparison of OP estimates resulting from DIS-IAD with those from SR-DR acquisition an inverse problem solving (see Chapter 3). It is this comparative approach that needs to be extended in the future. We can imagine to design optical phantoms more complex including 5 layers to get closer to the model defined in section 2.5, for which OP in some layers can be estimated from *SpectroLive* acquisition (inverse problem) and compared to DIS-IAD characterization of each layer (of each of them successively).

General Conclusion

This thesis entitled "Modeling and estimation of human skin optical properties using spatially resolved autofluorescence and diffuse reflectance spectroscopy" presented the work achieved to optically characterize the human skin to improve the carcinoma diagnosis. These **optical properties estimation** was made possible thank to **inverse problem solving**, where experimental data (acquired *in-vivo* during a clinical study) were spatially-resolved autofluorescence and diffuse reflectance spectra, using a Monte Carlo photon transport simulation adapted to fit real acquisitions. Our work was articulated around three guidelines.

The first one was to **keep the clinical dimension** in our inverse problem solving. Bringing a physiological and morphological explanation to the acquired spectra was our will. This is manifested by the design of a numerical skin model with 5 layers and whose scattering and absorption properties are directly related to the chromophores concentrations, which allow to tune the optical properties to represent a wide range of skin types (intra- and inter-individual). Among the existing parameters, the epidermal layers thicknesses, the melanin concentration and the blood dermal content were considered as variable in the inverse problem solving to converge toward target spectra. The local evolution of these parameters can then be directly linked to the pathological state of the tissue thanks to the database (under development) which associates to each acquisition the anamapathological results. More statistical approaches using classification methods with this database would also be of interest to compare diagnosis resulting from these complementary methods.

The second one was to **enhance the depth information** provided by the spatial resolution existing on the device. Indeed, even if it was known that the short distances between the exciting and collecting fibers was associated to shallower photons trajectories in skin, whereas the larger separations corresponded to deeper ones, to specify this behavior was important. Using our 5-layer skin model for several skin configurations, the simulation was modified to add numerical outputs to quantify the propagation in skin layers of the detected photons at different source to detector distances and a each wavelength of the device. Knowing the origin in depth of those photons, it is then easier to interpret the resulting spectra. The knowledge gathered allowed to better apprehend the inverse problem solving, by developing an optimization algorithm that sequentially estimate parameter(s) in isolated skin layers. The application of this algorithm to the aforementioned data-set of clinical spectra is envisaged.

Finally, the last one was to bring a **metrological analysis to the experimental measurements**. An optical bench including integrating sphere was designed, allowing for optical parameters estimation of *ex-vivo* samples. Although the work presented in this manuscript is more about the design of the experiment, the idea behind is to soon use this bench as an alternative way to cross validate the *in-vivo* optical properties estimates (using the clinical spectroscopic device). A calculation method (based on photometry) was also provided as well as an experimental one allowing to express the experimental diffuse reflectance spectra in absolute unit, *i.e.*, as a light ratio between the amount of collected an sent light. Although they deserve to be improved, those techniques allow to obtain spectra whose intensity is directly (without normalization) comparable to those of the spectra resulting from the numerical simulation.

Annexes

Appendix A

Chapter 1 appendix

A.1 Annular detection surface approximation

A.1.1 Context and experimental protocol description

An approximation is done when considering the annular detecting surfaces before applying a ratio of surface to obtain our circular point fiber, this is described in section 1.5.2.1. Complementary experiment and analysis were carried out to precisely quantify this approximation. Simulations were run at $\lambda = 565\ nm$ (middle of the visible spectrum) and for the healthy skin model with SC and LE intermediate thicknesses and phototype I (5 layered skin model described in section 2.5).

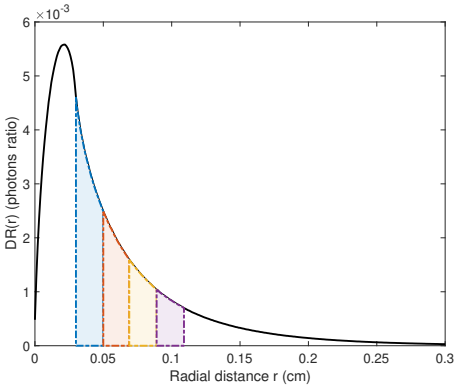

Figure A.1: Radial diffuse reflectance $DR(r)$. The color areas show the integration we do to get the signal collected in each annular surface associated to D_n SD distance.

A.1.2 Calculation to quantify the error introduced by the approximation

In our 3D simulation geometrical configuration, the cylindrical medium is sampled into elementary cylinders. Viewed from the top, it corresponds to annular elementary surfaces of thickness dr (assuming rotation symmetry, there is no angular cut). Running the photon propagation simulation provides the $DR(r)$ as a function of the radial distance r from the emitting fiber center. In other words, is the latter corresponds to the ratio of photon re-emitted towards the surface in each elementary ring centered on r and of thickness dr. Fig. A.1 illustrates this $DR(r)$, in which colored integration surfaces highlight the area under the curve corresponding to the signal captured in the ring of width $2 * r_{DF}$ centered at D_n SD distance. In our simulations, this quantity is corrected by the area ratio (6 collecting circular fibers over the annular detection surface) factor:

$$C_{area} = \frac{6\pi r_{DF}^2}{\pi(r_{ext}^2 - r_{int}^2)} \tag{A.1}$$

With $r_{int} = D_n - r_{DF}$ and $r_{ext} = D_n + r_{DF}$, to finally get $DR_{Dn}(\lambda)$ corresponding to the 6 collecting fiber around the source emission. The error associated with this approximation comes from the fact that the irradiance is not homogeneous between r_{ext} and r_{int}. From the $DR(r)$ signal, this radial irradiance can be calculated (dividing by elementary ring surface), to then build the associated 2D $DR(x, y)$ map in Cartesian coordinates. Such map is shown on Fig. A.2 hereafter, on which the local disk surfaces corresponding to 1 DF of each distance were added (in our medium 3D sampling with $dx = dy = dr$, each DF area is composed of 316 square elementary surfaces $dS = dxdy$). We then integrated the signal within those surfaces, before multiplying it by 6 (6 DF for each D_n distance). Table A.1 below sums up the results and the relative error (%) calculated between both geometrical configurations.

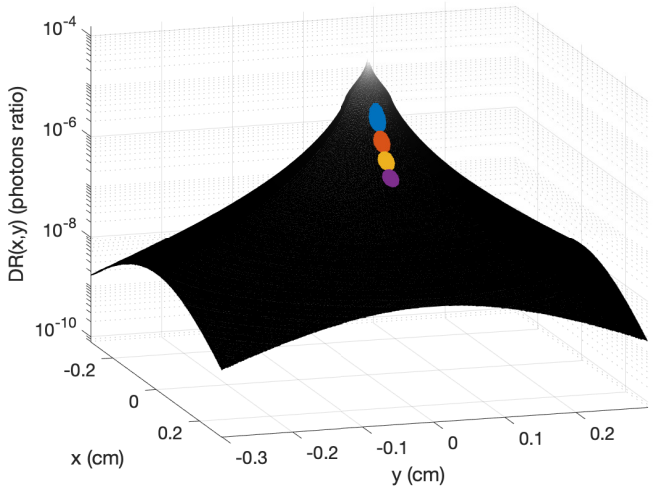

Figure A.2: 2D $DR(x, y)$ map in Cartesian coordinates. The intensity unit is in log scale. The circular areas represent the DF surfaces we integrate to get the acquired signal in each fiber.

D_n SD distance (μm)	$DR_{Dn}(\lambda)$ (approx.)	$DR_{Dn}(\lambda)$ (truth)	Relative error (%)
400	0.0263	0.0262	0.13
600	0.0103	0.0102	0.18
800	0.0049	0.0049	0
1000	0.0026	0.0026	0

Table A.1: Relative errors calculated for each SD distance between "ground truth" (6 disks) and approximated (ring and areas ratio correction) geometrical configurations.

The results obtained (relative error is smaller than 0.2%) show that for our geometrical configuration, and for our skin medium, the approximation made by considering annular collection surfaces rather than local circular fibers is valid.

Appendix B

Chapter 2 appendix

B.1 Skin error margins of MC DR results

B.1.1 Motivations and error definition

No error margins appear in different DR spectra of the manuscript and particularly in the depth study chapter 2. However, the spectra result from MC stochastic approach so an error that sums up this variability could be provided. We want to prove there that this error is negligible for the quantity of photons we launched, and thus justify the the absence of these margins of error in the representation of our spectra. For that, ten simulations performed with 10^8 photons each were performed for the healthy mean epidermal thickness medium of phototype I (see section 2.1). For each of the ten simulations, the relative error was calculated for all wavelengths and all source to detector distances D_n, according to formula:

$$\varepsilon_{Dn}(\lambda) = 100 \times \frac{DR_{Dn}(\lambda) - \overline{DR_{Dn}(\lambda)}}{\overline{DR_{Dn}(\lambda)}} \tag{B.1}$$

Where $\overline{DR_{Dn}(\lambda)}$ is the average spectrum of the 10 simulations.

B.1.2 Error

The Fig. B.1 below illustrates those values for the 10 simulations. Maximum errors ($< 0.5\%$) appears when detected photons are rare, *i.e.* in the hemoglobin absorption peak at 415 nm and for D_4 SD distance. This error is obviously a function of the optical properties and therefore of the type of medium simulated. However, we can legitimately assume that by restricting ourselves to the environment simulating the range of possible skin types, the order of magnitude of this error must remain similar.

B.2 Study of variation of the epidermal thickness, the phototype and the blood concentration

B.2.1 Purpose of the annex

For the sake of brevity, the tools for in-depth characterization of DR spectra developed in section 2.6.3 were applied for a few kind of skin media. Especially, the DR signal decomposition proposed in Eq .(2.6.5) was proposed for only the skin model of intermediate thickness of SC and LE layers, mean dermal blood content and phototype I. The aim here is to simply provide (i) the spectra of $DR_{Dn}(\lambda)$ as well as (ii) the weight fraction $w_{Dn}^{layer}(\lambda)$ introduced in Eq. (2.14) for all trios (epidermal thickness, blood concentration, phototype) among the 3 healthy epidermal thicknesses provided in Table 2.1, the 3 blood dermal volume fraction given in Table. 2.3 and finally the 4 phototype provided in in Table 2.2.

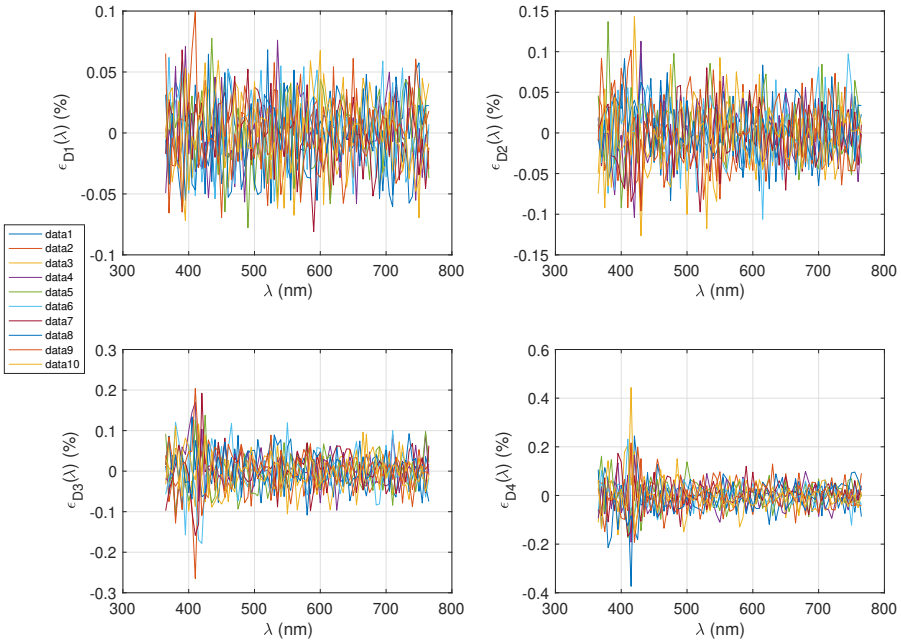

Figure B.1: Repeatability error described in Eq. (B.1) for 10 identical simulation runs for the 4 SD *SpectroLive* distances.

B.2.2 Variation study on DR spectra

We provide here the 36 $(3 \times 3 \times 4)$ $DR_{Dn}(\lambda)$ spectra for healthy skin configurations described in the previous paragraph.

B.2.3 Variation study on weight fraction in DR spectra

We provide here the 36 $(3 \times 3 \times 4)$ $w_{Dn}^{layer}(\lambda)$ weight fractions in DR spectra for healthy skin configurations described in the previous paragraph.

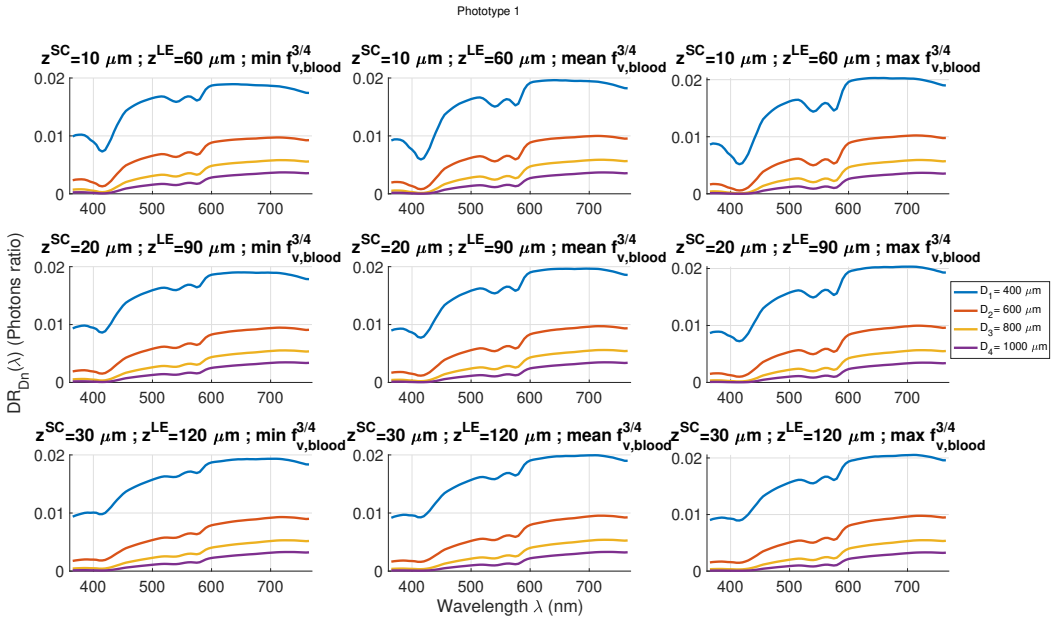

Figure B.2: DR spectra for several skin configuration and fixed phototype I. Epidermal thickness increases from top to bottom while blood volume fraction increases left to right.

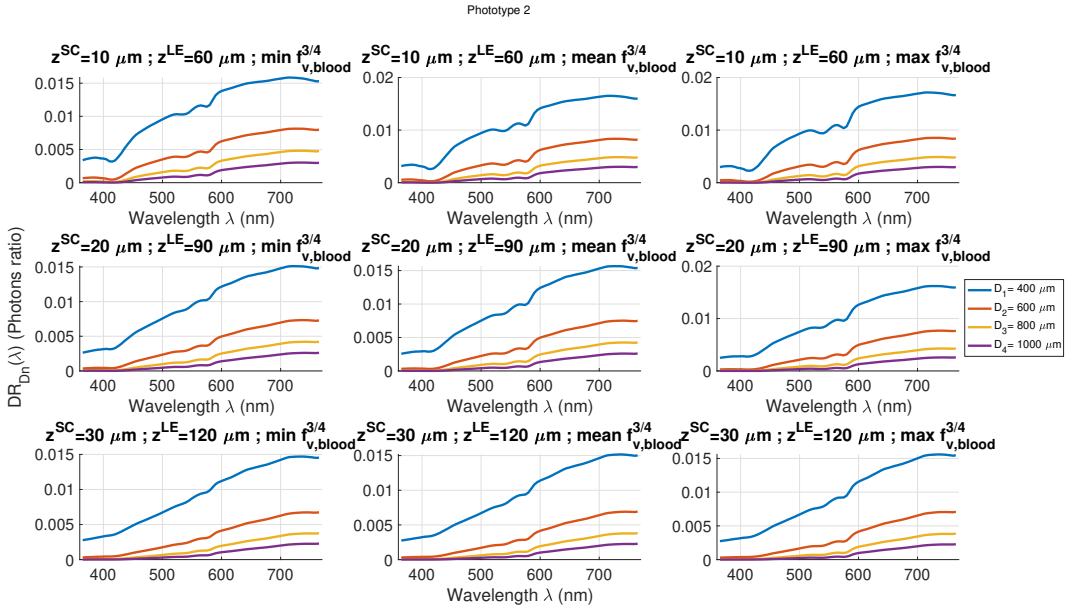

Figure B.3: DR spectra for several skin configuration and fixed phototype II. Epidermal thickness increases from top to bottom while blood volume fraction increases left to right.

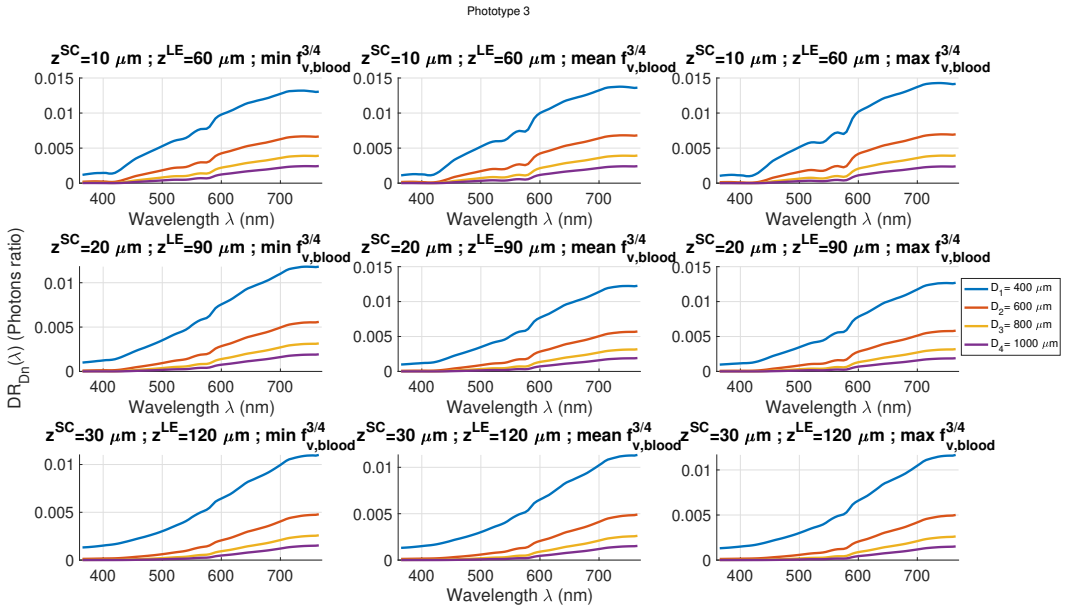

Figure B.4: DR spectra for several skin configuration and fixed phototype III. Epidermal thickness increases from top to bottom while blood volume fraction increases left to right.

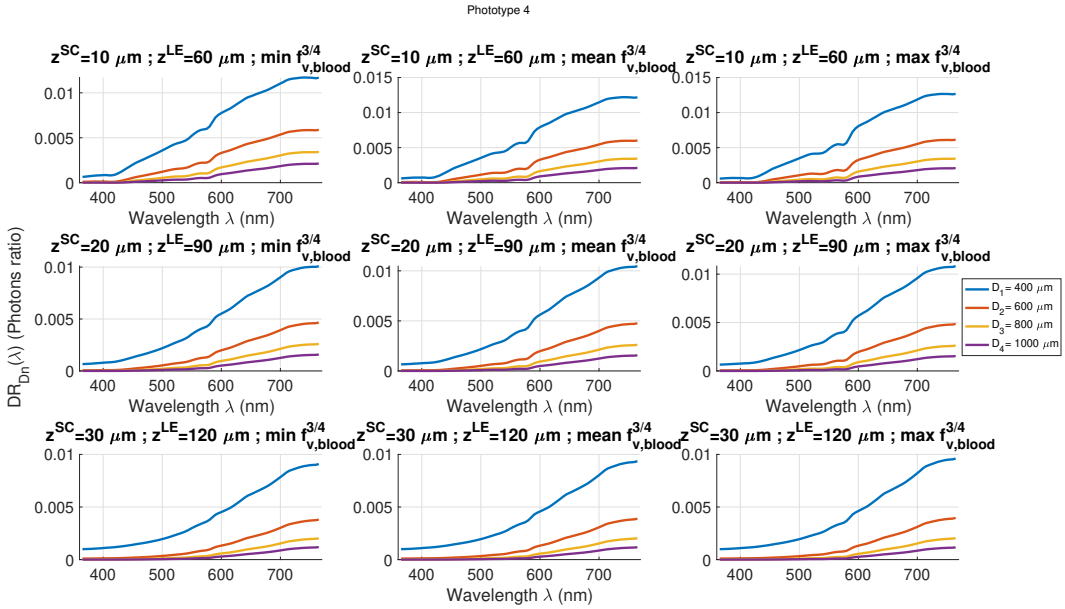

Figure B.5: DR spectra for several skin configuration and fixed phototype IV. Epidermal thickness increases from top to bottom while blood volume fraction increases left to right.

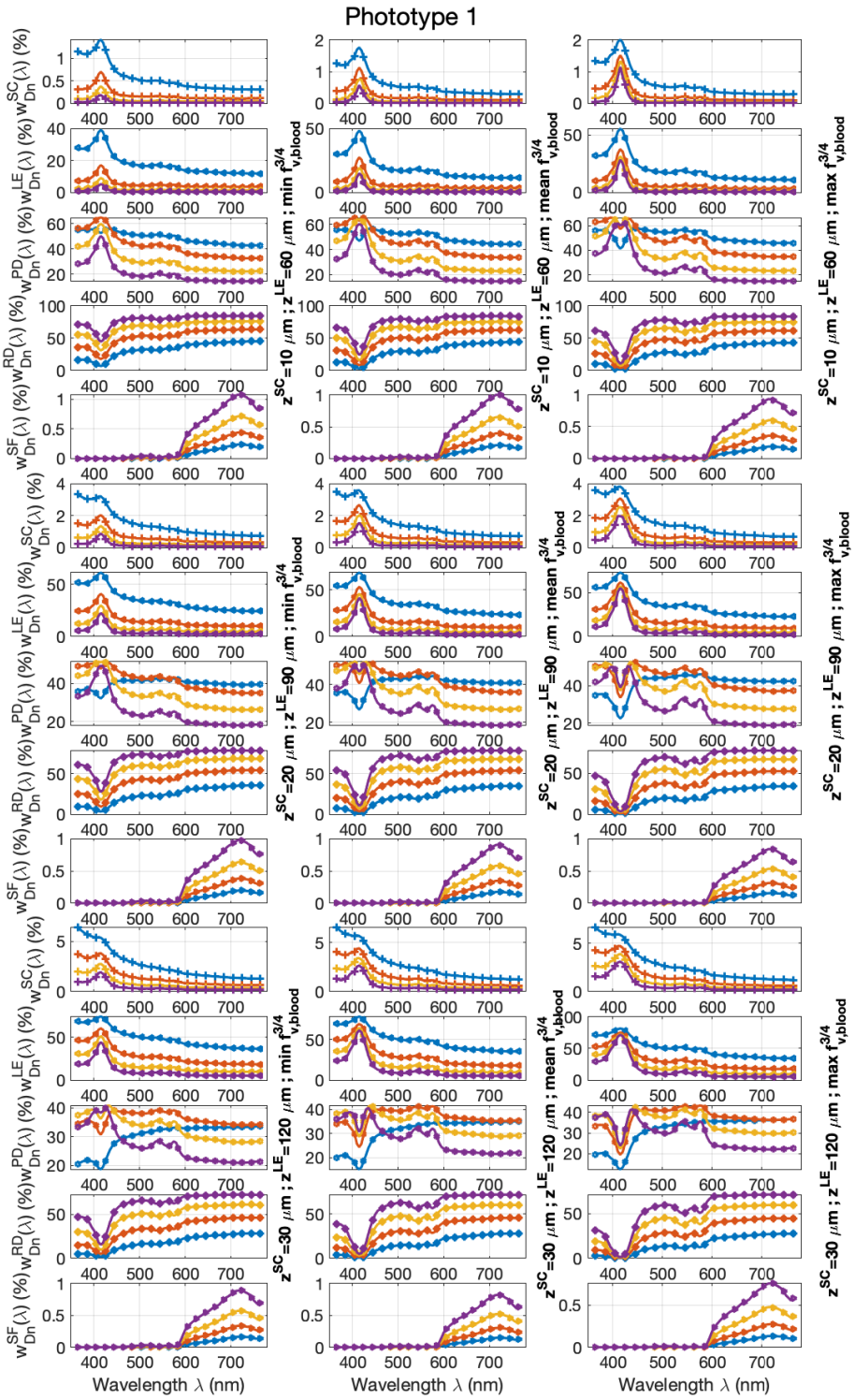

Figure B.6: Weight fraction in DR spectra for several skin configuration and fixed phototype I given in Fig. B.2. Epidermal thickness increases from top to bottom while blood volume fraction increases left to right.

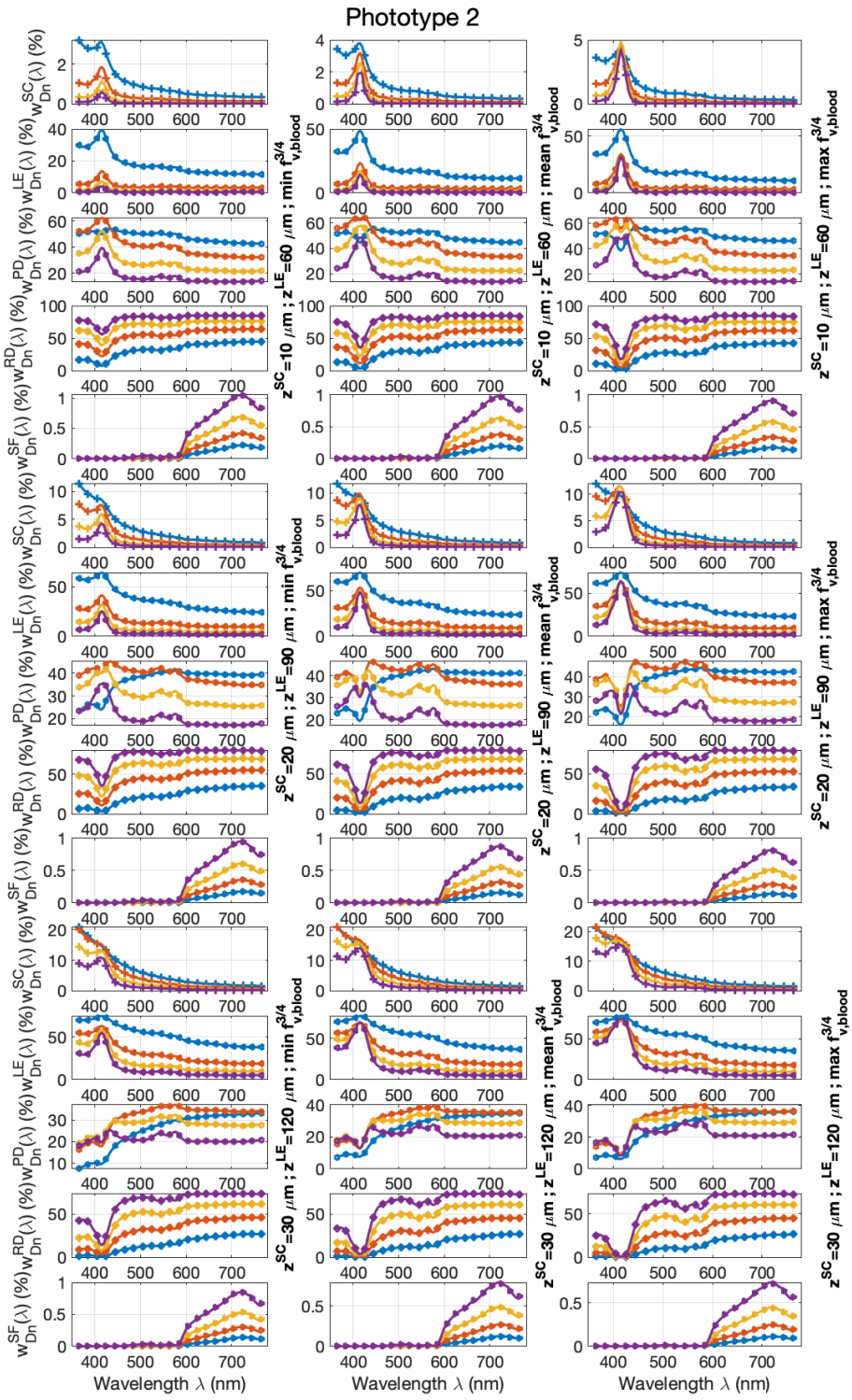

Figure B.7: Weight fraction in DR spectra for several skin configuration and fixed phototype II given in Fig. B.3. Epidermal thickness increases from top to bottom while blood volume fraction increases left to right.

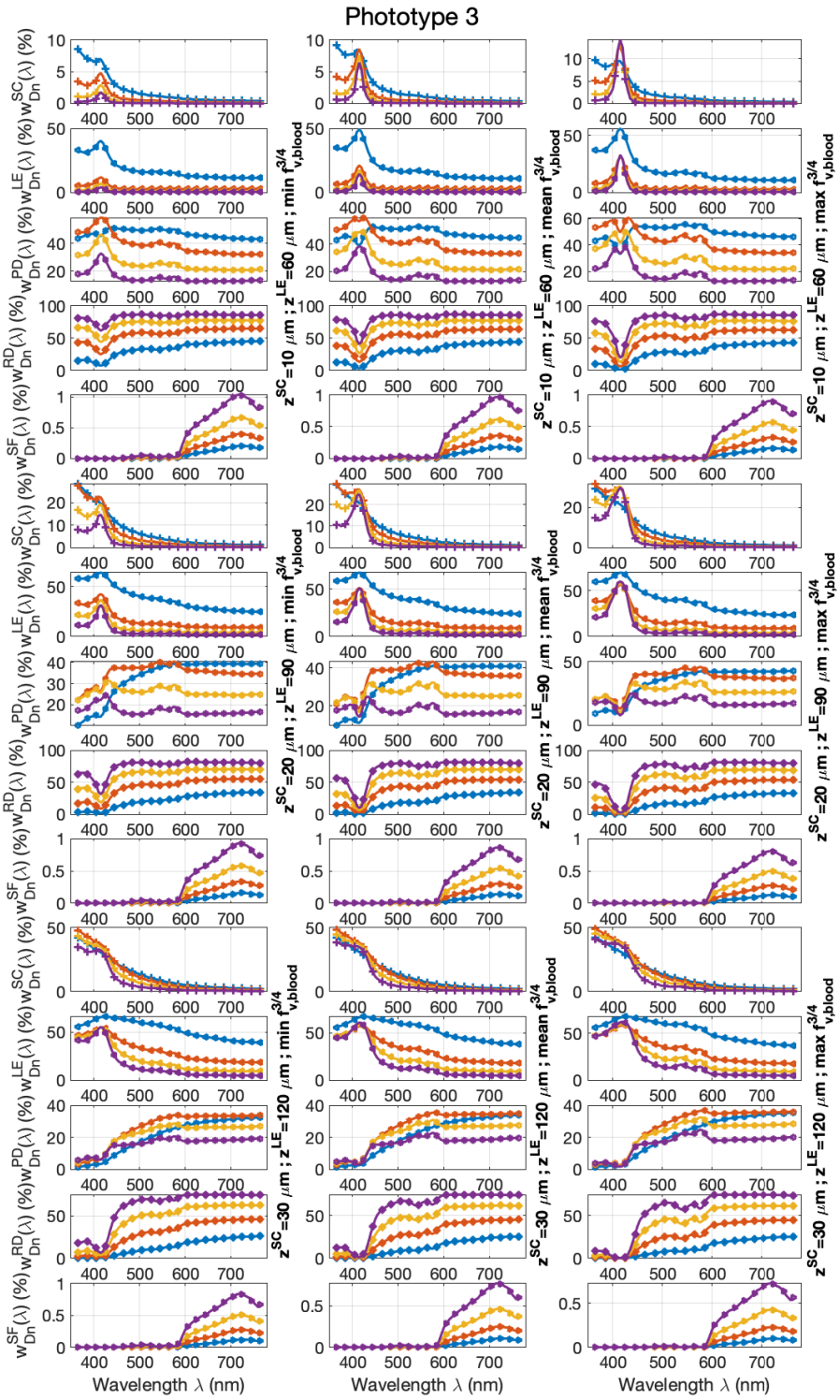

Figure B.8: Weight fraction in DR spectra for several skin configuration and fixed phototype III given in Fig. B.4. Epidermal thickness increases from top to bottom while blood volume fraction increases left to right.

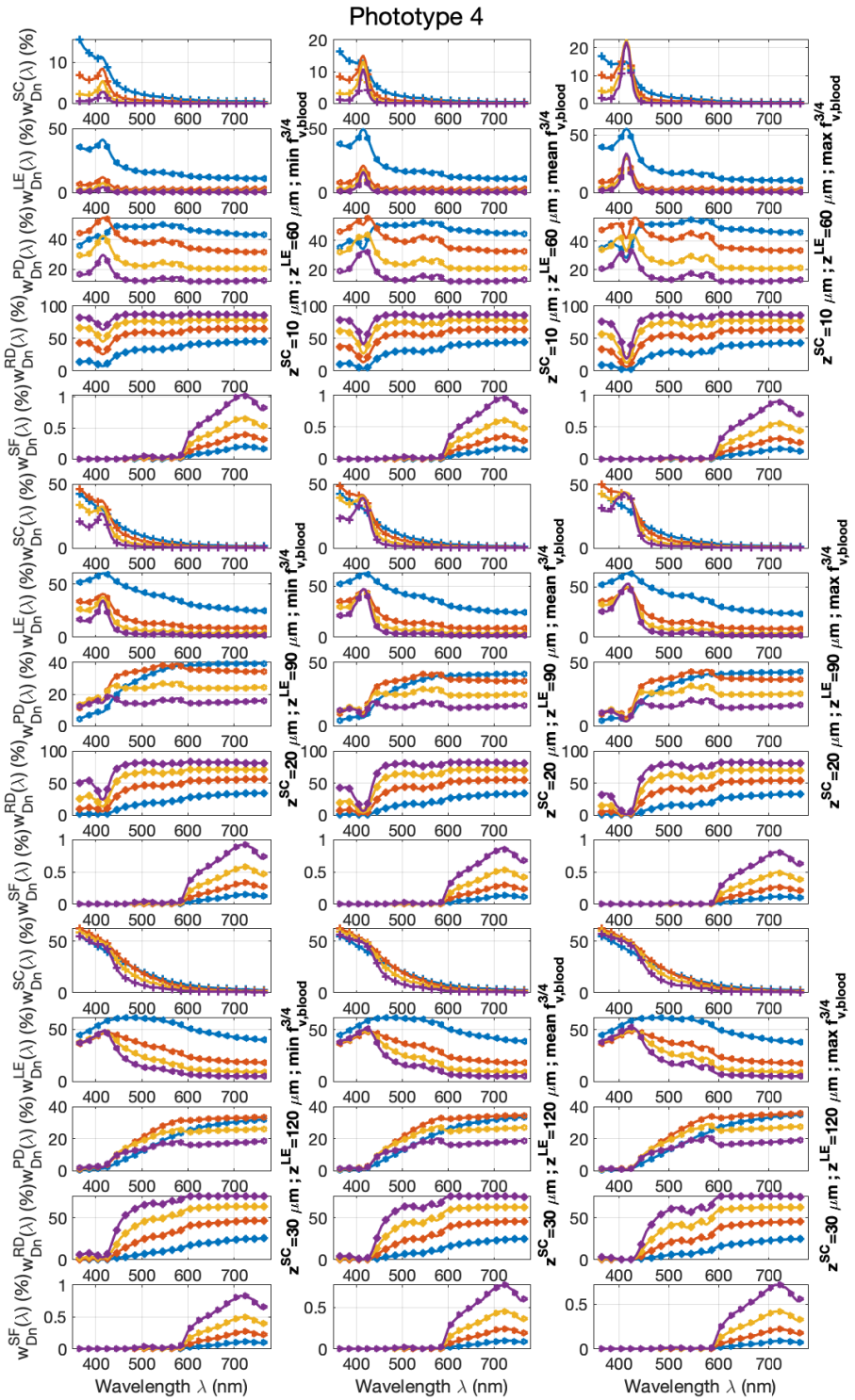

Figure B.9: Weight fraction in DR spectra for several skin configuration and fixed phototype IV given in Fig. B.5. Epidermal thickness increases from top to bottom while blood volume fraction increases left to right.

Appendix C

Chapter 3 appendix

C.1 Illustrative example of inverse problem solving convergence using PSO

C.1.1 Experimental protocol description

We present here an example of the realization of a purely numerical inverse problem. This was done on the one hand, to become familiar with the PSO algorithm described in algorithm 4, and on the other hand to check its convergence. This is possible here, thanks to the knowledge of the ground truth, since the target spectra are themselves derived from simulations. The direct method parameters correspond to a *SpectroLive* configuration. The medium is a mono-layer one, in which we introduced 2 fluorophores with distinct areas of absorption and emission. Those are represented on Fig. C.1. The first one was introduced with a concentration $c_1 = 0.005$ while the second is associated to the concentration $c_2 = 0.002$. The fluorophore absorption coefficient is linked to both parameter according:

$$\mu_{a,fluo}(\lambda) = c_{fluo}\mu^{norm}_{a,fluo}(\lambda) \tag{C.1}$$

Where $\mu^{norm}_{a,fluo}$ is the normalized fluorophore absorption coefficient modeled by a Gaussian function of maximum 1 cm^{-1}. We consider all the other medium parameters known. In other words, the parameter vector to estimate is reduced to $\mathbf{p_{target}} = (c_1\ c_2)$.

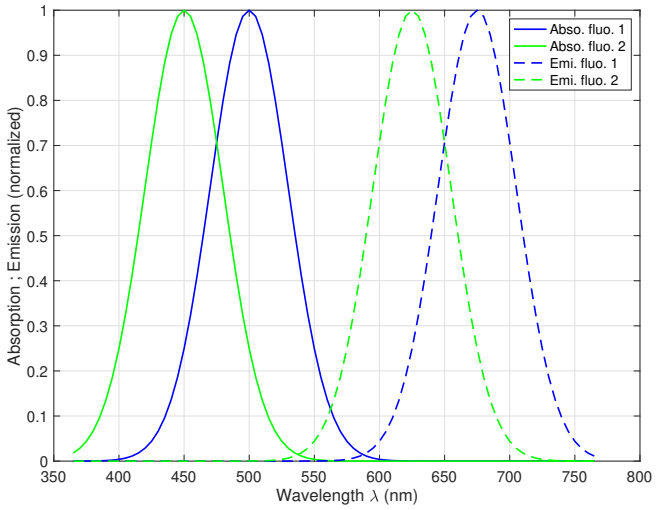

Figure C.1: Absorption and emission shapes of the 2 target fluorophores.

C.1.1.1 Convergence to target parameters

We chose to set $N_{iter} = 51$, and the particles number was $N_{par} = 20$. The simulated target spectra were obtained by sending 10^6 photons for each wavelength while the iterative ones were get by sending 10^5 photons. Indeed, we have to be thrifty, because the inverse problem will, in these conditions, call $N_{iter} \times N_{par} = 1020$ times the direct method. The cost function was one provided in Eq. (3.3)). To illustrate the convergence process, we decided to present the positions of the 20 particles, and the score associated in a 3D-plot. The x-axis and y-axis represent respectively the value of the fluorophore 1 concentration and the value of the fluorophore 2 concentration tested while the z-axis represents the cost associated to the described configuration. This 3D-plot is represented for 9 iterations on Fig. C.2. The black cross is the ground truth point $\mathbf{p_{target}} = (c_1, c_2)$ with null cost *i.e.* $z = 0$. One can clearly see that particles converge toward this position.

$\hat{\mathbf{p}}$ and the cost associated to this estimation are output of the PSO program. Here, we get $\hat{\mathbf{p}} = \mathbf{p_{target}}$, so the algorithm has converged toward the ground truth. The residual cost was $cost_{total}(\hat{\mathbf{p}}) = 5.47$ and it comes from the noise caused by the low number of photons sent during the inverse problem. The calculation duration was about 30 minutes, but the Fig. C.2 shows that the convergence was almost finished after 23 iterations. It would be useful to subsequently introduce a stop criterion, which would stop the search without reaching the maximum number of iterations.

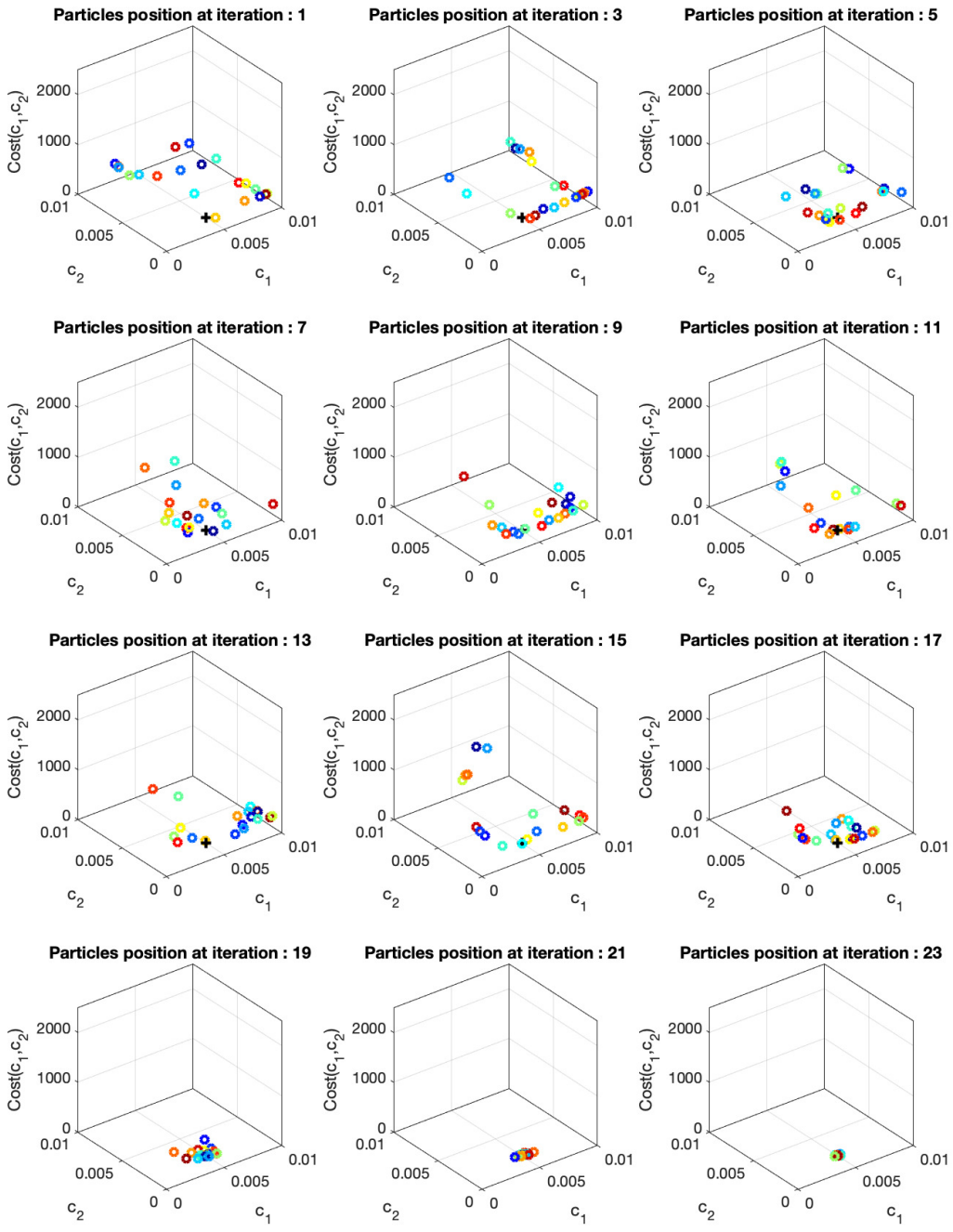

Figure C.2: Particles convergence toward the expected solution

Appendix D

Chapter 4 appendix

D.1 User interface for optical bench acquisition (DIS)

D.1.1 Specifications

As quickly introduced in section 4.3, a user interface has been developed to monitor and automate as much as possible the signals acquisition. As indicated in protocol description in section 4.3.2.1, the manipulations are very repetitive and moreover very time consuming. Indeed for each measurement of voltage, we must first impose the wavelength of the laser, then read the voltage of the photo-multiplier with a voltmeter before transferring it in a table. To characterize a sample with this manual method on the whole spectrum *i.e.* $\lambda \in [400 - 850]\ nm$ with $\Delta\lambda = 25\ nm$, we approximately took 40 minutes (for M_R and M_T measurements). Moreover, acquiring signals in this way is prone to errors.

This is why a man-machine interface is being designed. This one is coded in *LabView* thanks to the expertise of an assistant engineer colleague (Clarice Perrin-Mozet), and allows to (i) shift the laser emission wavelength, (ii) acquire the photo-multiplier voltages at each λ, (iii) display live the voltages acquired by the different photo-detectors of the optical bench, (iv) do the calculation appearing on Eq.(4.7), (4.8) and (4.9), (v) write all the tensions and calculated data in a table file (.csv) and (vi) saving and then loading of all the voltages acquired independent of the sample to be characterized (measurements of the dark voltages, standard and empty transmissions). In other words the remaining tasks that have to be done by the experimenter are the positioning of the integrating spheres and samples/standard for the step k described in section 4.3.2.1 and 4.3.2.2, and the selection of this step k in the man-machine interface. For a similar characterization of a sample, the duration of the acquisition decrease at approximately 10 minutes.

D.1.2 User interface overview

Fig. D.1 shows screen captures of the 4 tabs of the user interface.

D.2 User interface for optical properties estimation (IAD)

D.2.1 Motivations

Once the data set is acquired, the optical parameters are obtained by the IAD method. The use of this algorithm is rather complex since it requires so far the design of an input text file including (i) the measurement vectors from the optical bench, and (ii) all the parameters of the optical bench (e.g. the diameter of the laser beam, the diameter of the spheres, the thickness and optical index of the glass slides that "sandwich" the sample...). The architecture of this document must be scrupulously respected otherwise the algorithm can not work. The program was also called from the command line, which was not necessarily pleasant. For these reasons, a

graphical interface (in *Python* language) has been designed by internship students from *Telecom Nancy engineering school* (Amadis Lemore and Ambroise Sander) to apply the IAD from the transmittance, reflectance (and optionally collimated transmittance, see table 4.1) measurements and to obtain the optical parameters of the sample, *i.e.* $\mu_a(\lambda)$, $\mu'_s(\lambda)$ (and optionally $g(\lambda)$).

D.2.2 User interface overview

Fig. D.2 shows the the settings page (user input of the experiment parameters and loading of the optical measurement vectors) and the results page after IAD calculation of the designed interface.

D.3 Test of the linearity of the photo-detector response

D.3.1 Problem description

The correct calculation of transmittance, reflectance and reported transmittance is based on the assumption that the photo-detector provides tension proportional to optical flux (see Eq. (4.8), (4.7) and (4.9)). After several weeks of unexpected results (*i.e.* optical properties estimated at astonishing values), we cast our suspicions on this point. We should mention that our photo-detectors are actually photo-multipliers (the team in charge of purchases before the beginning of the thesis had obtained this choice to be sensitive to weak photonic fluxes). This choice is debatable and probably conventional photodiodes would be more effective. However, we had to make do with these PM. Unlike a photodiode, the PM has an adjustable gain G (V) which amplifies the number of electrons associated with the detection of a photon. The manufacturer advised in the data-sheet to use the PM in the range $[0.3 - 1]$ V while the controller accept G in $[0 - 1.2]$ V. The increase in gain is also responsible for an earlier saturation of the detector. The light power dynamics being important between the white measurements (transmittance and reflectance at 100%) and the sample measurement (sometimes very opaque), we are faced with a difficult compromise to satisfy. Unfortunately, we made the wrong choice at first, by keeping G weak to ensure to not saturate, without suspecting that being out of the advised range would be responsible for non-linear answer of the PM as described in Fig. D.3. This one shows the tension output provided for several values of G as a function of the incident optical power measured by a power-meter. To not saturate with bigger G values, we introduce OD in the laser beam.

D.3.2 Validation of the linearity of each PM

Based on observation of the Fig.D.3, we decided to increase the gain of our 3 PM (see Fig.4.3), while adding OD to compensate and then not saturate. Although physically illogical, we opted for this temporary solution while waiting to exchange our photo detectors with conventional photodiodes. For the sake of rigor, we also decided to (i) test the 3 PM concerned to ensure that their response was identical and (ii) on 5 wavelengths covering the entire visible spectrum. Resulting characteristics are provided in Fig. D.4, which also provide the R^2 for all the curve to validate the linearity of each answer. The gain values for each of the PM, as well as the presence or not of OD in the laser path in indicated in the sub-figure title. The chosen configuration finally provides the expected behavior for reflectance, transmittance and unscattered transmittance measurements.

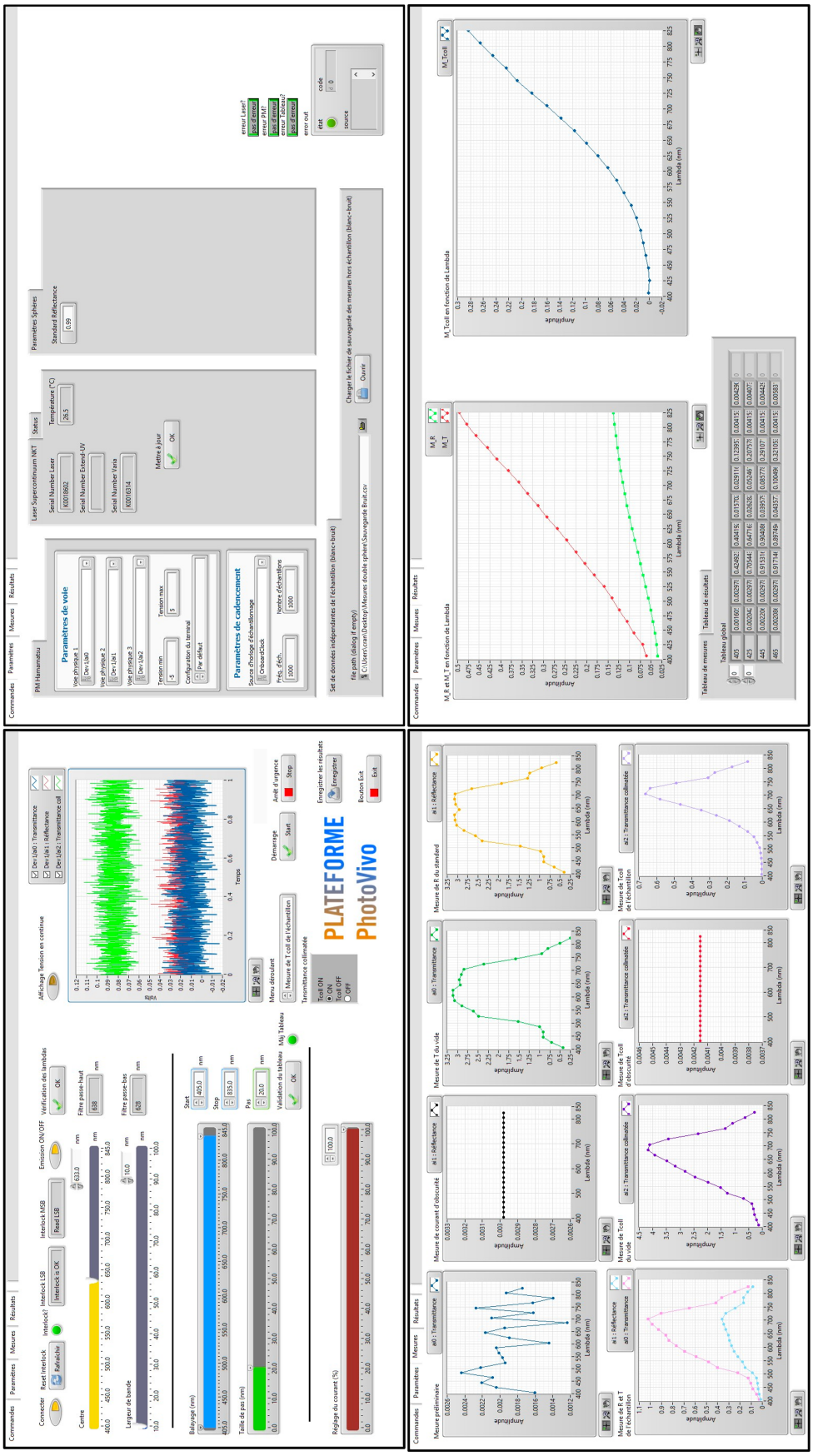

Figure D.1: Man-machine interface we design to conduct the double integrating spheres measurements.

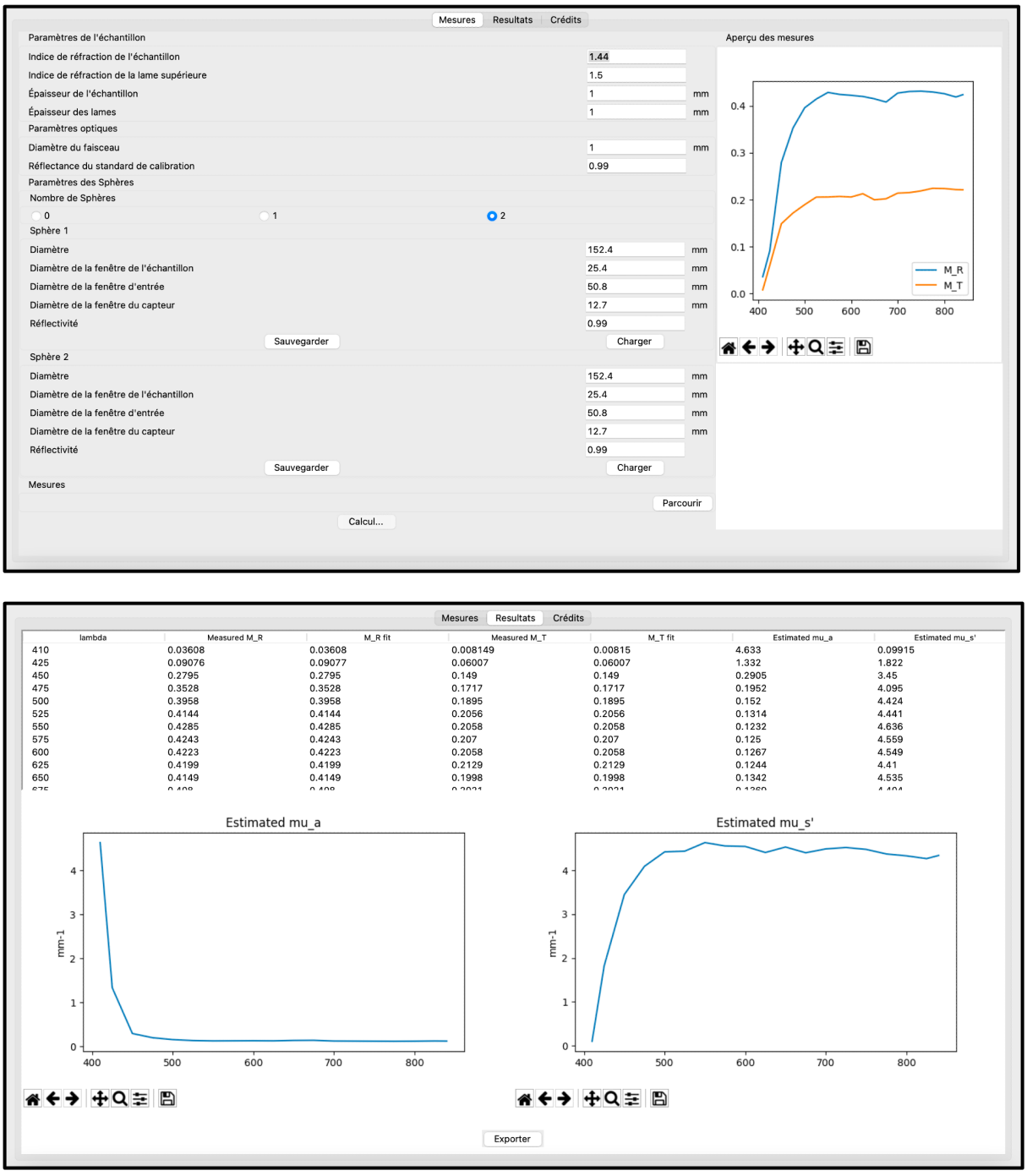

Figure D.2: Graphical interface to run the IAD method calculation. Top sub-figure shows the input data tab, whereas the bottom one illustrates the result tab after calculation.

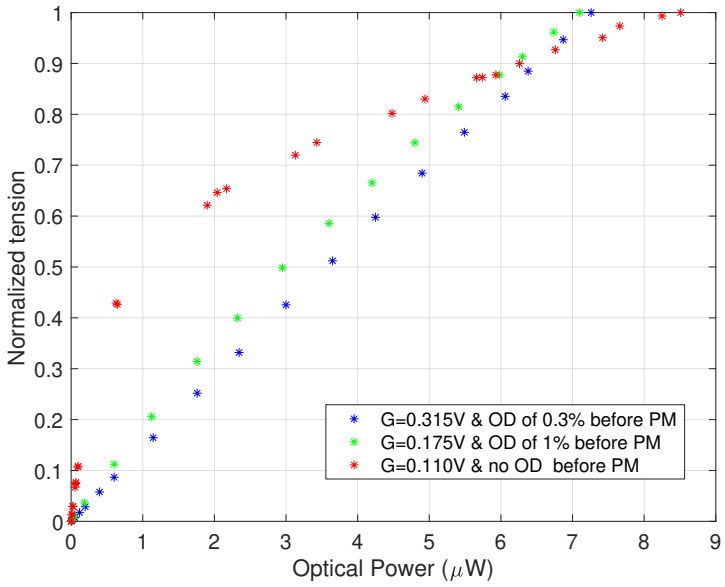

Figure D.3: Normalized tension output of the PM for 3 values of the gain G as a function of the optical incident power.

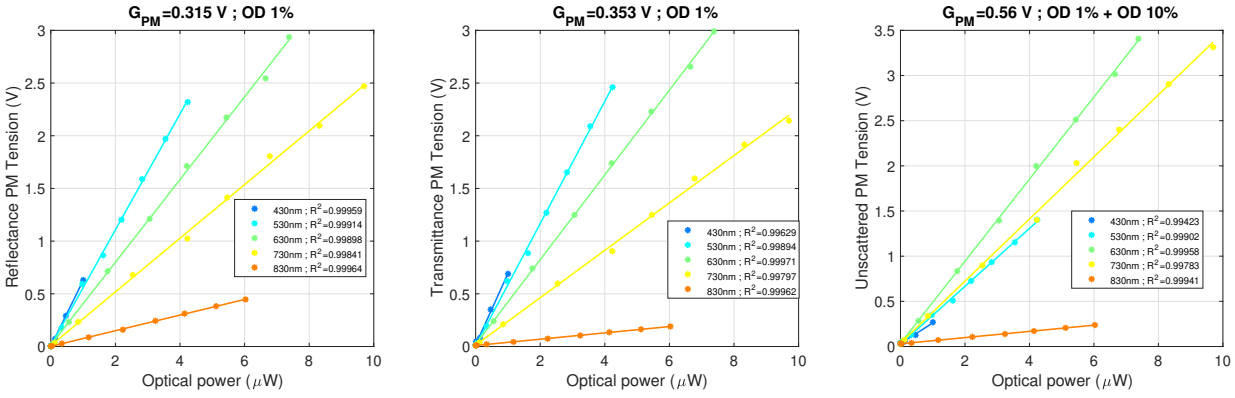

Figure D.4: Verification of the linear response of reflectance (left), transmittance (middle) and collimated transmittance (right) PM. The gain values for each of the PM, as well as the presence or not of OD in the laser path in indicated in the sub-figure title.

Bibliography

[Abdat 2012] F. Abdat, M. Amouroux, Y. Guermeur et W. Blondel. *Hybrid feature selection and svm-based classification for mouse skin precancerous stages diagnosis from bimodal spectroscopy.* Optics Express, vol. 20, page 228–244, 2012. (Cité en page 35.)

[Aernouts 2013] Ben Aernouts, Eduardo Zamora-Rojas, Robbe Van Beers, Rodrigo Watté, Ling Wang, Mizuki Tsuta, Jeroen Lammertyn et Wouter Saeys. *Supercontinuum laser based optical characterization of Intralipid® phantoms in the 500-2250 nm range.* Opt. Express, vol. 21, no. 26, pages 32450–32467, Dec 2013. (Cité en pages xviii, 109, 110, 111, 134 et 135.)

[Ahlgrimm-Siess 2018] Verena Ahlgrimm-Siess, Martin Laimer, Harold S. Rabinovitz, Margaret Oliviero, Rainer Hofmann-Wellenhof, Ashfaq A. Marghoob et Alon Scope. *Confocal Microscopy in Skin Cancer.* Current Dermatology Reports, vol. 7, pages 105 – 118, 2018. (Cité en page 28.)

[Alerstam 2008] E. Alerstam, T. Svensson et S. Andersson-Engels. *Parallel computing with graphics processing units for high-speed monte carlo simulation of photon migration.* Journal of Biomedical Optics, vol. 13, 2008. (Cité en page 38.)

[Altshuler 2005] Gregory Altshuler, Mikhail Smirnov et Ilya Yaroslavsky. *Lattice of optical islets: a novel treatment modality in photomedicine.* Journal of Physics D: Applied Physics, vol. 38, no. 15, page 2732, 2005. (Cité en page 65.)

[Amouroux 2008] Marine Amouroux. *Caractérisation de la transformation néoplasique de la peau par spectroscopies optiques sur fantôme de mélanome et carcinome épidermoïde murin photo-induit.* PhD thesis, Université Henri Poincaré - Nancy, 2008. (Cité en pages 19, 54 et 62.)

[Amouroux 2009] M. Amouroux, G. Díaz-Ayil et W. C. P. M. Blondel. *Classification of ultraviolet irradiated mouse skin histological stages by bimodal spectroscopy: multiple excitation autofluorescence and diffuse reflectance.* Journal of Biomedical Optics, vol. 14, page 14011–14, 2009. (Cité en page 35.)

[Amouroux 2017] M. Amouroux, W. Blondel et A. Delconte. *Medical device for fibered bimodal optical spectroscopy*, World patent number: WO2017093316 (A1), 2017. (Cité en page 31.)

[Arifler 2005] Dizem Arifler, Richard A. Schwarz, Sung K. Chang et Rebecca Richards-Kortum. *Reflectance spectroscopy for diagnosis of epithelial precancer: model-based analysis of fiber-optic probe designs to resolve spectral information from epithelium and stroma.* Appl. Opt., vol. 44, no. 20, pages 4291–4305, Jul 2005. (Cité en pages 55, 76 et 86.)

[Astner 2004] S. Astner et R. R. Anderson. *Skin phototypes 2003.* J Invest Dermatol, vol. 122, 2004. (Cité en pages 21 et 22.)

[Aydin 2002] E.D. Aydin. *A comparison between transport and diffusion calculations using a finite element-spherical harmonics radiation transport method.* American Association of Physicists in Medicine, 2002. (Cité en page 37.)

[Bashkatov 2007] Alexey N. Bashkatov, Elina A. Genina, Vyacheslav I. Kochubey, Anna A. Gavrilova, Sergey V. Kapralov, Veniamin A. Grishaev et Valery V. Tuchin. *Optical properties of human stomach mucosa in the spectral range from 400 to 2000 nm: Prognosis for gastroenterology.* Medical Laser Application, vol. 22, page 95–104, 2007. (Cité en page 121.)

[Bass 2017] Leonid P. Bass, Olga V. Nikolaeva, Alexander V. Bykov et Mikhail Yu. Kirillin. *Finite difference methods for solving the transport equation in the problems of optical biomedical diagnostics.* Special Issue. Years in Biophotonics: 70th Anniversary of Prof. A.V. Priezzhev, 2017. (Cité en page 37.)

[Blondel 2021] Walter Blondel, Alain Delconte, Grégoire Khairallah, F. Marchal, A. Gavoille et Marine Amouroux. *Spatially-Resolved Multiply-Excited Autofluorescence and Diffuse Reflectance Spectroscopy: SpectroLive Medical Device for Skin In Vivo Optical Biopsy.* Electronics, vol. 10, page 243, 2021. (Cité en pages xiii, 31, 32 et 65.)

[Borisova 2014] Ekaterina G. Borisova, Liliya P. Angelova et Elmira P. Pavlova. *Endogenous and Exogenous Fluorescence Skin Cancer Diagnostics for Clinical Applications.* Journal of Selected Topics in Quantum Electronics, vol. 20, 2014. (Cité en pages 27, 28, 30, 54 et 65.)

[Bratchenko 2017] Ivan A. Bratchenko, Dmitry N. Artemyev, Oleg O. Myakinin, Yulia A. Khristoforova, Alexander A. Moryatov, Sergey V. Kozlov et Valery P. Zakharova. *Combined Raman and autofluorescence ex vivo diagnostics of skin cancer in near-infrared and visible regions.* Journal of Biomedical Optics, vol. 22, 2017. (Cité en page 30.)

[Breslin 2003] Tara M. Breslin et Nirmala Ramanujam. *Autofluorescence and Diffuse Reflectance Properties Malignant and Benign Breast Tissues.* Annals of Surgical Oncology, vol. 11, pages 65–70, 2003. (Cité en page 54.)

[Cen 2010] Haiyan Cen, Renfu Lu et Kirk Dolan. *Optimization of inverse algorithm for estimating the optical properties of biological materials using spatially-resolved diffuse reflectance.* Inverse Problems in Science and Engineering, vol. 18, no. 6, pages 853–872, 2010. (Cité en page 89.)

[Chan 1996] Eric K. Chan, Brian Sorg, Dmitry Protsenko, Michael O'Neil, Massoud Motamedi et Ashley J. Welch. *Effects of Compression on Soft Tissue Optical Properties.* IEEE JOURNAL OF SELECTED TOPICS IN QUANTUM ELECTRONICS, vol. 2, 1996. (Cité en page 121.)

[Chopra 2015] K. Chopra, D. Calva, M. Sosin, KK. Tadisina, A. Banda, C. De La Cruz, MR. Chaudhry, T. Legesse, CB. Drachenberg, PN. Manson et MR. Christy. *A comprehensive examination of topographic thickness of skin in the human face.* Aesthet Surg J, vol. 35, pages 1007–13, 2015. (Cité en page 62.)

[Colas 2020] Victor Colas, Christian Daul, Grégoire Khairallah, Marine Amouroux et Walter Blondel. *Spatially resolved diffuse reflectance and autofluorescence photon depth distribution in human skin spectroscopy: a modeling study.* In Qingming Luo, Xingde Li, Ying Gu et Dan Zhu, editeurs, Optics in Health Care and Biomedical Optics X, volume 11553, pages 82 – 96. International Society for Optics and Photonics, SPIE, 2020. (Cité en page 63.)

[Colas 2021a] Victor Colas, Walter Blondel, Grégoire Khairallah, Christian Daul et Marine Amouroux. *Proposal for a Skin Layer-Wise Decomposition Model of Spatially-Resolved Diffuse Reflectance Spectra Based on Maximum Depth Photon Distributions: A Numerical Study.* Photonics, vol. 8, no. 10, 2021. (Cité en pages 48 et 99.)

[Colas 2021b] Victor Colas, Christian Daul, Gregoire Khairallah, Marine Amouroux et Walter Blondel. *Influence of human epidermal thickness on penetration depth of detected photons in spatially-resolved diffuse reflectance spectroscopy: a numerical study.* In Bennett L. Ibey et Norbert Linz, editeurs, Optical Interactions with Tissue and Cells XXXII, volume 11640, page 116400H. International Society for Optics and Photonics, SPIE, 2021. (Cité en page 79.)

[Colas 2022a] Victor Colas, Marine Amouroux, Christian Daul, Clarice Perrin-Mozet et Walter Blondel. *Comparative study of optical properties estimation on liquid optical phantoms using spatially-resolved diffuse reflectance spectroscopy and double integrating spheres methods.* In Valery V. Tuchin, Walter C. P. M. Blondel et Zeev Zalevsky, editeurs, Tissue Optics and Photonics II, volume 12147, page 1214705. International Society for Optics and Photonics, SPIE, 2022. (Cité en page 134.)

[Colas 2022b] Victor Colas, Christian Daul, Grégoire Khairallah, Marine Amouroux et Walter Blondel. *Improved estimation of the optical properties in a skin five-layer model from spatially resolved diffuse reflectance spectra using a layer-by-layer approach and optimized combinations of wavelengths and source-detector distances.* In Adam Wax et Vadim Backman, editeurs, Biomedical Applications of Light Scattering XII, volume 11974, page 1197408. International Society for Optics and Photonics, SPIE, 2022. (Cité en page 98.)

[Colas 2022c] Victor Colas, Christian Daul, Grégoire Khairallah M.D., Marine Amouroux et Walter Blondel. *Theoretical definition and experimental validation of an correction factor to standardize the absolute magnitude of simulated and clinical spatially-resolved diffuse reflectance spectra.* In Adam Wax et Vadim Backman, editeurs, Biomedical Applications of Light Scattering XII, volume 11974, pages 1 – 8. International Society for Optics and Photonics, SPIE, 2022. (Cité en page 135.)

[Ding 2006a] Huafeng Ding, Jun Q Lu, William A Wooden, Peter J Kragel et Xin-Hua Hu. *Refractive indices of human skin tissues at eight wavelengths and estimated dispersion relations between 300 and 1600 nm.* Phys. Med. Biol., vol. 51, page 1479–1489, 2006. (Cité en page 27.)

[Ding 2006b] Huafeng Ding, Jun Q Lu, William A Wooden, Peter J Kragel et Xin-Hua Hu. *Refractive indices of human skin tissues at eight wavelengths and estimated dispersion relations between 300 and 1600 nm.* Phys. Med. Biol., vol. 51, page 1479–1489, 2006. (Cité en page 65.)

[Drakaki 2009] E. Drakaki, E. Kaselouris, M. Makropoulou, A.A. Serafetinides, A. Tsenga, A.J. Stratigos, A.D. Katsambas et C. Antoniou. *Laser-Induced Fluorescence and Reflectance Spectroscopy for the Discrimination of Basal Cell Carcinoma from the Surrounding Normal Skin Tissue.* Skin Pharmacol Physiol, vol. 22, pages 158–165, 2009. (Cité en pages 27 et 28.)

[Dubois 2018a] A. Dubois, O. Levecq, H. Azimani, A. Davis, J. Ogien, D. Siret et A. Barut. *Line-field confocal time-domain optical coherence tomography with dynamic focusing.* Optics express, vol. 26, page 33534–33542, 2018. (Cité en page 28.)

[Dubois 2018b] A. Dubois, O. Levecq, H. Azimani, D. Siret, A. Barut, M. Suppa, J. Del Marmol V.and Malvehy, E. Cinotti et P. Rubegni. *Line-field confocal optical coherence tomography for high-resolution noninvasive imaging of skin tumors.* Journal of Biomedical Optics, vol. 23, page 106007, 2018. (Cité en page 28.)

[Fang 2010] Q. Q. Fang. *Mesh-based Monte Carlo method using fast ray-tracing in Plucker coordinates.* Biomed. Opt. Express, vol. 1, page 165–175, 2010. (Cité en page 38.)

[Farrell 1992] T. J. Farrell, M. S. Patterson et B. Wilson. *A diffusion theory model of spatially resolved, steady-state diffuse reflectance for the noninvasive determination of tissue optical properties in vivo.* Med. Phys., vol. 19, page 879 – 888, 1992. (Cité en page 36.)

[Flock 1988] Stephen T Flock, Brian C Wilson et Michael S Patterson. *Hybrid Monte Carlo - Diffusion Theory Modelling Of Light Distributions In Tissue.* In Michael W. Berns, editeur, Laser Interaction with Tissue, volume 0908, pages 20 – 28. International Society for Optics and Photonics, SPIE, 1988. (Cité en page 38.)

[Fredriksson 2012] Ingemar Fredriksson, Marcus Larsson et Tomas Strömberg. *Inverse Monte Carlo method in a multilayered tissue model for diffuse reflectance spectroscopy.* Journal of Biomedical Optics, vol. 17, no. 4, pages 1 – 13, 2012. (Cité en pages 55, 79, 86 et 92.)

[Garcia-Uribe 2012] Alejandro Garcia-Uribe, Jun Zou et et al. Madeleine Duvic. *In Vivo Diagnosis of Melanoma and Non-melanoma Skin Cancer Using Oblique Incidence Diffuse Reflectance Spectrometry.* Cancer Res., vol. 72, pages 2738–2745, 2012. (Cité en page 27.)

[Genina 2009] E. A. Genina, A. N. Bashkatov, V. I. Kochubey et V. V. Tuchin. *Effect of Storage Conditions of Skin Samples on Their Optical Characteristics.* Optics and Spectroscopy, vol. 107, page 986–991, 2009. (Cité en page 121.)

[Ghervase 2015] Luminita Ghervase, Simona Dontu Dan Savastru, Ana-Maria Forsea et Ekaterina Borisova. *Characterization of Human Skin by Fluorescence, Exemplified by Dermatofibroma, Keratoacanthoma, and Seborrheic Keratosis.* Analytical Letters, 2015. (Cité en pages 26 et 65.)

[Greening 2018] Gage Greening, Ariel Mundo, Narasimhan Rajaram et Timothy J. Muldoon. *Sampling depth of a diffuse reflectance spectroscopy probe for in-vivo physiological quantification of murine subcutaneous tumor allografts.* Journal of Biomedical Optics, vol. 23, no. 8, pages 1 – 14, 2018. (Cité en page 78.)

[Hennessy 2014] Ricky Hennessy, Will Goth, Manu Sharma, Mia K. Markey et James W. Tunnell. *Effect of probe geometry and optical properties on the sampling depth for diffuse reflectance spectroscopy.* Journal of Biomedical Optics, vol. 19, no. 10, pages 1 – 6, 2014. (Cité en page 78.)

[Hidenobu Arimoto 2005] Mariko Egawa Hidenobu Arimoto et Yukio Yamada. *Depth profile of diffuse reflectance near-infrared spectroscopy for measurement of water content in skin.* Skin Research and Technology, vol. 11, pages 27–35, 2005. (Cité en pages 33, 55 et 78.)

[Jacques 2013] Steven L Jacques. *Optical properties of biological tissues: a review.* Physics in Medicine and Biology, vol. 58, no. 11, pages R37–R61, may 2013. (Cité en pages 23, 24 et 64.)

[Jonasson 2018] Hanna Jonasson, Ingemar Fredriksson, Sara Bergstrand, Carl Johan Östgren, Marcus Larsson et Tomas Strömberg. *In vivo characterization of light scattering properties of human skin in the 475- to 850-nm wavelength range in a Swedish cohort.* Journal of Biomedical Optics, vol. 23, no. 12, pages 1 – 6, 2018. (Cité en page 88.)

[Karsten 2012] Aletta E. Karsten et Jacoba E. Smit. *Modeling and Verification of Melanin Concentration on Human Skin Type.* Photochemistry and Photobiology, vol. 88, no. 2, pages 469–474, 2012. (Cité en page 64.)

[Kazanci 2015] Huseyin Ozgur Kazanci et Murat Canpolat. *Depth Normalization Algorithm for Continuous Wave Reflectance Diffuse Optical Tomography System.* El-Cezeri Journal Of Science And Engineering, vol. 2, pages 40–46, 01 2015. (Cité en pages 57 et 74.)

[Keller 2010] Matthew D. Keller, Robert H. Wilson, Mary-Ann Mycek et Anita Mahadevan-Jansen. *Monte Carlo Model of Spatially Offset Raman Spectroscopy for Breast Tumor Margin Analysis.* Appl. Spectrosc., vol. 64, no. 6, pages 607–614, Jun 2010. (Cité en page 37.)

[Khairallah 2018] Grégoire Khairallah, Marine Amouroux, François Plénat, Prisca Rakotomanga, Charles Soussen, Frédéric Marchal, Alain Delconte, Hang Chen et Walter Blondel. *Spatially resolved spectroscopy for guiding margin delineation during human skin carcinomas resection: first clinical results on diffuse reflectance and autofluorescence spectra and in vivo skin optical properties.* In Jürgen Popp, Valery V. Tuchin et Francesco Saverio Pavone, editeurs, Biophotonics: Photonic Solutions for Better Health Care VI, volume 10685, pages 200 – 206. International Society for Optics and Photonics, SPIE, 2018. (Cité en page 65.)

[Kholodtsova 2016] Maria N. Kholodtsova, Christian Daul, Victor B. Loschenov et Walter C. P. M. Blondel. *Spatially and spectrally resolved particle swarm optimization for precise optical property estimation using diffuse-reflectance spectroscopy.* Opt. Express, vol. 24, no. 12, pages 12682–12700, Jun 2016. (Cité en page 92.)

[Kienle 1998] A. Kienle, M. S. Patterson, N. Dögnitz, R. Bays, G. Wagnières et H. van den Bergh. *Noninvasive determination of the optical properties of two-layered turbid media.* Applied optics, page 779 – 791, 1998. (Cité en page 36.)

[Kirkby 1997] D. R. Kirkby et D. T. Delpy. *Parallel operation of Monte Carlo simulations on a diverse network of computers.* Phys. Med. Biol., vol. 42, 1997. (Cité en page 38.)

[Koenig 2015] Anne Koenig, Blandine Roig, Jimmy Le Digabel, Gwendal Josse et Jean-Marc Dinten. *Accessing deep optical properties of skin using diffuse reflectance spectroscopy.* In J. Quincy Brown et Volker Deckert, editeurs, Clinical and Biomedical Spectroscopy and Imaging IV, volume 9537, pages 42 – 49. International Society for Optics and Photonics, SPIE, 2015. (Cité en pages 57 et 74.)

[Kollias 2002] N. Kollias, G. Zonios et G. Stamatas. *Fluorescence spectroscopy of skin.* Vibrational Spectroscopy, page 17–23, 2002. (Cité en pages 26 et 65.)

[Krishnaswamy 2010] Aravind Krishnaswamy et Gladimir Baranoski. Light and skin interactions, 1st edition. Elsevier, 2010. (Cité en pages 24 et 65.)

[Larsson 2003] Marcus Larsson, Henrik Nilsson et Tomas Strömberg. *In vivo determination of local skin optical properties and photon path length by use of spatially resolved diffuse reflectance with applications in laser Doppler flowmetry.* Appl. Opt., vol. 42, no. 1, pages 124–134, 2003. (Cité en page 55.)

[Liebert 2004] A. Liebert, H. Wabnitz, J. Steinbrink, H. Obrig, M. Möller, R. Macdonald, A. Villringer et H. Rinneberg. *Time-resolved multidistance near-infrared spectroscopy of the adult head: intracerebral and extracerebral absorption changes from moments of distribution of times of flight of photons.* Appl Opt., vol. 43, no. 15, pages 3037 – 3047, 2004. (Cité en pages 55 et 86.)

[Liemert 2013] A. Liemert et A. Kienle. *Exact and efficient solution of the radiative transport equation for the semi-infinite medium.* Scientific Reports, page 2018, 2013. (Cité en page 36.)

[Lim 2014] Liang Lim, Brandon S. Nichols, Michael R. Migden, Narasimhan Rajaram, Jason Reichenberg, Mia K. Markey, Merrick I. Ross et James W. Tunnell. *Clinical study of noninvasive in vivo melanoma and nonmelanoma skin cancers using multimodal spectral diagnosis.* Journal of Biomedical Optics, vol. 19, 2014. (Cité en page 30.)

[Liu 2007] Q. Liu et N. Ramanujam. *Scaling method for fast Monte Carlo simulation of diffuse reflectance spectra from multilayered turbid media.* J. Opt. Soc. Am., vol. 24, page 1011–1025, 2007. (Cité en page 38.)

[Liu 2012] H. Liu, H. Gisquet, W. C. P. M. Blondel et F. Guillemin. *Bimodal spectroscopy for in vivo characterization of hypertrophic skin tissue : pre-clinical experimentation, data selection and classification.* Biomedical optics express, page 3278 – 3290, 2012. (Cité en page 30.)

[Lucassen 1996] Gerald W. Lucassen, Wim Verkruysse, Marleen Keijzer et Martin J.C. van Gemert. *Light distributions in a port wine stain model containing multiple cylindrical and curved blood vessels.* Lasers Surg. Med., vol. 18, pages 345–357, 1996. (Cité en page 38.)

[Lui 2012] H. Lui, J. Zhao, D. McLean et H. Zeng. *Real-time raman spectroscopy for in vivo skin cancer diagnosis.* Cancer research, vol. 72, page 2491–2500, 2012. (Cité en page 29.)

[Maiti 2020] Raman Maiti, Mengqui Duan, Simon G. Danby, Roger Lewis, Stephen J. Matcher et Matthew J. Carré. *Morphological parametric mapping of 21 skin sites throughout the body using optical coherence tomography.* Journal of the Mechanical Behavior of Biomedical Materials, vol. 102, page 103501, 2020. (Cité en page 62.)

[Martelli 2016] Fabrizio Martelli, Tiziano Binzoni, Antonio Pifferi, Lorenzo Spinelli, Andrea Farina et Alessandro Torricelli. *There's plenty of light at the bottom: statistics of photon penetration depth in random media.* Scientific Reports, vol. 6, 2016. (Cité en page 55.)

[Meglinski 2002] I. V. Meglinski et S. J. Matcher. *Quantitative assessment of skin layers absorption and skin reflectance spectra simulation in the visible and near-infrared spectral regions.* Physiol. Meas, 2002. (Cité en pages 23, 63 et 65.)

[Michels 2008] René Michels, Florian Foschum et Alwin Kienle. *Optical properties of fat emulsions.* Opt. Express, vol. 16, no. 8, pages 5907–5925, Apr 2008. (Cité en pages xviii, 109, 111 et 135.)

[Migacheva 2010] E. Migacheva, A. Pravdin et V. Tuchin. *Alterations in autofluorescence signal from rat skin ex vivo under optical immersion clearing.* Journal of Innovative Optical Health Sciences, vol. 3, page 147–152, 2010. (Cité en page 30.)

[Mogensen 2007] M. Mogensen et G. B. E. Jemec. *Diagnosis of nonmelanoma skin cancer/keratinocyte carcinoma : a review of diagnostic accuracy of nonmelanoma skin cancer diagnostic tests and technologies.* Dermatologic surgery : official publication for American Society for Dermatologic Surgery, vol. 33, page 1158–74, 2007. (Cité en page 29.)

[Moreau 2019] Julien Moreau. *Radiométrie*, FAll 2019. (Cité en pages xiii, 14 et 18.)

[Nachbar 1994] F. Nachbar, Stolz W., Merkle T., A. B. Cognetta, Vogt T., Landthaler M., Bilek P., Braun-Falco O. et Plewig G. *The abcd rule of dermatoscopy : high prospective value in the diagnosis of doubtful melanocytic skin lesions.* Journal of the American Academy of Dermatology, vol. 30, page 551–559, 1994. (Cité en page 28.)

[Nader 2010] Victor Le Nader. *Approche expérimentale et théorique de la diffusion Raman exaltée : résonance des plasmons de surface et effet de pointe.* PhD thesis, Université de Nantes, 2010. (Cité en page 15.)

[Nilsson 2002] H. Nilsson, M. Larsson, G. Nilsson et T. Strömberg. *Photon pathlength determination based on spatially resolved diffuse reflectance.* Journal of Biomedical Optics, vol. 7, pages 475–485, 2002. (Cité en page 55.)

[Nishidate 2007] Izumi Nishidate, Takaaki Maeda, Yoshihisa Aizu et Kyuichi Niizeki. *Visualizing depth and thickness of a local blood region in skin tissue using diffuse reflectance images.* Journal of Biomedical Optics, vol. 12, no. 5, pages 1 – 12, 2007. (Cité en page 64.)

[Ostermeyer 1997] M. R. Ostermeyer et S. L. Jacques. *Perturbation theory for diffuse light transport in complex biological tissues.* J. Opt. Soc. Am., vol. 14, page 255–261, 1997. (Cité en page 38.)

[Palmer 2006] Gregory M. Palmer et Nirmala Ramanujam. *Monte Carlo-based inverse model for calculating tissue optical properties. Part I: Theory and validation on synthetic phantoms.* Appl. Opt., vol. 45, no. 5, pages 1062–1071, Feb 2006. (Cité en pages 89 et 92.)

[Pickering 1992] John W Pickering, Christian J. M. Moes, H. J. C. M. Sterenborg, Scott A. Prahl et Martin J. C. van Gemert. *Two integrating spheres with an intervening scattering sample.* Opt. Soc. Am, 1992. (Cité en pages xix, 119 et 120.)

[Pickering 1993] John W. Pickering, Scott A. Prahl, Niek van Wieringen, Johan F. Beek, Henricus J. C. M. Sterenborg et Martin J. C. van Gemert. *Double-integrating-sphere system for measuring the optical properties of tissue.* Appl. Opt., vol. 32, no. 4, pages 399–410, Feb 1993. (Cité en page 132.)

[Pires 2016] L. Pires, V. Demidov, I. A. Vitkin, V. S. Bagnato, C. Kurachi et B. C. Wilson. *Optical clearing of melanoma in vivo : characterization by diffuse reflectance spectroscopy and optical coherence tomography.* Journal of Biomedical Optics, vol. 21, page 081210, 2016. (Cité en page 30.)

[Prahl 1993] Scott A. Prahl, Martin J. C. van Gemert et Ashley J. Welch. *Determining the optical properties of turbid media by using the adding-doubling method.* Opt. Soc. Am, 1993. (Cité en page 120.)

[Prahl 1995] Scott Prahl. *The Adding-Doubling Method*, 1995. (Cité en page 119.)

[Prahl 2011] Scott Prahl. *Everything I think you should know about Inverse Adding-Doubling*, 2011. (Cité en pages xix, 102, 109, 120, 124, 125 et 127.)

[Prahl 2018] Scott Prahl. *A compendium of tissue optical properties*, 2018. http://omlc.ogi.edu/spectra/. (Cité en pages xiii, 23, 24, 25, 64, 65, 123 et 134.)

[Prokhorov 2003] Alexander V. Prokhorov, Sergey N. Mekhontsev et Leonard M. Hanssen. *Monte Carlo modeling of an integrating sphere reflectometer.* Appl. Opt., vol. 42, no. 19, pages 3832–3842, Jul 2003. (Cité en page 107.)

[Péry 2009] E. Péry, Blondel, W. C. P. M., J. Didelon, A. Leroux et F. Guillemin. *Simultaneous Characterization of Optical and Rheological Properties of Carotid Arteries via Bimodal Spectroscopy : Experimental and Simulation Results.* IEEE transactions on biomedical engineering, page 1267–1276, 2009. (Cité en page 30.)

[Rakotomanga 2019] Prisca Rakotomanga. *Inversion de modèle et séparation de signaux de spectroscopie optique pour la caractérisation in vivo de tissus cutanés.* PhD thesis, Université de Lorraine - Nancy, 2019. (Cité en pages xiii, 21, 39, 41 et 92.)

[Reble 2010] Carina Reble, Ingo H. Gersonde, Stefan Andree, Hans-Joachim Eichler et Jürgen Helfmann. *Quantitative Raman spectroscopy in turbid media.* Journal of Biomedical Optics, vol. 15, no. 3, pages 1 – 8, 2010. (Cité en page 37.)

[Robertson 2010] Karen Robertson et Jonathan L. Re. *Variation in Epidermal Morphology in Human Skin at Different Body Sites as Measured by Reflectance Confocal Microscopy.* Medical Journals Limited, vol. 90, pages 368–373, 2010. (Cité en page 62.)

[Saager 2010] Rolf B. Saager, Clement Kondru, Kendrew Au, Kelly Sry, Frederick Ayers et Anthony J Durkin. *Multilayer silicone phantoms for the evaluation of quantitative optical techniques in skin imaging.* Proc. SPIE 7567, Design and Performance Validation of Phantoms Used in Conjunction with Optical Measurement of Tissue II, 2010. (Cité en page 120.)

[Sardar 2001] Dhiraj K. Sardar, Michael L. MayoMelanin et Randolph D. Glickman. *Optical characterization of melanin.* Society of Photo-Optical Instrumentation Engineers, 2001. (Cité en page 121.)

[Sdobnov 2018] A. Y. Sdobnov, M. E. Darvin, E. A. Genina, J. Bashkatov A. N.and Lademann et V. V. Tuchin. *Recent progress in tissue optical clearing for spectroscopic application.* Spectrochimica Acta Part A : Molecular and Biomolecular Spectroscopy, vol. 197, page 216–229, 2018. (Cité en page 30.)

[Selifonov 2020] A. Selifonov, O. A. Zyuryukina, E. N. Lazareva, J. S. Skibina, M. Zagorovskaya, O. V. Syrova, O.Y. Aleshkina et V.V. Tuchin. *Measurement of Optical Properties of Human Gums and Dentin in the Spectral Range from 350 to 800 nm.* Izvestiya of Sarat. Univ. Physics., vol. 20, no. 4, pages 258 – 267, 2020. (Cité en page 137.)

[Shangguan 1998] HanQun Shangguan, Scott A. Prahl, Steven L. Jacques, Lee W. Casperson et Kenton W. Gregory M.D. *Pressure effects on soft tissues monitored by changes in tissue optical properties.* In Steven L. Jacques et Jeff Lotz, editeurs, Laser-Tissue Interaction IX, volume 3254, pages 366 – 371. International Society for Optics and Photonics, SPIE, 1998. (Cité en page 126.)

[Sharma 2014] Manu Sharma, Ricky Hennessy, Mia K. Markey et James W. Tunnell. *Verification of a two-layer inverse Monte Carlo absorption model using multiple source-detector separation diffuse reflectance spectroscopy.* Biomed. Opt. Express, vol. 5, no. 1, pages 40–53, Jan 2014. (Cité en pages 79 et 92.)

[Shen 2010] H. Shen et G. Wang. *A tetrahedron-based inhomogeneous Monte Carlo optical simulator.* Phys. Med. Biol., vol. 55, pages 947–962, 2010. (Cité en page 38.)

[SL. 2010] Jacques SL. *Optical assessment of cutaneous blood volume depends on the vessel size distribution: a computer simulation study.* J Biophotonics, vol. 3, pages 75–81, 2010. (Cité en page 88.)

[Smithies 1995] D. J. Smithies et P. H. Butler. *"Modeling the distribution of laser-light in port-wine stains with the Monte-Carlo method.* Phys. Med. Biol., vol. 40, pages 701–731, 1995. (Cité en page 38.)

[Sokolov 2002] K. Sokolov, M. Follen et R. Richards-Kortum. *Optical spectroscopy for detection of neoplasia.* Curr Opin Chem Biol., vol. 6, pages 651–658, 2002. (Cité en page 27.)

[Spinelli 2014] L. Spinelli, M. Botwicz, N. Zolek, M. Kacprzak, D. Milej, P. Sawosz, A. Liebert, U. Weigel, T. Durduran, F. Foschum, A. Kienle, F. Baribeau, S. Leclair, J.-P. Bouchard, I. Noiseux, P. Gallant, O. Mermut, A. Farina, A. Pifferi, A. Torricelli, R. Cubeddu, M. Mazurenka, H. Wabnitz, K. Klauenberg, O. Bodnar, C. Elster, M. Benazech-Lavou, Y. Berub, F. Lesage, D. Khoptyar, A. A. Subash, S. Andersson-Engels, P. Di Ninni, F. Martelli et G. Zaccanti1. *Determination of reference values for optical properties of liquid phantoms based on Intralipid and India ink.* BIOMEDICAL OPTICS EXPRESS, vol. 5, page 2037, 2014. (Cité en pages 120 et 128.)

[Stratonnikov 2001] Alexander Stratonnikov et Victor Loschenov. *Evaluation of blood oxygen saturation in vivo from diffuse reflectance spectra.* Journal of Biomedical Optics, vol. 6, pages 457–67, 11 2001. (Cité en pages 57 et 74.)

[Sun 2021] Chanjun Sun, Ben Aernouts et Wouter Saeys. *Bridging the gap between measurement-based and simulation-based metamodels for deriving bulk optical properties from spatially-resolved reflectance profiles: effect of illumination and detection geometry.* Opt. Express, vol. 29, no. 11, pages 15882–15905, May 2021. (Cité en pages 70 et 102.)

[Swartling 2003] Johannes Swartling, Antonio Pifferi, Annika M. K. Enejder et Stefan Andersson-Engels. *Accelerated Monte Carlo models to simulate fluorescence spectra from layered tissues.* J. Opt. Soc. Am. A, vol. 20, no. 4, pages 714–727, Apr 2003. (Cité en page 37.)

[Thueler 2003] Philippe Thueler, Igor Charvet, Frédéric P. Bevilacqua, Michel Saint Ghislain, G. Ory, Pierre Marquet, Paolo Meda, Ben Vermeulen et Christian D. Depeursinge. *In vivo endoscopic tissue diagnostics based on spectroscopic absorption, scattering, and phase function properties.* Journal of Biomedical Optics, vol. 8, no. 3, pages 495 – 503, 2003. (Cité en pages 102 et 136.)

[Tseng 2012] Sheng-Hao Tseng, Shih-Yu Tzeng, Yu-Kai Liaw, Chao-Kai Hsu, Julia Lee et Wan-Rung Chen. *Noninvasive evaluation of collagen and hemoglobin contents and scattering property of in vivo keloid scars and normal skin using diffuse reflectance spectroscopy: pilot study.* Journal of Biomedical Optics, vol. 17, no. 7, pages 1 – 12, 2012. (Cité en pages 55 et 77.)

[Tsui 2018] Sheng-Yang Tsui, Chiao-Yi Wang, Tsan-Hsueh Huang et Kung-Bin Sung. *Modelling spatially-resolved diffuse reflectance spectra of a multi-layered skin model by artificial neural networks trained with Monte Carlo simulations.* Biomed. Opt. Express, vol. 9, no. 4, pages 1531–1544, Apr 2018. (Cité en page 65.)

[Tuchin 2007] Valery Tuchin. Tissue optics: Light scattering and intruments for medical diagnostics. SPIE PRESS, 2007. (Cité en page 26.)

[Tuchin 2014] Valery Tuchin. Tissue optics: Light scattering and intruments for medical diagnostics. SPIE PRESS, 2014. (Cité en page 23.)

[Valdes 2011] Pablo A. Valdes, Frederic Leblond, Keith D. Paulsen, Anthony Kim, Brian C. Wilson, Olga M. Conde, Brent T. Harris et David W. Roberts. *Combined fluorescence and reflectance spectroscopy for in vivo quantification of cancer biomarkers in low- and high-grade glioma surgery.* Journal of Biomedical Optics, vol. 16, no. 11, pages 1 – 15, 2011. (Cité en page 30.)

[van de Hulst 1980] HC van de Hulst. *Multiple Light Scattering, Vol.1*, 1980. (Cité en page 119.)

[Vincely 2018] Vinoin Vincely et Karthik Vishwanath. *Extracting broadband optical properties from uniform optical phantoms using an integrating sphere and inverse adding-doubling.* Proc. SPIE 10486, Design and Quality for Biomedical Technologies XI, 2018. (Cité en page 120.)

[Vrabie 2007] V. Vrabie, C. Gobinet, O. Piot, A. Tfayli, P. Bernard, R. Huez et M. Manfait. *Independent component analysis of raman spectra : Application on paraffin-embedded skin biopsies.* Biomedical Signal Processing and Control, vol. 2, page 40–50, 2007. (Cité en page 29.)

[Wagnières 1998] Geroges A. Wagnières, Willem M. Star et Brian C. Wilson. *In vivo fluorescence spectroscopy and imaging for oncological applications.* Photochemistry and Photobiology, vol. 5, no. 68, pages 603–632, Aug 1998. (Cité en pages xiii et 27.)

[Wang 1995] Lihong Wang, Steven L. Jacques et Liqiong Zheng. *MCML—Monte Carlo modeling of light transport in multi-layered tissues.* Computer Methods and Programs in Biomedicine, vol. 47, no. 2, pages 131–146, 1995. (Cité en page 38.)

[Welch 1987] A. J. Welch, Yoon G et van Gemert MJ. *Practical models for light-distribution in laserirradiated tissue.* Opt. Lett., vol. 6, 1987. (Cité en page 38.)

[Welch 1997] A. J. Welch, Craig Gardner, Rebecca Richards-Kortum, Eric Chan, Glen Criswell, Josh Pfefer et Steve Warren. *Propagation of fluorescent light.* Lasers Surg. Med., vol. 21, pages 166–178, 1997. (Cité en page 37.)

[Wu 2006] Yicong Wu et Jianan Y. Qu. *Autofluorescence spectroscopy of epithelial tissues.* Journal of Biomedical Optics, 2006. (Cité en page 65.)

[Ye Yuan 2008] Patricia Relue Ye Yuan. *Enzymatic degradation of human skin dermis revealed by fluorescence and reflectance spectroscopy.* Opt. Exp., vol. 16, 2008. (Cité en page 54.)

[Yoo 1990] K. M. Yoo et R. R. Alfano. *Determination of the scattering and absorption lengths from the temporal profile of a backscattered pulse.* Opt. Lett., vol. 15, 1990. (Cité en page 38.)

[Yu 2011] Bing Yu, Henry L. Fu et Nirmala Ramanujam. *Instrument independent diffuse reflectance spectroscopy.* Journal of Biomedical Optics, vol. 16, no. 1, pages 1 – 12, 2011. (Cité en page 102.)

[Yudovsky 2010] Dmitry Yudovsky et Laurent Pilon. *Rapid and accurate estimation of blood saturation, melanin content, and epidermis thickness from spectral diffuse reflectance.* Appl. Opt., vol. 49, no. 10, pages 1707–1719, Apr 2010. (Cité en pages 79 et 88.)

[Zamora-Rojas 2013] Eduardo Zamora-Rojas, Ben Aernouts, Ana Garrido-Varo, Dolores Pérez-Marín, José Emilio Guerrero-Ginel et Wouter Saeys. *Double integrating sphere measurements for estimating optical properties of pig subcutaneous adipose tissue.* Elsevier, Innovative Food Science and Emerging Technologies, vol. 19, page 218–226, 2013. (Cité en page 121.)

[Zhang 2016] Hairong Zhang, Daniel C. Salo, David M. Kim, Sergey Komarov, Yuan-Chuan Tai et Mikhail Y. Berezin. *Penetration depth of photons in biological tissues from hyperspectral imaging in shortwave infrared in transmission and reflection geometries.* Journal of Biomedical Optics, vol. 21, no. 12, pages 1 – 10, 2016. (Cité en page 55.)

[Zhu 2011] Caigang Zhu et Quan Liu. *Validity of the semi-infinite tumor model in diffuse reflectance spectroscopy for epithelial cancer diagnosis: a Monte Carlo study.* Opt. Express, vol. 19, no. 18, pages 17799–17812, Aug 2011. (Cité en page 88.)

[Zhu 2013a] Caigang Zhu et Quan Liu. *Review of Monte Carlo modeling of light transport in tissues.* Journal of Biomedical Optics, vol. 18, 2013. (Cité en pages xiv et 37.)

[Zhu 2013b] D. Zhu, K. V. Larin, Q. Luo et V. Tuchin. *Recent progress in tissue optical clearing.* Laser and photonics reviews, vol. 7, page 732–757, 2013. (Cité en page 30.)

[Šćepanović 2009] Obrad R. Šćepanović, Zoya Volynskaya, Chae-Ryon Kong, Luis H. Galindo, Ramachandra R. Dasari et Michael S. Feld. *A multimodal spectroscopy system for real-time disease diagnosis.* REVIEW OF SCIENTIFIC INSTRUMENTS, vol. 80, 2009. (Cité en page 30.)

Modélisation et estimations des propriétés optiques de la peau humaine à l'aide de spectroscopie d'autofluorescence et reflectance diffuse résolues spatialement

Résumé : Dans le contexte du carcinome cutané, la biopsie optique offre une alternative *in-vivo* non destructive à la biopsie conventionnelle pour informer le praticien dermatologue de l'état de santé du tissu en profondeur lors de la résection du cancer. Ce dernier est en effet à l'origine de modifications morphologiques et physiologiques de la peau, ce qui explique que les mesures optiques resultantes des interactions lumière/tissue y soient sensibles.
Les travaux présentés dans ce manuscrit exploitent les données obtenues l'aide du dispositif de biopsie optique *SpectroLive* sur une centaine de patients juste avant la résection du cancer par le clinicien. Au contact de la peau, ce dispositif spectroscopique acquiert des signaux de réflectance diffuse (excitation large bande blanche) et d'autofluorescence (émission monochromatique pour exciter les fluorophores endogènes de la peau) résolus spatialement, *i.e.*, pour plusieurs distances de séparation entre la fibre émettrice de lumière est les fibres collectrices en périphérie. Cette résolution spatiale est particulièrement d'intérêt pour la peau, puisque les différentes distances introduites permettent de collecter des photons parcourant les différentes couches en profondeur (épiderme, derme et hypoderme) de l'organe.
L'essentiel des travaux présentés ici concerne l'estimation des propriétés optiques de la peau grâce à la résolution du problème inverse à partir de ces acquisitions cliniques. Cela consiste d'abord à établir une simulation de transport de photons fidèle aux caractéristiques (géométriques et spectrales) du dispositif réel avant de construire un modèle multicouche de la peau dans lequel les paramètres optiques (*e.g.* coefficients d'absorption et de diffusion, le facteur d'anisotropie) et géométriques (*e.g.* épaisseur des couches) peuvent être estimées par un processus d'optimisation visant à minimiser les différences entre les spectres générés par la simulation et les spectres "cibles" obtenus en clinique.
Dans ce but, les contributions principales développées dans ce manuscrit sont d'abord le développement et l'exploitation totale de la simulation, avec notamment une étude visant à caractériser la pénétration des photons détectés aux différentes séparation source/détecteur, et ceci pour différents modèles de peau afin de représenter les différences inter- et intra-individu. Les connaissances acquises avec cette étude de profondeurs sondées sont ensuite utilisées dans la seconde contribution majeure, visant à adapter le processus d'estimations des propriétés optiques à partir des spectres cliniques (problème inverse) à la peau. Enfin, la dernière contribution, plus métrologique, est l'élaboration d'un banc optique à double sphères intégrantes permettant d'obtenir ces mêmes propriétés optiques pour un échantillon *ex-vivo*, et ainsi permettre la comparaison des estimations issues des deux modalités.

Mots clés : Spectroscopie tissulaire, Carcinome cutané, Reflectance diffuse, Autofluorescence, Simulation de transport de photons, Estimation de propriétés optiques, Biophotonique

Modeling and estimation of human skin optical properties using spatially resolved autofluorescence and diffuse reflectance spectroscopy

Abstract: In the context of cutaneous carcinoma, optical biopsy offers a *in-vivo* non-destructive alternative to conventional biopsy to inform the dermatologist of the state of health of the deep tissue during cancer resection. The latter is indeed at the origin of morphological and physiological modifications of the skin, which explains why the optical measurements resulting from the light/tissue interactions are sensitive to it.

The work presented in this manuscript exploits the data obtained with the optical biopsy device *SpectroLive* on about a hundred patients just before cancer resection by the clinician. In contact with the skin, this spectroscopic device acquires diffuse reflectance (white broadband excitation) and autofluorescence (monochromatic emission to excite endogenous fluorophores in the skin) spatially resolved signals, *i.e.*, for several separation distances between the light emitting fiber and the collecting fibers at the periphery. This spatial resolution is of particular interest for the skin, since the different distances introduced allow the collection of photons traveling through the different layers in depth (epidermis, dermis and hypodermis) of the organ.

The main part of the work presented here concerns the estimation of the optical properties of the skin by solving the inverse problem from these clinical acquisitions. This consists first in establishing a photon transport simulation faithful to the characteristics (geometrical and spectral) of the real device before building a multilayer model of the skin in which the optical parameters (*e.g.* absorption and scattering coefficients, the anisotropy factor) and geometrical parameters (*e.g.* layer thickness) can be estimated by an optimization process aiming at minimizing the differences between the spectra generated by the simulation and the "target" spectra obtained in clinic.

The main contributions developed in this manuscript are first the development and the full exploitation of the simulation, with in particular a study whose purpose is to characterize the penetration of the photons detected at the various source/detector separations, and this for various skin models in order to represent the inter- and intra-individual differences. The knowledge acquired with this study of probed depths is then used in the second major contribution, aiming at adapting the process of estimating optical properties from clinical spectra (inverse problem) to the skin. Finally, the last contribution, more metrological, is the development of an optical bench with double integrating spheres allowing to obtain these same optical properties for a sample *ex-vivo*, and thus to allow the comparison of the estimates resulting from the two modalities.

Keywords: Tissue spectroscopy, Skin carcinoma, Diffuse reflectance, Autofluorescence, Photon transport simulation, Optical properties estimation, Biophotonics